Propagation Handbook for Wireless Communication System Design

Robert K. Crane

CRC PRESS

Boca Raton London New York Washington, D.C.

Library of Congress Cataloging-in-Publication Data

Crane, Robert K., 1935-
Propagation handbook for wireless communication system design / Robert K. Crane.
p. cm. — (Electrical engineering and applied signal processing series; 13)
Includes bibliographical references and index.
ISBN 0-8493-0820-8 (alk. paper)
1. Radio wave propagation—Mathematical models—Handbooks, manuals, etc. 2. Wireless communication systems—Handbooks, manuals, etc. I. Title. II. Series.

TK6552.C73 2003
621.384'11—dc21 2003043556

International Standard Book Number 0-8493-0820-8
Library of Congress Card Number 2003043556
Printed in the United States of America 1 2 3 4 5 6 7 8 9 0
Printed on acid-free paper

Preface

Wireless means different things to different people. For this book, it refers to the radio systems that provide point-to-point, point-to-multipoint, and Earth-space communications over transmission links that propagate outside buildings through the lower atmosphere. Wireless systems are being built that provide data transmission between computers and other devices on one's own desk. These are part of the wireless world but not the part where, except for interference perhaps, the atmosphere has any influence. The intent of this book is to provide a description of the physical phenomena that can affect propagation through the atmosphere, present sample measurements and statistics, and provide models that system designers can use to calculate their link budgets and estimate the limitations the atmosphere may place on their design.

In the late 1980s, the National Aeronautics and Space Administration (NASA) embarked on an observation program to provide propagation data to aid in the design of the next generation satellite communication systems, employing small and very small aperture antennas at the ground terminals. The Advanced Communication Technology Satellite (ACTS) was launched in 1993 and the ACTS propagation experiment began collecting calibrated data on January 1, 1994. The author was chair of the science panel for this experiment. The seven-site data collection phase of the experiment lasted for 5 years. The experiment was designed to collect data in climate regions that had not been previously explored and, at the same time, collect additional data at two locations that had been previously studied. An interim report of this experiment was published in 1997 (*Proc. IEEE*, June 1997), but no final reporting has been attempted. Many of the sample measurements presented in this book came from the ACTS propagation experiment. Some results from the entire 5-year observation set are presented. As a result of analyses of the ACTS data, several new propagation models were developed, which are explained in detail in this book.

The propagation models presented in this book are useful for long and short terrestrial paths and Earth-space paths. They are not specific to a small band of frequencies, but will be useful as systems are designed to operate at higher and higher frequencies. Propagation modeling should not be viewed as a mature science. Improved models will become available as we move to the higher frequencies or to new climates. An attempt has been

made to discuss the physical bases of each model and occasionally to indicate directions for improvement. Some of the measurements and modeling results presented in this book come from earlier unpublished work by the author. They are included to expand on and support some of the more recent results.

Chapter 5 presents a new model for the prediction of rain-rate statistics and a revision and improvement of the author's two-component model for the prediction of rain-attenuation statistics. The improved models predict rain-rate and attenuation statistics for monthly, seasonal, and annual time periods. The models also provide a prediction of the expected yearly variations of measured distributions about the predictions. Empirical distributions from the ACTS propagation experiment for annual, seasonal, and monthly time periods are presented to confirm the applicability of the new models. The use of these models to predict space diversity improvement or worst-month statistics has not changed from that given in an earlier monograph and is not considered here.

This book focuses on propagation effects that can affect the availability of a communication channel. It does not consider interference problems, although they in turn may affect availability. The propagation models presented in the book can be coded for use in a spreadsheet or in a stand-alone program that runs on a personal computer. No programs are included with the book. A list of symbols is included at the end of each chapter. Some of the symbols have different meanings in different sections.

The author wishes to acknowledge the patience and support of his wife especially during the time taken to prepare this book. The author wishes to acknowledge the support provided by NASA, NSF, and the U.S. Army and Air Force with his research over the past four decades.

Robert K. Crane
Grantham, New Hampshire

Contents

chapter one

Propagation phenomena affecting wireless systems

1.1 Types of systems

The phrase *wireless system* refers to any system that uses electromagnetic waves to transfer information from one location to another without using wires. The applications can include transmitting voice between hand-held walkie-talkies, transmitting data from a satellite to ground or from one computer to another within a room, or using radar to sense rain. This handbook considers only the propagation of electromagnetic waves in the microwave through millimeter wave radio frequency spectrum, 0.3 through 300 gigaHertz (GHz). These frequencies lie in the ultra high (UHF: 0.3 to 3 GHz), super high (SHF: 3 to 30 GHz), and extra high (EHF: 30 to 300 GHz) communication bands. Frequency bands are often referenced by their radar band designations as shown in Table 1.1. Actual band identification is often less precise than that indicated in the table. For fixed satellite communication services, Ka band refers to the 20- to 30-GHz frequency range.

This handbook focuses on transmission in and through the lower atmosphere, the region of the atmosphere where weather phenomena occur. The properties of the lower atmosphere are highly variable and change hourly, daily, monthly, and yearly. Their effects on radio wave propagation produce random variations in the amplitude, phase, frequency, polarization, coherence bandwidth, delay spread, and propagation direction of the electromagnetic waves. Knowledge of the statistics of one or more of these effects may be necessary for system design.

A wireless system of considerable interest is the cellular system. For this system, the domain of interest is subdivided into a number of smaller cells with transmitters and receivers that handle communications within each cell or complex of cells. The organization and structure of a cellular system are not considered in this handbook, but the statistics of the properties of a transmission channel between a transmitter and receiver in a cell and the joint statistics for multiple transmission paths within a cell or between cells

Table 1.1 Frequency Band Nomenclatures

Radar band	Lowest frequency (GHz)	Highest frequency (GHz)	Communication band
UHF	0.3	1	UHF
L	1	2	UHF
S	2	4	UHF/SHF
C	4	8	SHF
X	8	12	SHF
Ku	12	18	SHF
K	18	27	SHF
Ka	27	40	SHF/EHF
V	40	75	EHF
W	75	110	EHF
Mm	110	300	EHF

are. The context is the statistics for a single path and the joint statistics for multiple paths.

Much propagation data has been collected for use in the design of fixed service satellite and terrestrial communication systems. Fixed service means a communication system employing fixed terminals on the Earth's surface. For satellite systems, the satellite can be in geostationary orbit or in any other orbit that produces a variation in the pointing direction from the fixed ground station to the satellite. Considerable data has also been collected for cellular systems and mobile satellite systems. Published annual attenuation statistics are available from many locations in Europe and North America. Some data are available from other locations too. Study Group 3 of the Radiocommunication Study Groups of the International Telecommunications Union (ITU-R) provides data banks for model development and verification and for use in system design.[1] The empirical statistics in the data banks for fixed service systems are generally for observations of limited duration, that is, from records that span only 1 to 5 years. The data collected for mobile service systems are more limited. Models that summarize the data in the data banks will provide a better estimate of the expected statistics for a particular path than the empirical results from measurements of limited duration on that path.

Point-to-multipoint fixed line-of-sight terrestrial systems are now in development, using frequencies in the EHF band. Long-duration empirical statistics are not available at frequencies above 30 GHz for single paths or joint statistics for two or more paths originating from a single point. Physical propagation models are required to extend predictions to locations or conditions where adequate observations are not available. These models can be validated using data from available data banks. The extrapolation of empirical curve-fitting or regression models is not recommended.

This handbook describes physical propagation models for the prediction of statistics for a wide variety of communication, broadcast, navigation, radar, and remote sensing systems operating in the UHF, SHF, and EHF

communication frequency bands. The models are developed from meteorological data and depend on the availability of climate data. The models were validated over limited ranges by comparing with available data. Error statistics are presented for each model. Where possible, the expected interannual variability of the predictions is presented to establish the risk associated with a prediction. The expected prediction uncertainty is used when comparing predictions to empirical statistics.

1.2 *Design criteria*

Communication systems are designed to specific availability requirements. For the simplest transmission path between a single transmitting antenna and a single receiving antenna, the amplitude of the received signal relative to the unwanted noise in the receiver may be the statistic of interest. If the received signal level is too low, the signal may not be detected in the noise; if too high, nonlinear receiver effects may distort the signal and render it unintelligible. The error rate for a digital communication link depends on the signal-to-noise ratio as well as other factors. The statistics of the signal-to-noise ratio are therefore important. The signal-to-noise ratio depends on the receiver design, the gains and losses of the transmitting and receiving antennas, the modulation and coding of the transmitted signal, the transmitted signal power, the path loss between the antennas, and the possibility of interference from other transmitters. Availability is the fraction of time that the communication link is available for use with a signal-to-noise that exceeds the design specification for a given error performance. The outage time is the fraction of time for which the desired error performance is not obtained.

The atmosphere may affect the performances of the antennas and transmission path (Figure 1.1). At frequencies above 10 GHz and depending on antenna design, rainwater or wet snow on an antenna may reduce the magnitude of the received signal (increase the path loss). The geometric spreading of the electromagnetic energy transmitted by the antenna produces a change in signal strength with distance along the path to the receiving antenna. Water vapor and oxygen in the atmosphere may cause signal absorption on the path, producing a loss or attenuation relative to the geometric spreading. Scattering by clouds and rain produce an excess attenuation relative to the geometrical spreading and gaseous absorption. For a particular path, the total attenuation, gaseous absorption plus excess attenuation, changes with time as clouds and rain drift across the path and temperature and humidity change along the path. The statistics of changing path loss may therefore be important in the design of a system. Depending on carrier frequency and path length through the atmosphere, the total attenuation statistics may constrain system design.

Time series of attenuation observations at two Ka-band frequencies on an Earth space path for a single day with rain is presented in Figure 1.2. The beacon transmitters were on the NASA ACTS. The receiver was located in

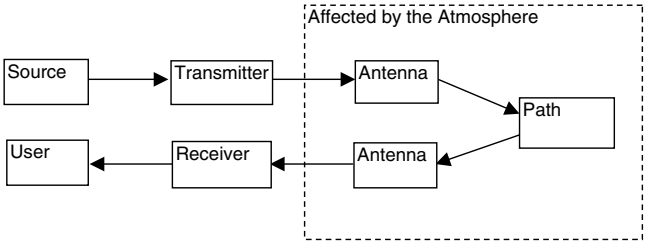

Figure 1.1 Block diagram for a single path.

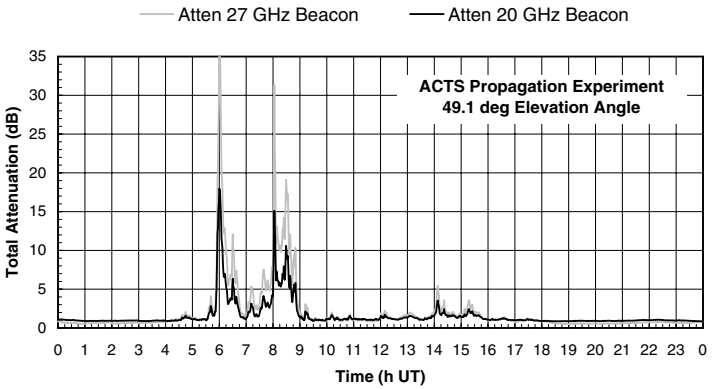

Figure 1.2 Total attenuation time series for Norman, OK, on July 25, 1994.

Norman, OK. The data were collected as a part of the ACTS propagation experiment.[2] The measurements are 1-min averages of the received signal plus receiver noise. The dynamic range of the system set the maximum observable total attenuation to about 30 decibels (dB). When only receiver noise was present, the total attenuation values were set to 35 dB. For this day, the attenuation produced by gaseous absorption during clear-sky conditions, before 3:30 universal or Greenwich Mean Time (UT) and after 18:30 UT, was near 1 dB at 20.2 GHz and lower, at about 0.6 dB, at 27.5 GHz.

The time series of rain rate observed at a collocated rain gauge is presented in Figure 1.3. In this figure, a second estimate is presented for the 1-min average rain rate to extend the dynamic range to lower rates. Total attenuation values at 20.2 GHz exceeded 10 dB during the two rain events, indicated by rain rates in excess of a few millimeters/hour (mm/h). The total attenuation observed on the path did not vary in direct proportion to the rain rate observed at a point a few feet from the receiving antenna aperture. The lower attenuation events were due to clouds along the path. The event just after 14:00 UT may have had some light rain as well as clouds on the path.

The occurrences of attenuation events such as those shown in Figure 1.2 are random and must be treated statistically. Figure 1.4 presents empirical

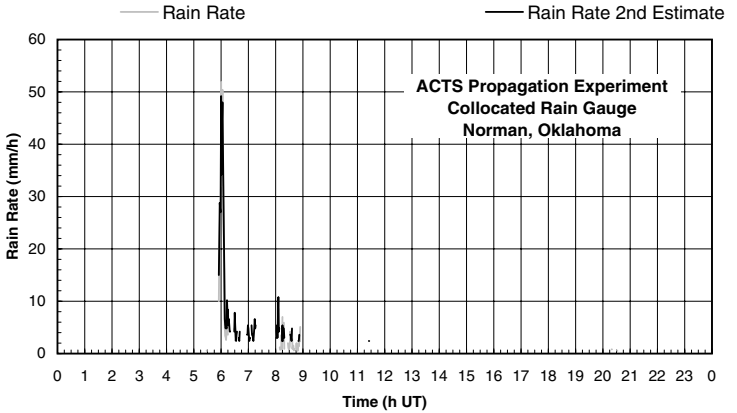

Figure 1.3 Rain rate time series for Norman, OK, on July 25, 1994.

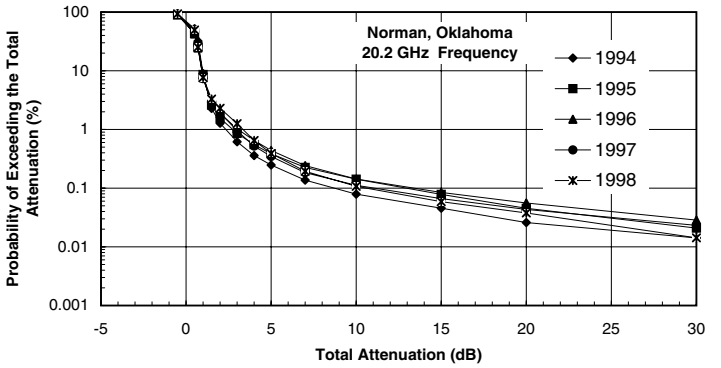

Figure 1.4 Empirical annual distribution functions for total attenuation at 20.2 GHz for Norman, OK.

annual probability distributions for total attenuation observed over a 5-year period at the Norman, OK, site.[3] The empirical distribution functions (EDFs) give the probability of exceeding the attenuation indicated on the abscissa for each year of observation. The probabilities are expressed in percentage of a year. The distributions were compiled from continuous observations of 1-sec average signal levels. If the system design could maintain the desired error rate with a total attenuation of 5 dB, outages would occur on this path between 1300 and 2300 min/year, depending on the year. For this path, at a higher frequency of 27.5 GHz and the same total attenuation threshold, the outages would range from 3200 to 5200 min/year.

The several atmospheric phenomena that affect this path have different seasonal dependencies. Figure 1.5 presents the average annual EDF for the 5-year period together with the 5-year average EDFs for each season. The probability of exceeding a specified attenuation is higher in the summer than

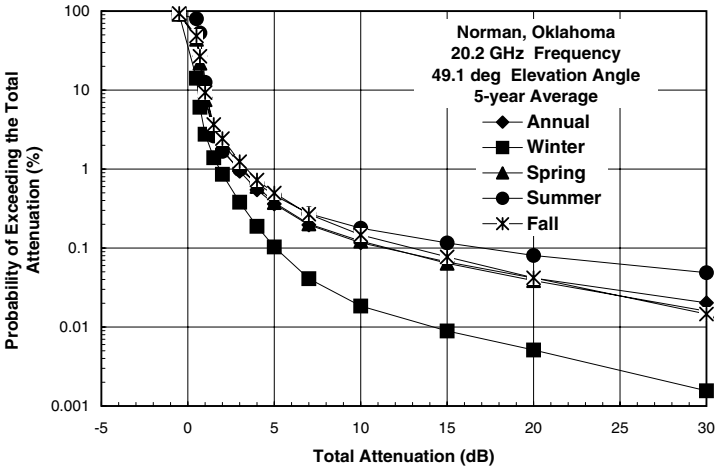

Figure 1.5 Empirical seasonal distribution functions for total attenuation at 20.2 GHz for Norman, OK.

in the winter for the Oklahoma site. Gaseous absorption by oxygen and water vapor is present all the time. In the summer, with higher temperatures, the increased water vapor produces measurable attenuation as much as 80% of the time. Clouds affected the path for from 2% to perhaps 20% of the average year. At lower percentages, attenuation by rain on the path and on the antenna reflector and feed produces attenuation values ranging from a few decibels to above 30 dB and could cause a complete loss of signal.

Seasonal variations in attenuation statistics indicate that the processes that produce the attenuation are not stationary over periods shorter than a year. These processes can be considered cyclostationary. Empirical annual statistics therefore have to be collected from measurements made over a full year or an integral number of years. Statistics for a particular month can be collected for a number of years, but only during that month of the year.

The attenuation statistics presented in Figure 1.4 and Figure 1.5 can arise from attenuation events as short as 1 sec or as long as several hours. If all the fades were of very short duration, say 1 sec or less, they may not be significant. If they were much longer, say 1 h or more, they may disrupt communication. A second statistic of interest for system design is the fade duration distribution. Figure 1.6 presents the fade duration distribution for total attenuation events of 5 dB or higher that occurred during the 5-year measurement program. A large number of very short fades are evident, but a significant number of fades had durations longer than 1 min and a few were longer than 1 h.

The yearly variations in the EDFs shown in Figure 1.4 may also be important for system design. The performance specifications may require a design that is compromised only once in a specified number of years. The risk to be assigned to a particular design threshold must then be assessed.

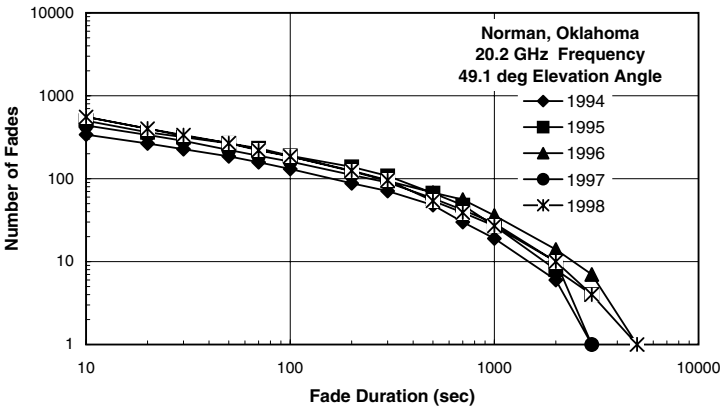

Figure 1.6 Empirical annual distribution functions for fade duration at 20.2 GHz for Norman, OK.

Design to the median expected performance of a link would be successful only for half the years the system is in operation.

1.3 Antenna considerations

Wireless systems use antennas to transmit and receive electromagnetic waves. The antennas may be wire antennas, aperture antennas, arrays of wire or aperture antennas, or reflector antennas with the energy fed to the reflector by a combination of antennas. Often an antenna is covered or enclosed by a radome to protect it from the weather. Depending on the antenna and radome design, some antennas are more susceptible than others to a loss of gain due to rainwater or wet snow on the antenna or radome, or both. The ground terminal antenna used to collect the data presented in Figure 1.2 to Figure 1.6 could suffer from a signal reduction of over 24 dB due to wet snow on the reflector.[4] Snow events were censored from the data prior to compiling the statistics presented in the figures. Rainwater on the antenna reflector and radome over the antenna feed could produce an additional 5 dB or more loss at high rain rates.[5] The EDFs presented in these figures were not corrected for the effects of rainwater on the antenna.

1.3.1 Transmission loss

The antennas at each end of a path direct the electromagnetic energy toward each other. The equation for free space propagation between two antennas is given by the Friis transmission equation:[6]

$$\left(\frac{P_R}{P_T}\right) = \left(\frac{G_T G_R \lambda^2}{(4\pi R)^2}\right) g_T(\theta,\phi) g_R(\theta',\phi') \tag{1.1}$$

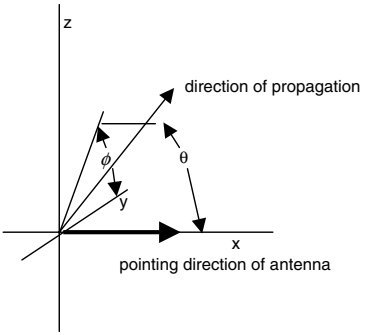

Figure 1.7 Spherical coordinate system for antenna gain analysis.

where P_T and P_R are the transmitted, T, and received, R, powers, respectively; G_T and G_R the transmitting and receiving antenna gains, respectively; λ the wavelength of the electromagnetic wave, R the distance between the antennas, and $g_T(\theta,\phi)$ and $g_R(\theta,\phi)$ the relative directive gains at spherical angles (θ, ϕ) measured from the pointing direction of each antenna (Figure 1.7) with a convenient reference direction for ϕ. The transmission loss equation is often expressed in decibels:

$$P_R = P_T\left(\frac{G_T G_R \lambda^2}{(4\pi R)^2}\right) g_T(\theta,\phi) g_R(\theta',\phi')$$

$$\mathbf{P_R} = 10Log_{10}(P_R) = 10Log_{10}\left(\frac{P_T G_T g_T G_R g_R \lambda^2}{(4\pi R)^2}\right)$$

$$\mathbf{P_R} = \mathbf{P_T} + \mathbf{G_T} + \mathbf{g_T} + \mathbf{G_R} + \mathbf{g_R} + 20Log_{10}(\lambda) - 20Log_{10}(R) - 22 \qquad (1.2)$$

$$\mathbf{L} = \mathbf{P_T} - \mathbf{P_R} = -\left(\mathbf{G_T} + \mathbf{g_T} + \mathbf{G_R} + \mathbf{g_R} + 20Log_{10}(\lambda) - 20Log_{10}(R) - 22\right)$$

$$\mathbf{L_B} = -\left(20Log_{10}(\lambda) - 20Log_{10}(R) - 22\right)$$

where **L** is the transmission loss, $\mathbf{L_B}$ the basic transmission loss; the powers, **P**, are in decibels, the antenna gains, **G**, in decibels relative to an isotropic antenna (dBi), and the range (or distance) and wavelength are in the same units of length. The basic transmission loss is just the free space loss, that is, the loss between two isotropic antennas. If the unit of power is a watt, the power is in decibel watt (dBW). In many applications, it is convenient to mix some of the units. For antennas pointed toward each other to maximize their gains, $g_T(\theta,\phi) = 1$ and $g_R(\theta,\phi) = 1$; for $\lambda = c/f$ with frequency, f, in gigaHertz and $c \approx 3 \times 10^8$ m/s the speed of light. For range in kilometers and for received power expressed in milliwatts and transmitter power in watts, the transmission equation becomes:

$$\mathbf{P_R} = \mathbf{P_T} + \mathbf{G_T} + \mathbf{G_R} - 20Log_{10}(f) - 20Log_{10}(R) - 62.4 \quad \text{dBm} \tag{1.3}$$

The directive gain of an antenna, D, is:

$$eD(\theta,\phi) = Gg(\theta,\phi) \tag{1.4}$$

where e is the antenna efficiency. The directive gain of an antenna describes the ability of the antenna to concentrate the energy radiated by the antenna in a specified direction. It is the ratio of the energy propagating in the specified direction to the energy that would have been transmitted in that direction by an isotropic antenna.[7] For an isotropic antenna, the energy transmitted per unit solid angle is $P_T/4\pi$. The radiated power flux density (the magnitude of the time average Poynting vector, the radiated power per unit area per unit solid angle) at a distance R from an isotropic antenna is $S = P_T/4\pi R^2$. The power collected by a receiving antenna is the power flux density times the effective area of the receiving antenna normal to the direction of propagation, A_e. The gain of a receiving antenna is related to A_e by $G_R = 4\pi/\lambda^2\ A_e$. The free space loss between the two antennas is then given by $\lambda^2/(4\pi R)^2$. The gain of an antenna differs from the directive gain for that antenna by accounting for losses in the antenna.

The transmission equation considers only the geometric spreading of the electromagnetic energy in the propagating wave, the far-field directive gain of each antenna, and the antenna efficiency. It is for the idealized situation, with no adjustment for the possible polarization mismatch, weather-induced radome or reflector loss, or attenuation along the path through the atmosphere. It is also for use when only one propagation path exists between the antennas. A more complete representation of the transmission loss identifies the factors that can be affected by the atmosphere (Figure 1.8).

$$\left(\frac{P_R}{P_T}\right) = \left(\frac{G_T G_R \lambda^2}{(4\pi R)^2}\right) g_T(\theta,\phi) g_R(\theta',\phi') m \cdot 10^{-\left(0.1\left(\mathbf{A}_T + \mathbf{A}_R + \int_0^R \alpha dr\right)\right)} \tag{1.5}$$

where $\mathbf{A_R}$ and $\mathbf{A_T}$ are the losses (dB) due to environmental effects on the antennas, m the signal reduction due to a polarization mismatch between the receiving antenna and the incoming electromagnetic wave, and α the specific attenuation (dB/km for r in km) due to atmospheric processes along the propagation path. The transmitter power may be measured at some convenient location along the transmission line or wave guide connecting the transmitter and antenna. The antenna gain is then calculated relative to that reference point (or plane). The attenuation produced by the atmosphere is a loss in addition to the geometrical spreading loss. A mismatch can occur when the polarization of the incoming wave differs from the polarization expected for the antenna design. The equation for basic transmission loss is for the

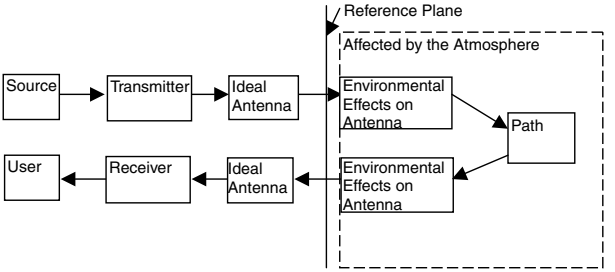

Figure 1.8 Block diagram showing the reference plane for propagation loss calculations.

path between the antennas. It includes any attenuation due to the propagation medium, polarization mismatch, and any antenna losses not included in the antenna gains.

In some applications, the receiving antenna may collect energy from more than one path. The antenna will combine coherently the signals from the several paths incident on it. In this case, the amplitude and relative phase of each signal are important because it is the phasor sum of the signals that the antenna will present to the receiver. The amplitude and phase of the spherically spreading far-field electromagnetic wave radiated by an antenna are given by:

$$E = E_0 \frac{e^{-j(kR-\omega t)}}{4\pi R}$$

$$S = \frac{EE^*}{2\eta_0} = \frac{E_0 E_0^*}{32\eta_0 \pi^2 R^2} \tag{1.6}$$

$$|E_0| = \sqrt{8\pi\eta_0 P_T G_T g_T}$$

where $j = \sqrt{-1}$, $k = 2\pi/\lambda = 2\pi f/c$, $\omega = 2\pi f$, t is time, f the frequency, c the speed of light, η_0 the impedance of free space, and E^* is the complex conjugate of E. For two paths operating at the same frequency, the received power is then given by:

$$E = E_1 + E_2 = \frac{e^{j\omega t}}{4\pi}\left(E_{01}\frac{e^{-j(kR_1)}}{R_1} + E_{02}\frac{e^{-j(kR_2)}}{R_2}\right)$$

$$E = \frac{\sqrt{8\pi\eta_0}\,e^{j\omega t}}{4\pi}\left(\sqrt{P_{T1}G_{T1}g_{T1}}\frac{e^{-j(kR_1)}}{R_1} + \sqrt{P_{T2}G_{T2}g_{T2}}\frac{e^{-j(kR_2)}}{R_2}\right) \tag{1.7}$$

$$P_R = \frac{\lambda^2 G_R}{(4\pi)^2}\left|\sqrt{P_{T1}G_{T1}g_{T1}g_{R1}}\frac{e^{-j(kR_1)}}{R_1} + \sqrt{P_{T2}G_{T2}g_{T2}g_{R2}}\frac{e^{-j(kR_2)}}{R_2}\right|^2$$

This equation can be simplified to:

$$P_R = \left(\frac{\lambda}{4\pi}\right)^2 G_R \left(\frac{P_{T1} G_{T1} g_{T1} g_{R1}}{R_1^2} + \frac{P_{T2} G_{T2} g_{T2} g_{R2}}{R_2^2} + \frac{2\sqrt{P_{T1} G_{T1} g_{T1} g_{R1} P_{T2} G_{T2} g_{T2} g_{R2}}}{R_1 R_2} \cos(k(R_2 - R_1)) \right) \tag{1.8}$$

If the two paths originate from the same transmitting antenna:

$$\frac{P_R}{P_T} = \left(\frac{\lambda}{4\pi}\right)^2 G_T G_R \left(\frac{g_{T1} g_{R1}}{R_1^2} + \frac{g_{T2} g_{R2}}{R_2^2} + \frac{2\sqrt{g_{T1} g_{R1} g_{T2} g_{R2}}}{R_1 R_2} \cos(k(R_2 - R_1)) \right) \tag{1.9}$$

Further, if the relative directive gains are near unity and the path lengths are only slightly different:

$$\frac{P_R}{P_T} = \frac{2 G_T G_R \lambda^2}{(4\pi R)^2} \left(1 - \cos(k\Delta R)\right) \tag{1.10}$$

where $\Delta R = R_2 - R_1$ and $\Delta R/R_1 << 1$. The nearly equal received signals from the two paths can then combine to produce a received power that varies from zero to four times the power on one of the paths.

1.3.2 *Antenna beamwidth*

The directive gain of an antenna describes its antenna pattern, that is, the variation in directive gain about pointing direction of the antenna. Figure 1.9 presents the principal plane patterns for a 10-wavelength square-aperture antenna. The beamwidth of an antenna is the angle enclosing the main lobe or twice the angle between the boresight direction and a reference power on the main lobe of the antenna pattern. Several different beamwidth definitions are in use: the half-power beamwidth, the tenth-power beamwidth, and the beamwidths between nulls. The half-power beamwidth, Θ_H, for this antenna is 5.06°. The maximum directive gain or directivity may be approximated by:

$$D_0 = D(0,0) \approx \frac{4\pi}{\Theta_{H1} \Theta_{H2}} \tag{1.11}$$

where the half-power beamwidths for the two principal planes are in radians. For the 10-wavelength square aperture, the maximum directive gain is approximately 1610 or 32 dBi. The theoretical directivity for this antenna is 31 dBi.

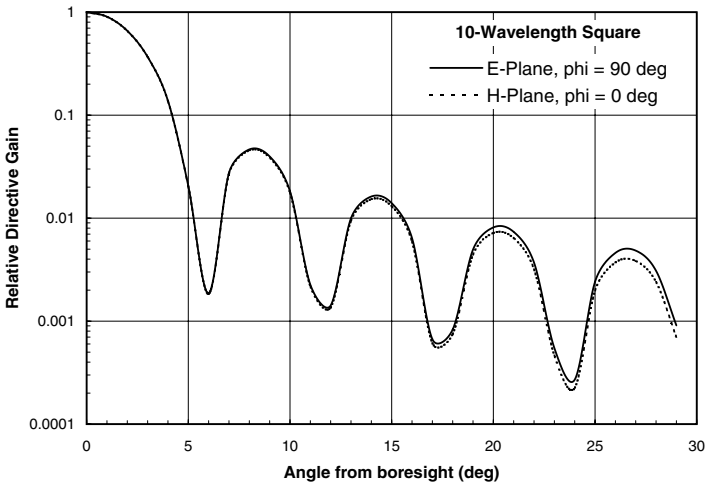

Figure 1.9 Relative directive gain for a uniformly illuminated 10-wavelength square aperture.

The far-field half-power beamwidth is approximately inversely proportional to the dimension of the antenna in wavelengths in the plane used to calculate the beamwidth.

$$\Theta_H = C\left(\frac{\lambda}{d}\right) \tag{1.12}$$

where C is the proportionality coefficient for beamwidth and d is the maximum dimension in the plane of the half-power beamwidth. For a rectangular aperture with a constant phase and uniform amplitude distribution across the aperture, $C = 0.88$. The directivity factor, δ, relates the directivity to the directivity for a uniform aperture illumination:

$$D_0 = \delta\frac{4\pi A}{\lambda^2} \tag{1.13}$$

where A is the aperture area and for uniform illumination $\delta = 1$. For a circular aperture with a constant phase and uniform amplitude distribution, $C = 1.02$ and $\delta = 1$. The first sidelobe peak is –13.2 dB for a rectangular aperture and –17.6 dB for the circular aperture. If the illumination amplitude distribution is tapered across an aperture, the first sidelobe level decreases, the directivity factor decreases, and the proportionality coefficient for beamwidth increases. For a uniform phase and a $[1–(2r/d)^2]^n$ amplitude distribution where r is distance across the aperture from its center, the directivity factor, first sidelobe level, and efficiency are given in Table 1.2.

Table 1.2 Coefficients for a Circular-Aperture Antenna

n	δ	C	First sidelobe level
0	1.00	1.02	–17.6
1	0.75	1.27	–24.6
2	0.56	1.47	–30.6

Source: From Silver, S., Ed., *Microwave Antenna Theory and Design*, Dover Publishing, New York, 1965.

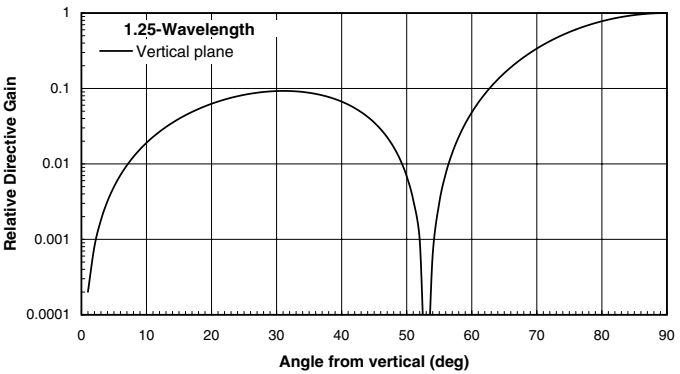

Figure 1.10 Relative directive gain for a 1.25-wavelength vertical dipole.

Wire antennas, such as dipoles or loops, produce an antenna pattern that is uniform in one dimension and has a main lobe and sidelobes in the other. An infinitesimal dipole or loop has a directivity of 1.5, a beamwidth of 90°, and an effective aperture of $3\lambda^2/8\pi$. The radiation pattern is symmetrical around the dipole or the normal to the loop. The lobe structure in the radiation pattern is in the plane containing the dipole or the normal to the loop. As the length of the dipole increases beyond a wavelength, the number of lobes increases, the half-power beamwidth for the main lobe decreases, and the directivity increases. Figure 1.10 displays the relative directive gain for a vertical dipole with a 1.25-wavelength length. The pattern is isotropic around the dipole. It has a beamwidth in the vertical of 33° and a directivity of about 3.3 or 5.2 dBi. The directivity of a dipole antenna is often expressed as a ratio of the maximum radiated power to that radiated by a half-wave dipole. The directivity of a half-wave dipole is 1.64 or 2.16 dBi. The directivity of the 1.25-wavelength dipole is thereby 3.0 dBd (decibels relative to a half-wave dipole).

1.4 *Propagation effects*

Different propagation mechanisms are important at different frequencies. For frequencies below 3 GHz, path attenuation due to atmospheric gases, clouds, and rain is small and often neglected, whereas for terrestrial paths

the relatively large vertical antenna beamwidths in use at these frequencies invite problems due to multipath propagation. At frequencies above 30 GHz, narrow beamwidth antennas may prevent multipath but path attenuation due to rain or antenna-pointing errors will be important. The propagation effects illustrated here are considered in more depth in subsequent chapters.

1.4.1 Path attenuation

Electromagnetic wave propagation through the ground, building material, buildings, vegetation, water, atmospheric gases, fog, clouds, wet snow, wet snow on a roof or radome, rain, and hail produces attenuation. Depending on frequency and application, some of these sources of path attenuation may be important in system design.

1.4.1.1 Atmospheric gases

Oxygen and water vapor in the lower atmosphere significantly affect path attenuation at higher frequencies. As an example, Figure 1.11 and Figure 1.12 present the specific attenuation for a location at the Earth's surface (a pressure of 1000 hPa = 10^5 Pascal (Pa) = 1 bar), a temperature of 20°C, and 100% relative humidity (RH). The oxygen curve gives the specific attenuation for 0% RH. The frequency bands below 22.3 GHz and between the specific attenuation peaks at 22.3, 50 to 70, 118, and 183 GHz are called atmospheric windows. In the frequency window below the water vapor absorption line at 22.3 GHz, the specific attenuation increases with frequency and can be more that 10 times higher at 15 GHz than at 2 GHz. Long-distance terrestrial microwave links are possible at the lower frequencies in this window but not at the high-frequency limit. Early Earth-space communication systems were developed in the 2- to 5-GHz frequency range to benefit from the low values of path attenuation, but had to compete for the radio frequency (rf) spectrum with terrestrial radio relay systems and long-range radar applications that required low path attenuation.

1.4.1.2 Clouds and fog

Scattering by the very small liquid water droplets that make up liquid water fogs near the Earth's surface and liquid water clouds higher in the atmosphere can produce significant attenuation at the higher frequencies. Figure 1.13 and Figure 1.14 present the specific attenuation per unit liquid water content as a function of frequency. Typical liquid water contents range from 0.003 to 3 g/m^3 depending on location, height in the atmosphere, and meteorological conditions. Clouds in the most active parts of mid-latitude thunderstorms may have liquid water contents in excess of 5 g/m^3. The liquid water cloud heights in the atmosphere can range from 0 km above ground (a fog) to 6 km above ground in the strong updrafts in convective clouds. For a 1-g/m^3 cloud at a water temperature of 10°C, the specific attenuation increases monotonically with frequency through the UHF, SHF, and EHF frequency bands (see Figure 1.13 and Figure 1.14). For frequencies lower

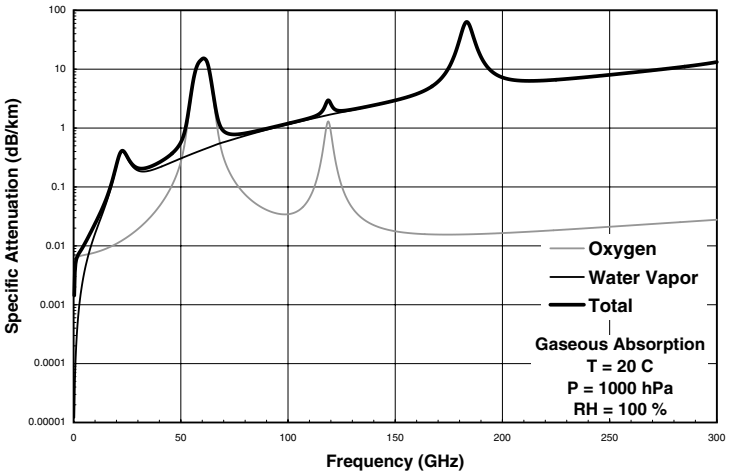

Figure 1.11 Clear air specific attenuation vs. frequency in the UHF, SHF, and EHF bands.

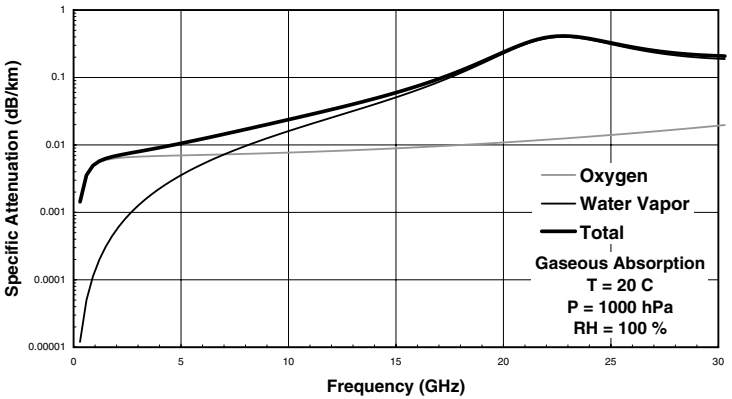

Figure 1.12 Clear air specific attenuation vs. frequency in the UHF and SHF bands.

than 10 GHz, cloud (or fog) attenuation can be ignored. At a frequency of 30 GHz, cloud attenuations on a 50° elevation angle path may approach 3 to 4 dB. At a frequency of 120 GHz, this result translates to 30 to 40 dB.

1.4.1.3 Rain

Scattering from the much larger liquid raindrops can produce significant path attenuation at frequencies above 10 GHz. Figure 1.15 and Figure 1.16 illustrate the specific attenuation values in rain at a water temperature of 10°C at rain rates ranging from low (0.25 mm/h) to heavy (25.4 mm/h). These rates correspond to liquid water contents of 0.02 and 1 g/m^3, respectively. At a 1-g/m^3 liquid water content, rain produces a higher specific

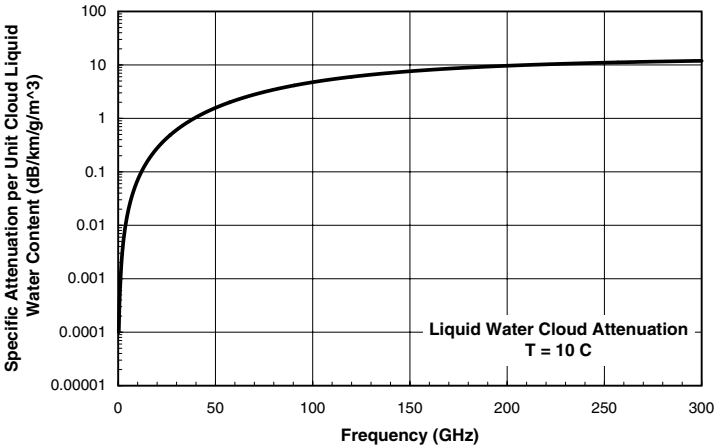

Figure 1.13 Liquid water cloud specific attenuation vs. frequency in the UHF, SHF, and EHF bands.

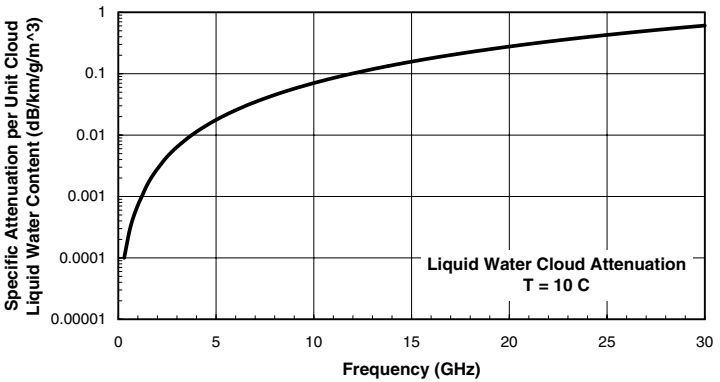

Figure 1.14 Liquid water cloud specific attenuation vs. frequency in the UHF and SHF bands.

attenuation than do clouds of the same liquid water content at frequencies below 150 GHz for the drop size distribution models used to generate the figures.

1.4.1.4 Water layer

A water layer on a radome produces attenuation on the path when the antenna is considered part of the path. Terrestrial microwave links generally employ radomes to protect the antennas from the weather. In using path attenuation models that are based on empirical relationships between path-attenuation statistics and rain-rate statistics (the ITU-R model,[9] for

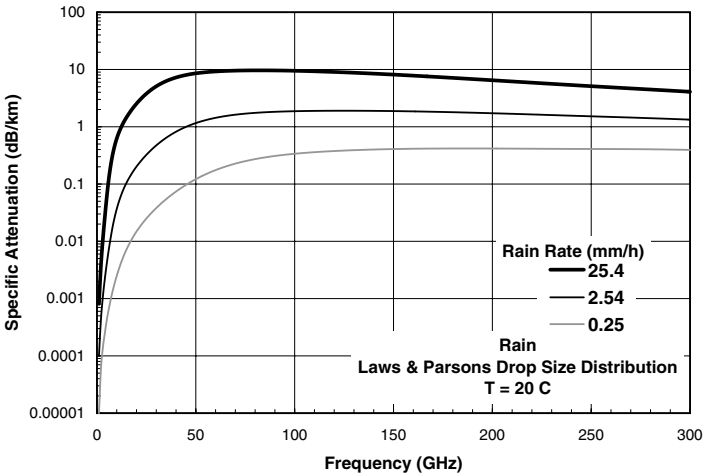

Figure 1.15 Rain specific attenuation vs. frequency in the UHF, SHF, and EHF bands.

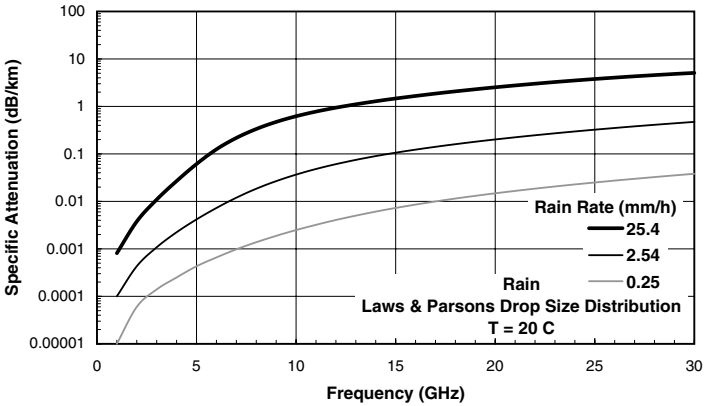

Figure 1.16 Rain specific attenuation vs. frequency in the UHF and SHF bands.

instance), the effects of the antenna design have not been separated from the effects of using different path lengths.

The specific attenuation (dB/mm) for transmission through fresh water is presented in Figure 1.17 and Figure 1.18 for three water temperatures. For frequencies above 5 GHz, the path loss is over 1000 dB/m. For transmission through a thin water layer, reflections at the water–air and water–radome interface must also be considered.

1.4.1.5 Building material

The complex dielectric properties of some building materials have been measured and published in tables (Table 1.3). The complex relative permittivity

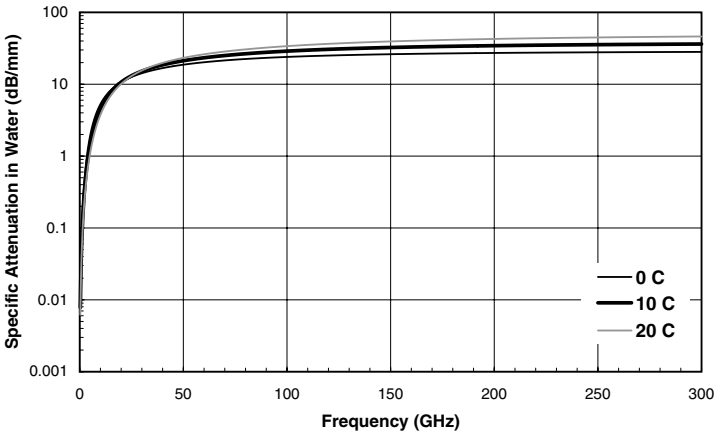

Figure 1.17 Water layer specific attenuation vs. frequency in the UHF, SHF, and EHF bands.

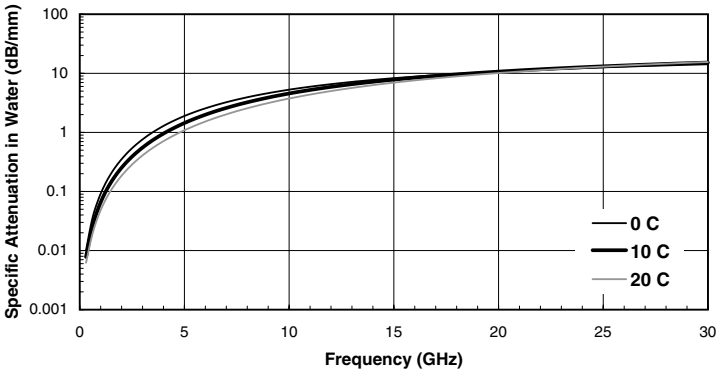

Figure 1.18 Water layer specific attenuation vs. frequency in the UHF and SHF bands.

of a lossy material is related to its loss tangent, complex index of refraction, and specific attenuation by:

$$\begin{aligned}
\varepsilon &= \varepsilon_0 \varepsilon_r = \varepsilon_0 \left(\varepsilon_r' - j\varepsilon_r'' \right) \\
\tan(\delta) &= \frac{\varepsilon_r''}{\varepsilon_r'} \\
n &= n' - jn'' = \sqrt{\varepsilon_r} \\
\alpha &= 4.343 \left(\frac{4\pi f}{c} \right) n''
\end{aligned} \tag{1.14}$$

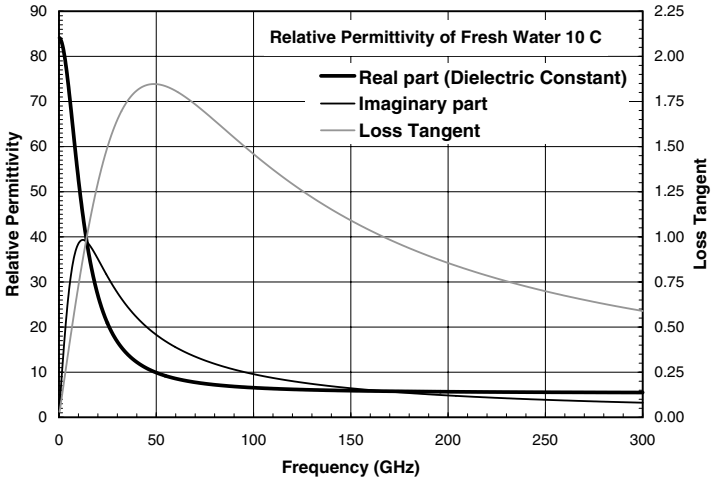

Figure 1.19 Complex permittivity and loss tangent vs. frequency in the UHF, SHF, and EHF bands.

where ε is the complex permittivity, ε_0 the permittivity of free space, ε_r the complex relative permittivity ε_r' the real part of the relative permittivity which is defined to be the dielectric constant, tan(δ) the loss tangent, n the complex index of refraction, and α the specific attenuation in decibels per meter (dB/m) when f is frequency in hertz and c is the speed of light in meters per second. The complex permittivity and loss tangent for water at 10°C are displayed in Figure 1.19 and Figure 1.20. The specific attenuation was presented in Figure 1.17 and Figure 1.18. The specific attenuation values for the building materials in Table 1.3 are significantly lower than the values for water. Water contained in wood or as a mixture in any other material (such as wet sand) increases the specific attenuation. Both concrete and glass produce significantly higher specific attenuation values in the EHF band.

The elements of building structures — the walls, floors, and roofs — are generally constructed from several different materials, each with its own dielectric and conductivity properties. Electromagnetic waves are scattered by, reflected from, and transmitted through buildings. Buildings have openings such as windows and doors that have transmission properties different from the surrounding walls. The calculation of the scattered fields is complex. Measurements have been made to characterize the scattering properties of "typical" buildings. Some measurements are summarized in Table 1.4.

Within a building, the received power levels vary widely with location. Multiple propagation paths between the transmitter and receiver cause these variations. Therefore, statistics of the received signals are important. Table 1.4 presents the median loss and the losses that were exceeded at 95% and 5% of the locations within the building. Loss was calculated relative to a single path to a receiver outside the building.[11] The transmitting antenna was above the building at a height of 20 m. The receiving antenna had a 60°

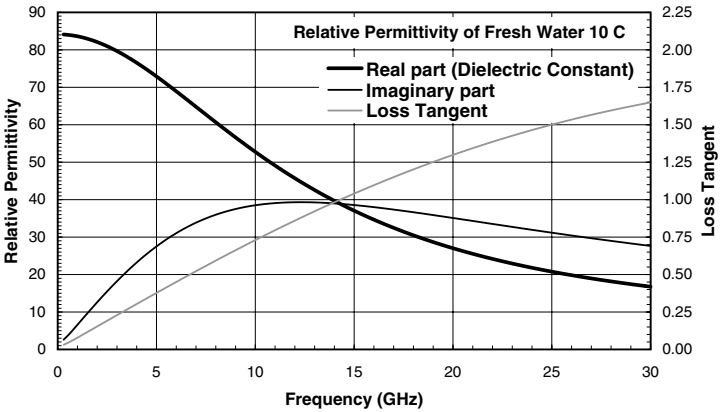

Figure 1.20 Complex permittivity and loss tangent vs. frequency in the UHF and SHF bands.

Table 1.3 Dielectric Properties of Building Materials

Frequency (GHz)	Material	Dielectric constant	Loss tangent	Specific attenuation (dB/m)
1.0	Concrete	7	0.12	28.8
1.0	Fiberglass	1.2	0.083	8.3
1.0	Glass	7	0.014	3.4
1.0	Lightweight concrete	2	0.25	31.9
2.45	Concrete (dry)	4.5	0.011	5.2
2.45	Sandy soil (dry)	2.55	0.0062	2.2
2.45	Teflon	2.1	0.0003	0.1
2.45	Wood	1.2–5	0.004–0.42	1–205
57.5	Concrete	6.5	0.066	880
57.5	Glass	6.81	0.025	341
95.9	Concrete	6.2	0.055	1194

Source: From ITU-R, Recommendation ITU-R P.679–2, International Telecommunications Union, Geneva, 1999; and Goldhirsh, J. and Vogel, W.J., Report A2A-98-U-0–021, Applied Physics Laboratory, Johns Hopkins University, Laurel, MD, 1998.

beamwidth in the vertical plane and an omnidirectional pattern in the horizontal. The receiving antenna was pointed at a 30° elevation angle.

1.4.1.6 Vegetation

Leaves and branches of individual trees scatter electromagnetic waves. Measurements show differences in the path loss through a tree with season and, at higher frequencies, with the amount of water in and on the leaves. Path loss also depends on the number and species of trees along the path and the height and orientation of the propagation path through the trees. A summary

Table 1.4 Attenuation on a Path from Outside to Inside a Building

Frequency (GHz)	Building type	Construction	Median loss (dB)	95% Loss (dB)	5% Loss (dB)
1.62	Public	Concrete	18.6	8	36
2.49	Public	Concrete	17.1	7	30
1.62	Office	Block brick	14.7	3	28
2.49	Office	Block brick	15.1	4	28
1.62	Farmhouse	Wood frame	6.5	–1	20
2.49	Farmhouse	Wood frame	7.5	–3	19
1.62	House	Wood frame	9.1	8	23
2.49	House	Wood frame	8.4	7	19
1.62	Motel	Brick	18.5	12	33
2.49	Motel	Brick	19.7	13	31
1.62	Store	Steel frame	13.7	6	27
2.49	Store	Steel frame	14.5	8	32

Source: From Goldhirsh, J. and Vogel, W.J., Report A2A-98-U-0–021, Applied Physics Laboratory, Johns Hopkins University, Laurel, MD, 1998.

Table 1.5 Single-Tree Attenuation Statistics

Tree	Frequency (GHz)	Median loss (dB)	Loss exceeded 1% of samples (dB)
Bare pecan	1.6	10	18
Pecan in leaf	1.6	12	19
Bare pecan	19.6	7	25
Pecan in leaf	19.6	23	43
Magnolia	19.6	20	40

Source: From Goldhirsh, J. and Vogel, W.J., Report A2A-98-U-0–021, Applied Physics Laboratory, Johns Hopkins University, Laurel, MD, 1998.

of some measurements in Austin, TX, is presented in Table 1.5. The measurements were made through the tree canopies at a 30° elevation angle.

1.4.1.7 Obstacles

Obstacles such as buildings, trees, Earth mounds, and hills may attenuate the electromagnetic waves. If the attenuation through the obstacle is high enough, the obstacle will diffract the wave over or around the obstruction. A single propagation path between a transmitting antenna and a receiving antenna is a clear line-of-sight path if no obstructions occur within the first few Fresnel zones about the path. Fresnel zones are enclosed within equiphase ellipsoids enclosing the path (Figure 1.21). The phase path distance along r_1 and r_2 (Figure 1.22) is given by:

$$r_1 + r_2 = \sqrt{d_1^2 + h^2} + \sqrt{d_2^2 + h^2} \approx d_1\left(1 + \frac{h^2}{2d_1^2}\right) + d_2\left(1 + \frac{h^2}{2d_2^2}\right) \qquad (1.15)$$

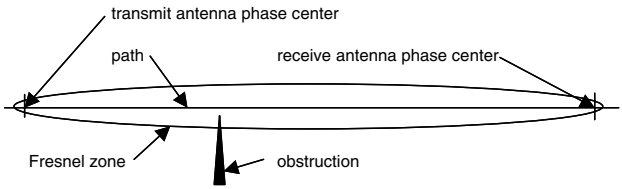

Figure 1.21 The Fresnel zone.

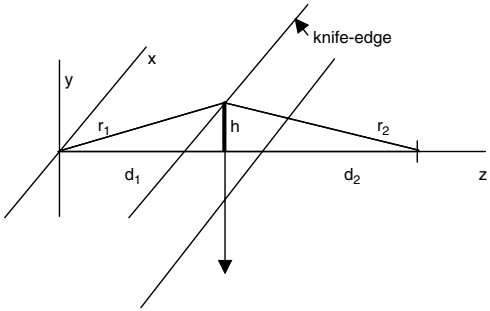

Figure 1.22 A knife edge

when $d_1 << h$ and $d_2 << h$. The phase path difference between the direct path and the phase path distance along r_1 and r_2 is then given by:

$$r_1 + r_2 - (d_1 + d_2) = \left(\frac{h^2 (d_1 + d_2)}{2 d_1 d_2} \right) = \frac{n\lambda}{2} \tag{1.16}$$

where $n/2$ is the path difference in wavelengths. The radius of the Fresnel zone is then:

$$h = \sqrt{\frac{n\lambda d_1 d_2}{(d_1 + d_2)}} \tag{1.17}$$

Diffraction by a single absorbing screen (a knife edge) provides a model to describe the general behavior of path loss in the presence of a high-attenuation object. Figure 1.23 presents the path loss due to knife-edge diffraction. The Fresnel diffraction parameter, ν, is given by:[12]

$$\nu = \left(\frac{h}{|h|} \right) \sqrt{2n} \tag{1.18}$$

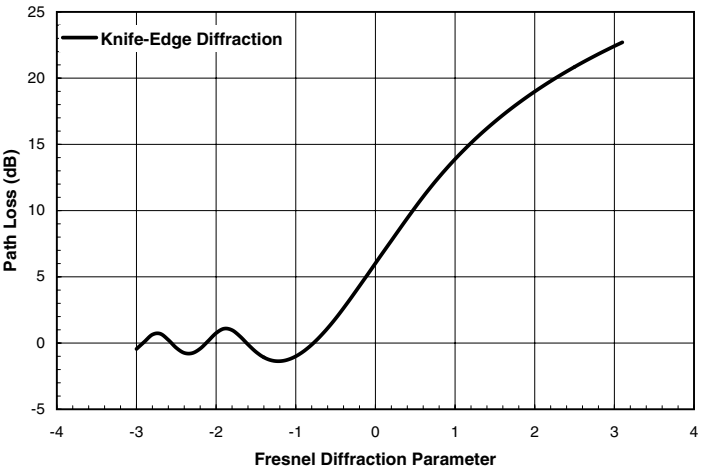

Figure 1.23 Path loss due to knife-edge diffraction.

A knife edge is the top of an absorbing half-space shown parallel to the x-axis in Figure 1.22. The distance h (minimum Fresnel zone radius to the knife edge) from the knife edge to the line of sight is positive if the absorbing half-space crosses the line of sight and negative if it does not obstruct the line of sight. For negative values of h, the path is in the interference region with both positive and negative loss values. When $h = 0$, the loss is 6 dB. For higher values of h, the path loss increases monotonically with frequency. For a given path loss, the values of $|h|$ that can produce that value decrease with increasing frequency.

Figure 1.24 presents a practical example of the frequency dependence of path loss as a function of knife-edge geometry. The path length is 2 km and the knife-edge is in the center of the path at h meters above or below the path. For positive h, the path loss increases with frequency; for negative h, the region of oscillation about zero loss is confined to lower values of h as frequency increases.

1.4.2 Refraction

The index of refraction for electromagnetic wave propagation through the lower atmosphere and ionosphere varies on many spatial and temporal scales. At the larger spatial and longer time scales, the effects of atmospheric refraction at the frequencies in the UHF through EHF bands can be obtained from ray tracing by using geometric optics. These effects include ray bending and ducting. Variations on much smaller spatial and temporal scales may cause scintillation. Scintillation refers to the random variation in amplitude, phase, and angle of arrival of electromagnetic waves. The diffraction theory must be invoked to describe scintillation.

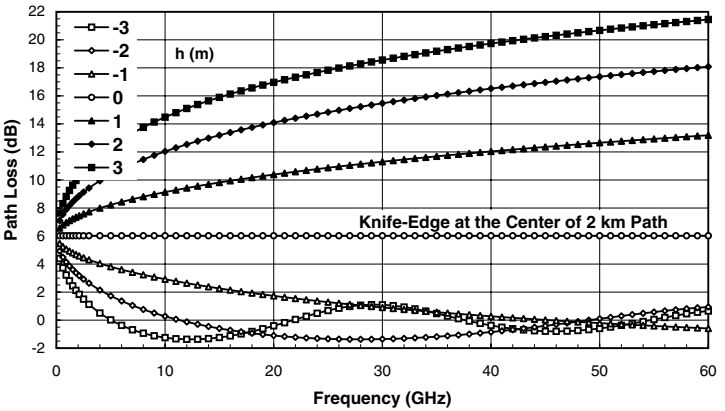

Figure 1.24 Path loss as a function of frequency for a knife edge at the center of a 2-km path.

1.4.2.1 Ray tracing

The index of refraction of air in the lower troposphere can differ from unity by as much as 4.5×10^{-4}. Radio refractivity, N, is used to describe the change in the index of refraction from unity (free space or in vacuum) where $N = (n - 1) \cdot 10^6$ and n is the index of refraction. The radio refractivity is related to the properties of the lower atmosphere by:[13]

$$N = 77.6\left(\frac{P}{T}\right) + 3.73 \cdot 10^5\left(\frac{P_V}{T^2}\right) \tag{1.19}$$

where P is pressure (hPa), T the temperature (K), P_V the vapor pressure (hPa) and N is in "N units."

For propagation above a spherical Earth, Snell's law becomes (see Section 2.5):[6,14]

$$\begin{aligned} &nr\cos(\alpha) = mA\cos(\alpha) = \text{constant along a ray} \\ &\therefore m\cos(\alpha) = m_0\cos(\alpha_0) = K = \text{constant} \end{aligned} \tag{1.20}$$

which is also known as Bouguer's law. $m = nr/A$ is the modified index of refraction and α the local elevation angle of the ray relative to a horizontal plane tangent to a spherical shell at a distance, r, from the center of the spherical Earth of radius A. The index of refraction is assumed to depend only on height above the surface of the Earth (spherically symmetric atmosphere). A modified radio refractivity or refractive modulus,[6] M, is also defined by $M = (m - 1) \cdot 10^6$.

Vertical profiles of N and M for the ITU-R mid-latitude standard atmosphere[15] and derived from two rawinsonde ascents, one made at 6:00

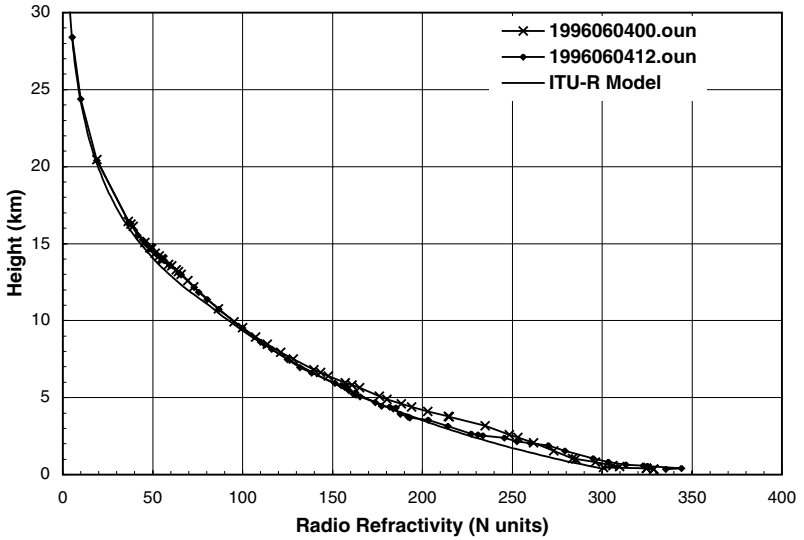

Figure 1.25 *N* profiles for the ITU-R standard mid-latitude atmosphere[15] and derived from rawinsonde ascents on June 4, 1996, at Norman, OK.

p.m. local time on June 3, 1996, and the other 12 hours later on June 4 (00:00 and 12:00 UT) from Norman, OK (oun), are given in Figure 1.25 and Figure 1.26. The vertical variation in radio refractivity produces a bending of the ray as described by Bouguer's law. An increase in m with height produces a corresponding decrease in $\cos(\alpha)$, resulting in an increase in the local elevation angle of the ray with height but generally with a downward bending of the ray relative to propagation in a straight line. Ray bending as a function of ray height is depicted in Figure 1.27 for the modified refractive index profiles shown in Figure 1.26. Most of the bending occurs below a 10-km height, and by 30 km the radio refractivity is nearly zero and little additional bending takes place. The curves in this Figure 1.27 are for an initial or apparent elevation angle of the ray at the ground (or lower height) terminal equal to zero. Sufficient bending for trapping occurred for the 00:00 UT ray to keep the ray below 57 m above the ground. The trapped ray is not plotted (but see Figure 4.2). The indicated heights are above mean sea level (msl). The Norman balloon launch site is at a height of 357 m msl.

The bending of the ray relative to a straight line causes a straight line from a ground terminal to the target (or other terminal) to have a true elevation angle at the ground terminal different from the initial or apparent elevation angle of the ray. The difference between the initial elevation angle and the true elevation angle is the elevation angle error. The elevation angle error is a function of target height and the M profile. Elevation angle error is shown in Figure 1.28 as a function of target height. In contrast to ray bending, the elevation angle error continues to increase with target height (see also Figure 4.14).

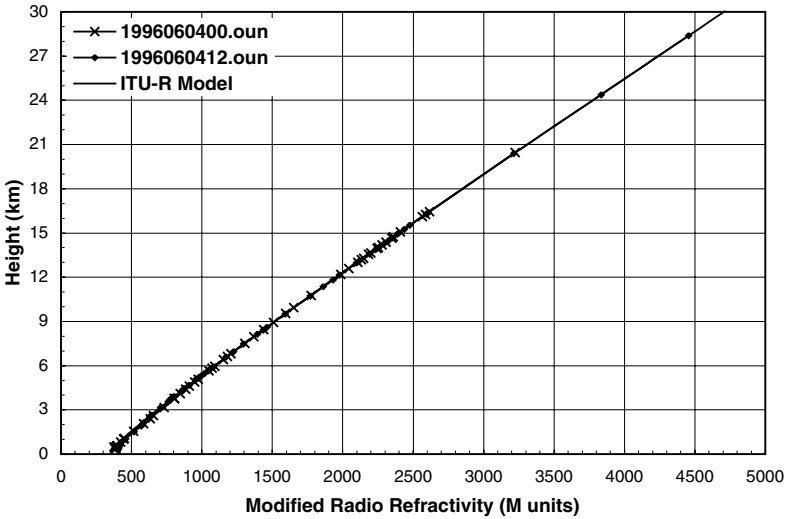

Figure 1.26 *M* profiles for the ITU-R standard mid-latitude atmosphere[15] and derived from rawinsonde ascents on June 4, 1996, at Norman, OK.

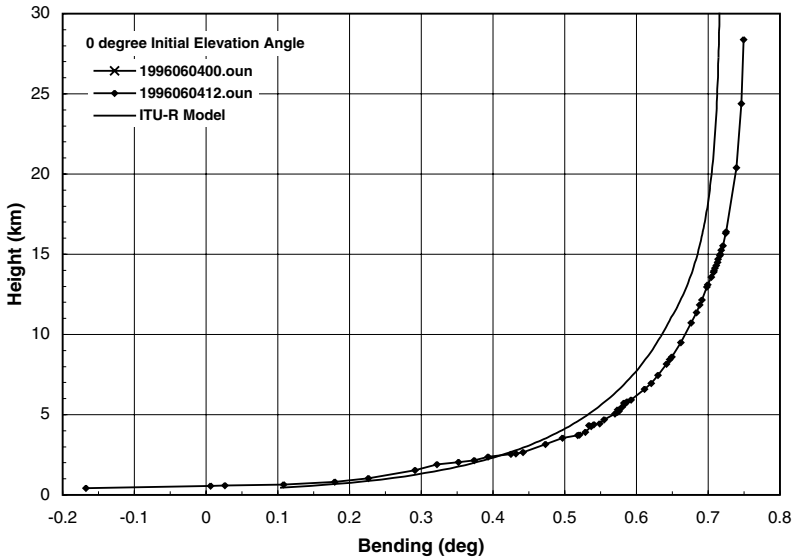

Figure 1.27 Ray bending as a function of ray height for the *M* profiles in Figure 1.26.

At frequencies between 0.3 and 10 GHz, the ionosphere produces an additional downward bending at heights below the F2 region electron density maximum (see Figure 1.29) and an upward bending at higher heights. The index of refraction for propagation in the ionosphere in the presence of the Earth's magnetic field is described by the Appleton–Hartree equation.[16]

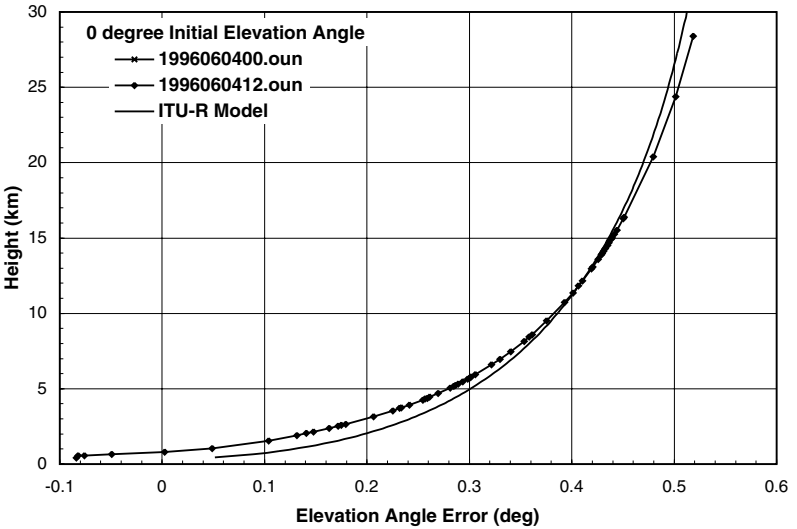

Figure 1.28 Elevation angle error as a function of ray height for the *M* profiles in Figure 1.26.

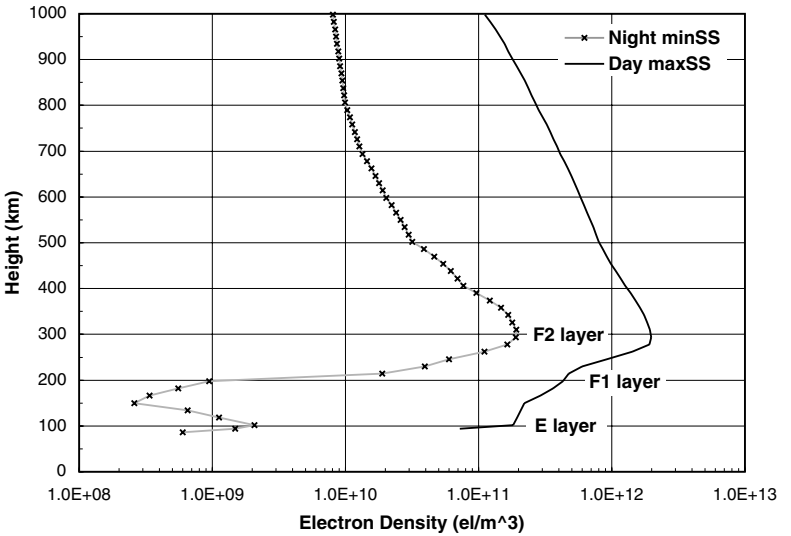

Figure 1.29 Typical mid-latitude electron density profiles for daytime at sunspot maximum and nighttime at sunspot minimum. (From Flock, W.L., *NASA Reference Publ*. 1108(02), 1987.)

For frequencies above 0.3 GHz, this equation simplifies by the exclusion of ionospheric absorption and the effects of the Earth's magnetic field except for the calculation of Faraday rotation. In this high-frequency approximation, the radio refractivity is given by:

$$N = -\left(\frac{4.03N_e}{f^2}\right)\cdot 10^{-11} = -N_G \tag{1.21}$$

where N_e is the electron density (electrons/m^3), N_G the effective refractivity for group delay, and f is carrier frequency (GHz). Examples of electron density profiles are given in Figure 1.29. Two extreme mid-latitude profiles are given, one a typical daytime profile near sunspot maximum (Day maxSS) and the other a nighttime profile near sunspot minimum (Night minSS).[17] These profiles generally bound the expected range for mid-latitude profiles. The E, F1, and F2 layers are identified in the figure.

The radio refractivity profiles for the ITU-R standard mid-latitude lower atmosphere combined with the ionospheric contributions at 0.3 GHz from the minimum and maximum electron density profiles from Figure 1.29 are shown in Figure 1.30. The ray bending produced by the lower atmosphere and ionosphere is shown in Figure 1.31 for rays with an initial elevation angle of 0°. Bending in the absence of any ionospheric contribution is also shown (labeled as "No Ionosphere," a high-frequency asymptote obtained from the ITU-R standard mid-latitude atmosphere). At frequencies above 10 GHz, the ionospheric contribution can be neglected. The frequency dependence of ray bending is illustrated in Figure 1.32.

Ray bending is a function of the initial elevation angle, as shown in Figure 1.33. Figure 1.31 and Figure 1.32 are for a 0° initial elevation angle to maximize the effects of the ionosphere to provide an illustration of the effect of the ionosphere. For a communication system operating at initial elevation angles

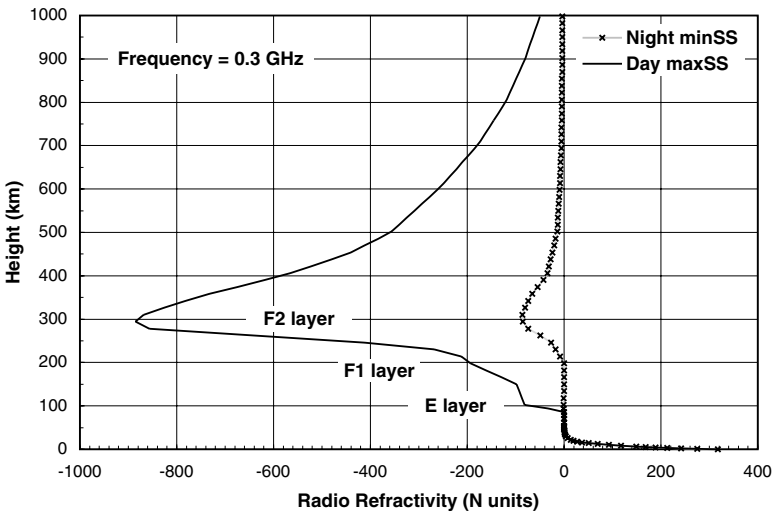

Figure 1.30 Radio refractivity profiles for daytime at sunspot maximum and nighttime at sunspot minimum. (From Flock, W.L., *NASA Reference Publ*. 1108(02), 1987.)

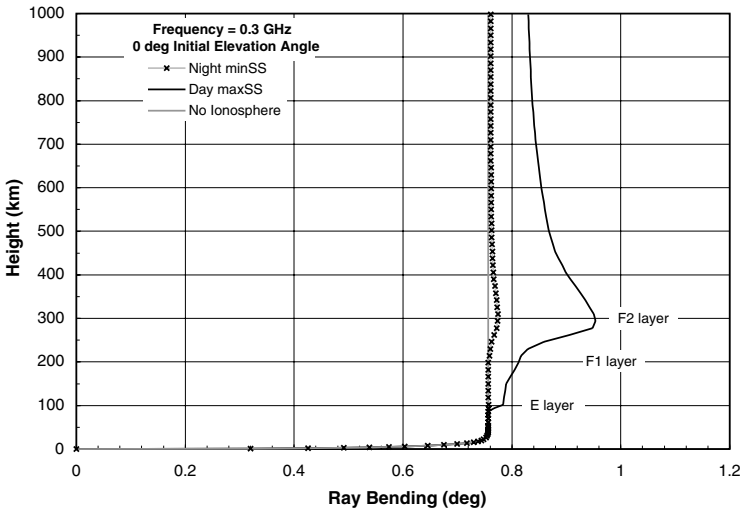

Figure 1.31 Ray bending as a function of ray height for two extreme ionospheric electron density profiles.

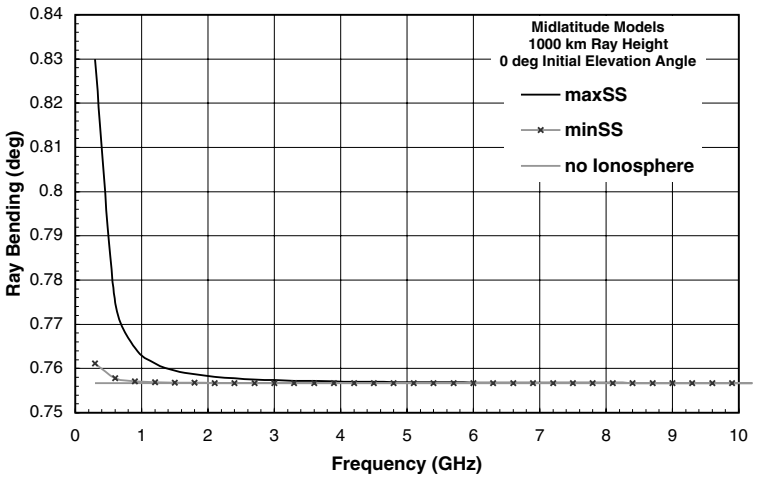

Figure 1.32 Ray bending as a function of frequency for two extreme ionospheric electron density profiles.

above 10°, ray bending is less than 0.14° for the profiles considered. For a target (satellite) at 1000-km height above the Earth's surface, the elevation angle error (pointing error) is less than 0.15°, as illustrated in Figure 1.34. Variations in the pointing error of the may be important in applications where the pointing errors are more than a fraction of the antenna elevation beamwidth.

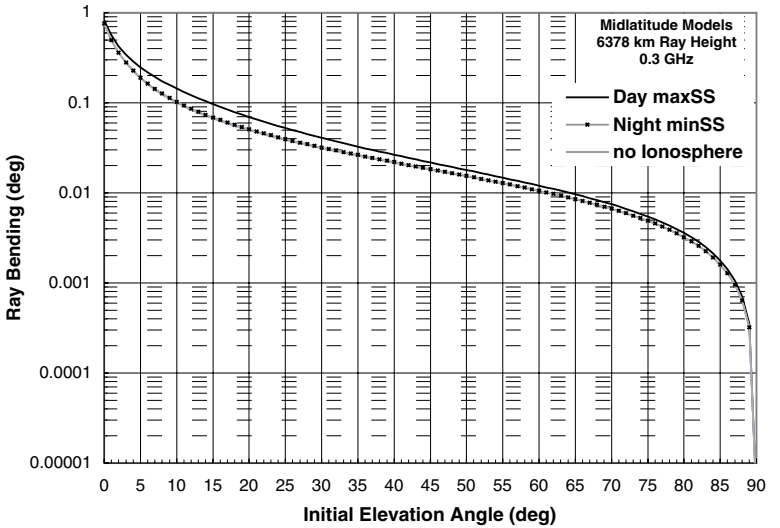

Figure 1.33 Ray bending as a function of initial elevation angle for two extreme ionospheric electron density profiles.

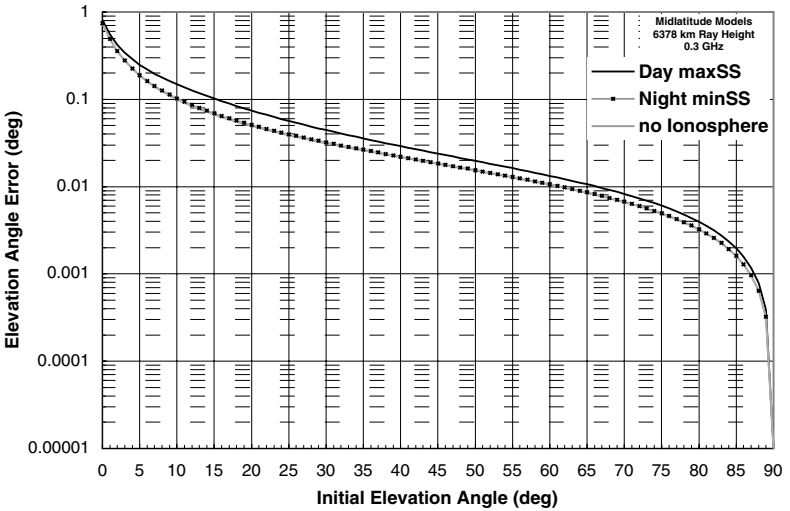

Figure 1.34 Elevation angle pointing error as a function of initial elevation angle for two extreme ionospheric electron density profiles.

The vertical gradients of N in the first few kilometers of the lower atmosphere produce most of the bending and pointing error. If N decreases fast enough with height, M will also decrease with height. If M decreases in height, the corresponding increase in $\cos(\alpha)$ required by Bouguer's law might exceed unity. Geometric optics does not allow for $\cos(\alpha)$ greater than

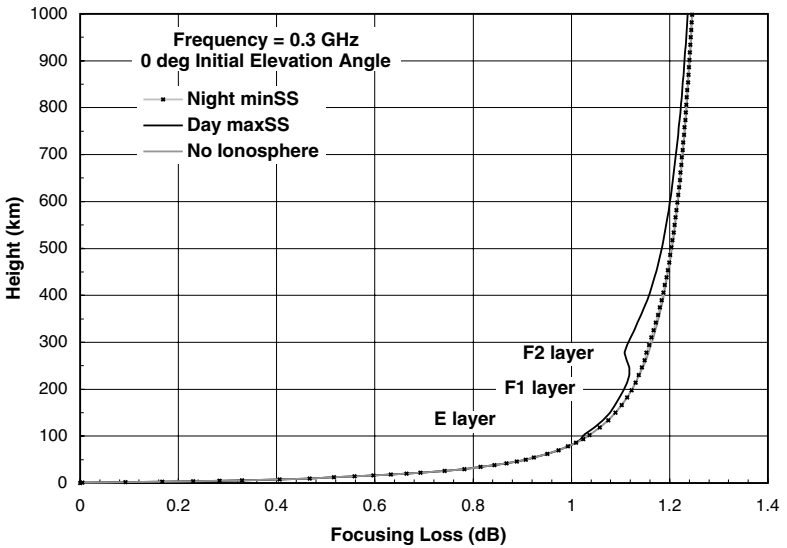

Figure 1.35 Focusing loss as a function of ray height for two extreme ionospheric electron density profiles.

unity. A turning point occurs when cos(α) equals unity and the ray cannot go higher. In this case, the ray is trapped in a radio duct.

Ray bending and elevation angle error vary as a function of elevation angle (see Figure 1.33 and Figure 1.34). In the limit of geometric optics, the power contained within a tube of rays is constant. When the rays on the top and bottom of the tube bend at different rates, the tube has a cross section normal to the direction of propagation that is different from the cross section that would result if all the rays went in straight lines. The result is a change in the power flux density relative to the power flux density for a tube of rays at the same distance and with the same initial elevation angles but propagating in free space. The change in power flux density yields a focusing loss or gain relative to free space. Because the rays generally bend more as the initial elevation angles decrease, the result is usually a loss. Focusing loss profiles as a function of ray height for a 0° initial elevation angle and the radio refractivity profiles shown in Figure 1.30 are presented in Figure 1.35. Focusing loss is mainly a problem at low elevation angles, as shown in Figure 1.36. The changes in focusing loss within the ionosphere are frequency dependent but may be neglected for rays that pass through the ionosphere (see Figure 1.37).

In a nonionized medium (the lower atmosphere), the electrical length of the path between terminals or the range to a target is more than the straight-line distance between the path end points because (1) the path is curved and (2) the velocity of propagation is slower than the speed of light in a vacuum. In the ionosphere, the phase velocity is faster than the speed of light ($N < 0$) but the group velocity is slower ($N_G > 0$). The range error

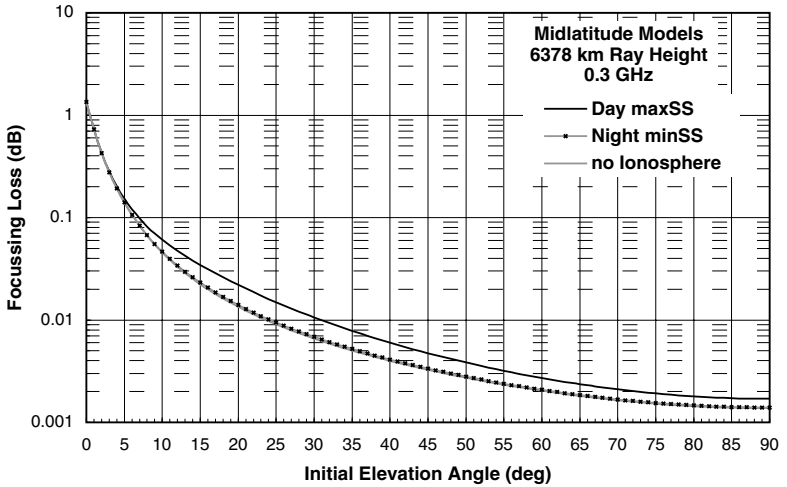

Figure 1.36 Focusing loss as a function of initial elevation angle for two extreme ionospheric electron density profiles.

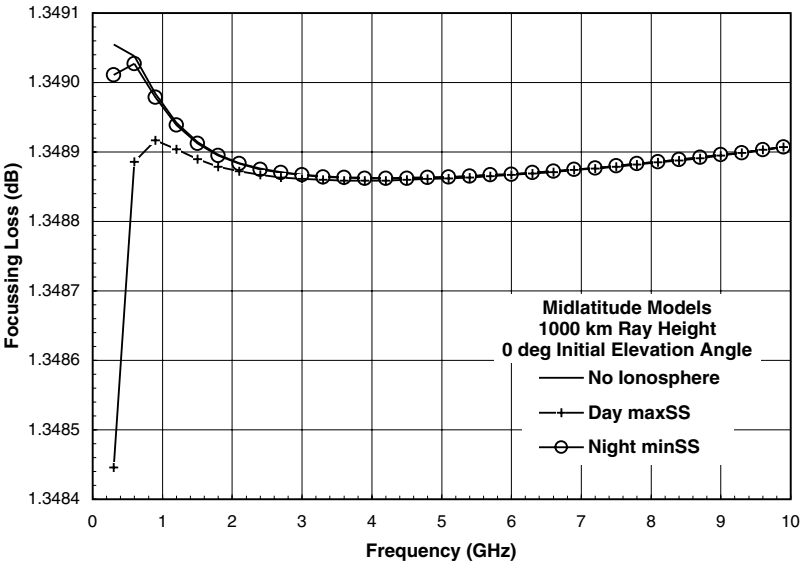

Figure 1.37 Focusing loss as a function of frequency for two extreme ionospheric electron density profiles.

for an electrical measurement of distance through the ionosphere therefore depends on the measurement technique employed (see Figure 1.38). Both types of range error are shown in Figure 1.38. The group range error is for measurement using the propagation time of a pulse.

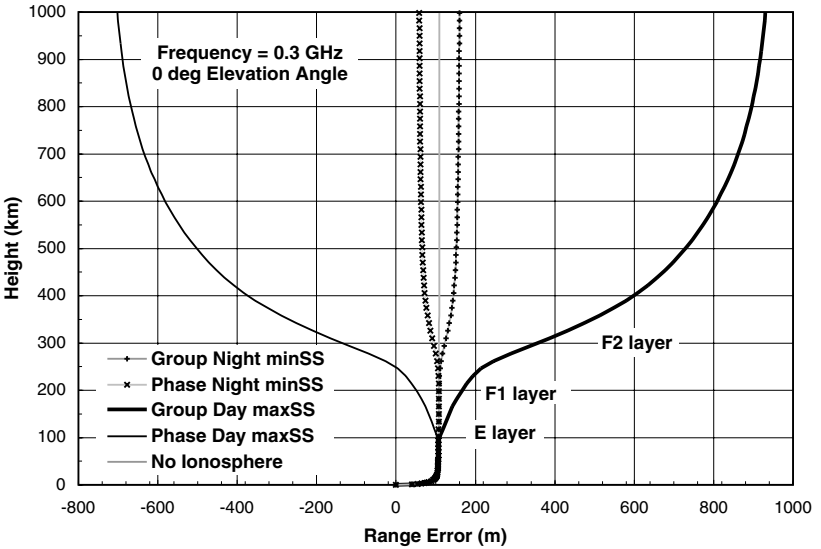

Figure 1.38 Range errors as a function of ray height for two extreme ionospheric electron density profiles.

The characteristic polarization for propagation through the ionosphere at frequencies in the UHF or higher bands is circular. The two orthogonal circular polarizations have different phase velocities. A linearly polarized wave propagating through the ionosphere is split into two characteristic circularly polarized components of equal magnitude. At any location in the ionosphere, the two circularly polarized components recombine to make a linearly polarized wave but with an orientation different from that of the original linear polarization. The apparent rotation of the plane of polarization on propagation through the ionosphere is called Faraday rotation. Figure 1.39 presents the calculated rotation angles as a function of height through the ionosphere and Figure 1.40 presents the rotation angles as a function of elevation angle for propagation to a height of 1000 km. The magnitude of the rotation is inversely proportional to the square of the frequency (see Equation 1.21). At 10 GHz and 0° initial elevation angle, the Faraday rotation for the maxSS profile is only 1.08°. At 1 GHz, the rotation increases to 108°. Faraday rotation can be ignored at frequencies above 10 GHz.

The radio refractivity profiles shown in Figure 1.25 and Figure 1.30 are model profiles that represent worldwide mid-latitude average conditions. Individual profiles will vary from the averages, especially at heights just above the Earth's surface.[18] Ducting conditions will produce the largest deviations from the model calculations. Focusing loss calculations made using 273 measured N profiles calculated from twice daily rawinsonde ascents during August and February for a 2-year period at a mid-latitude site (Albany, NY) show focusing losses of 0.4 ± 0.1 dB at a 1° initial elevation

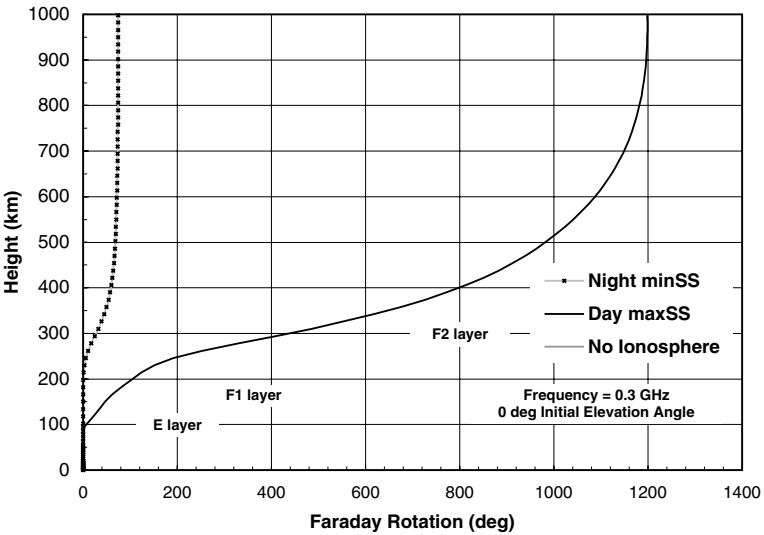

Figure 1.39 Faraday rotation as a function of ray height for two extreme ionospheric electron density profiles.

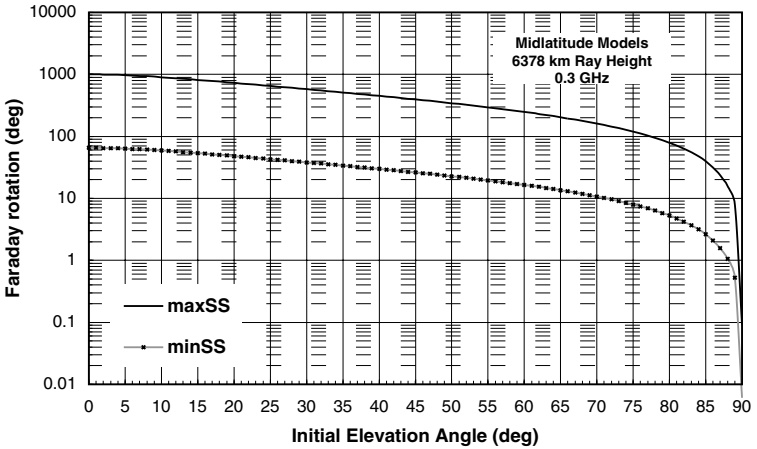

Figure 1.40 Faraday rotation as a function of initial elevation angle for two extreme ionospheric electron density profiles.

angle and 0.02 ± 0.002 dB at a 10° initial elevation angle.[19] The high-frequency asymptote model ("No Ionosphere," Figure 1.36) gives 0.44 dB at 1°, and 0.035 dB at 10°, values outside the standard deviation bounds from the Albany data set.

1.4.2.2 *Ducting*

Radio refractivity in the lower atmosphere depends on temperature, pressure, and RH (Equation 1.19). The refractive modulus or modified radio refractivity, M, is related to the physical properties of the lower atmosphere by:

$$M = N + \frac{z}{A} \cdot 10^6 + \frac{Nz}{A} \approx N + \frac{z}{A} \cdot 10^6 \tag{1.22}$$

where z is the height coordinate for distance above the Earth's surface. The vertical gradient in M is then given by:

$$\frac{dM}{dz} = \frac{77.6}{T}\frac{dP}{dz} - \left(\frac{77.6P}{T^2} + \frac{7.46 \cdot 10^5 P_V}{T^3}\right)\frac{dT}{dz} + \frac{3.73 \cdot 10^5}{T^2}\frac{dP_V}{dz} + \frac{10^6}{A} \tag{1.23}$$

For an atmosphere in hydrostatic equilibrium, the vertical gradient in pressure is given by the hydrostatic equation:[20]

$$\frac{dP}{dz} = -g\rho = -g\frac{m_d P}{RT_v} \tag{1.24}$$

where $m_d = 28.98$ is the mean molecular weight of dry air, g the acceleration due to gravity, ρ the density of air, R the universal gas constant, and T_v the virtual temperature. The virtual temperature is given by:

$$T_v = \frac{T}{1 - \frac{P_V}{P}\left(1 - \frac{m_v}{m_d}\right)} = \frac{T}{1 - 0.378\frac{P_V}{P}} \tag{1.25}$$

where $m_v = 18.02$ is the molecular weight of water. The virtual temperature is employed to allow the use of the perfect gas law with moist air. In practical units, Equation 1.24 becomes:

$$\frac{dP}{dz} = -34.1\frac{P}{T_v} \quad \text{hPa/km} \tag{1.26}$$

Both pressure and density decrease exponentially with height if the virtual temperature is constant and not a function of height.

RH, water vapor density (ρ_V, also known as absolute humidity), specific humidity, mixing ratio, dew point temperature, and vapor pressure may be used to describe the amount of water vapor in the atmosphere. The specific humidity, q, is defined as the ratio of the mass of water vapor to the mass of

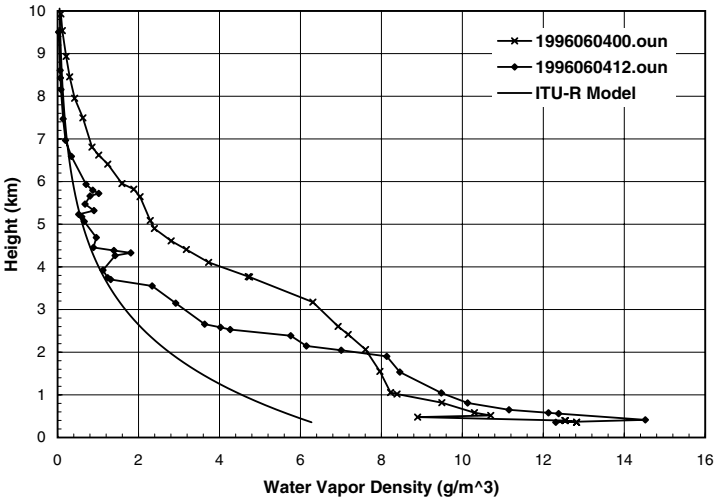

Figure 1.41 Specific humidity profiles for up to a 10-km height for the ITU-R standard mid-latitude atmosphere and derived from rawinsonde ascents on June 4, 1996, at Norman, OK.

moist air containing the water vapor (g/kg). The mixing ratio, x, is defined as the ratio of the mass of water vapor to the mass of dry air containing the water vapor (g/kg). The expression for radio refractivity uses vapor pressure (Equation 1.19). Observations are usually reported as RH or dew point temperature. For the study of the profile of water vapor variation with height, the best parameter to use is specific humidity, because it is conservative (does not vary) within a parcel (or mass) of air during atmospheric motion as long as no change of state and no influx of moisture into the parcel by evaporation or transpiration, or loss by condensation occur. In a well-mixed region of the atmosphere, q is constant throughout.[6] The specific humidity profiles for the ITU-R mid-latitude standard atmosphere and the June 4, 1996, rawinsonde ascents are shown in Figure 1.41. The resulting radio refractivity profiles for the water vapor profiles shown in this figure are presented in Figure 1.42. The morning profile (1996060412.oun) shows a rapid increase in q just above the surface, followed by a rapid decrease, and then a gradual decrease. The afternoon profile (1996060400.oun) shows a well-mixed region between 1 and 2 km msl and a drying above 3.2 km. The morning profile shows a thin moist layer above 4 km msl. The refractive index profile shows a stronger negative gradient just above the surface for the morning sounding than for the afternoon sounding.

The maximum amount of water vapor a volume of air can contain is a function of air temperature. The saturation mixing ratio describes the maximum amount of water vapor a volume of moist air can hold. The RH is defined as the ratio of the mixing ratio to the saturation mixing ratio:[20]

$$\mathrm{RH} = \frac{x}{x_S(T)} = \frac{P_V}{P_{VS}(T)} \tag{1.27}$$

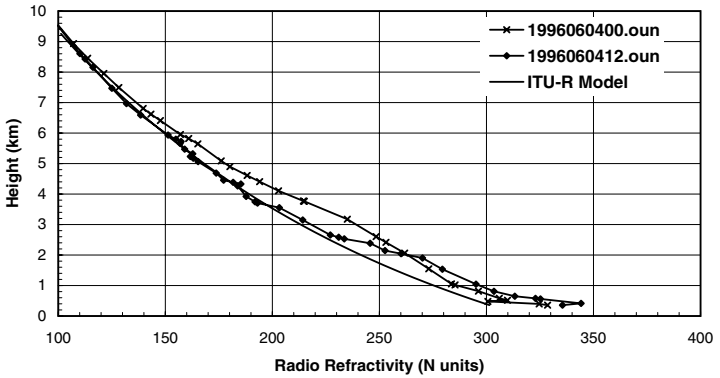

Figure 1.42 N profiles for up to a 10-km height for the ITU-R standard mid-latitude atmosphere derived from rawinsonde ascents on June 4, 1996, at Norman, OK.

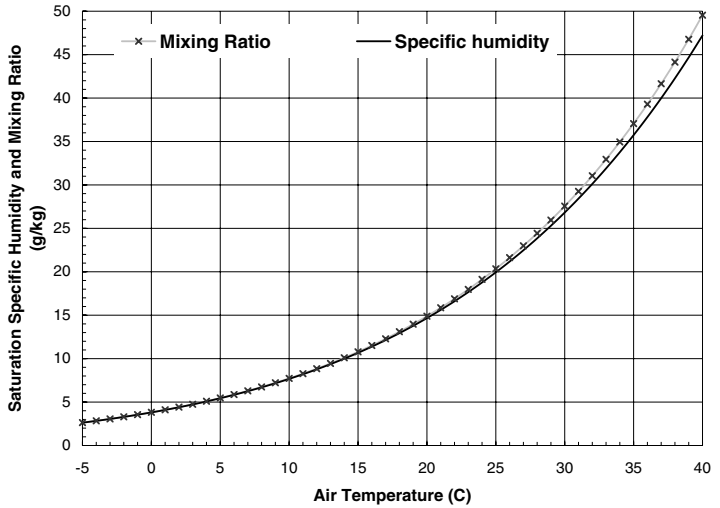

Figure 1.43 Saturation mixing ratio over a plane water surface as a function of air temperature.

where x_S is the saturation mixing ratio (see Figure 1.43) and P_{VS} is the saturation vapor pressure (Figure 1.44). The saturation vapor pressure is for air in contact with a plane water surface. At air temperatures below 0°C, the saturation vapor pressure is higher over a water surface than over an ice surface. The dew point temperature is the temperature the volume of air would take when cooled to saturation. The dew point is usually computed relative to a water surface even when the air temperature is below 0°C.

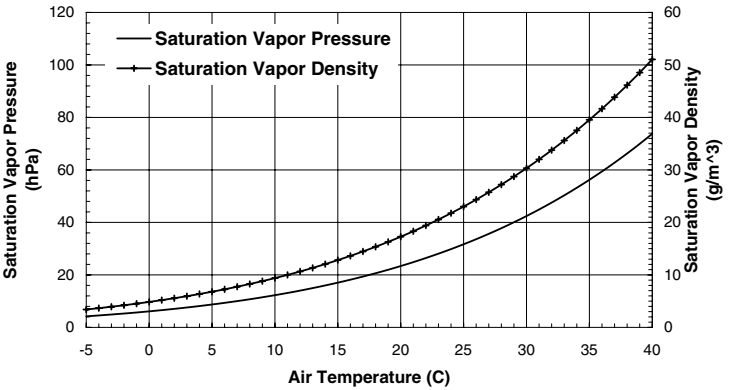

Figure 1.44 Saturation vapor pressure over a plane water surface as a function of air temperature.

The vapor pressure is related to specific humidity and to water vapor density by:

$$P_V = \left(\frac{q}{1000}\right)\frac{P}{0.622 + 0.000378q} \approx \frac{qP}{622}$$
$$\rho_V = \frac{216.7P_V}{T} \tag{1.28}$$

and then

$$N \approx \left(77.6 + \frac{600q}{T}\right)\frac{P}{T} \tag{1.29}$$

Noting that to the same order of approximation, $T_v \approx T$, the vertical gradient of N is:

$$\frac{dN}{dz} = -\left(2510 + \frac{19400q}{T}\right)\frac{P}{T^2} + \left(\frac{600P}{T^2}\right)\frac{dq}{dz} - \left(77.6 + \frac{1200q}{T}\right)\frac{P}{T^2}\frac{dT}{dz} \tag{1.30}$$

The vertical gradient of M is then:

$$\frac{dM}{dz} = \frac{dN}{dz} + \frac{10^6}{A} \approx \frac{dN}{dz} + 157 \tag{1.31}$$

At a pressure of 1000 hPa, a temperature of 10°C, and a RH of 50%, q = 3.8 g/kg and the vertical gradient of M is:

$$\frac{dM}{dz} = -30.1 + 7.5\frac{dq}{dz} - 1.2\frac{dT}{dz} + 157 \tag{1.32}$$

Trapping or ducting is possible when the vertical gradient of M is negative somewhere on the profile. Then, the decrease in M with height may cause $\cos(\alpha)$ to increase to unity creating a turning point. This could occur whenever $dN/dz < -157$ N units/km.

Under well-mixed conditions for unsaturated moist air, q does not vary with height and the temperature decreases with height. Well-mixed conditions apply when a parcel (or mass) of air does not exchange heat with its environment and cools adiabatically as it rises. The potential temperature, θ, is defined as the temperature a mass of moist, unsaturated air would take if moved dry adiabatically to a pressure of 1000 hPa (no evaporation or condensation).[6,21] The potential temperature is given by:[20]

$$\theta = T\left(\frac{1000}{P}\right)^{0.286} \tag{1.33}$$

The vertical gradient in temperature then is:

$$\frac{dT}{dz} = \left(\frac{P}{1000}\right)^{0.286}\frac{d\theta}{dz} - 9.78 \text{ K/km} \tag{1.34}$$

and, for a dry adiabatic profile $d\theta/dz = 0$, so $dT/dz = -9.78$ K/km. The temperature and potential temperature profiles for the soundings and model used for Figure 1.41 and Figure 1.42 are shown in Figure 1.45 and Figure 1.46, respectively.

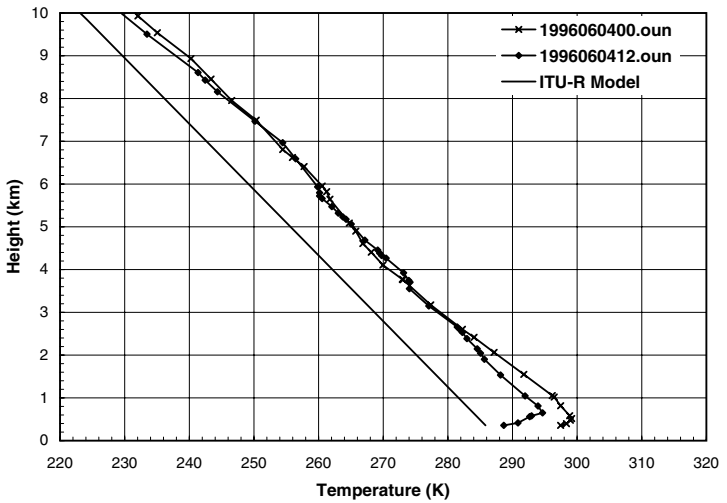

Figure 1.45 Temperature profiles for up to a 10-km height for the ITU-R standard mid-latitude atmosphere and derived from rawinsonde ascents on June 4, 1996, at Norman, OK.

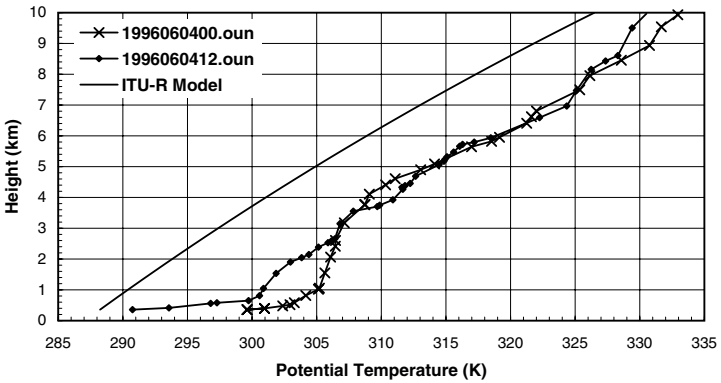

Figure 1.46 Potential temperature profiles for up to a 10-km height for the ITU-R standard mid-latitude atmosphere and derived from rawinsonde ascents on June 4, 1996, at Norman, OK.

Figure 1.45 shows temperature inversions in the measured profiles in a surface layer and a capping inversion at a 3.5-km height in the morning profile (local time). The potential temperature shows a kilometer-thick well-mixed region just below the capping inversion (near vertical segment of the curve). The regions of positive potential temperature gradients are stable layers.[21] An adiabatic vertical motion of an air parcel would produce a colder temperature than that of the surrounding air. The cold air is therefore heavier than the surrounding air and will sink. The sinking air will become warmer than its surroundings and rise again to seek a position of neutral buoyancy. A mechanical lifting of the air would produce an oscillation of the height of the air parcel about the position where its temperature is equal to that of its surroundings (buoyancy oscillations, see Section 4.1.3). If the potential temperature profile had zero slope (vertical line on this plot), there would be no restoring force and the parcel would mix with the surrounding air.

Ducting cannot occur within the well-mixed region, but the upper and lower boundaries of that region can have stable nonadiabatic (or diabatic) temperature profiles or specific humidity gradients that could produce ducting. Radiation cooling of the Earth's surface can produce a sharp temperature increase from the surface to a few tens to hundreds of meters above the surface. Evaporation from a water surface such as the ocean or from the hot land during cooling by rain showers can produce a sharp reduction in q with height above the surface. In either case, a large negative gradient in N near the surface would occur, which might produce ducting conditions.

Examples of N gradient profiles for the ITU-R model and twice daily measurements on June 4, 1996, at Norman, OK, are shown in Figure 1.47. The measured data show a rapid decrease in q near the surface (Figure 1.41) and a temperature inversion (increase in temperature with height, Figure 1.45) over the lowest 200 m of the atmosphere. The result is the more negative

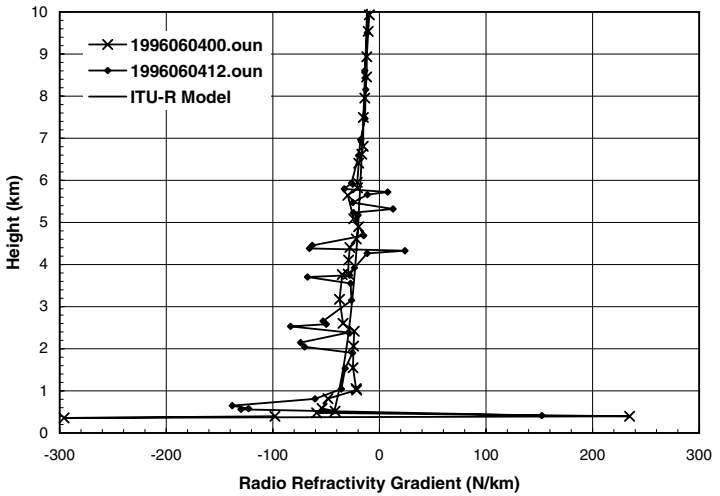

Figure 1.47 Temperature gradient profiles for up to a 10-km height for the ITU-R standard mid-latitude atmosphere and derived from rawinsonde ascents on June 4, 1996, at Norman, OK.

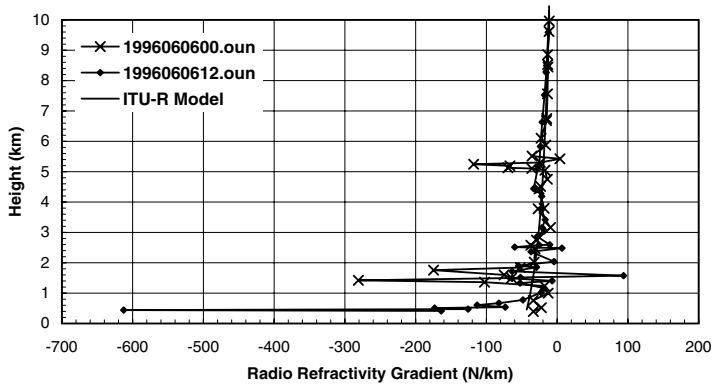

Figure 1.48 Temperature gradient profiles for up to a 10-km height for the ITU-R standard mid-latitude atmosphere and derived from rawinsonde ascents on June 6, 1996, at Norman, OK.

gradient of N shown in Figure 1.47. A second set of gradient profiles for June 6, 1996, at Norman, OK (Figure 1.48) shows a sharper decrease in N just above the surface due to a more rapid decrease in q and an increase in temperature. In this case, a surface duct was present just after the passage of several rain showers that cooled the surface and increased the specific humidity by evaporation. The rawinsonde sounding hinted a possible duct but, with the inherent integration time of the humidity sensor, the observed gradient was not more negative than the –157 N units/km needed for ducting.

Worldwide maps of the occurrence statistics for vertical gradients of N less than –100 N units/km in the lowest hundred meters of the atmosphere are available for predicting duct occurrence in different seasons.[22] Although this gradient is not sufficient to produce a reduction of M with height as indicated in Equation 1.31, it is often used as an indicator of ducting to compensate for measurement problems and for the possibility of stronger gradients over a depth lower than 100 m. The morning soundings for June 1996 in Oklahoma had 3 days out of 30 with measured N gradients less than –100 N units/km. Measurements along the New Jersey coast for a 2-week period in August 1966 showed that ducting occurred for 50% of the time.[23] A compendium of interference studies made in northwest Europe[24] presents basic transmission models and occurrence statistics for ducting and other transhorizon propagation phenomena.[25] Kerr[6] presents a number of examples of surface ducts with accompanying meteorology and radio transmission data.

Elevated layers with gradients lower than –157 N units/km are possible throughout the lower atmosphere. They often occur at temperature inversion layers capping regions of convection. The major contribution to the decrease in N with height then is a rapid reduction in moisture content. Because trapping can only occur when $\cos(\alpha) = 1$, entry of the ray into a trapping layer requires an elevation angle at the edge of the trapping layer that is near zero. From Bouguer's law, at the turning point $\alpha = 0$ and in a region of constant m gradient:

$$\cos(\alpha_0) \approx 1 - \frac{1}{2}\alpha_0^2 = \frac{m_0 + \frac{dm}{dz}(z - z_0)}{m_0} = 1 + \frac{\frac{dm}{dz}(z - z_0)}{m_0} \tag{1.35}$$

which simplifies to

$$\alpha_0 = \pm\sqrt{-2\frac{dM}{dz}(z - z_0)\cdot 10^{-6}} \tag{1.36}$$

when $|\alpha_0| << 1$, $z/A << 1$, and $m_0\cos(\alpha_0)$ is the constant for the ray at height z_0. Elevated layers at heights as high as several kilometers can produce trapping and the associated radio holes or multipath (or both) for elevated transmitters and receivers as can occur in aircraft-to-aircraft communication or airborne radar observations of aircraft aloft (see Figure 4.24).

1.4.2.3 Effective Earth's radius

The radius of curvature, r, of a ray is given by:[6,14]

$$\frac{1}{r} = -\frac{1}{n}\frac{dn}{dz}\cos(\alpha) \approx -\frac{dn}{dz} \tag{1.37}$$

where the approximation is valid at low elevation angles. In a layer of constant n gradient within which the elevation angle is near zero, the effect of the downward curvature (bending per unit distance along the ray) can be compensated by assuming straight-line propagation (no bending) over the Earth with an effective Earth's radius of $A_E = k_E A$. The curvature $1/A_E$ is therefore the curvature of the Earth's surface minus the curvature of the ray:

$$\frac{1}{A_E} = \frac{1}{A} - \frac{1}{r} \tag{1.38}$$

and the k_E factor for the effective Earth's radius is:

$$k_E = \frac{1}{1 + \frac{A}{n}\frac{dn}{dz}} \approx \frac{1}{1 + A\frac{dN}{dz}10^{-6}} \approx \frac{1}{1 + 0.00638\frac{dN}{dz}} \tag{1.39}$$

Standard refraction is often taken as $k_E = 4/3$ or $A_E = 8500$ km. This corresponds to a vertical gradient $dN/dz \approx -40$ N units/km. Using the effective Earth's radius model, ray paths between transmitters and receivers near the Earth's surface can be approximated by straight lines over a spherical Earth with radius A_E. This model requires the layer of the atmosphere containing both end points of the ray path to have a constant vertical gradient in N and the elevation angles be small. The model is most useful for terrestrial paths. It should not be used for paths through the entire atmosphere.

The effective Earth's radius approximation is often used to analyse and display radar data for targets in the lower atmosphere. In this case the requirement is a k_E factor that enables the rapid calculation of target height when the range and initial elevation angle are known. By working backward from a complete ray tracing analysis, a k_E factor can be determined that provides an acceptable approximation for a range of target positions.

The radio refractivity gradient for the ITU-R mid-latitude profile (see Figure 1.47) when averaged over the first kilometer of height is $dN/dz = -25.2$ N units/km. The resulting k_E factor from Equation 1.39 is 1.19 (see Figure 1.49 and Figure 1.50 for ray tracing results). By ray tracing, the k_E factor for the lowest kilometer is also 1.19. If the ray tracing is done in 100-m steps, the k_E factor increases slightly because the N gradient is more negative near the surface and the bending of the ray is slightly more than for the results obtained using the gradients averaged over a kilometer. As the target height increases, the k_E factor needed to compensate for refraction decreases.

Worldwide maps of the average N gradient in the lowest 1 km of the atmosphere are available to calculate the k_E factor for any location and season.[22] These maps provide only a general indication of the changes in k_E factor as a function of terrain and location. For Norman, OK, the monthly average N gradient for May from the maps is –50 N units/km. The average

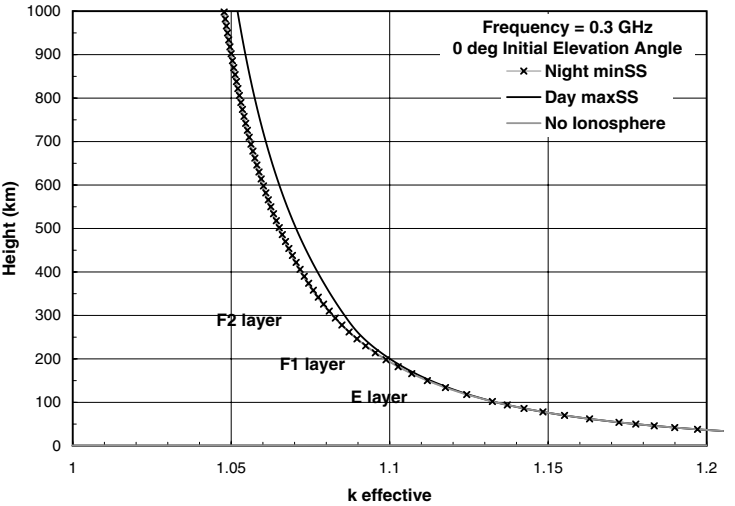

Figure 1.49 k_E factor for the *M* profile presented in Figure 1.26 for heights up to 1000 km.

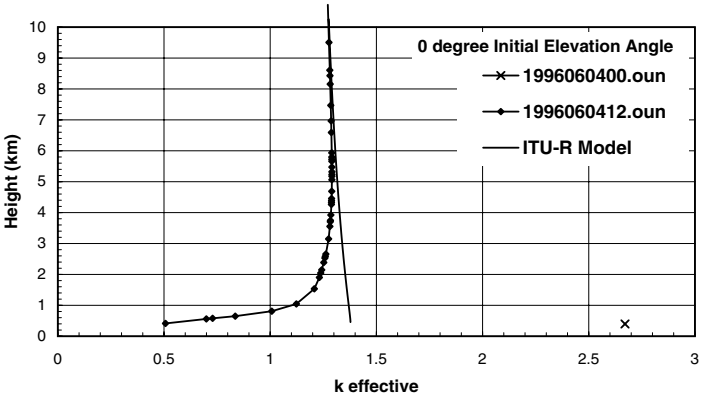

Figure 1.50 k_E factor for the model *N* profile presented in Figure 1.42 for heights up to 10 km and rawinsonde soundings from Norman, OK.

for the morning soundings for June 1996 was –57 N units/km with a standard deviation of 26 N units/km.

The expression for the ray curvature, Equation 1.37, indicates the k_E factor is also a function of initial elevation angle. Curves for several different initial elevation angles are shown in Figure 1.51. At elevation angles above 1° and heights above 2 km, a k_E factor of 1.2 is a reasonable approximation. Early refraction studies for height-finding radars resulted in a k_E factor of 1.2 as the best approximation for a wide range of mid-latitude continental refraction conditions. The "standard" k_E value of 4/3 often used in weather

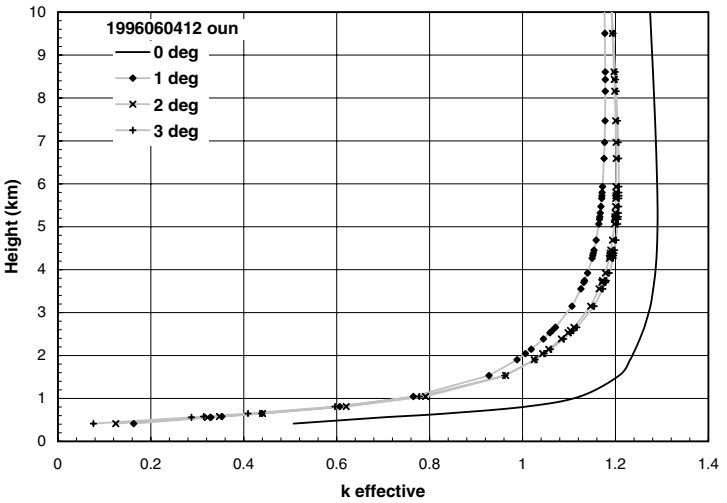

Figure 1.51 k_E factor for the morning rawinsonde profile presented in Figure 1.42 for heights up to 5 km and initial elevation angles between 0° and 3°.

radar analysis and display is not correct. The horizontal bright bands caused by melting snow often droop at longer ranges due to the incorrect correction for average refraction.

1.4.2.4 Tropospheric scatter

Long-distance communications between a transmitter and receiver on the ground well beyond their radio horizons is possible in the UHF and higher frequency bands. Surface ducts can provide a mechanism for propagation well beyond the horizon if ducting conditions exist and no obstacle is present to break up the duct. An obstacle such as a hill or mountain can interrupt the duct, but diffraction from the top of the obstacle can provide transhorizon fields. The field diffracted by a knife edge dies off beyond the horizon, as indicated by the path loss curve in Figure 1.23. Observations made during and after World War II showed that the transmission loss values observed on transhorizon paths were lower than expected for diffraction (fields were higher than expected), present much of the time, but not as small or as infrequent as would be expected for ducting. The mechanism responsible for these intermediate-intensity transhorizon fields is tropospheric forward scattering (troposcatter) by small-scale fluctuations in radio refractivity produced by atmospheric turbulence. Troposcatter was used for long-distance communication links before the advent of satellite communications. At present, troposcatter is used only under special circumstances and mainly by the military. It also provides a potential mechanism for causing interference between widely separated systems operating at the same frequency.

Observations on a 161-km transhorizon path from Prospect Hill in Waltham, MA, to Mt. Tug in Enfield, NH, provide examples of transhorizon

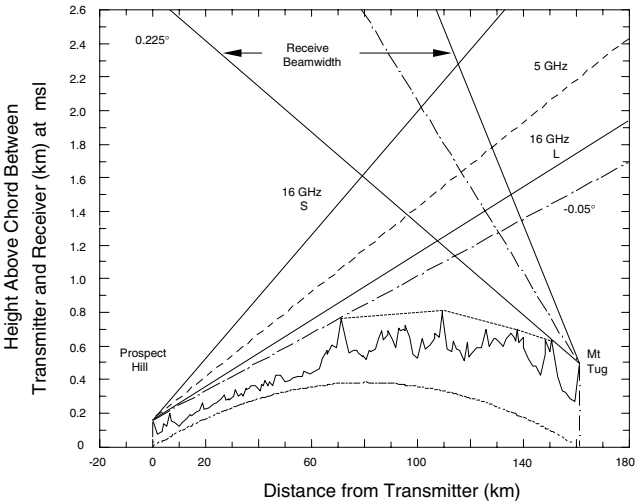

Figure 1.52 Path profile for the Prospect Hill to Mt. Tug troposcatter path.

signal strengths together with an identification of the propagation mechanisms that produced the observations.[26] The profile for the measurement path is given in Figure 1.52. The path profile was constructed using straight-line propagation over a curved Earth employing a k_E factor of 4/3 (see Figure 1.50). The terrain height values obtained from topographic maps were plotted above the curve of the Earth's surface (at msl) along a great circle route. Straight lines from the transmitting antenna to the top of the highest close obstacle and on into space and from the receiving antenna to the top of the highest close obstacle on the receiving end of the path and on into space are indicated in the figure. The peak of the transmitting antenna main beam was pointed at the radio horizon (the highest close obstacle). During the first part of the measurement, the lower half-power angles on the receiving antenna patterns were pointed at the radio horizon as indicated in the figure; for the rest of the experiment the peaks of the receiving main beams were pointed at the radio horizon. The center line for each pattern in the great circle plane is indicated by the dot-dished lines in the figure (for the first part of the experiment). The upper half-power beamwidth angles for each antenna pattern are also indicated in the figure along with the elevation angles to the radio horizons. The narrow dotted line from peak to peak is the multipeak diffraction path between the transmitter and receiver.

Simultaneous measurements were made at two frequencies: 4.95 GHz (C band) and 15.73 GHz (Ku band). Early in the experiment, a single 8.3-m antenna aperture at the Prospect Hill site was used for the two frequencies (5 GHz and 16 GHz L). Later, a second, smaller 0.9-m aperture was used at Ku band (16 GHz S). Two separate antennas were used for reception. They were sized to have the same beamwidth (3-m aperture at 5 GHz and 0.9–m aperture at 16 GHz). The receiver input could be computer switched to

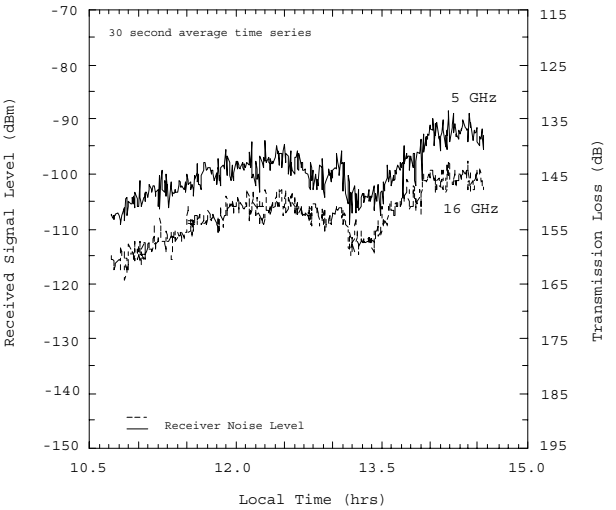

Figure 1.53 Received power time series for the Prospect Hill to Mt. Tug troposcatter path on August 3, 1987.

standard gain horn antennas mounted above and beside the larger aperture antennas. The receivers could also be switched to noise diodes for receiver calibration.

Four separate propagation modes were identified for this path: elevated layer ducting, turbulent forward scatter, scattering by rain, and scattering by aircraft. To aid in propagation mode identification, the delay spread was measured at Ku band and the Doppler shift and Doppler spread were measured at both frequencies. A short segment of the time series of received signal levels for observation on August 3, 1987, is presented in Figure 1.53. The measurements are for a period with tropospheric forward scatter as the dominant propagation mechanism. The received signal levels are for a 30-W transmitted carrier power at each frequency. The transmission loss is also indicated. Most observers use basic transmission loss (see Equation 1.2), but for the models that predict tropospheric forward scattering the full antenna gains are not realized. If basic transmission loss is used, an aperture to medium coupling loss must also be invoked as a correction. For the data presented in this figure, a 30-sec averaging filter was employed to reduce the more rapid Rayleigh distributed fluctuations characteristic of scattering from a volume filled with independent randomly placed scatterers.

The time series of hourly minimum, median, and maximum 120-sec averaged received power values for July 1989 is shown in Figure 1.54. Both the large and small Ku band aperture antennas at the transmitter were used at different times for the measurements reported in this figure. Only the large transmitting antenna was used at C band. The receiving antennas were pointed at the radio horizon. In this plot, the received power is for a 30-W transmitted power. The dark lines represent the median values and the light

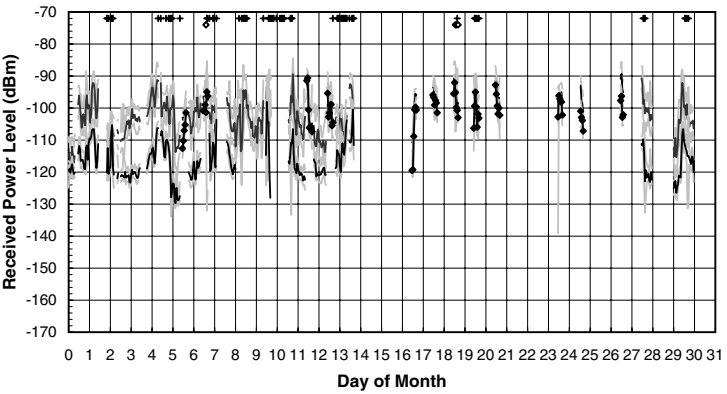

Figure 1.54 Received power time series for hourly values for the Prospect Hill to Mt. Tug troposcatter path in July 1989.

lines the bounding minimum and maximum hourly values. The Ku band measurements employing the large-aperture antenna are marked by diamonds along the dark line. The C band measurements had higher received power levels when the small Ku band transmitting antenna was used. Receiver noise was about –147 dBm at C band and –145 dBm at Ku band. Hours with rain are marked by + across the top of the figure; hours affected by scattering from aircraft are marked by open diamonds. The average difference between the median hourly values at the two frequencies for turbulent forward scatter conditions was 14 dB when the small Ku band transmitting antenna was employed and 3.5 dB when the large Ku band antenna was used. Note that the difference decreased by 10 dB when the large-aperture antenna was used, but the difference in transmitting antenna gain was 19 dB.

Figure 1.55 presents the hourly median Doppler shifts and Figure 1.56 the median Doppler spreads at each frequency for each hour of observations. The troposcatter measurement system can be viewed as a continuous wave bistatic radar.[27] Scattering from turbulence or rain in the scattering volume common to both the transmitting and receiving antenna main beams produces a Doppler shift to the scattered electromagnetic wave when the scatterers move. This frequency shift can be used to measure the velocity and variance of the velocity of the scatterers across the constant phase ellipses within the common scattering volume. In rain, the downward motion of falling drops produces the positive Doppler shifts evident at Ku band. Updrafts can produce negative Doppler shifts in clear sky, turbulent forward scattering conditions. Even in rain, the smaller common volume when the large Ku band antenna is used produced smaller median Doppler shifts than those observed with the smaller transmitting antenna. Aircraft also produced large Doppler shifts during the limited observation time of an aircraft transit through the common volume. The large Doppler spread shown for one of the aircraft-affected hours is an example.

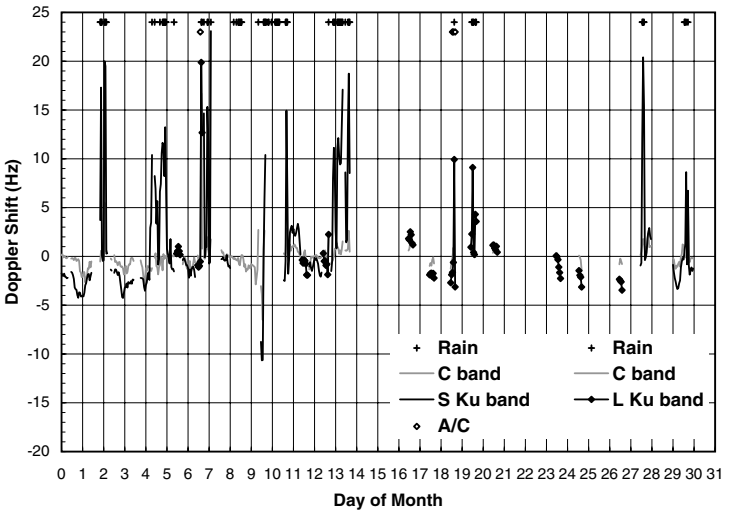

Figure 1.55 Doppler shift time series for hourly values for the Prospect Hill to Mt. Tug troposcatter path for July 1989.

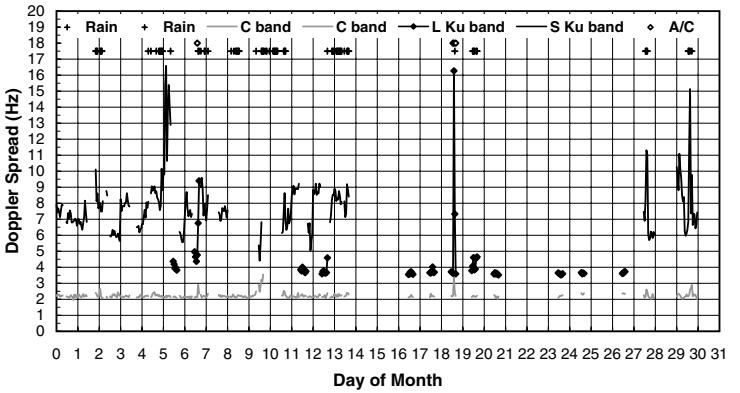

Figure 1.56 Doppler spread time series for hourly values for the Prospect Hill to Mt. Tug troposcatter path for July 1989.

Delay spread was measured using a pseudorandom noise sequence (PRN code) phase modulation at Ku band. Two code rates were used: a 12.5-MHz bit rate for the data shown in Figure 1.57 and a 400-MHz bit rate used later in the experiment. After processing, the minimum resolution for the lower bit rate was about 80 ns. Observations made using the large-aperture transmitting antenna (smaller common volume) showed delay spreads of the order of the system resolution during turbulent forward scatter conditions. Under similar propagation conditions, the delay spreads observed

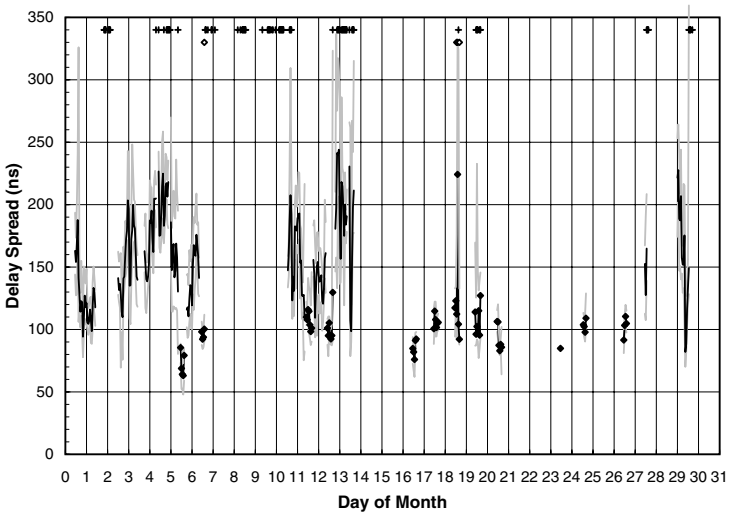

Figure 1.57 Delay spread time series for hourly values for the Prospect Hill to Mt. Tug troposcatter path for July 1989.

with the large common volume were much higher. The largest delay spreads were during periods with rain.

Figure 1.58 and Figure 1.59 show the cumulative EDFs for received power conditioned on the occurrence of turbulent forward scatter conditions during July 1998. They are plotted on normal probability graphs with the reduced variate on the abscissa. The 95% and 5% curves are the expected bounding curves for a normal probability distribution with the same mean and variance as the observations. As a graphical hypothesis test at a 0.1 significance level, the normal distribution is not consistent with the observations if the observations lie outside the bounding curves. At C band, the EDF is consistent with a lognormal distribution (received power [dBm] is normally distributed) for observations made simultaneously with both the large and small Ku band transmitting antennas. The case for Ku band is not as strong, and some departure from a lognormal distribution may be caused by the added effect of path attenuation variations.

The Prospect Hill to Mt. Tug experiment was designed to determine the dominant propagation mechanism for each hour of observations. Table 1.6A presents the summary statistics for the occurrence by mechanism for measurements made with the small Ku band transmitting antenna and the 12.5-MHz bit rate for the PRN code; Table 1.6B presents the summary statistics for observations made using the small Ku band transmitting antenna and the 400-MHz bit rate for the PRN code.

The occurrence statistics show that for this path and the two measurement campaigns, turbulent forward scatter occurred most often and propagation via elevated ducting layers occurred least often. This experiment was not designed to obtain long-term continuous observations. Much transmission

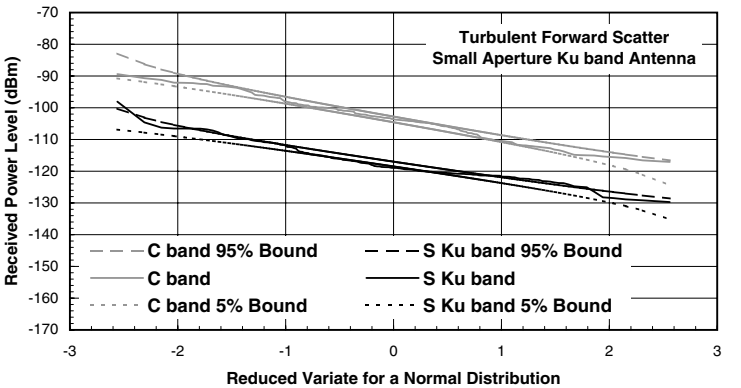

Figure 1.58 Received power EDFs for hourly median values for turbulent forward scatter conditions, small-aperture Ku band antenna for the Prospect Hill to Mt. Tug troposcatter path for July 1989.

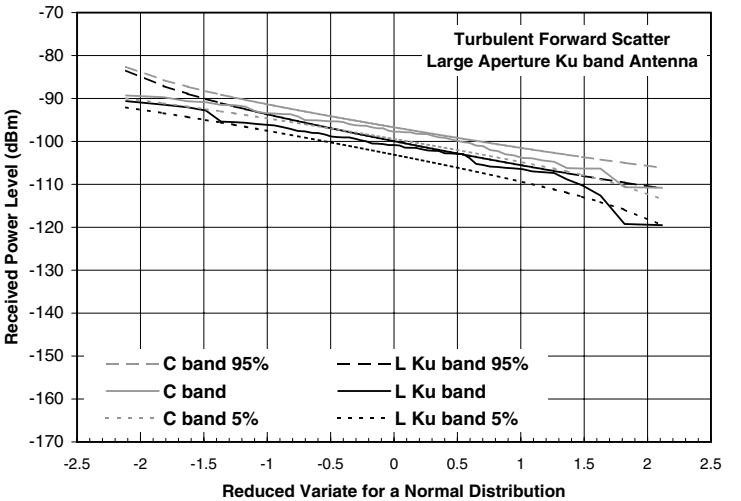

Figure 1.59 Received power EDFs for hourly median values for turbulent forward scatter conditions, large-aperture Ku band antenna for the Prospect Hill to Mt. Tug troposcatter path for July 1999.

loss data from transhorizon paths has been collected worldwide. Several organizations have cataloged the available data and prepared models curve-fit to the EDFs compiled from the data.[24,25,28] These models summarize the available data. The models generally attempt to follow physical models for the dominant propagation mode on a path. The data collection period and dynamic range of an observation set were often limited. Data collected for communication system design generally emphasized the higher transmission loss events whereas data collected for interference studies focused on

Table 1.6a Hours of Occurrence by Propagation Mode for Low Bit Rate Observations

Mode	Spring '89	Summer '89	Fall '89	Winter '90	Spring '90	Total
Turbulent scatter	247	670	294	179	1472	2862
Rain scatter	40	148	36		137	361
Elevated duct	14	54	2			70
Total time observations	301	872	359	179	1609	3293

Table 1.6b Hours of Occurrence by Propagation Mode for High Bit Rate Observations

Mode	Winter '91	Spring '91	Summer '89	Total
Turbulent scatter	796	1164	270	2230
Rain scatter	4	134	56	194
Elevated duct		10	33	43
Total time observations	800	1308	332	2467

the low transmission loss events. The data collection intervals usually did not span an integral number of years, and seasonal effects definitely dominate some of the observations. One of the models attempts to describe the variability (or uncertainty) of a prediction based on the model.[28]

1.4.2.5 Scintillation

Path attenuation or loss refers to relatively slow variations in the average signal level; scintillation refers to faster variations about the average value. Scintillation is caused by (1) rapid temporal changes in properties of the propagation medium; (2) rapid temporal changes in propagation geometry, which results in interference between multiple paths; or (3) changes in the spatial properties of the medium or changes in the propagation geometry, which produce temporal changes in signal strength as the medium drifts by the line of sight or the line of sight moves. Drifting electron density variations in the ionosphere can produce scintillation on Earth-space paths at UHF; drifting water vapor density changes in the lower atmosphere can produce scintillation in the SHF and EHF bands. In either case, scintillation is produced by spatial variations in the index of refraction of the medium.

1.4.2.5.1 Ionospheric scintillation. Fluctuations in amplitude, phase, and angle of arrival can occur in transionospheric propagation with changes in frequency, location, time of day, and levels of solar activity. Electron density fluctuations occurring within the auroral ovals at invariant latitudes above 55° or below –55° and the equatorial region between –20° and +20° invariant latitude (see shaded areas in Figure 1.60) produce measurable scintillation at frequencies between 0.3 and perhaps 10.0 GHz.

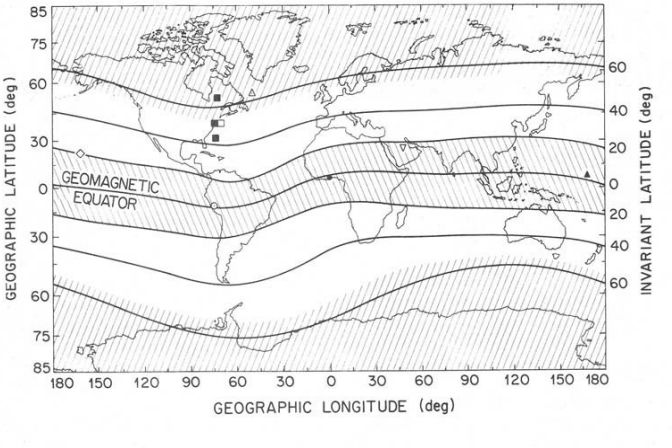

Figure 1.60 Map of equatorial and high-latitude ionospheric scintillation regions. (From Crane, R.K., *Proc. IEEE*, 65(2), 180, 1977. With permission.)

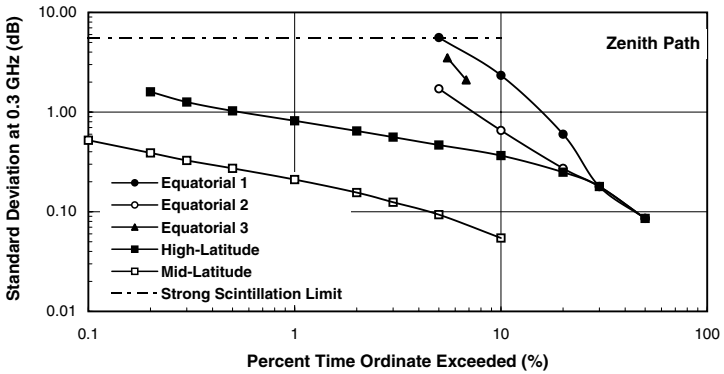

Figure 1.61 Ionospheric scintillation intensity EDFs at 0.3 GHz.

The invariant latitudes shown in Figure 1.60 are for a height of 300 km (peak of the F2 layer, see Figure 1.29). Annual occurrence statistics for zenith paths are presented for 0.3 GHz (Figure 1.61) and 1.5 GHz (Figure 1.62). The standard deviation statistics summarized in Figure 1.61 and Figure 1.62 were collected at frequencies between 0.13 and 0.4 GHz from 1969 to 1972 during a maximum of the sun spot cycle. The statistics are keyed to the measurement sites, shown as isolated symbols in Figure 1.60. The standard deviation measurements were scaled in frequency by using the $\lambda^{1.5}$ frequency dependence for weak scintillation and the elevation angle adjustment factor model shown in Figure 1.63.[29]

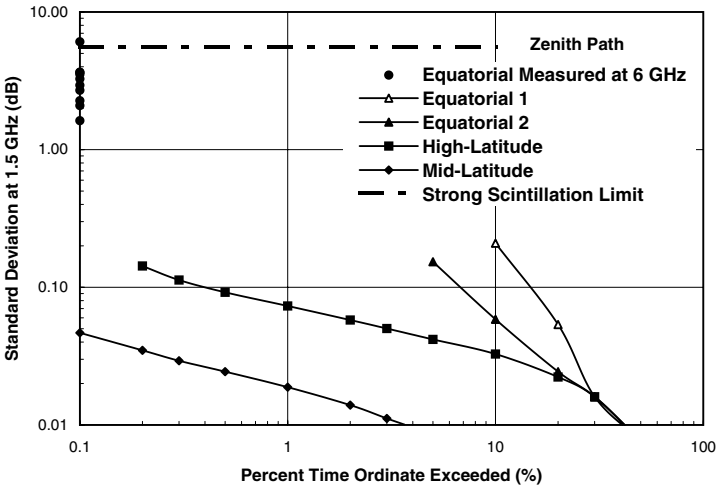

Figure 1.62 Ionospheric scintillation intensity EDFs at 1.5 GHz.

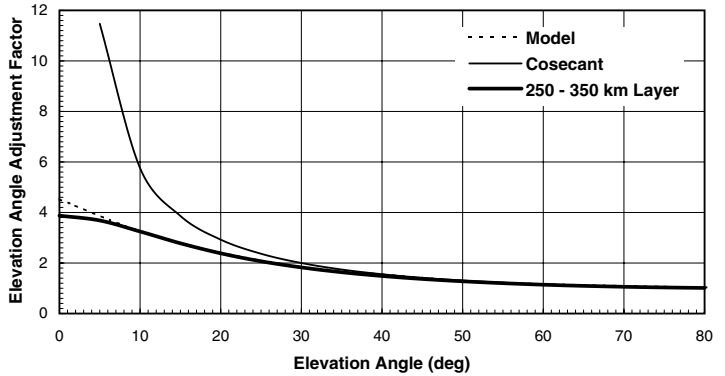

Figure 1.63 Elevation angle adjustment factor for weak ionospheric scintillation.

Zenith path statistics are presented for the high latitudes (auroral region), the geomagnetic equatorial region, and the intervening mid-latitude regions. At 0.3 GHz, ionospheric scintillation can occur in each region. The scintillation intensity is highest in the equatorial region. At this frequency, strong scintillation (at the indicated limit) occurred 5% of the time or less. Equatorial scintillation is a nighttime phenomenon. It starts about an hour after local sunset, reaches its peak before local midnight, and lasts about eight hours. The occurrence distributions for equatorial scintillation show that measurable scintillation occurs nearly every night. At a 45° elevation angle, strong scintillation at 0.3 GHz occurs on about a third of the evenings. The occurrence statistics for equatorial scintillation show a seasonal variation, with an increase in occurrences during the equinox periods. A tendency for higher

occurrences during the sunspot maximum has also been noted. At 1.5 GHz, additional statistics are indicated for the equatorial region at 0.1% time exceeded. The statistics were scaled to 1.5 GHz from observations made within 1° of the geomagnetic equator at 6.0 GHz.[30] Each symbol represents a different site.

The statistics are for the standard deviation of the logarithm of received power, σ_χ (dB). The S_4 index is usually employed to describe the intensity of ionospheric scintillation. S_4 is the standard deviation of received power (linear in power) divided by the average received power during the interval used to calculate the standard deviation. The distribution of received power within a scintillation episode is well approximated by a Nakagami-*m* distribution given the m parameter for the scintillation interval:[29]

$$\mathsf{m} = 1 / S_4^2 \tag{1.40}$$

The σ_χ and S_4 parameters can be related only when the received power distribution within the processing interval is specified. Figure 1.64 presents the relationship for the Nakagami-*m* distribution.[29]

The scale for scintillation intensity can be broken into several ranges: (1) very weak scintillation, in which the distribution of received signal power is asymptotically normal ($\sigma_\chi < 0.5$); (2) weak scintillation, in which the distribution is approximately lognormal ($\sigma_\chi < 3$); (3) stronger scintillation,

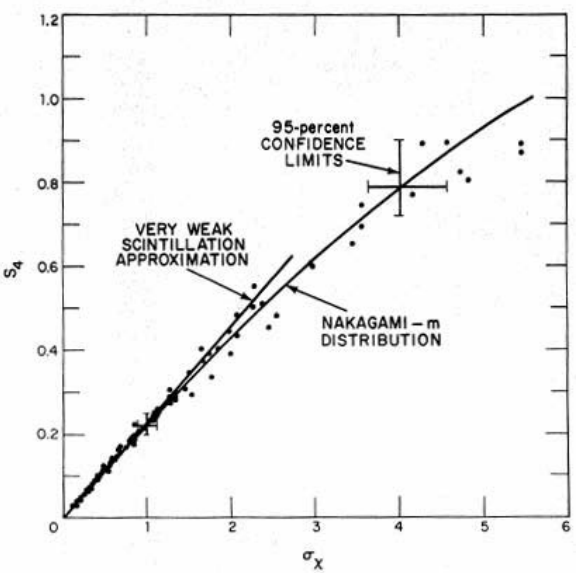

Figure 1.64 Observed and modeled relationship between intensity parameters for ionospheric scintillation. (From Crane, R.K., *Proc. IEEE*, 65(2), 180, 1977. With permission.)

in which the Nakagami-*m* distribution should be used ($\sigma_\chi < 5.0$); and (4) strong scintillation, in which the Rayleigh distribution ($\sigma_\chi = 5.6$, $\mathbf{m} = 1$, $S_4 = 1$) is obtained. The Rayleigh limit of strong scintillation is the maximum scintillation intensity to be expected. The frequency scaling used to prepare Figure 1.61 and Figure 1.62 was extrapolated from weak scintillation occurrence statistics.

1.4.2.5.2 Tropospheric scintillation. Tropospheric scintillation usually refers to fluctuations in amplitude, phase, or angle of arrival caused by variations in refractive index in the clear atmosphere. Scintillation on paths propagating through the lower atmosphere can also be caused by variations in attenuation or refractive index in clouds or rain (sometimes called wet scintillation), by variations in multipath interference on a moving line-of-sight, or any other process that can produce rapid variations in amplitude or phase. During clear sky conditions, scintillation is caused by turbulent fluctuations in the dry air density and water vapor content.

The time series of standard deviation in attenuation, σ_χ for tropospheric scintillation, and total attenuation for one day of observations at frequencies of 20.2 and 27.5 GHz are presented in Figure 1.65 and Figure 1.66, respectively. The standard deviation estimates were calculated from the 60 1-sec average samples that were collected in 1 min. The day included a rain attenuation event that caused a loss of signal at 27.5 GHz, attenuation by an earlier shower, attenuation by clouds and periods with clear sky. The clear sky scintillation was higher during the daytime hours (15:00 UT to 21:00 UT or 10:00 a.m. to 6:00 p.m. local time) than at night. The scintillation intensity, σ_χ, was higher at 27.5 GHz than at 20.2 GHz.

Scintillation can be generated by the diffraction of electromagnetic waves by phase variations produced by refractive index changes or by variations in amplitude caused by changes in specific attenuation along the propagation path. Diffraction by phase variations is a coherent process that affects the phase and amplitude of beacon measurements. Scintillation produced by variations in the specific attenuation affects both beacon measurements (amplitude and phase) and attenuation estimates derived from radiometer observations of changes in received power. Figure 1.67 and Figure 1.68 present the standard deviation of attenuation time series for the beacon receiver at 20.2 GHz and 27.5 GHz, respectively, and for attenuation estimates derived from radiometer measurements at each frequency. The radiometers used the same antenna as the beacon receiver and an 80-MHz bandwidth centered on the beacon carrier frequency. Scintillation caused by diffraction from phase variations (clear sky) does not cause an increase of scintillation intensity derived from radiometer observations but affects the scintillation on the beacon. The scintillation of attenuation derived from the radiometer shows the component of the fluctuation produced by variations in path attenuation due to water vapor changes, clouds, and rain.

The beacon-derived attenuation fluctuations also contain power level variations produced by the combination of receiver noise and received

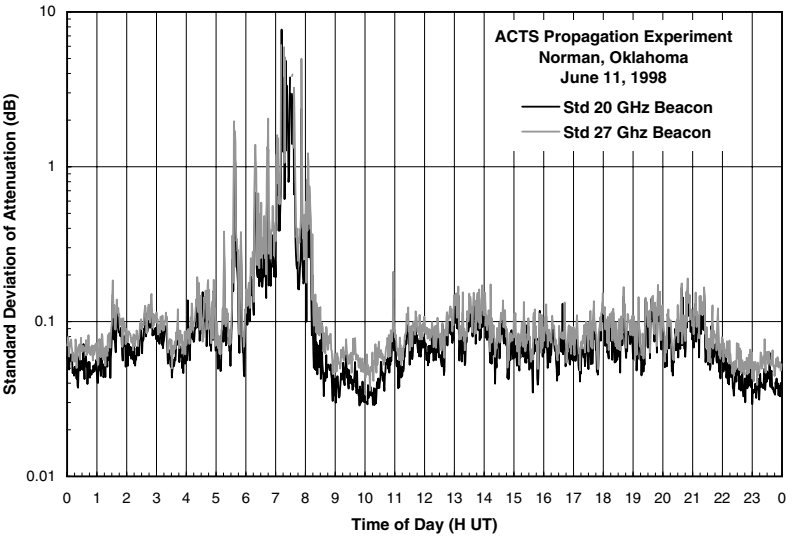

Figure 1.65 Standard deviation time series of within-the-minute beacon power measurements for Norman, OK, for June 11, 1998.

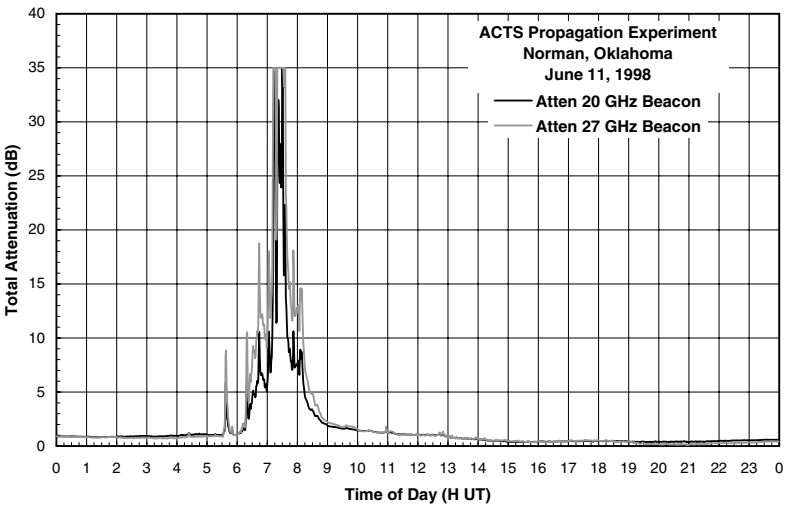

Figure 1.66 Total attenuation time series for Norman, OK, for June 11, 1998.

signal. As the attenuation increases, the signal-to-noise ratio decreases and an apparent increase in standard deviation results. In the absence of a signal and for a constant receiver noise, the standard deviation of the sampled receiver noise in the beacon channel would result in a σ_χ of 5.6 dB. The ACTS data processing system detected this loss of signal condition and removed those values from the reported statistics. The dynamic range of the receiver

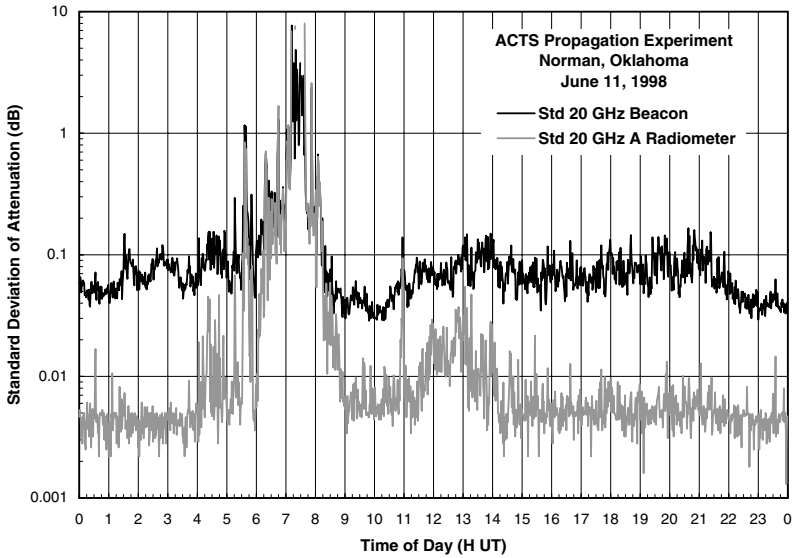

Figure 1.67 Standard deviation time series of within-the-minute total attenuation measurements at 20.2 GHz for Norman, OK, for June 11, 1998.

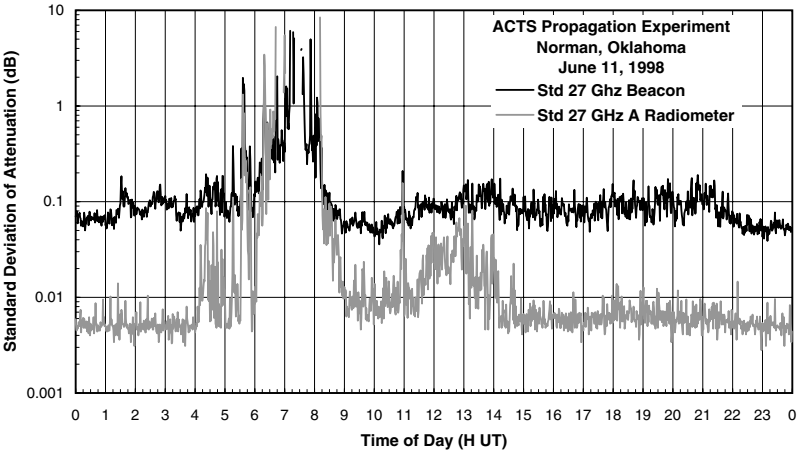

Figure 1.68 Standard deviation time series of within-the-minute total attenuation measurements at 27.5 GHz for Norman, OK, for June 11, 1998.

system limited the range of total attenuation observations to 30 dB. A combination of 35-dB total attenuation and zero scintillation values were used to indicate loss of signal.

Scintillation occurrence statistics for Norman, OK, at 20 GHz for different years and seasons are presented in Figure 1.69 and Figure 1.70, respectively. Noting that scintillation intensities above about 0.2 dB were due to

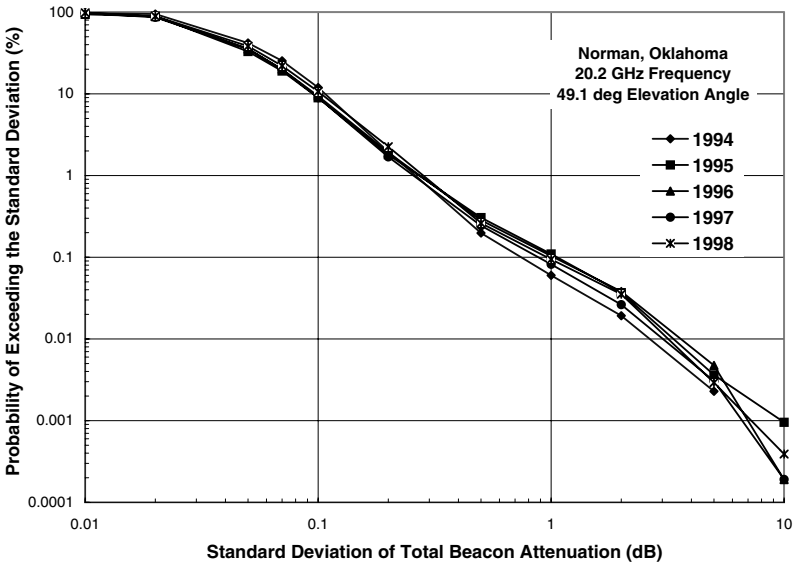

Figure 1.69 Standard deviation of 20.2-GHz total attenuation EDFs for different years at Norman, OK.

precipitation, the yearly variations in clear sky scintillation are lower than the yearly variations in wet scintillation. A strong seasonal variation in scintillation intensity is evident. For clear sky conditions, $\sigma_\chi < 0.2$, summer time with higher water vapor densities produced higher occurrences of scintillation whereas winter produced nearly an order of magnitude less scintillation at the same intensity. In Oklahoma, convective precipitation occurs more often in the spring, summer, and fall than in the winter.

Figure 1.71 presents the occurrence statistics for variations in beacon power and in total attenuation derived from atmospheric radiation detected by a radiometer. The statistics are presented for two frequencies. For standard deviation values lower than 0.2 dB, diffraction by phase variations is the dominant mechanism for producing scintillation. At higher scintillation intensities, variations in specific attenuation are more important. Note that the frequency dependence of scintillation intensity is mechanism dependent. The occurrence statistics are also a function of location and path type. A long, low elevation angle path (or terrestrial path) will experience higher occurrences of scintillation than a high elevation angle Earth-space path. The range of scintillation intensities is the same as that shown in Figure 1.71.

1.4.3 Receiver noise

Receiver noise is composed of the noise produced within the receiver, noise incident on the receiving antenna from atmospheric sources and beyond, and interference incident on the antenna from other transmitters. An absorbing medium both absorbs and emits atmospheric radiation in equal measure

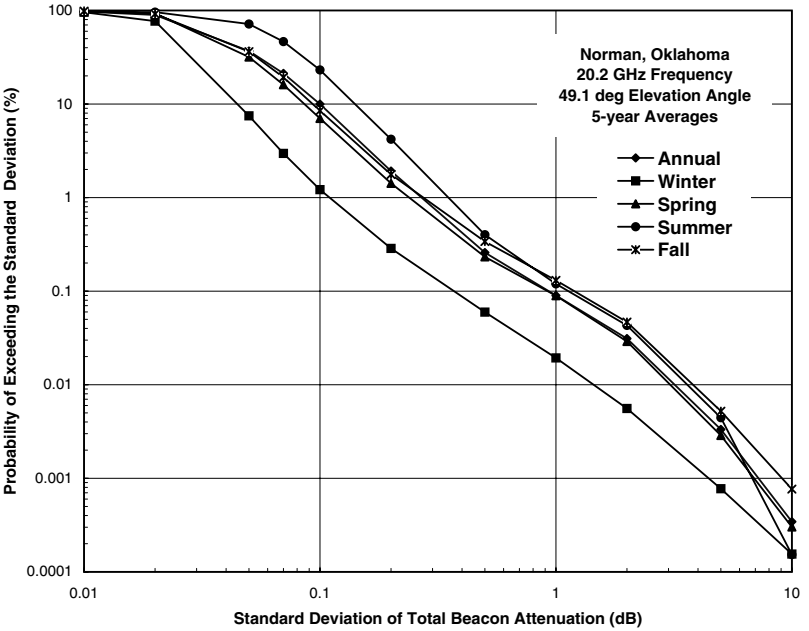

Figure 1.70 Standard deviation of 20.2-GHz total attenuation EDFs for different seasons at Norman, OK.

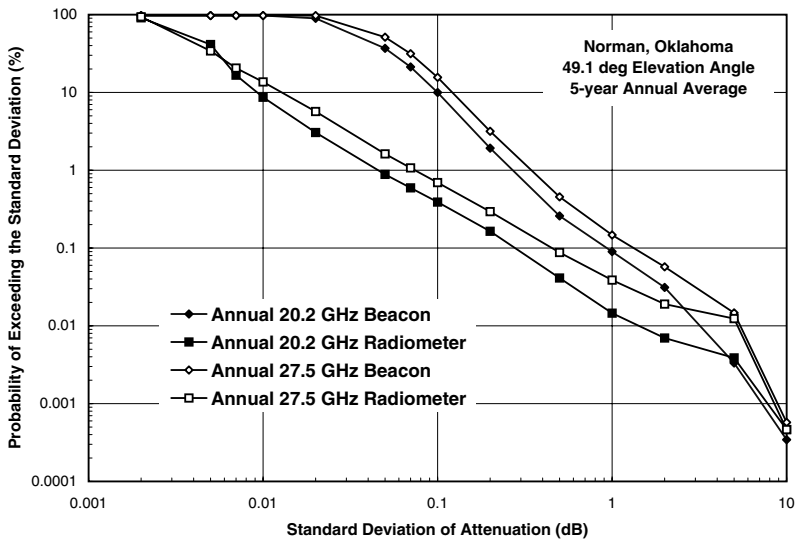

Figure 1.71 Standard deviation of 20.2- and 27.5-GHz beacon- and radiometer-derived total attenuation EDFs for Norman, OK.

to maintain thermal equilibrium. This emission is called thermal noise. The received noise power from thermal emission is related to the brightness temperature of the emission by:

$$P_B = \mathsf{K} T_B B \tag{1.41}$$

where K is Boltzmann's constant = $1.38 \cdot 10^{23}$ (J/K), T_B the brightness temperature (K), B the receiver detection bandwidth (Hz), and P_B the noise power (W). Equation 1.41 is also used to relate the noise power generated in the receiver to an effective receiver noise temperature.

The propagation of radiation through the atmosphere is governed by Beer's law:[31]

$$\frac{dI_f}{ds} = \frac{dS}{dsdf} = -\beta_e I_f = -k_e \rho I_f \tag{1.42}$$

where I_f is the radiance or brightness, β_e the monochromatic extinction cross section per unit volume, k_e the mass extinction coefficient, ρ the density of the atmosphere, and s the distance along the propagation path. The radiance from a volume of air is given by the monochromatic Planck's function:[31]

$$B_f(T) = \frac{hf}{\left(e^{\frac{ht}{\mathsf{K}T}} - 1\right)} \approx \mathsf{K}T \tag{1.43}$$

where the approximation obtains in the UHF–EHF frequency bands. The radiative transfer equation in a nonscattering medium is then given by:[31]

$$\frac{dI_f}{ds} = -\beta_e I_f + \beta_a B_f(T) \tag{1.44}$$

where the absorption, β_a, and extinction cross sections per unit volume are identical. For a nonscattering medium, the radiative transfer equation can be integrated to yield:

$$I_f(s) = I_f(0) e^{-\int_0^s \beta_e(r)dr} + \int_0^s \beta_a(r) B_f(T(r)) e^{-\int_r^s \beta_e(r')dr'} dr \tag{1.45}$$

In the frequency range of interest, T_B is proportional to I_f and the radiative transfer equation for an upward-looking narrow beamwidth antenna reduces to:

$$T_B(s) = 2.75e^{-\int_0^s \beta_e(r)dr} + \int_0^s \beta_a(r)T(r)e^{-\int_r^s \beta_e(r')dr'}dr \qquad (1.46)$$

where the integration is downward along the curved propagation path through the entire atmosphere and T_B (0) = 2.75 K is the brightness temperature of the "big bang" incident on the top of the atmosphere.

Sky brightness temperature (for an upward-looking antenna) for the ITU-R standard mid-latitude atmosphere is presented in Figure 1.72 as a function of frequency for four initial elevation angles. The calculations are for an idealized narrow beamwidth antenna without sidelobes. To model the response of a real antenna, the brightness temperature must be integrated over the entire antenna pattern. Emission from the Earth into the far sidelobes of the antenna pattern can produce measurable increases in sky brightness temperature. Figure 1.73 presents calculations of the Earth brightness temperature for upwelling radiation as observed at a satellite as a function of the elevation angle of the ray at the Earth's surface. The emissivity of the Earth's surface, assumed to be independent of frequency, had a value of 0.7. Downwelling radiation reflected into the direction of the observing satellite is included in the calculation.

Radiometric observations of sky brightness temperature are shown in Figure 1.74 for the day that produced the attenuation by rain displayed in Figure 1.66. Clear-air absorption dominated from 0:00 to 4:00 UT and after 15:00 UT. Attenuation and scattering by rain occurred between 5:00 and 9:00 UT. A radiometer observes the noise power produced by the receiver, thermal emission collected by the receiving antenna, and other interfering sources. In the absence of interference, the noise power caused by the atmo-

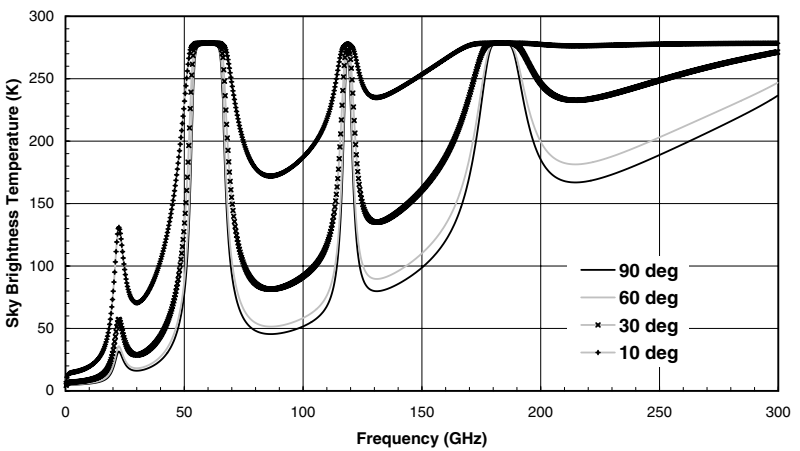

Figure 1.72 Sky brightness temperature as a function of frequency at select elevation angles for the ITU-R standard mid-latitude atmosphere.

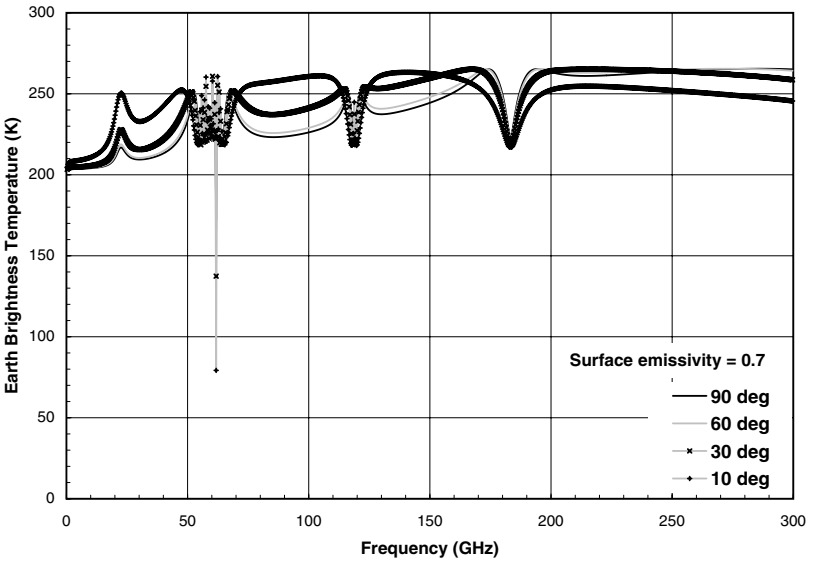

Figure 1.73 Earth brightness temperature as a function of frequency at select elevation angles for the ITU-R standard mid-latitude atmosphere.

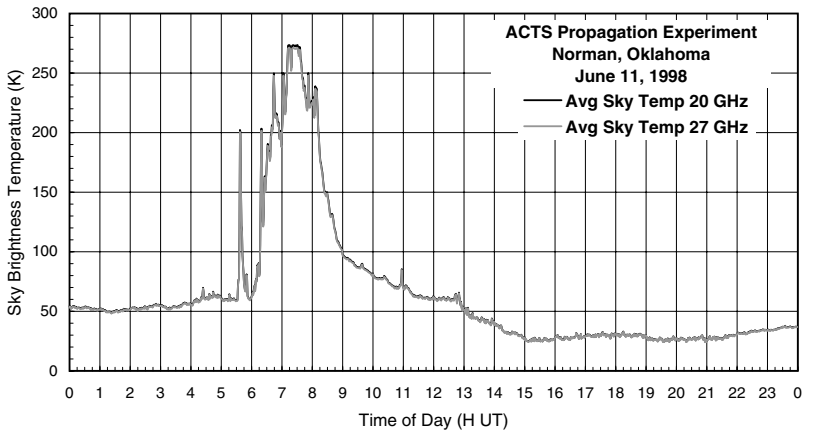

Figure 1.74 Sky brightness temperature time series for Norman, OK, for June 11, 1998.

sphere is obtained by subtracting the receiver noise power and an estimate of the thermal emission viewed through the antenna sidelobes. The result is then corrected for antenna efficiency and converted to sky brightness temperature (as shown in Figure 1.74). Equation 1.46 can be integrated for a constant temperature medium. By defining an effective medium temperature, T_M, a constant temperature that would provide the same answer as Equation 1.46 for the actual temperature variation along the path, the equation reduces to:

$$T_B = 2.75e^{-\tau(0,s)} + T_M \int_0^s e^{-\tau(r,s)} d\tau(r,s) \tag{1.47}$$

where

$$\tau(r,s) = \int_r^s \beta_e(r')\, dr'$$

is the optical depth. This equation may be integrated to yield:

$$T_B(s) = T_M + (2.75 - T_M) e^{-\tau(0,s)} \tag{1.48}$$

Equation 1.48 can be rearranged to yield equations for optical depth or path attenuation:

$$\begin{aligned} \tau(0,s) &= \ln\left(\frac{T_M - 2.75}{T_M - T_B}\right) \\ A(0,s) &= 10 \log_{10}\left(\frac{T_M - 2.75}{T_M - T_B}\right) \end{aligned} \tag{1.49}$$

where $A(0,s)$ is total path attenuation.

The total attenuation estimates obtained from beacon measurements (Figure 1.66) and the attenuation estimated from the 20.2-GHz sky brightness measurements (Figure 1.74) are presented in Figure 1.75. The effective medium temperature was estimated for each hour, using surface meteorological data. The logarithmic scale used in the figure allows a comparison between beacon observations and total attenuation estimates obtained using Equation 1.50. For attenuation values lower than 1.0 dB, the maximum differences were 0.1 dB. During the periods with rain, the attenuation estimates were within 1 dB of the beacon measurements for total attenuation values less than 10 dB. Similar results were obtained at 27.5 GHz as shown in Figure 1.76. The largest differences between beacon attenuation and the radiometer-derived attenuation estimates were during rain. Small errors in the estimates of the effective medium temperature will produce large errors in the estimated attenuation when the sky brightness temperature is close to the medium temperature. As a rule of thumb, attenuation estimates derived from radiometer measurements higher than about 10 dB are suspect. The basic assumption of a nonscattering medium used to establish Equation 1.44 is violated also for propagation through rain.

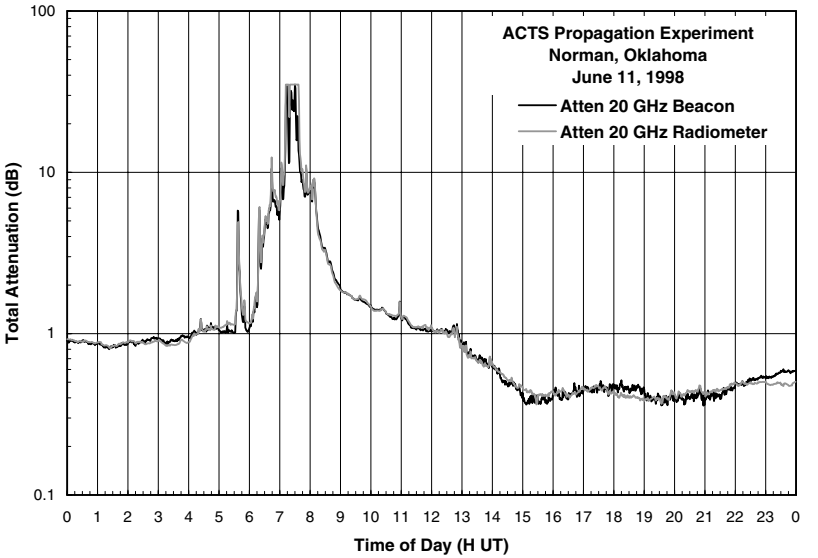

Figure 1.75 Total attenuation estimates derived from 20.2-GHz beacon and radiometer measurements for Norman, OK, for June 11, 1998.

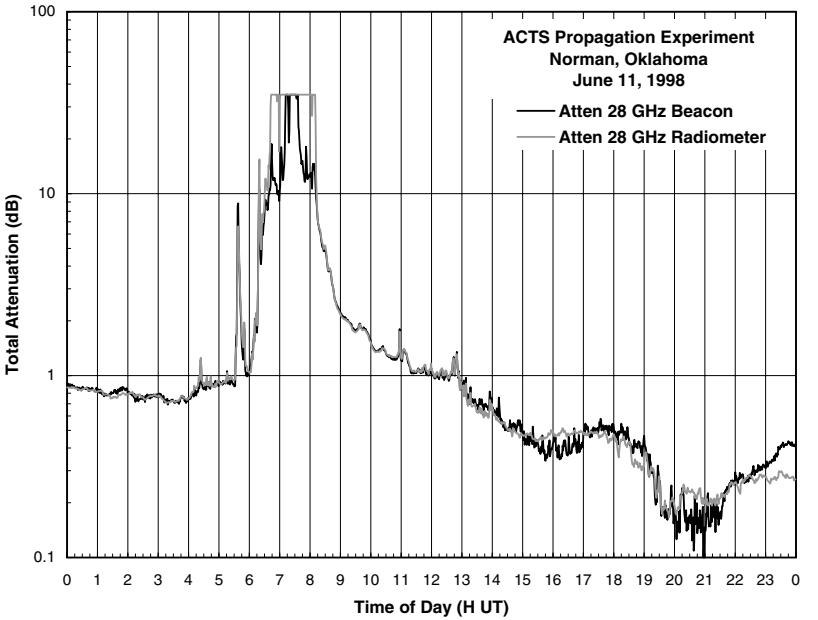

Figure 1.76 Total attenuation estimates derived from 27.5-GHz beacon and radiometer measurements for Norman, OK, for June 11, 1998.

1.5 *Propagation models*

The observations and calculations presented in Section 1.4 were a mixture of direct measurements of the effects of a propagation mechanism or theoretical calculations based on the physics of the propagation phenomenon. Measurements are specific to a path, and statistics obtained on that path may not be applicable to another or on the same path at a different time, season, or year. Theoretical calculations require a complete description of the medium and its boundaries, but a complete description is never available.

Required for system design is a set of statistics that describes the expected performance of a propagation path. Propagation models are employed to provide the required statistics. Propagation models vary in type and ease of use. Two general classes of models are available: (1) models that summarize the statistics for path performance derived from entries in databases containing statistics from a large collection of propagation measurements and (2) models that use assumptions about propagation physics and the statistics of the underlying processes that affect the path. An example of the first type of model is a prediction procedure that relies on empirical attenuation statistics collected in a database from mid-latitude, continental climate sites to extrapolate the expected variation in attenuation with occurrence probability to other locations and carrier frequencies (the ITU-R prediction model circa 1995[32]). An example of the second type is a model that relies on climatological rainfall intensity statistics as a function of occurrence probability to calculate the expected attenuation occurrence probabilities (the Crane two-component model[33]). The first type of model uses the measured attenuation and rain-rate statistics to set the model parameters; the second derives its parameters from meteorological statistics but does not use a comparison with attenuation statistics to adjust any parameter.

The first type of model is a regression model; the second type is a physical model. Both are necessary to evolve adequate modeling procedures. In the case of the development of models for slant path attenuation by rain, the early reports and recommendations of the ITU-R (then the International Radio Consultative Committee or CCIR) published statistics and path parameters for a handful of paths, with the assumption that other paths would have similar statistics. Alternatively, bounds on statistics were generated by using physical models. Medhurst made theoretical calculations of specific attenuation as a function of rain rate for spherical drops, and prepared bounds on the possible values of specific attenuation for the wide range of all possible drop size distributions that could produce the specified rain rate.[34] When he compared available short horizontal path attenuation observations with simultaneous rain rate observations made along the path, he found that for the most careful measurements, the observed attenuation exceeded any possible value based on the theoretical predictions and measured rain rates. He concluded that the theory was wrong. However, a careful review of the measurements suggested that the rain rate measurements were in error.[35] In retrospect, a radome on either the transmitting or receiving

antenna or both could also increase the measured attenuation relative to the predictions.[5]

As additional long-term attenuation measurements and simultaneous rain-rate observations became available, a sequence of regression models was developed to estimate attenuation statistics, given equiprobable rain-rate statistics (e.g., see Stutzman and Dishman[36]). However, a model was still required to estimate the rain-rate statistics. The ITU-R rain attenuation prediction procedures recommended the use of rain-rate measurements made at the site of interest.[32] Most designers did not have the luxury of spending 3 to 5 years in making rain-rate measurements at a site before starting their design. Rice and Holmberg[37] developed the first rain-rate distribution prediction model based on long-term hourly rain-rate statistics and excessive precipitation data. Their model used annual precipitation occurrence values and the ratio of thunderstorm to total rainfall as input. The former parameter was readily available worldwide, but the latter was not.

Crane[38] followed with a "global" climate zone model that used the median of all the rain-rate occurrence distributions obtained within a rain climate zone at the time the model was developed as the predicted rain-rate distribution for that rain zone. The climate zone boundaries were set by using climatological statistics on average annual rain accumulation and number of thunderstorm days, and climate maps based on vegetation type. The CCIR developed a similar climate zone model but with zone boundaries set by the consensus of CCIR delegates. The CCIR (now ITU-R) rain zone model boundaries and rain-rate statistics were regularly updated as new rain-rate data became available.[32]

Recently, the ITU-R has moved to a new worldwide model developed by the European Space Agency (ESA).[39,40] It is based on long-term (15-year) numerical model reanalysis data from the European Centre for Medium-Range Weather Forecast (ECMWF) and long-term monthly rain accumulation statistics from the Global Precipitation Climate Project (GPCP). These data were not in a form directly useful to estimate rain-rate statistics. A further regression analysis was required to relate the numerical analysis output and rain accumulation statistics to available rain-rate statistics.

Prediction results for the two rain zone models and the new ESA map model are presented in Figure 1.77. The predictions of each model were compared to the 113 single-year annual rain-rate EDFs in the ITU-R slant path database.[1] The natural logarithms of the ratio of measured-to-modeled rain rate at selected annual probability values were used as the comparison measure. The logarithm was employed because observations of yearly variations in the EDFs at fixed probabilities are well described by lognormal distributions.[33] The root-mean-square-deviation (RMSD) values were nearly identical statistically at 0.01% of a year for each of the models, the original Crane global rain zone model, the updated ITU-R rain zone model, and the new ESA map model. The rain rate at 0.01% of a year is employed in the ITU-R rain attenuation prediction models.[9,40] For the set of rain-rate distributions in the slant path rain attenuation database, these three models did

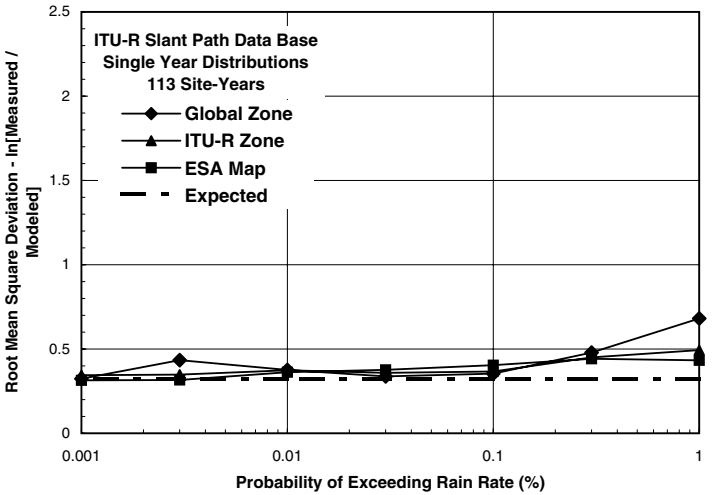

Figure 1.77 RMSD vs. exceedance probability for single-year rain-rate distributions in the ITU-R slant path database.

not differ statistically for percentages of the year lower than 0.3%. The comparisons at these percentages were not significantly different from the expected interannual variations predicted by the global model.

A second statistic of interest in evaluating prediction models is the average prediction error or bias error. Figure 1.78 displays the bias errors as a function of rain exceedance probability. This figure presents the biases of two of the models. The bounds shown for each model span the range of deviations expected for 90% of the calculated biases for independent collections of 113 rain-rate EDFs. An unbiased model would have bounds that enclose zero error (the measured statistic equals the model prediction). For use in the ITU-R attenuation prediction model, the global rain zone model is unbiased at 0.01% of a year but the ESA map model is biased based on data in the data bank. It is noted that parameters for the ESA map model were set by using the rain-rate EDFs in this data bank.

The development of prediction models for any propagation phenomena of importance in system design follows the pattern described previously for modeling rain-rate statistics. First, a few measurements are used to illustrate the phenomenon. Then, a simple physical model is employed to bound the possible range of effects on system design. Finally, as more data become available, a series of ever-improving regression and physical models are developed to provide advice to system designers. Reference has been made repeatedly to the recommendations of the ITU-R. The role of ITU-R Study Group 3 (formerly Study Groups 5 and 6 of the CCIR) is to provide a forum for the continued presentation, development, and refinement of propagation models. Reference has also been made to different recommendations of the ITU-R. Their numbering system provides a version identifier after each recommendation number. The output from the study group evolves in time,

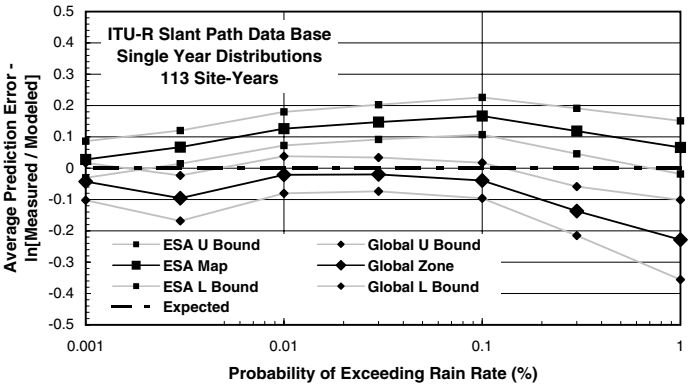

Figure 1.78 Average prediction error (bias) vs. exceedance probability for single-year rain-rate distributions in the ITU-R slant path database.

resulting in changing versions. A handbook such as this one is static and can only present the current state of propagation modeling. It can, however, recommend a consistent set of models drawn from the array of models that are available and present the background needed to select and use the model best fitted to a specific design problem.

1.6 *Model verification*

A number of competing models have been developed to predict the occurrence and magnitude of each of the propagation phenomena presented in Section 1.4. As an example, Figure 1.77 and Figure 1.78 compare prediction errors for three of a number of the models available to generate the rain-rate distributions needed for input to the ITU-R model currently recommended for the prediction of excess rain attenuation on a slant path to a satellite[40]; input to the ITU-R model for the prediction of excess path attenuation on terrestrial paths[9]; and input to the ITU-R model for interference by rain.[25] The two measures used for model comparison were the RMSD and bias values at probability values separated by half decades.

A measured annual rain-rate distribution (EDF) is a sample or realization from the random processes that produced the annual EDF. The natural logarithm of the ratio of measured to modeled distribution values, ξ_{ij}, at probability level i was calculated for empirical distribution function j (EDF, a cumulative distribution obtained from measurements). The large, half-decade spacings between probability levels were required to reduce the correlations between values at adjacent probability levels in a distribution. This correlation is forced by the process of constructing an ordered (or cumulative) distribution.[41,42] The logarithm was used because the random yearly and locational variations of ξ_{ij} at a single probability level within a climate region are well modeled by the lognormal distribution.[33] The ordered distributions for ξ_{ij} at i for 0.01% of a year for a set of independent rain-rate

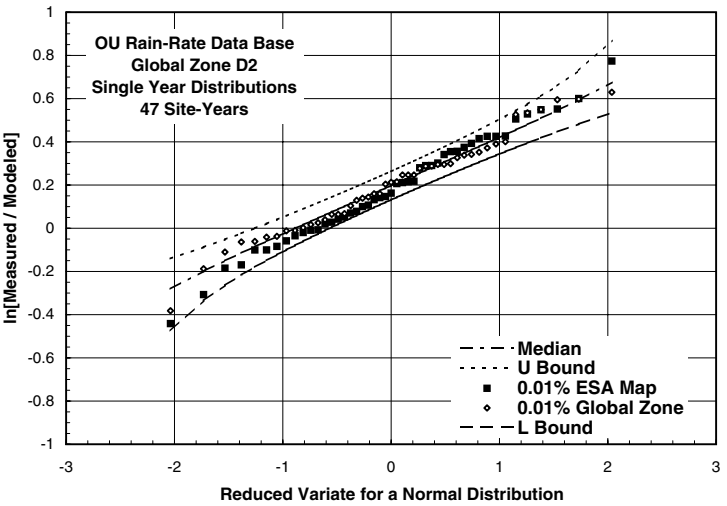

Figure 1.79 Ordered distribution of ln[measured/modeled] distribution values for 0.01% of a year and for 47 single-year EDFs in rain climate region D2.

distributions in zone D2 of the global rain zone model are presented in Figure 1.79.

The 0.01% values from the EDFs ordered for this distribution were obtained from data in the University of Oklahoma (OU) rain-rate data bank. The abscissa is the reduced variate for a normal probability distribution. The plot uses a normal distribution scale for probability and a logarithmic scale for the observed ratio values. The reduced variate is the variate for a zero mean, unity standard deviation normal distribution. If the underlying random process were lognormal, the ordered set of measured values would lie along a straight line.[42] The parameters for the lognormal model were maximum likelihood (ML) estimates based on the global rain zone model predictions.[41] The ordered global zone values of measured to modeled ratio lay along the median curve in the central region of the distribution, between ±1 standard deviation. The bounds are curves expected to contain 90% of the distributions of EDFs that would be obtained from similar sets (independent databases) of observations if the underlying random variability process were lognormal. As a visual hypothesis test, empirical ordered ξ_{ij} distributions contained within the bounds are consistent with the lognormal model distribution hypothesis at the 0.1 significance level.

The model prediction value for the global zone model was a constant because all the EDFs are from the same rain zone. Except for model bias, the shape of this distribution represents only the changes in rain-rate statistics for yearly and locational variations within the rain zone. The 47 sample distributions in the OU database were obtained from 17 different locations. The ESA map model uses a spatial interpolation of parameters obtained from the accumulation adjusted numerical model output within a 1.5° latitude by

1.5° longitude grid square to calculate each rain-rate prediction. For this model, both the observed and modeled values change with location. The ξ_{ij} distributions for both the global zone and ESA map models were consistent with the lognormal hypothesis.

The bias and RMSD values for probability level i are calculated using:

$$\begin{aligned} \text{bias} &= \bar{\xi}_i = \frac{1}{N}\sum_{j=1}^{N}\xi_{ij} \\ \sigma_{\xi_i}^2 &= \frac{1}{(N-1)}\sum_{j=1}^{N}\left(\xi_{ij}-\bar{\xi}_i\right)^2 \\ \text{RMSD} &= \sqrt{\sigma_{\xi_i}^2 + \bar{\xi}_i^{\,2}} \end{aligned} \tag{1.50}$$

where the overbar signifies average value, σ_ξ^2 is the unbiased variance estimator, σ_ξ the standard deviation, and N the number of EDFs. For the rain-rate distribution prediction models used to generate Figure 1.79, the biases were 0.20 nepers for the global rain zone model and 0.18 nepers for the ESA map model. The RMSD values were 0.30 and 0.31 nepers for the two models, respectively. These values may be converted to percent error for each prediction model when the model value is used for reference by:

$$\Xi = 100 \cdot (e^{\xi} - 1) \tag{1.51}$$

where Ξ is in percent and ξ is in nepers. The biases then are 22% and 20%, respectively, and the RMSD values become 34% and 37%, respectively. Although these prediction errors may seem large, they are typical of results for rain-rate distribution models because the interannual variation with a perfect model is the order of these RMSD values.[33]

The bias and RMSD values given are for a single probability level. The current ITU-R models for rain effects use rate statistics at only one probability level, 0.01% of a year, as input. Most other models use the entire rain-rate distribution. The merit of a prediction model should be judged for a range of probability levels. The bias and RMSD values are then calculated by using the average and variance values summed over both i and j. The bias and RMSD values for the probability range from 0.001% to 1% for the 47 site-year data set are given in Table 1.7. This table presents two sets of bias and RMSD values, one for the prediction of rain rate at fixed probability levels and the other for the prediction of probability at fixed rain-rate values. Regression models generally have parameter values selected to minimize one of the comparison measures, typically the RMSD value at fixed probability levels. The best model depends on the application. It should produce the lowest

Table 1.7 Bias and RMSD Values (nepers) for 47 Site Years of Observations from Data in the OU Rain-Rate Database for Probabilities from 0.001% to 1.0% of a Year

Model	Bias for fixed probability	RMSD for fixed probability	N	Bias for fixed rain rate	RMSD for fixed rain rate	N
Global zone	–0.052	0.424	344	0.013	0.565	337
ITU-R zone	0.166	0.379	344	0.239	0.625	337
ESA map	0.082	0.409	308	0.223	0.589	337

RMSD value for the range of probability or rain-rate values of interest with perhaps the minimum complexity or computational burden. If the application needs the predicted probability for a given rain rate, the lowest RMSD value for fixed rain rate is the appropriate selection criterion.

The model comparison measures — the bias and RMSD values — may be used to select the best model for a particular application. The question of model validity has not been addressed. A valid model is one that provides an estimate of the statistic of interest, in this case the expected rain rate or probability, that is within the expected range of values for the phenomenon of interest at the location or time of interest. It must be valid for all locations where it will be used. For instance, a model that is valid in global rain zone D2 may not be valid in another rain zone. The verification that a model is valid requires comparison statistics from a wide range of geographic locations. The model must also be tested by using data different from those employed to set the model parameters.

The ordered distribution of ξ_{ij} at i for 0.01% of a year from all the independent annual rain-rate distributions in the OU rain-rate distribution database is presented in Figure 1.80 for the global zone and ESA map models. In this case, 194 sample EDFs were available, but with model predictions that varied with location and climate zone. The bounding curves are for zero bias and the same standard deviation as used for Figure 1.79 (σ_ξ = 0.22 or 25%). Within the central region of the distribution (between –1.7 and +1 standard deviations on the reduced variate scale), the ESA map model provided a good match to the measured distributions at 0.01% of a year, that is, the values lie within the bounds. The global zone distribution provided a good match to the lognormal variability model but with a 0.06 (6%) bias error. The upper and lower tails of the ordered distributions lie outside the expected bounds for a lognormal process. This could be caused by measurement error, modeling error, or a change in variability statistics with climate region.

The statistics presented in Figure 1.77 to Figure 1.80 do not provide valid tests for the rain-rate distribution models because the rain-rate EDFs in the data banks were used to set the model parameters. The model distributions for the rain zones in the global climate zone model are the medians for all the distributions within a climate zone available at the time the model was developed.[38] Figure 1.81 presents the number of site-years of data employed

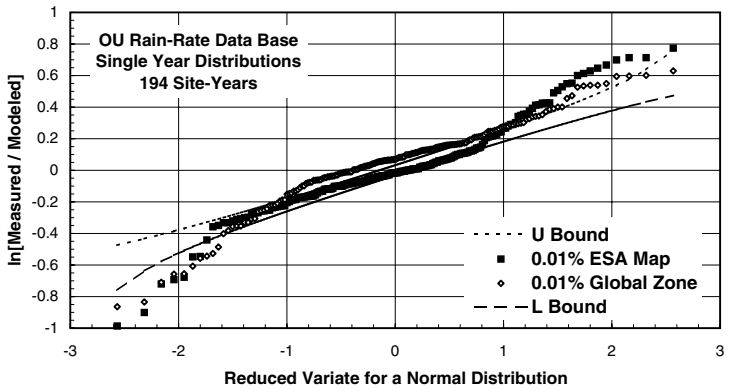

Figure 1.80 Ordered distribution of ln[measured/modeled] distribution values for 0.01% of a year and for all single-year EDFs in the OU rain-rate database.

to construct the median distributions. Based on the variability standard deviation employed to calculate the bounding curves in Figure 1.79 and Figure 1.80, 5 years of observations at a single location are needed to estimate a rain-rate value in the distribution with an estimation error of less than 0.1 nepers (10%). Including the added variability associated with the expected locational variations within a climate zone, the minimum number of annual distribution observations needed to establish a model distribution for a climate zone is eight.[43] Insufficient data were available for the global rain climate zones B, G, and H. The global model should perform better in regions with adequate data.

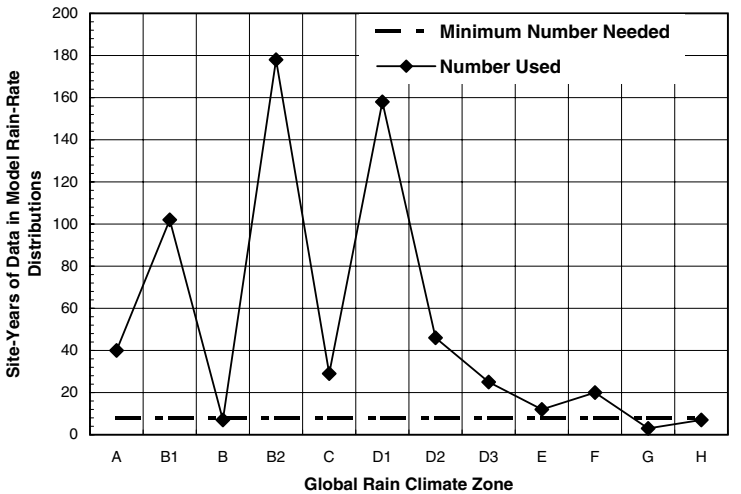

Figure 1.81 Site-years of data used to generate the median rain-rate distribution for each global rain climate zone.

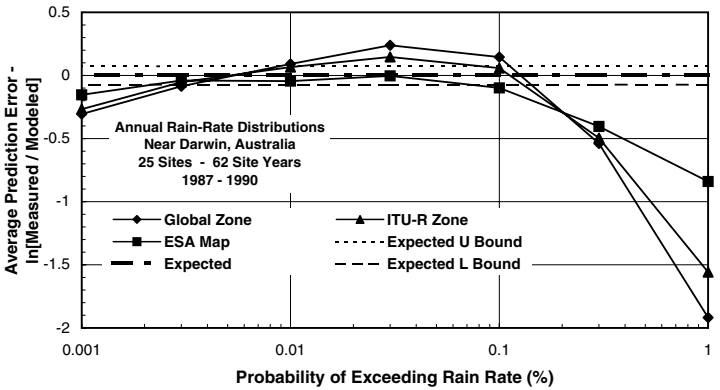

Figure 1.82 Average prediction error (bias) versus exceedance probability for single-year rain-rate distributions near Darwin, Australia, in the ITU-R rain-rate database.

The ITU-R rain-rate database (circa 1999) was compiled to provide distributions for testing that were not used in the preparation of parameters for any model developed prior to 1999. This database contained 99 EDFs from two climatologically different regions, one in the tropics near Darwin, Australia, and the other in a coastal mid-latitude region near Wallops Island, VA. The measurements near Darwin were from gauges in global rain climate zone G and ITU-R rain climate zone N. Model bias errors for this region are presented in Figure 1.82. At 0.01% of a year, the ESA map and ITU-R zone models were unbiased (bias values within the expected bounds). The ESA map model was unbiased for annual probabilities from 0.003% to 0.1%. The global zone model had significant bias (bias values outside the expected bounds) at all probability levels. All three models did poorly at annual probabilities greater than 0.1%.

Bias estimates for observations near Wallops Island, VA, are presented in Figure 1.83. For this data set, all but the Crane local model were biased at 0.01% of a year. The Crane local model was developed recently for application within the United States.[44] It uses local climatological data based on 30 or more years of observation to generate the predictions. Figure 1.84 and Figure 1.85 present the RMSD values for Darwin and Wallops Island data sets, respectively. Using the expected RMSD value as a measure of model performance, all three model predictions for the Darwin region produced less deviations from observations than expected for probabilities less than 0.3% of a year. For application near Wallops Island, VA, the four models produced less error than expected. Model performance statistics for two ranges of probability levels are presented in Table 1.8 to Table 1.11.

The bias and RMSD values listed in Table 1.8 to Table 1.11 were calculated by using the average and standard deviation values for all the entries for each climate region within the specified probability ranges. They differ from

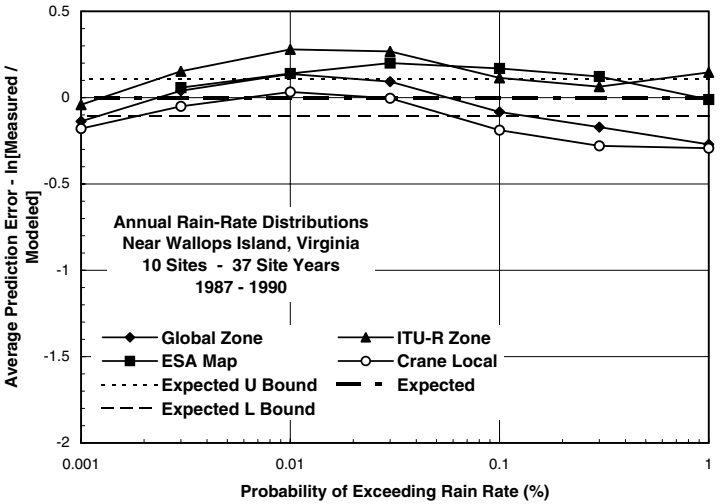

Figure 1.83 Average prediction error (bias) vs. exceedance probability for single-year rain-rate distributions near Wallops Island, VA, in the ITU-R rain-rate database.

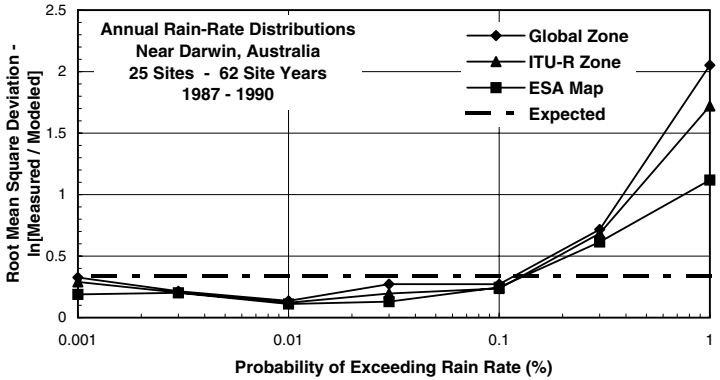

Figure 1.84 RMSD vs. exceedance probability for single-year rain-rate distributions near Darwin, Australia, in the ITU-R rain-rate database.

averages of the values shown in Figure 1.82 to Figure 1.85 because the number of EDFs that contribute at each probability level vary with the probability levels. For the Wallops Island region, the best match of model to observations was the Crane local model for the prediction of rain rate for a given probability level for the full range of probability levels. When the limited range of probability levels was used, the models were all equivalent statistically. For the prediction of probability for a given rain rate, all the models were equivalent statistically.

The summary figures for the region near Darwin show the ESA map model to be best. The performance of the other models improved for the

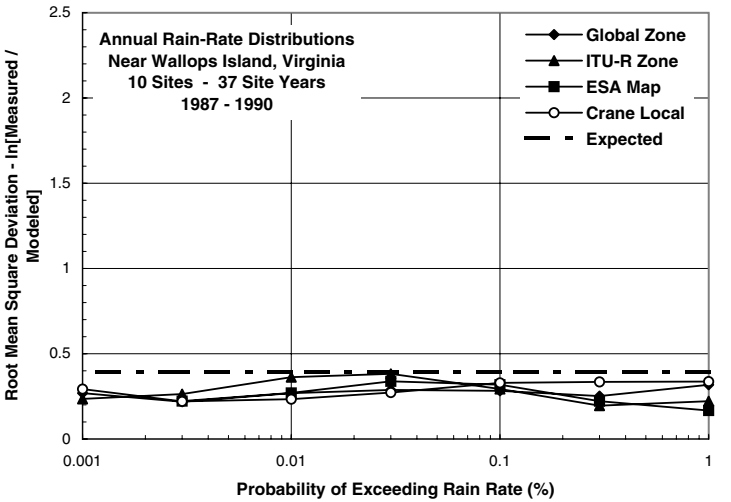

Figure 1.85 RMSD vs. exceedance probability for single-year rain-rate distributions near Wallops Island, VA, in the ITU-R rain-rate database.

Table 1.8 Bias and RMSD Values (nepers) for 37 Site Years of Observations near Wallops Island, VA, for Probabilities from 0.001% to 1.0% of a Year

Model	Bias for fixed probability	RMSD for fixed probability	N	Bias for fixed rain rate	RMSD for fixed rain rate	N
Global zone	–0.178	0.457	296	–0.072	0.470	278
ITU-R zone	0.163	0.311	296	0.282	0.528	278
ESA map	–0.007	0.387	259	0.187	0.460	278
Crane local	–0.098	0.301	296	–0.195	0.471	278

Table 1.9 Bias and RMSD Values (nepers) for 37 Site Years of Observations near Wallops Island, VA, for Probabilities from 0.001% to 0.1% of a Year

Model	Bias for fixed probability	RMSD for fixed probability	N	Bias for fixed rain rate	RMSD for fixed rain rate	N
Global zone	0.010	0.263	185	0.180	0.568	130
ITU-R zone	0.155	0.310	185	0.410	0.682	152
ESA map	0.142	0.288	148	0.279	0.574	152
Crane local	–0.078	0.270	185	–0.026	0.533	130

Table 1.10 Bias and RMSD Values (nepers) for 62 Site Years of Observations near Darwin, Australia, for Probabilities from 0.001% to 1.0% of a Year

Model	Bias for fixed probability	RMSD for fixed probability	N	Bias for fixed rain rate	RMSD for fixed rain rate	N
Global zone	–0.468	1.060	455	–0.670	1.128	496
ITU-R zone	–0.352	0.768	455	–0.428	0.724	496
ESA map	–0.248	0.518	454	–0.309	0.466	496

Table 1.11 Bias and RMSD Values (nepers) for 62 Site Years of Observations near Darwin, Australia, for Probabilities from 0.001% to 0.1% of a Year

Model	Bias for fixed probability	RMSD for fixed probability	N	Bias for fixed rain rate	RMSD for fixed rain rate	N
Global zone	–0.018	0.251	309	0.228	0.474	173
ITU-R zone	–0.009	0.215	309	0.092	0.408	173
ESA map	–0.068	0.181	309	–0.202	0.446	141

limited range of probabilities, but for application in the region near Darwin, the ESA map model is still clearly the best. To complete the validity test for a model, the model should be used to predict a quantity that can be checked by independent statistics. The measured and modeled rain-rate distributions can be integrated to estimate the total annual rain accumulation for a site. Rain accumulation statistics have been collected worldwide for many years and are generally available from national meteorological services. The measured distribution should also be checked to ensure that the observations are representative of the rain expected in a region. Figure 1.86 presents the comparisons between measured and modeled rain accumulation for each of the rain-rate models considered here.

The 37 annual accumulation values for the Wallops Island area are plotted at values below a modeled 1200 mm (to the left of the step in the climate curve). The climate values are the long-term average accumulation averages for Wallops Island and Darwin. The gauges near Wallops Island were all within a 35-km radius and the locations of the gauges in the database were all given the latitude and longitude of Wallops Island. The gauges near Darwin were entered in the database with the latitude and longitude of the gauge. The spread in ESA map model rain accumulations for the Darwin region was caused because a separate location was used for each gauge. The measured accumulation values for each region show a wide variation. For Wallops Island, the expected standard deviation is 34%. The expected range to enclose 90% of the measured annual accumulation values then is 580 to 1578 mm. All but two of the observed values fall within this range. The two zone models did not provide rain accumulation predictions that were central to the observations.

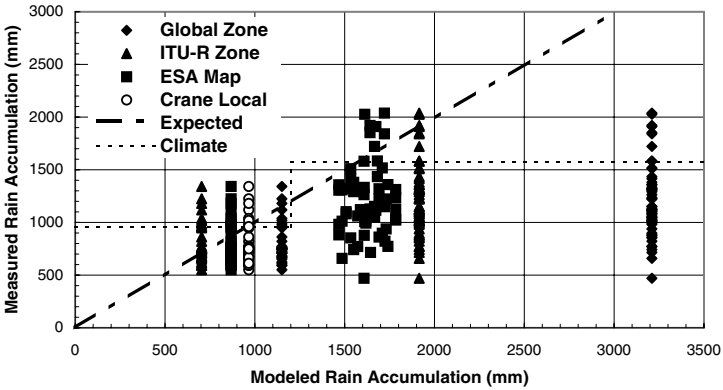

Figure 1.86 Comparison of measured to modeled annual rain accumulation for entries in the ITU-R rain-rate database.

The majority of the 67 annual accumulation values for the Darwin region were lower than the 121-year average for Darwin (Figure 1.86 and Figure 1.87) or the predictions of any of the models. The ESA map model was closest in predicting the average annual rain accumulation value. However, the spread in measured accumulation values was very large and the predicted accumulations for most of the gauge sites were much higher than the observed values. This lack of agreement suggests either a major overestimation of the rain-rate occurrences or a gauge problem at lower rain rates or higher probabilities as is indicated in Figure 1.82. The observations were made during a 4-year period, which is short compared to the time interval used to calculate the long-term average. The rain process in this area may undergo large changes over intervals of several years.

Figure 1.87 presents a time series of July through June rain accumulation values observed at the Darwin airport. Figure 1.88 presents the ordered distribution of these annual accumulation values together with lognormal distribution bounds based on maximum likelihood parameters calculated from the data. Rain in the region about Darwin is a northern winter phenomenon, with little rain falling from June to July (Figure 1.89). The annual July through June curve presents annual accumulations through the peak of each seasonal cycle. Large changes are evident with rapid fluctuations over annual intervals of 3 to 8 years. The El Nino– Southern Oscillation (ENSO) describes variations on this time scale.[20] The southern oscillation is an alternation in air pressure differences between Darwin in the western South Pacific and Tahiti in the eastern South Pacific. El Nino events occur when sea surface temperatures off the coast of Peru are significantly higher than normal for several months to more than a year. La Nina events occur when the sea surface temperature in the same location is lower than normal for periods of several months or more. Nine of the eleven El Nino events in the twentieth century with the highest sea surface temperature anomalies are indicated in the figure. The two other events occurred in the last decade of

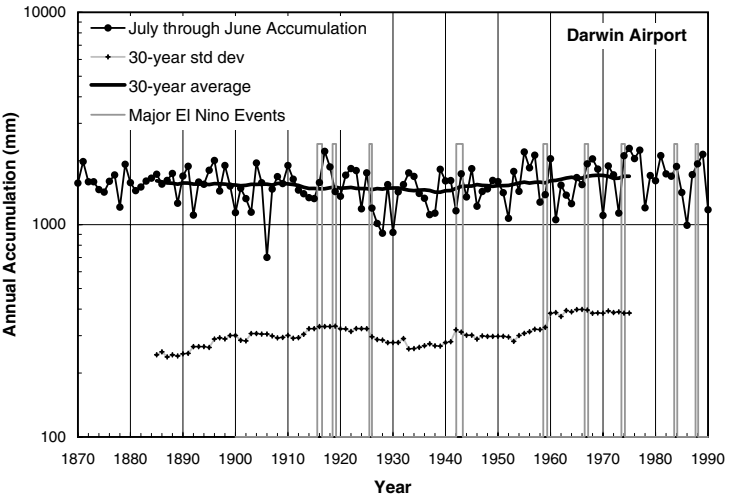

Figure 1.87 The 121-year July through June annual rain accumulation time series for Darwin, Australia.

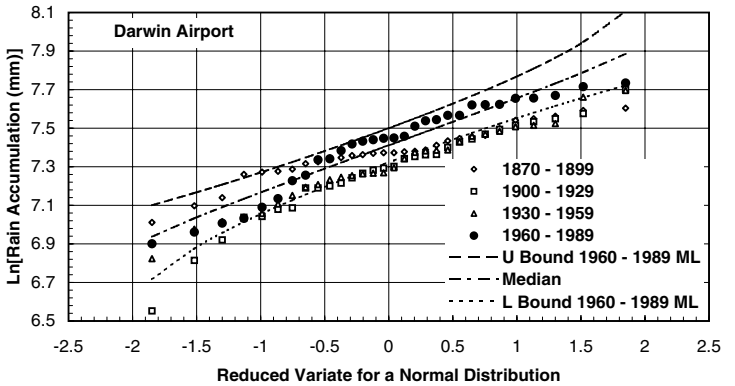

Figure 1.88 Ordered 30-year observation sets and lognormal model distribution for 1960–1989 data using ML parameters for Darwin, Australia.

the century. The vertical lines bound each extreme El Nino event. Other weaker El Nino events were also recorded during the 90-year period. Tropical and mid-latitude rainfall patterns change in response to the ENSO, producing multiyear changes in the amount and occurrence of precipitation.

The observations summarized in the ITU-R rain-rate database for the Darwin area are from 1987 to 1990. This period spans the last rain accumulation peak in the time series and one of the stronger El Nino events. The gauge response was an underestimate of the catch or rain collected in the gauge. The gauges used for the measurements in the data bank may have catch, timing, or calibration errors at low rates. A report on rain-rate

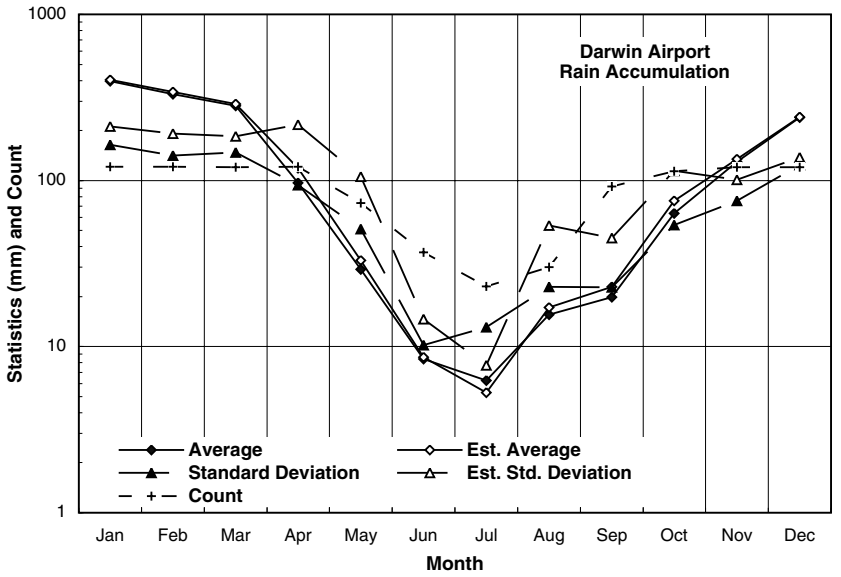

Figure 1.89 Monthly statistics for the 121-year observation set for Darwin, Australia.

measurements made in Darwin during another rain accumulation peak following an El Nino event from 1975 to 1978 showed significantly higher rain rates in the 0.1% to 1.0% probability range, but rain rates comparable to those for sites in the data bank at smaller percentages of a year.[45] In any case, the measurements and all the model predictions were not consistent for the area around Darwin.

1.7 Statistics and risk

An experimentally observed annual probability distribution for a meteorological or propagation variable is a random variable. Many independent samples from a stationary random process are required to provide an empirical distribution that provides a reasonable approximation to the parent distribution for the random process. Some phenomena occur only rarely, requiring many years of observation to construct a reasonable estimate of the parent distribution. For instance, elevated ducting may occur only several times per year in some locations, and, in many locations, rain intense enough to affect propagation paths occurs for less than 1% of a year. In parts of India at locations where the monsoon occurs some years but not others, several significant rain events may occur one year but not the next.

1.7.1 Stationarity

The time series in Figure 1.87 shows both the annual accumulation values and the 30-year running average and standard deviation values. From one

30-year period to the next, statistics are relatively stable, but a trend of increasing standard deviation values is evident between 1930 and 1990. The 16% increase in the 30-year running average is still low compared with the yearly variations and the corresponding 48% increase in the 30-year standard deviation. To first order, the rain accumulation process shown in this figure may be considered stationary in the mean but shows changes in the variance. Figure 1.88 presents the ordered distributions for the natural logarithms of the annual accumulation values in 30-year blocks together with the median and bounding distributions for a lognormal distribution based on ML parameters calculated from the most recent data block.[41] The lognormal distribution provides a good estimator of the underlying parent distribution for the 1960 to 1989 year block. The ordered distributions for the earlier data blocks lie in part outside the model distribution bounds. The lack of stationarity for the process restricts the interval of years that correspond to the modeled distribution.

The median and bounding distributions in Figure 1.88 were calculated using the exact distributions of order statistics and the assumed lognormal distribution for the underlying probability distribution. If, for a set of N independent samples drawn from the parent distribution with values ordered from the lowest, $n = 1$ to the highest, $n = N$, the exact probability density function for the nth largest value, $\phi_n(x,N)$, is given by:

$$\phi_n(x,N) = \frac{N!}{(n-1)!(N-n)!}\left(F(x)\right)^{n-1}\left(1-F(x)\right)^{N-n} f(x) \tag{1.52}$$

where $F(x)$ is the parent probability distribution function and $f(x)$ the parent probability density function.[41,42] The median and bounding probability distribution functions were obtained from Equation 1.52 as a function of x and n for the total number of samples, N, in the ordered distribution.

Other geophysical processes show similar variations over long periods of time. Some ionospheric processes depend on the magnitude of the sunspot number. The sunspot number changes in a nearly cyclical manner, with approximately an 11-year period. Statistics such as the scintillation index for transionospheric propagation should be conditioned on the level of sunspot activity. In Figure 1.29 to Figure 1.40, model calculations were presented for typical sunspot minima and sunspot maxima to bound the range of values to be expected over a sunspot cycle.

Rain accumulation statistics for Darwin have large seasonal variations. Figure 1.89 presents the averages and standard deviations of the monthly accumulations for the entire 121-year observation period. The count presents the number of months with recorded rainfall. The statistics for a month are conditioned on the occurrence of rain in that month. For example, for July, recorded rainfall occurred during only 23 of the 121 years of record, and the average monthly rain accumulation for those 23 years with data was only 6.3 mm. If measurements were only made during the months of June, July,

and August, Darwin would be considered a very dry location; conversely, if measurements were only made in December, January, and February, Darwin would be considered a very rainy location. Because of the seasonal nature of rain at this location, statistics should only be computed for single months or for complete 12-month years.

Two sets of average and standard deviation values are presented in the figure, the first calculated from the accumulation value obtained each month conditioned on the occurrence of rain and the second (labeled "Est.") from the natural logarithm of the accumulation and the assumption of a lognormal distribution. The two estimates should be the same if the underlying statistical process was lognormal and stationary. The estimated average values were close, but the standard deviation values showed differences.

1.7.2 Variability model distribution

The model distribution employed to characterize the yearly variation of annual or monthly statistics must represent the underlying parent distribution for that process. This distribution must be selected based on the available empirical evidence; there are no theoretical predictions of the distribution for many of the parameters of interest. The lognormal model was selected to represent the annual rain accumulation observations for Darwin on the basis of the observation that the distribution bounds enclosed all of the 30 annual observations in the most recent 30-year data block (see Figure 1.88). This distribution did not fit the other 30-year blocks. Different lognormal distributions could have been generated for the other data blocks. Each in turn would have enclosed the observations for that data block as illustrated in Figure 1.90 for the 1930 to 1959 data block. Using the ML parameters for the entire 121-year data set, the model distribution for the entire data set is also consistent with the lognormal model, as displayed in Figure 1.91.

1.7.2.1 Lognormal model

The lognormal model is but one of many distribution models that could represent the observations. Rain accumulation, rain rate, or ratios of rain-rate values conditioned on the requirement that rain occurred are always greater than zero. The lognormal distribution applies to positive variates only. The normal distribution applies to both positive and negative values and is therefore not strictly applicable, but often used if the average value is much larger than the standard deviation. The gamma and Weibull distributions can also be used for positive variates as can a number of distributions that are special cases of the gamma or Weibull distributions.[41] For each of these distributions, ML parameter estimates can be calculated to fit the distribution to the observations.

A lognormal distribution fit to the ordered distribution of rain-rate values exceeded 0.01% of a year from the EDFs in the University of Oklahoma (OU) rain-rate database are displayed in Figure 1.92. The data presented in this figure are from all the EDFs collected from the global rain zone D2. This

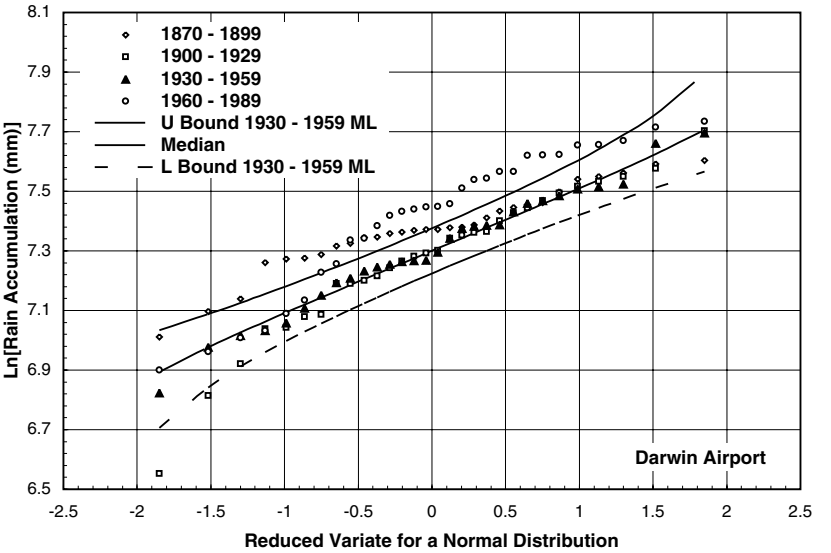

Figure 1.90 Ordered 30-year observation sets and lognormal model distribution for 1930–1959 data using ML parameters for Darwin, Australia.

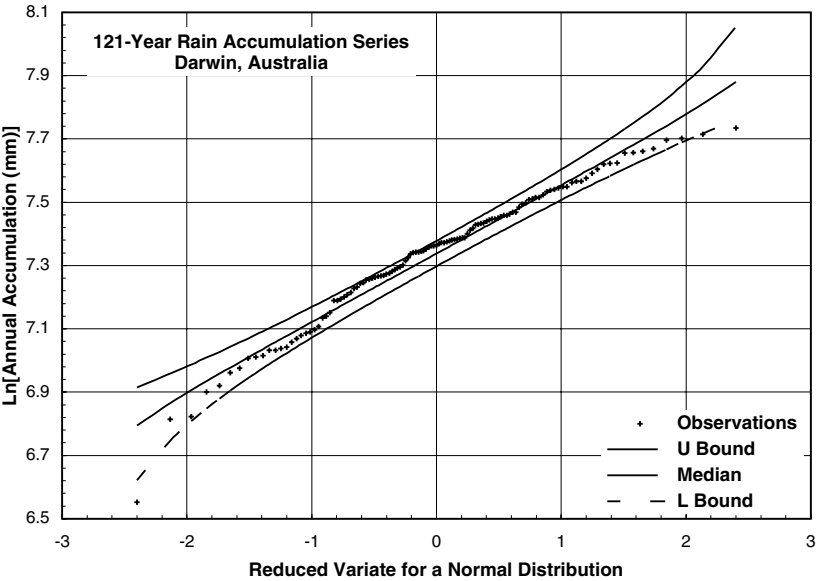

Figure 1.91 Ordered 121-year observations and lognormal model distribution using ML parameters for the entire data set for Darwin, Australia.

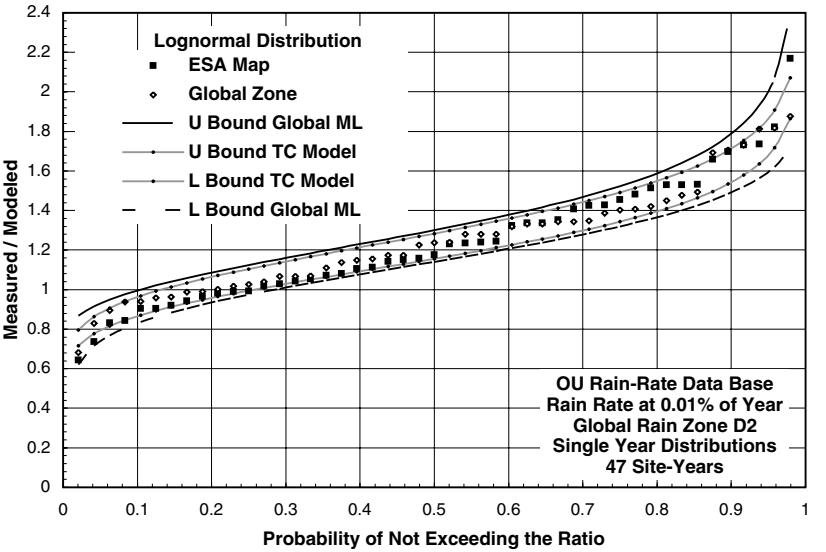

Figure 1.92 Ordered 47-year observations and lognormal distribution estimates for 0.01% of a year measured to modeled ratio for global D2 rain zone data in the OU data bank.

distribution was displayed in Figure 1.79 but with plotting scales that would make the best-fit distribution a straight line. The abscissa in Figure 1.92 is the cumulative probability of not exceeding the ratio of measured to modeled rain rate (on a linear scale). Note again that for the ML parameters calculated using data from this global zone, all the ratio values are within the expected bounds. In this case, the global zone model produced a constant value; therefore the ML parameters represent the variability of the measurements. The ESA map model includes an additional variability produced by the application of the model. The TC model bounds were calculated by using the global version of the Crane two-component model. Ninety percent of the observations fell within the TC model bounds.

The probability density, f_{LN}, and distribution, F_{LN}, functions for the lognormal model are given by:[41]

$$f_{LN}(x:m,s) = \frac{1}{xs\sqrt{2\pi}} e^{-\frac{1}{2}\left(\frac{\ln(x)-m}{s}\right)^2}$$

$$F_{LN}(x:m,s) = \frac{1}{s\sqrt{2\pi}} \int_0^x e^{-\frac{1}{2}\left(\frac{\ln(y)-m}{s}\right)^2} \frac{dy}{y} \tag{1.53}$$

$$F_{LN}(x:m,s) = \frac{1}{s\sqrt{2\pi}} \int_{-\infty}^x e^{-\frac{1}{2}\left(\frac{\ln(y)-m}{s}\right)^2} d\ln(y) = F_N(\ln(x):m,s)$$

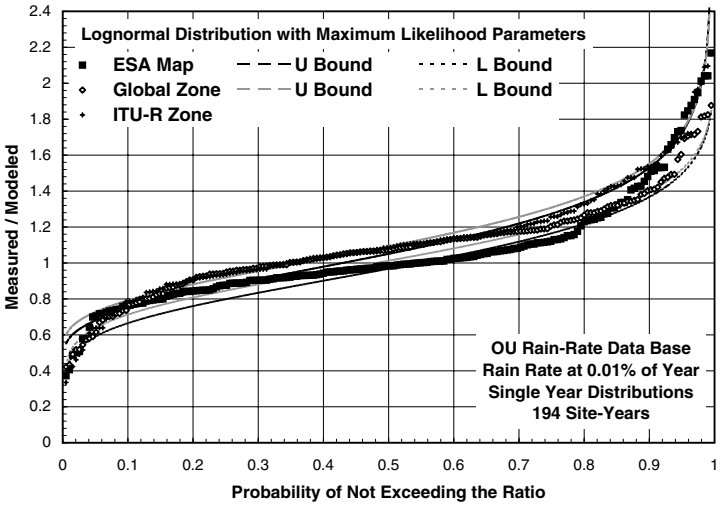

Figure 1.93 Ordered 194-year observations and lognormal distribution estimates for 0.01% of a year measured to modeled ratio for all the data in the OU data bank.

where m is the location parameter, s the scale parameter for the model, and F_N the normal probability distribution. The lognormal distribution values are readily obtained from normal probability tables or normal distribution functions in spreadsheets. The ML estimates for m and s are given by: [41]

$$\hat{m} = \frac{1}{N}\sum_{i=1}^{N} \ln(x_i)$$
$$\hat{s} = \sqrt{\frac{1}{N}\sum_{i=1}^{N} \left(\ln(x_i) - m\right)^2} \tag{1.54}$$

where ˆ specifies an estimated value.

Results of using the lognormal model, when applied to the entire set of 194 annual distributions recorded in the OU database, are shown in Figure 1.93. The empirical distributions shown in this figure are the same as those in Figure 1.80 but plotted on different scales. The distribution obtained by using the ITU-R climate zone model is also shown. Two sets of lognormal model distribution bounds are displayed in this figure, one for ML parameters calculated for the ESA map model and the other for ML parameters for the global zone model. A relatively large fraction of the empirical ordered distribution lies outside the expected bounds. A summary of the fraction of empirical distribution values that are outside the bounds is presented in Table 1.12.

The use of the lognormal model to represent the deviations of the observed rain rates from the predicted values is not justified in this case. If

Table 1.12 Fraction of Ordered Distribution Values Outside the Expected Bounds for a Lognormal Model for all 194 Distributions in the OU Data Bank

Parameters	Percentage outside		
Maximum likelihood	Global zone	ITU-R zone	ESA map
Global zone	39	40	55
ESA map	53	70	55

the model were consistent with the observations, less than 10% of the ordered distribution values would lie outside the bounds. Because of the possible correlation between adjacent values in the ordered distributions, a hypothesis test based on a strict 10% threshold may be too restrictive. A relative comparison between the models is useful in selecting the model that best matches the observations. As discussed previously, the problem for the climate zone models is the lack of representative rain-rate distributions for use in constructing a climate zone model distribution for all the climate zones. A second problem is possible measurement error.

1.7.2.2 Normal distribution model

The probability density, f_N, and distribution, F_N, functions for the normal model are given by:[41]

$$f_N(x{:}\mu,\sigma) = \frac{1}{\sigma\sqrt{2\pi}} e^{-\frac{1}{2}\left(\frac{x-\mu}{\sigma}\right)^2}$$
$$F_N(x{:}\mu,\sigma) = \frac{1}{\sigma\sqrt{2\pi}} \int_{-\infty}^{x} e^{-\frac{1}{2}\left(\frac{y-\mu}{\sigma}\right)^2} dy \tag{1.55}$$

where μ is the location parameter and σ the scale parameter for the model. The normal distribution values are readily obtained from normal probability tables or normal distribution functions in spreadsheets. The ML estimates for μ and σ are given by: [41]

$$\hat{\mu} = \frac{1}{N}\sum_{i=1}^{N} x_i$$
$$\hat{\sigma} = \sqrt{\frac{1}{N}\sum_{i=1}^{N}\left(x_i - m\right)^2} \tag{1.56}$$

where ˆ specifies an estimated value. Note that the ML estimate for the standard deviation is a minimum variance bound estimate and is biased when the number of samples is limited.

If the underlying variability model is lognormal, the parameters m and s for the lognormal model are related to the parameters μ and σ calculated using Equation 1.56. The relationships are given by:

$$\begin{aligned} \mu &= e^{m+\frac{1}{2}s^2} \\ \sigma &= \mu\sqrt{\left(e^{s^2}-1\right)} \\ m &= \ln(\mu)-\frac{1}{2}\sigma^2 \\ s &= \sqrt{\ln\left(\frac{\sigma^2}{\mu^2}+1\right)} \end{aligned} \tag{1.57}$$

Normal distributions fit to the ordered distributions of rain-rate values that exceeded 0.01% of a year from the EDFs in the OU rain-rate database are displayed in Figure 1.94. The data presented are from all the EDFs collected from global rain zone D2. Two sets of normal distribution bounds are presented, one calculated using the global zone model to set the ML parameters and the other with parameters set using the ESA map model. In contrast to the results obtained using the lognormal model, the ordered distribution spanned more of the region between the bounding curves. Several of the global zone distribution values were outside the global zone set of bounds; only one of the ESA map distribution values was outside the bounds constructed using the global zone model parameters. In either case, less than 10% of the distribution values were outside either set of bounds.

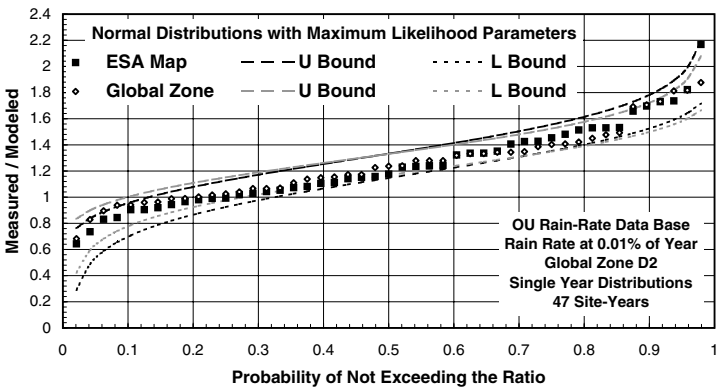

Figure 1.94 Ordered 47-year observations and normal distribution estimates for 0.01% of a year measured to modeled ratio for global D2 rain zone data in the OU data bank.

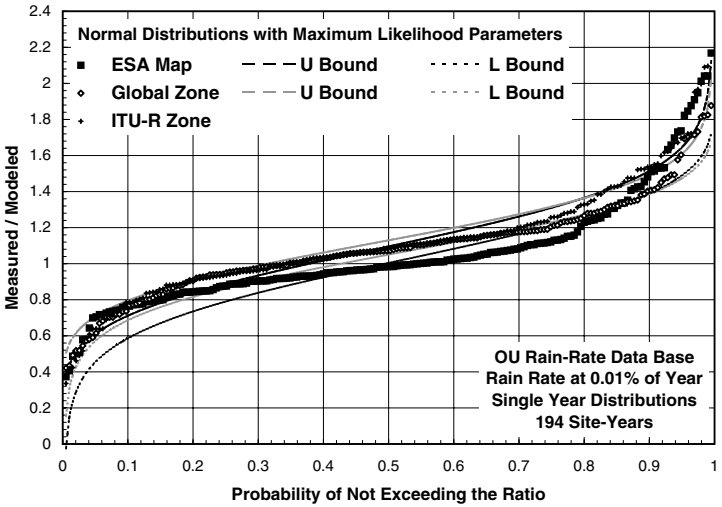

Figure 1.95 Ordered 194-year observations and normal distribution estimates for 0.01% of a year measured to modeled ratio for all the data in the OU data bank.

Table 1.13 Fraction of Ordered Distribution Values Outside the Expected Bounds for a Normal Model for all 194 Distributions in the OU Data Bank

Parameters	Percentage outside		
Maximum likelihood	Global zone	ITU-R zone	ESA map
Global zone	28	26	66
ESA map	54	57	65

The results of using the normal model, when applied to the entire set of 194 annual distributions recorded in the OU database, are shown in Figure 1.95. The distribution obtained by using the ITU-R climate zone model is also shown. Two sets of lognormal model distribution bounds are displayed in this figure, one for ML parameters calculated for the ESA map model and the other for ML parameters for the global zone model. A relatively large fraction of the empirical ordered distribution lies outside the expected bounds, a summary of which is presented in Table 1.13. Note that the normal model produced a smaller fraction of outliers than the lognormal model when the global zone model or ITU-R zone rain-rate distribution model was used.

1.7.2.3 Gamma distribution model

The probability density, f_G, and distribution, F_G, functions for the gamma model are given by:[41]

$$f_G(x{:}\sigma,\lambda) = \frac{1}{\sigma\Gamma(\lambda)}\left(\frac{x}{\sigma}\right)^{\lambda-1} e^{-\left(\frac{x}{\sigma}\right)}$$
$$F_G(x{:}\sigma,\lambda) = \frac{1}{\Gamma(\lambda)}\int_{-\infty}^{x}\left(\frac{x}{\sigma}\right)^{\lambda-1} e^{-\left(\frac{y}{\sigma}\right)}\frac{dy}{\sigma} \tag{1.58}$$

where σ is the scale parameter and λ is the shape parameter for the model and Γ(λ) is the gamma function and $F_G(x{:}\sigma,\lambda)$ is the incomplete gamma function.[46] The gamma distribution values can be obtained from chi square distribution probability tables or gamma distribution functions in spreadsheets. The ML estimates for σ and λ are given by: [41]

$$\hat{\sigma}\hat{\lambda} = \frac{1}{N}\sum_{i=1}^{N} x_i$$
$$\ln(\hat{\sigma}) + \psi(\hat{\lambda}) = \ln\left(\frac{\sum_{i=1}^{N} x_i}{\prod_{i=1}^{N} x_i^{1/N}}\right) \tag{1.59}$$

where ˆ specifies an estimated value and ψ(λ) is the digamma function. These equations may be solved iteratively.

Gamma distributions fit to the ordered distributions of rain-rate values exceeded 0.01% of a year from the EDFs in the OU rain-rate database are displayed in Figure 1.96. The data presented are from all the EDFs collected from global rain zone D2. Two sets of gamma distribution bounds are presented, one calculated using the global zone model to set the ML parameters and the other with parameters set using the ESA map model. For these models, all of the distribution values were inside either set of bounds.

The results of using the gamma model, when applied to the entire set of 194 annual distributions recorded in the OU database, are shown in Figure 1.97. The distribution obtained by using the ITU-R climate zone model is also shown. Two sets of lognormal model distribution bounds are displayed in this figure, one for ML parameters calculated for the ESA map model and the other for ML parameters for the global zone model. Again, a relatively large fraction of the empirical ordered distribution lies outside the expected bounds. A summary of the fraction of empirical distribution values that are outside the bounds is presented in Table 1.14.

1.7.2.4 Weibull distribution model

The probability density, f_W, and distribution, F_W, functions for the Weibull model are given by:[41]

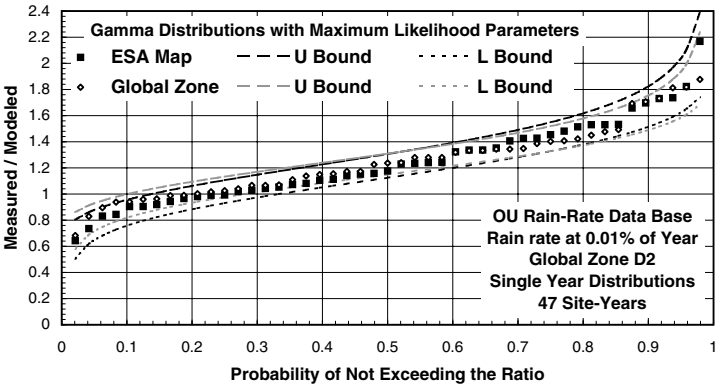

Figure 1.96 Ordered 47-year observations and gamma distribution estimates for 0.01% of a year measured to modeled ratio for global D2 rain zone data in the OU data bank.

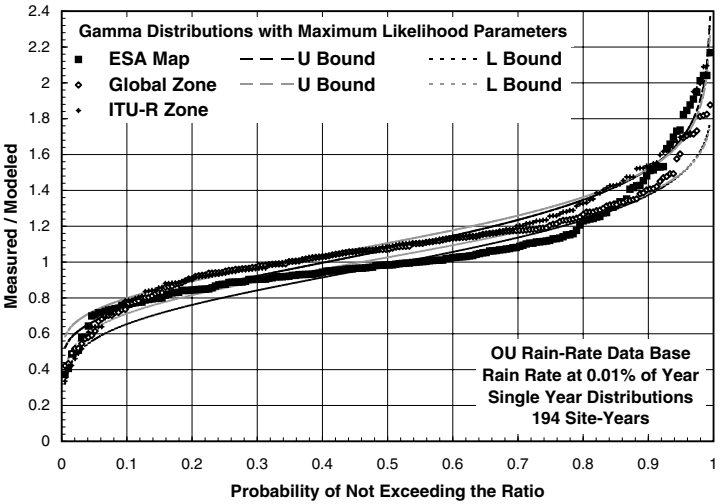

Figure 1.97 Ordered 194-year observations and gamma distribution estimates for 0.01% of a year measured to modeled ratio for all the data in the OU data bank.

Table 1.14 Fraction of Ordered Distribution Values Outside the Expected Bounds for a Gamma Model for all 194 Distributions in the OU Data Bank

Parameters	Percentage outside		
Maximum likelihood	Global zone	ITU-R zone	ESA map
Global zone	30	40	60
ESA map	45	66	55

$$f_W(x:\sigma,\lambda) = \frac{\lambda}{\sigma}\left(\frac{x}{\sigma}\right)^{\lambda-1} e^{-\left(\frac{x}{\sigma}\right)^{\lambda}}$$
$$F_W(x:\sigma,\lambda) = 1 - e^{-\left(\frac{x}{\sigma}\right)^{\lambda}} \tag{1.60}$$

where σ is the scale parameter and λ is the shape parameter for the model. The Weibull distribution values are readily obtained from equation 1.60. The ML estimates for σ and λ are given by: [41]

$$\hat{\sigma} = \left(\frac{1}{N}\sum_{i=1}^{N} x_i^{\hat{\lambda}}\right)^{1/\hat{\lambda}}$$
$$\frac{\sum_{i=1}^{N} x_i^{\hat{\lambda}} \ln(x_i)}{\sum_{i=1}^{N} x_i^{\hat{\lambda}}} - \frac{1}{\hat{\lambda}} = \ln\left(\frac{1}{N}\sum_{i=1}^{N}\ln(x_i)\right) \tag{1.61}$$

Weibull distributions fit to the ordered distributions of rain-rate values that exceeded 0.01% of a year from the EDFs in the OU rain-rate database are displayed in Figure 1.98. The data presented are from all the EDFs collected from global rain zone D2. Two sets of normal distribution bounds are presented, one calculated using the global zone model to set the ML parameters and the other with parameters set using the ESA map model. The ordered distributions each lie within the ML bounds set using data for that distribution. In either case, less than 10% of the distribution values were outside either set of bounds.

The results of using the Weibull model, when applied to the entire set of 194 annual distributions recorded in the OU database, are shown in Figure 1.99. The distribution obtained by using the ITU-R climate zone model is also shown. Two sets of lognormal model distribution bounds are displayed in this figure, one for ML parameters calculated for the ESA map model and the other for ML parameters for the global zone model. A relatively large fraction of the empirical ordered distribution lies outside the expected bounds. A summary of the fraction of empirical distribution values that are outside the bounds is presented in Table 1.15.

1.7.2.5 Model selection

Each of the variability models produced bounds that contained more than 90% of the ordered distribution values when rain-rate distributions from global rain zone D2 were tested. Based on the simple graphical hypothesis test, all these models were consistent with the observations. The selection of

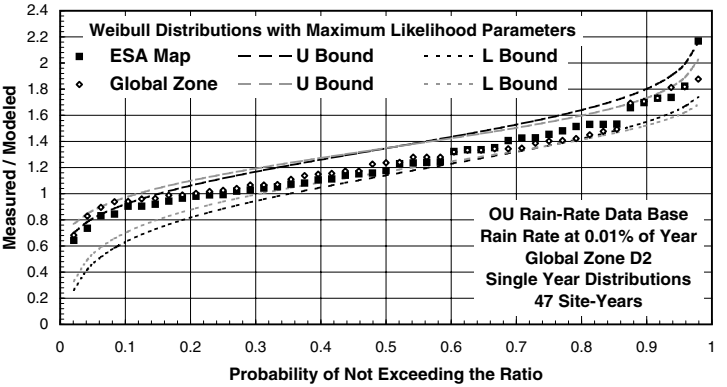

Figure 1.98 Ordered 47-year observations and Weibull distribution estimates for 0.01% of a year measured to modeled ratio for global D2 rain zone data in the OU data bank.

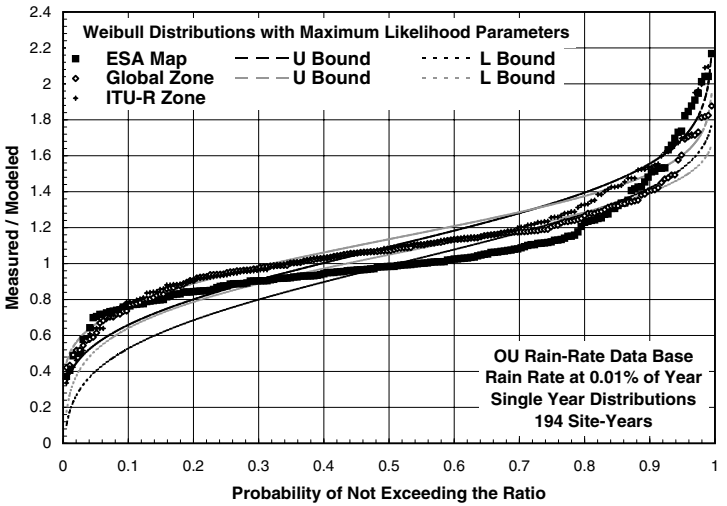

Figure 1.99 Ordered 194-year observations and Weibull distribution estimates for 0.01% of a year measured to modeled ratio for all the data in the OU data bank.

Table 1.15 Fraction of Ordered Distribution Values Outside the Expected Bounds for a Weibull Distribution Model for all 194 Distributions in the OU Data Bank

Parameters	Percentage Outside		
Maximum likelihood	Global zone	ITU-R zone	ESA map
Global zone	44	39	69
ESA map	69	52	74

a model for variability must then be based on convenience. The computations of the ML parameters for the gamma and Weibull distributions are more complex, and therefore, for ease of application, they can be eliminated. The lognormal model produced a slightly narrower spread between the bounds in the central region of the ordered distribution and a more consistent fit in the ordered distribution tails. It also was symmetric in the use of either the modeled or measured values as reference (denominator) for calculating the ratios. Selection on the basis of model performance for the entire 194 rain-rate distribution database was not possible because the rain zone models were known to have modeling errors when applied to tropical regions.[43]

1.7.3 Risk

The annual EDFs obtained for point rain-rate or path attenuation measurements show a yearly variation. Figure 1.4 presents annual total path attenuation distributions for 5 years of observation for Norman, OK. Figure 1.100 shows the annual rain-rate distributions for the same 5 years of observations in Norman, OK. Figure 1.101 presents the same data as in Figure 1.100 ("On Roof" distributions), but with values logarithmically interpolated to the probability levels used in the ITU-R and other data banks. For Norman, OK, the expected yearly variation in rain rate as given by the Crane local model is 0.22 nepers (25%) and the expected variation in occurrence probability is 0.18 nepers (20%).[44] The upper and lower bounds expected to contain 90% of the observed annual EDFs are displayed in the figure. These bounds were constructed from the rain-rate and occurrence variabilities. The "On Roof" EDFs in Figure 1.101 lie within the expected bounds for observed rain rates greater than 10 mm/h. At lower rates, the air flow across the top of the 15-story building limited the amount of rain captured in the rain gauge. The "On Airport" EDFs are for correctly sited rain gauges at a rain gauge evaluation facility operated by the university on the Norman airport grounds 7 km from the roof top site. For a year of observations, the "On Airport" and "On Roof" distributions should be identical except for catch errors. All the "On Airport" EDFs were within the expected bounds predicted by the local model. The local model parameters for Norman were obtained from more than 30 years of rain observations in Oklahoma City at a site 25 km from the roof top gauge site.

The upper bound is the distribution expected to be exceeded once in 20 years. It has a return period of 20 years.[41,45] System design should consider the risk involved in making a prediction about propagation effects. The expected distribution value at a given probability level (the curve labeled "Local Model" in Figure 1.101) is centered in the range of possible distributions that could occur as the weather conditions change from one year to the next. The upper bound curve at each probability level is expected to be exceeded by 5% of the annual EDFs for the site. The lower bound should be exceeded by 95% of the EDFs.

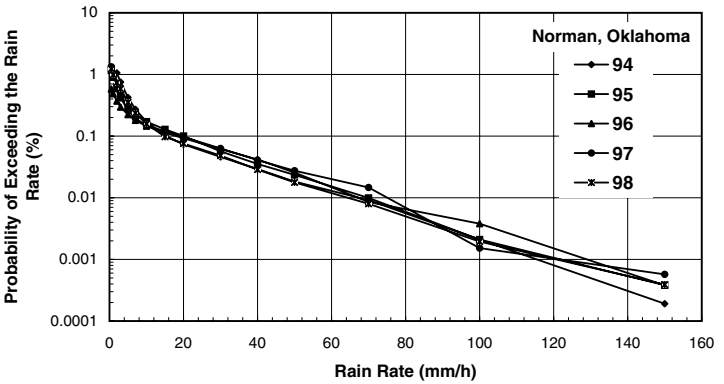

Figure 1.100 Annual rain-rate empirical distribution functions for Norman, OK.

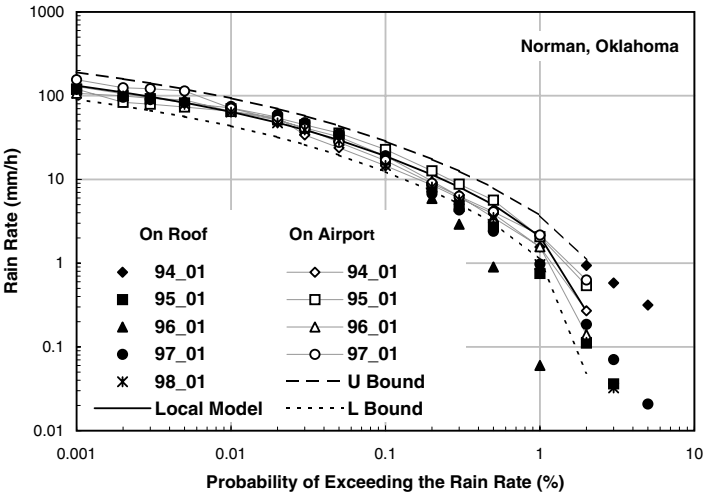

Figure 1.101 Annual rain-rate empirical distribution functions and Crane local model predictions for Norman, OK.

Figure 1.102 presents the upper bound curves for several different return periods. The median distribution has a 2-year return period. It closely approximates the expected distribution. In design, the expected propagation distribution may not be the distribution needed to specify the system. In some applications, it may be the distribution that is exceeded on average only once in a given number of years (the return period).

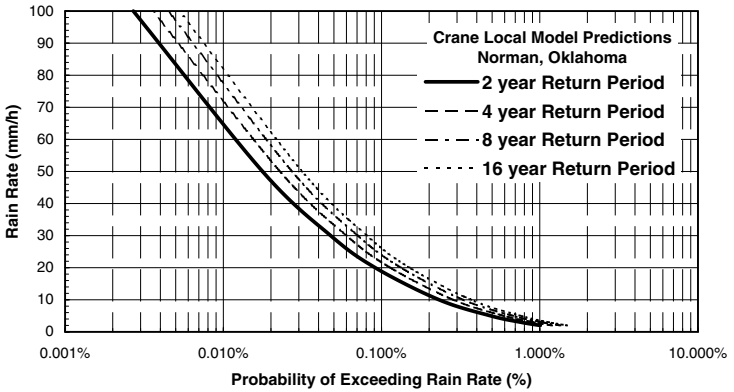

Figure 1.102 Upper bound distributions for different return periods for rain-rate distributions for Norman, OK.

1.8 List of symbols

Symbol	Quantity	Units	Equation
ε'	Dielectric constant		1.14
$\overline{\xi}$	Average value of ξ	nepers	1.50
σ_ξ	Standard deviation of ξ	nepers	1.50
Ξ	Percent deviation		1.51
A	Earth's radius = 6378.4 km	m	1.20
A	Attenuation	dB	1.49
A	Apperture	m^2	1.13
A_e	Effective area of the receiving antenna	m^2	1.6
A_E	Effective Earth's radius	m	1.38
$\mathbf{A_R}$	Receiving antenna losses	dB	1.5
$\mathbf{A_T}$	Transmitting antenna losses	dB	1.5
B	Receiver detection bandwidth	Hz	1.41
B_f	Planck's function	$W/m^2/sr/Hz$	1.43
c	Speed of light in free space; $c \approx 3 \cdot 10^8$	m/s	1.6
C	Proportionality constant		1.12
D	Directive gain		1.4
d	Distance	m	1.15
e	Antenna efficiency		1.4
E	Magnitude of electric field strength	Volts/m	1.6
f	Frequency	Hertz (Hz)	1.6
$f(x)$	Probability density function		1.52
$F(x)$	Probability distribution function		1.52
f_G	Gamma probability density		1.58
F_G	Gamma probability distribution		1.58
f_{LN}	Lognormal probability density		1.53

(continued)

1.8 List of symbols (continued)

Symbol	Quantity	Units	Equation
F_{LN}	Lognormal probability distribution		1.53
f_N	Normal probability density		1.55
F_N	Normal probability distribution		1.55
f_W	Weibull probability density		1.60
F_W	Weibull probability distribution		1.60
g	Acceleration due to gravity = 9.8 m/s^2	m/s^2	1.24
g	Relative directivity		1.4
G	Antenna gain		1.4
G_R	Receiving antenna gain		1.1
g_R	Relative directivity for receiving antenna		1.1
$\mathbf{G_R}$	Receiving antenna gain	dBi	1.2
$\mathbf{g_r}$	Relative directivity for receiving antenna	dB	1.2
G_T	Transmitting antenna gain		1.1
g_T	Relative directivity for transmitting antenna		1.1
$\mathbf{G_T}$	Transmitting antenna gain	dBi	1.2
$\mathbf{g_t}$	Relative directivity for transmitting antenna	dB	1.2
h	Fresnel zone radius	m	1.15
h	Planck's constant = 6.63 10^{-34}	Js	1.43
$j = \sqrt{-1}$			1.6
I_f	Radiance	W/m^2/sr/Hz	1.42
k	Wavenumber	m^{-1}	1.6
K	Boltzmann's constant = = 1.38 · 10^{23}	J/K	1.41
k_E	k_E factor		1.39
k_e	Mass extinction coefficient	m^2/kG	1.42
L	Transmission loss	dB	1.2
L_B	Basic transmission loss	dB	1.2
m	Polarization mismatch		1.5
m	Modified index of refraction		1.20
M	Modified radio refractivity		1.20
m	m partameter for a Nakagami-m distribution		1.40
m	Lognormal distribution location parameter		1.53
m_d	Mean molecular weight of dry air = 28.89	amu	1.24
m_D	Mean molecular weight of water = 18.02	amu	1.25
n	Index of refraction		1.14
N	Radio refractivity	N units	1.19
n	nth largest value		1.52
N	Number of samples in the ordered distribution		1.52
N_e	Electron density	electrons/m^3	1.21
N_G	Effective refractivity for group delay		1.21
P	Pressure	hPascal (hPa)	1.19
$\mathbf{P_R}$	Received power	Watts (W)	1.1
P_R	Received power	dBW	1.2
P_S	Saturation water vapor pressure	hPa	1.27

(continued)

1.8 List of symbols (continued)

Symbol	Quantity	Units	Equation
P_T	Transmited power	W	1.1
$\mathbf{P_T}$	Transmitted power	dBW	1.2
P_V	Water vapor pressure	hPa	1.19
q	Specific humidity	g/kg	1.28
R	Path lentfh or distance	m	1.1
r	Distance	m	1.5
R	Universal gas constant = 83.14 ≡ 8.314 J/mole/K	$\frac{\text{amu}\cdot\text{hPa}\cdot\text{m}^3}{\text{kg}\cdot\text{K}}$	1.24
r	radius of curvature	m	1.37
RH	Relative humidity		1.27
$RMSD$	Roof mean square deviation		1.50
S	Magnitude of the real part of the Poynting vector	$W/m^2/sr$	1.6
s	Distance	m	1.42
s	Lognormal distribution scale parameter		1.53
S_4	Scintillation intensity (linear)		1.40
t	Time	second (s)	1.6
T	Absolute temperature	Kelvin (K)	1.19
tan(δ)	Loss tangent		1.14
T_B	Brightness temperature	K	1.41
T_M	Effective medium temperature	K	1.47
T_v	Virtual temperature	K	1.24
x	Water vapor mixing ratio	g/kg	1.27
x	Sample value		1.53
x_S	Saturation water vapor mixing ratio	g/kg	1.27
z	Height coordinate	m	1.23
Θ_H	Half power beamwidth	r	1.11
Ω	Solid angle	steradian (sr)	1.6
α	Specific attenuation	dB/km	1.5
α	Elevation angle	r	1.20
β_a	Absorption cross section per unit volume	m^{-1}	1.43
β_e	Extinction cross section per unit volume	m^{-1}	1.42
δ	Directivity factor		1.13
ε	Complex relative permittivity = $\varepsilon' - j\varepsilon''$		1.14
ϕ	Azimuthal angle	r	1.1
$\phi_n(x,N)$	nth order statistic probability density		1.52
η_0	Impedence of free space = 377 ohms	ohms (Ω)	1.6
λ	Wavelength	meter (m)	1.1
λ	Gamma distribution shape parameter		1.58
λ	Weibull distribution shape parameter		1.60
μ	Normal distribution location parameter		1.55
ν	Fresnel diffraction parameter		1.18
θ	Polar angle	radian (r)	1.1
θ	Potential temperature	K	1.33
ρ	Density of air	kg/m^3	1.24

(continued)

1.8 List of symbols (continued)

Symbol	Quantity	Units	Equation
ρ_V	Water vapor density	g/m^3	1.28
σ	Normal distribution scale parameter		1.55
σ	Gamma distribution scale parameter		1.58
σ	Weibull distribution scale parameter		1.60
σ_χ	Scintillation intensity (logarithmic)	dB	1.40
τ	Optical depth	nepers	1.47
ω	Radian frequency, $\omega = 2\pi f$	r/s	1.6
ξ	Natural logarithm of measured to modeled distribution values at a fixed exceedance probability	nepers	1.50

References

1. ITU-R, Recommendation ITU-R P.311–7, Acquisition, Presentation and Analysis of Data in Studies of Tropospheric Propagation, International Telecommunications Union, Geneva, 1995.
2. Crane, R.K., Wang, X., Westenhaver, D.B., and Vogel, W.J., ACTS propagation experiment: Design, calibration, and data preparation and archival, *Proc. IEEE*, 85(7), 863, 1997.
3. Rogers, D.V. and Crane, R.K., Review of propagation results from the advanced communications technology satellite (ACTS) and related studies, *IE-ICE Trans. Commun.*, E88-B(9), 2357, 2001.
4. Crane, R.K. and Dissanayake, A.W., ACTS propagation experiment: Attenuation distribution observations and model predictions, *Proc. IEEE*, 85(7), 879, 1997.
5. Crane, R.K., Analysis of the effects of water on the ACTS propagation terminal antenna, *IEEE Trans. Ant. Propag.*, 50(7), 954, 2002.
6. Kerr, D.E., Ed., *Propagation of Short Radio Waves*, McGraw-Hill, New York, 1951.
7. Balanis, C.A., *Antenna Theory Analysis and Design*, Harper & Row, New York, 1982.
8. Silver, S., Ed., *Microwave Antenna Theory and Design*, Dover Publishing, New York, 1965.
9. ITU-R, Recommendation ITU-R P.530–9, Propagation Data Required for the Design of Terrestrial Line-of-Sight Systems, International Telecommunications Union, Geneva, 1999.
10. ITU-R, Recommendation ITU-R P.679–2, Propagation Data Required for the Design of Broadcasting-Satellite Systems, International Telecommunications Union, Geneva, 1999.
11. Goldhirsh, J. and Vogel, W.J., Handbook of Propagation Effects for Vehicular and Personal Mobile Satellite Systems, Report A2A-98-U-0–021, Applied Physics Laboratory, Johns Hopkins University, Laurel, MD, 1998.

12. ITU-R, Recommendation ITU-R P.526–4, Propagation by Diffraction, International Telecommunications Union, Geneva, 1995.
13. Smith, E.K. and Weintraub, S., The constants in the equation for atmospheric refractive index at radio frequencies, *Proc. IRE*, 41(8), 1035, 1953.
14. Bean, B.R. and Dutton, E.J., Radio Meteorology, Monograph No. 92, National Bureau of Standards, Washington, D.C., 1966.
15. ITU-R, Recommendation ITU-R P.835–2, Reference Standard Atmosphere, International Telecommunications Union, Geneva, 1999.
16. Davies, K., *Ionospheric Radio Waves*, Blaisdell Publishing, Waltham, MA, 1969.
17. Flock, W.L., Propagation Effects on Satellite Systems at Frequencies Below 10 GHz, NASA Reference Publication 1108(02), 1987.
18. Crane, R.K., Refraction effects in the neutral atmosphere, in *Methods of Experimental Physics*, Meeks, M.L., Ed., Vol. 12, Part B, Section 2.5, Academic Press, New York, 1976.
19. Crane, R.K., Propagation phenomena affecting satellite communication systems operating in the centimeter and millimeter wave bands, *Proc. IEEE*, 59(2), 173, 1971.
20. Barry, R.G. and Chorley, R.L., *Atmosphere, Weather and Climate*, 5th ed., Methuen, New York, 1987.
21. Moran, J.M. and Morgan, M.D., *Essentials of Weather*, Prentice Hall, NJ, 1995.
22. ITU-R, Recommendation ITU-R P.453–5, The Radio Refractive Index: Its Formula and Refractivity Data, International Telecommunications Union, Geneva, 1995.
23. Crane, R.K., Review of transhorizon propagation. *Radio Sci.*, 16(5), 649, 1981.
24. COST 210, Influence of the Atmosphere on Interference between Radio Communications Systems at Frequencies above 1GHz, Commission of the European Communities, EUR 13407, Luxembourg, 1991.
25. ITU-R, Recommendation ITU-R P.452–7, Prediction Procedure for the Evaluation of Microwave Interference between Stations on the Surface of the Earth at Frequencies above 0.7 GHz, International Telecommunications Union, Geneva, 1995.
26. Lammers, U.V., Marr, R.A., Crane, R.K., and Wennemyr, M., Comparative Study of C- and Ku-Band Propagation Mechanisms beyond the Horizon, AGARD Conf. Proc. 543, NATO, 26–1, 1993.
27. Crane, R.K., Bistatic scattering from rain, *IEEE Trans. Ant. Propag.*, AP-22(2), 312, 1974.
28. Rice, P.L., Longley, K.A., Norton, K.A., and Barsis, A.P., Transmission Loss Predictions for Tropospheric Communication Circuits, Technical Note 101, Vols. 1 and 2, National Bureau of Standards, Washington, D.C., 1966.
29. Crane, R.K., Ionospheric scintillation, *Proc. IEEE*, 65(2), 180, 1977.
30. Taur, R.R., Ionospheric scintillation at 4 and 6 GHz, *COMSAT Tech. Rev.*, 3(1), 145–163, 1973.
31. Liou, K.-N., *An Introduction to Atmospheric Radiation*, Academic Press, New York, 1980.
32. ITU-R, Recommendation ITU-R P.618–4, Propagation Data and Prediction Methods Required for the Design of Earth-Space Telecommunication Systems, International Telecommunications Union, Geneva, 1995.
33. Crane, R.K., *Electromagnetic Wave Propagation Through Rain*, Wiley, New York, 1996.

34. Medhurst, R.G., Rainfall attenuation of centimeter waves: Comparison of theory and measurement, *IEEE Trans. Ant. Propag*., AP-13, 550, 1965.
35. Crane, R.K., Attenuation due to rain: A mini-review, *IEEE Trans. Ant. Propag*., AP-23, 750, 1975.
36. Stutzman, W.L. and Dishman, W.K., A simple model for the estimation of rain-induced attenuation along earth-space paths at millimeter wavelengths, *Radio Sci*., 17, 1465, 1982 (Correction *Radio Sci*., 19, 946, 1984).
37. Rice, P.L. and Holmberg, N.R., Cumulative time statistics of surface-point rainfall rates, *IEEE Trans. Commun*., COM-21, 1131, 1973.
38. Crane, R.K., Evaluation of global and CCIR models for estimation of rain rate statistics, *Radio Sci*., 20(4), 865, 1985.
39. Poiares Baptista, J.P.V. and Salonen, E.T., Review of Rainfall Rate Modeling and Mapping, Proceedings of the URSI Commission-F. Symposium on Climatic Parameters in Radiowave Propagation Prediction, Communications Research Centre, Ottawa, Canada, 1998.
40. ITU-R, Recommendation ITU-R P.618–6, Propagation Data and Prediction Methods Required for the Design of Earth-Space Telecommunication Systems, International Telecommunications Union, Geneva, 2000.
41. Bury, K.V., *Statistical Models in Applied Science,* Robert E. Krieger Publishing Co., Malabar, FL, 1986.
42. Gumbel, E.J., *Statistics of Extremes*, Columbia University Press, New York, 1958.
43. Crane, R.K., Modelling attenuation by rain in tropical regions, *Int. J. Satell. Commun.*, 8(3), 197, 1990.
44. Crane, R.K., A local model for the prediction of rain-rate statistics for rain-attenuation models, *IEEE Trans. Ant. Propag.*, accepted.
45. Flavin, R.K., Earth-space path rain attenuation at 11 and 14 GHz — Darwin, Australia, *Aust. Telecom Res.,* 12(2), 9, 1978.
46. Abramowitz, M. and Stegun, I.A., *Handbook of Mathematical Functions*, Dover Publications, New York, 1965.

chapter two

Propagation fundamentals

2.1 Maxwell's equations

Maxwell's equations provide the starting point for studies of the propagation of electromagnetic waves through the propagation medium. Maxwell's field equations may be expressed as:[1]

$$\begin{aligned} \nabla \times \underline{H} &= \underline{J} + \frac{\partial \underline{D}}{\partial t} \\ \nabla \times \underline{E} &= -\frac{\partial \underline{B}}{\partial t} \\ \nabla \cdot \underline{D} &= \rho_v \\ \nabla \cdot \underline{B} &= 0 \end{aligned} \tag{2.1}$$

where $\underline{H} = \underline{H}(\underline{r}, t)$ is the magnetic field intensity, $\underline{r}$ the position vector, t the time, and the bar under the variable is the symbol for a three-dimensional vector. The other vector field quantities are the electric field intensity, $\underline{E}(\underline{r},t)$, electric flux density, $\underline{D}(\underline{r},t)$, and magnetic flux density, $\underline{B}(\underline{r},t)$. A vector variable without the under bar symbol represents the magnitude of the vector. The remaining variables, $\underline{J}$ and ρ_v, are current density (a vector) and volume charge density, respectively.

The constitutive relationships between field intensity and flux density are given by:

$$\begin{aligned} \underline{D} &= \underline{\underline{\varepsilon}} \cdot \underline{E} \\ \underline{B} &= \underline{\underline{\mu}} \cdot \underline{H} \\ \underline{J} &= \underline{\underline{\sigma}} \cdot \underline{E} + \rho_v \underline{u} \end{aligned} \tag{2.2}$$

where $\underline{\underline{\varepsilon}} = \underline{\underline{\varepsilon}}(\underline{r},t)$ is the permittivity tensor (farads/m), $\underline{\underline{\mu}} = \underline{\underline{\mu}}(\underline{r},t)$ the permeability tensor (henrys/m), $\underline{\underline{\sigma}} = \underline{\underline{\sigma}}(\underline{r},t)$ is the conductivity tensor (mhos/m), and $\underline{u}(\underline{r},t)$ the velocity of the charge density. The tensors describe the propagation medium. In general, temporal variations of the medium are slow compared to the variations of the fields with time and may be neglected. The medium may be anisotropic, requiring the use of the tensor matrix to relate the field intensity and flux density vectors but, for most applications, the medium is isotropic, the permittivity, permeability, and conductivity are scalar functions of position, and the field intensity and flux density vectors are parallel. To complete these equations, the continuity equation expresses the conservation of charge:

$$\nabla \cdot \underline{J} = \frac{\partial \rho_v}{\partial t} \tag{2.3}$$

The partial-differential field equations are solved subject to the boundary conditions:

$$\begin{aligned} \hat{n} \times (\underline{H}_2 - \underline{H}_1) &= \underline{J}_s \\ \hat{n} \times (\underline{E}_2 - \underline{E}_1) &= 0 \\ \hat{n} \cdot (\underline{B}_2 - \underline{B}_1) &= 0 \\ \hat{n} \cdot (\underline{D}_2 - \underline{D}_1) &= \rho_s \end{aligned} \tag{2.4}$$

where $\hat{n}$ is the unit vector normal to the bounding surface between mediums 1 and 2 and directed from medium 1 to 2. The subscript *s* indicates surface current and charge densities. For a propagation problem with finite dimension sources, the fields remain finite at infinite distances from the sources.

For most applications, these equations may be simplified by considering steady-state sinusoidal variations of the fields and sources with time. The time dependence for all variables then becomes:

$$F(\underline{r},t) = \mathrm{Re}\left[F(\underline{r},\omega)e^{j\omega t}\right] \tag{2.5}$$

and Maxwell's equations reduce to:

$$\begin{aligned} \nabla \times \underline{H} &= \underline{J}_v + j\omega \underline{D} \\ \nabla \times \underline{E} &= -j\omega \underline{B} \\ \nabla \cdot \underline{D} &= \rho_v \\ \nabla \cdot \underline{B} &= 0 \end{aligned} \tag{2.6}$$

where the field, current, and charge variables are a function of the radian frequency, $\omega = 2\pi f$, where f is frequency, and the continuity equation becomes:

$$\nabla \cdot \underline{J}_v = j\omega\rho_v \tag{2.7}$$

In an isotropic medium with no free charges or currents, $D = \varepsilon E$, $B = \mu H$, $J_v = \rho_v u = 0$, and $\rho_v = 0$. Then the steady-state field equations can be reduced to:

$$\begin{aligned} \nabla \times \underline{H} &= \sigma \underline{E} + j\omega\varepsilon \underline{E} \\ \nabla \times \underline{E} &= -j\omega\mu \underline{H} \\ \nabla \cdot (\varepsilon \underline{E}) &= 0 \\ \nabla \cdot (\mu \underline{H}) &= 0 \end{aligned} \tag{2.8}$$

where $\varepsilon = \varepsilon(\underline{r}, \omega)$, $\mu = \mu(\underline{r}, \omega)$, and $\sigma = \sigma(\underline{r}, \omega)$. After taking the curl of the second equation of Equation 2.8, the first two of the equations can be combined to yield:

$$\nabla \times \nabla \times \underline{E} - (\omega^2\mu\varepsilon - j\omega\mu\sigma)\underline{E} = j\omega \underline{H} \times \nabla\mu \tag{2.9}$$

and using the third equation and a vector identity:

$$\nabla^2 \underline{E} + \left(1 - \frac{j\sigma}{\omega\varepsilon}\right)\omega^2\mu\varepsilon \underline{E} = -\nabla\left(\frac{\underline{E} \cdot \nabla\varepsilon}{\varepsilon}\right) - j\omega \underline{H} \times \nabla\mu \tag{2.10}$$

which is the inhomogeneous vector wave equation.

2.2 *Plane waves*

Maxwell's equations simplify further if the permittivity, permeability, and conductivity scalars are homogeneous or constant throughout. Equation 2.10 then reduces to the homogeneous vector wave equation or the vector Helmhotz equation:

$$\nabla^2 \underline{E} + k^2 \underline{E} = 0 \tag{2.11}$$

where the complex constant $k(\omega)$ is given by $k^2 = \omega^2\mu\varepsilon(1 - j\sigma/\omega\varepsilon)$. The simplest propagating wave is a plane wave. By definition, a plane wave does not vary in any direction normal to the direction of propagation. Let z be the direction of propagation. Using a rectangular coordinate system,

$\underline{r} = x\hat{x} + y\hat{y} + z\hat{z}$ and $\underline{E} = E_x\hat{x} + E_y\hat{y} + E_z\hat{z}$, the vector wave equation reduces to three scalar wave equations, one for each vector component. A solution for the field intensity vector and each of its components is given by:

$$\begin{aligned} \underline{E}(z,\omega) &= \underline{E}^{+}e^{-jkz} + \underline{E}^{-}e^{jkz} \\ \underline{\mathrm{E}}(z,\omega,t) &= \mathrm{Re}\left[\underline{E}^{+}e^{-j(kz-\omega t)} + \underline{E}^{-}e^{j(kz+\omega t)}\right] \end{aligned} \tag{2.12}$$

subject to the appropriate boundary conditions and to each of Maxwell's equations. This solution consists of two traveling waves: the wave with a + superscript travels in the positive z direction with a phase velocity $v_p = \omega/k$, and the wave with the – subscript travels in the opposite direction with the same speed. If the medium is free space (or a vacuum), the phase velocity is given by the speed of light in a vacuum, c. Under free-space conditions, the conductivity is zero and

$$k_0 = \omega\sqrt{\mu_0\varepsilon_0}$$

where the subscript refers to free space. Then,

$$v_p = c = \frac{1}{\sqrt{\mu_0\varepsilon_0}} \quad \text{and} \quad k_0 = \frac{\omega}{c} = \frac{2\pi f}{c} = \frac{2\pi}{\lambda} = \frac{2\pi}{\lambda_0}$$

where λ is wavelength.

The third equation of Equation 2.8 reduces to $\nabla \cdot \underline{E} = 0$ for a homogeneous medium. Expanding this equation:

$$\frac{\partial E_x}{\partial x} + \frac{\partial E_y}{\partial y} + \frac{\partial E_z}{\partial z} = 0 \tag{2.13}$$

The first two terms are zero because the field can only be a function of z. Then, $E_z^{+} = E_z^{-} = 0$ to satisfy this equation, and the plane wave field is transverse to the direction of propagation. Four boundary conditions are then needed to set the four remaining constants for the transverse field intensity E_x^{+}, E_x^{-}, E_y^{+}, and E_y^{-}.

In a more concise notation, the solutions to the homogeneous vector wave equation for plane waves are:

$$\underline{E}(\underline{r},\omega) = \underline{E}^{\pm}e^{\mp j\underline{k}\cdot\underline{r}} \quad \text{with} \quad \underline{E}^{\pm} \cdot \hat{k} = 0 \tag{2.14}$$

subject to the boundary conditions on the transverse field intensity vectors for waves traveling in the positive and negative directions. The vector wavenumber now specifies the direction of propagation, with its magnitude equal

to the wavenumber. For the homogeneous medium, the complex wavenumber is related to the free-space wavenumber by:

$$
\begin{aligned}
k &= nk_0 = \sqrt{\varepsilon_r \kappa_m}\, k_0 \\
\varepsilon_r &= \varepsilon_r' - j\left(\varepsilon_r'' + \sigma/\omega\right) \\
\tan(\delta) &= \frac{\varepsilon_r'' + \sigma/\omega}{\varepsilon_r'} \\
\kappa_m &= \frac{\mu}{\mu_0}
\end{aligned}
\tag{2.15}
$$

where ε_r is the complex dielectric constant, κ_m the relative permeability, and n the complex index of refraction. Note that the imaginary part of ε_r can be produced by conductivity, by molecular absorption within the medium, or by both. In this equation, the two mechanisms are separated, but they can be combined as ε_r''.

A similar analysis to obtain the homogeneous vector wave equation for the magnetic field intensity yields:

$$\nabla^2 \underline{H} + k^2 \underline{H} = 0 \tag{2.16}$$

and

$$\underline{H}(\underline{r}, \omega) = \underline{H}^{\pm} e^{\mp j \underline{k} \cdot \underline{r}} \quad \text{with} \quad \underline{H}^{\pm} \cdot \hat{k} = 0 \tag{2.17}$$

This solution is dependent on the solution for the electric field intensity. Both $\underline{E}$ and $\underline{H}$ are coupled through Maxwell's equations. The two boundary conditions needed to complete the solution for each of the transverse vector components can be applied to Equation 2.14 or Equation 2.17, but not both. $\underline{H}$ can be found from $\underline{E}$ or vice versa. Noting that

$$\frac{\partial}{\partial z} \underline{E}^{\pm} e^{\mp jz} = \mp jk \underline{E}^{\pm} e^{\mp jz},$$

the second equation of Equation 2.8 becomes:

$$\nabla \times \underline{E} = \mp j \underline{k} \times \underline{E} = -j\omega\mu \underline{H} \tag{2.18}$$

where the sign of k depends on the direction of wave propagation. This equation yields the relationship between $\underline{E}$ and $\underline{H}$:

$$\underline{H} = \pm\frac{k}{\omega\mu}\hat{k}\times\underline{E} = \pm\frac{1}{\eta}\hat{k}\times\underline{E} \tag{2.19}$$

where

$$\eta = \sqrt{\frac{\mu}{\varepsilon}}$$

is the characteristic impedance of the medium. The time-averaged Poynting vector provides the power flow of the wave across a surface normal to the direction of propagation:

$$\underline{S} = \frac{1}{2}\mathrm{Re}\left[\underline{E}^{*}\times\underline{H}\right] = \pm\mathrm{Re}\left[\frac{1}{2\eta}\underline{E}^{\pm *}\times\hat{k}\times\underline{E}^{\pm}\right] = \pm\frac{\left|E^{\pm}\right|^{2}}{2|\eta|}\hat{k} \quad \mathrm{W/m^2} \tag{2.20}$$

The polarization of a plane wave describes the relationship between the two transverse wave components for the same frequency and direction of propagation. A wave propagating in the positive direction is given by:

$$\underline{\mathrm{E}}(\underline{r},\omega,t) = \mathrm{Re}\left[\underline{E}_{T}^{+}e^{j(\omega t-\underline{k}\cdot\underline{r})}\right] \tag{2.21}$$

The two components of the transverse vector, $\underline{E}_{T}^{+}$, are set by the boundary conditions and are complex constants for the wave. They are often represented in matrix form:

$$\underline{E}_{T}^{+} = \begin{pmatrix} E_{\xi}^{+} \\ E_{\psi}^{+} \end{pmatrix} \tag{2.22}$$

where $\hat{\xi}$, $\hat{\psi}$, and $\hat{k}$ form an orthogonal right-handed rectangular coordinate system (i.e., $\hat{\xi}\times\hat{\psi} = \hat{k}$). If E_{ξ}^{+} and E_{ψ}^{+} are in phase, the wave is linearly polarized; if they differ in phase by 90° and are of equal magnitude, the wave is circularly polarized. In general, a wave is elliptically polarized.

The polarization state describes the apparent motion of the endpoint of $\underline{\mathrm{E}}$ in the transverse plane at a point along k as a function of time (or along the path at an instant in time). The wave is linearly polarized if the endpoint is confined to a straight line and circularly polarized if it moves in a circle. The orientation of a linearly polarized wave is often described by the angle the straight line makes with the horizontal plane. The orientation always refers to the $\underline{\mathrm{E}}$ vector. The sense of a circularly or elliptically polarized wave is set by the direction of rotation of the $\underline{\mathrm{E}}$ vector. Viewed at a fixed point along k looking in the direction of propagation, the wave is right-hand

polarized if the vector rotates in the clockwise direction.[2] Because E_ξ^+ and E_ψ^+ are set by independent boundary conditions, they can be separately excited to carry independent signals along the same propagation path.

Two orthogonal polarization states exist for a plane wave. Circularly polarized waves can be decomposed into the sum of two orthogonal linearly polarized waves, and likewise the linearly polarized wave can be represented by the sum of two orthogonal circularly polarized waves:

$$\begin{pmatrix} E_R \\ E_L \end{pmatrix} = \frac{1}{\sqrt{2}} \begin{pmatrix} 1 & j \\ 1 & -j \end{pmatrix} \begin{pmatrix} E_\xi \\ E_\psi \end{pmatrix} \tag{2.23}$$

and

$$\begin{pmatrix} E_\xi \\ E_\psi \end{pmatrix} = \frac{1}{\sqrt{2}} \begin{pmatrix} 1 & 1 \\ -j & j \end{pmatrix} \begin{pmatrix} E_R \\ E_L \end{pmatrix} \tag{2.24}$$

where E_R is right-hand circular polarization and E_L the left-hand circular polarization. The decomposition of $E_R = 1$ is, from Equation 2.24, given by:

$$\begin{pmatrix} E_\xi \\ E_\psi \end{pmatrix} = \frac{1}{\sqrt{2}} \begin{pmatrix} 1 & 1 \\ -j & j \end{pmatrix} \begin{pmatrix} 1 \\ 0 \end{pmatrix} = \begin{pmatrix} 1/\sqrt{2} \\ -j/\sqrt{2} \end{pmatrix} \tag{2.25}$$

which has equal-magnitude linear components with a 90° phase difference. This decomposition is important for propagation through the ionosphere, where the index of refraction is different for the two orthogonal circular polarizations. The result after recombination is the Faraday rotation of the orientation of a linearly polarized wave.

2.3 *Spherical waves*

The homogeneous vector wave equation is separable in cartesian, cylindrical, or spherical coordinate systems. The plane wave solution is a simple example of using the cartesian coordinate system. The plane wave is of infinite extent in the transverse directions. For a system using a finite-sized antenna to launch the propagating wave, the wave spreads out spherically from the source. For a finite source region containing electric currents that produce the radiated field, the use of a vector potential provides a means to evaluate the waves in the far field of the source region.[2] The vector potential $\underline{A}$ is defined by its curl and divergence:

$$\nabla \times \underline{A} = \underline{B} \tag{2.26}$$

because $\nabla \cdot (\nabla \times \underline{A}) = 0 = \nabla \cdot \underline{B}$ for any $\underline{A}$. On substitution into the second equation in Equation 2.6, $\nabla \times (\underline{E} + j\omega \underline{A}) = 0$. A scalar potential ϕ_E is then defined by:

$$\nabla \phi_E = -\underline{E} - j\omega \underline{A} \tag{2.27}$$

because $\nabla \times (\nabla \phi_E) = 0$ for any ϕ_E, a function of position. Taking the curl of Equation 2.26 and combining with the first equation of Equation 2.8, the result is:

$$\nabla^2 \underline{A} + k^2 \underline{A} = -\mu J + \nabla (j\omega\mu\varepsilon\phi_E + \nabla \cdot \underline{A}) \tag{2.28}$$

The divergence of $\underline{A}$ is not set as yet. Using the Lorentz condition $\nabla \cdot \underline{A} = -j\omega\mu\varepsilon\phi_E$, the equation for the vector potential reduces to:

$$\nabla^2 \underline{A} + k^2 \underline{A} = -\mu \underline{J} \tag{2.29}$$

in the source region and

$$\nabla^2 \underline{A} + k^2 \underline{A} = 0 \tag{2.30}$$

elsewhere. Once $\underline{A}$ is found, $\underline{B}$ is obtained from the defining Equation 2.26 and the other field variables from Equation 2.8.

Outside the source region, this equation can be reduced to the scalar wave equation in a spherical coordinate system with vector components parallel to the current density vector components within the source region. For an infinitesimal source current element at the origin of the coordinate system, the solution of the scalar wave wave equation will be a function of radial distance only. Outside the source region, the equation for the radial component is:[2]

$$\frac{d^2\phi(r)}{d^2 r} + 2\frac{d\phi(r)}{r dr} + k^2\phi(r) = 0 \tag{2.31}$$

The solution for outgoing waves is:

$$\phi(r) = \phi_0 \frac{e^{-jkr}}{r} \tag{2.32}$$

The general solution for $\underline{A}$ is given by:[2]

$$\underline{A}(\underline{r}) = \frac{\mu}{4\pi} \iiint_{\text{vol}} \underline{J}(\underline{r}') \frac{e^{-jk|\underline{r}-\underline{r}'|}}{|\underline{r}-\underline{r}'|} dr' \tag{2.33}$$

Note that the kernel of the integral

$$G(\underline{r};\underline{r}') = \frac{e^{-jk|\underline{r}-\underline{r}'|}}{|\underline{r}-\underline{r}'|}$$

is sometimes called the free-space scalar Green's function.

The magnetic flux density is found from:

$$\underline{B} = \nabla_r \times \underline{A}(\underline{r}) = \frac{\mu}{4\pi}\iiint_{\text{vol}} \nabla_r \times \left(\underline{J}(\underline{r}') \frac{e^{-jk|\underline{r}-\underline{r}'|}}{|\underline{r}-\underline{r}'|} \right) dr' \tag{2.34}$$

where $\nabla_r \times$ operates on the field point variable, r, and not on the source point variable, r'.

In the far field where $r \gg r'$, this equation reduces to:

$$\underline{H} = \left[\frac{1}{4\pi}\iiint_{\text{vol}} \left(\underline{J}(\underline{r}') \times \hat{r} e^{jk\underline{r}\cdot\underline{r}'} \right) dr' \right] \frac{-jke^{-jkr}}{r} \tag{2.35}$$

where $\underline{H}$ is perpendicular to the radial direction of propagation. The $\underline{E}$ field is found from this equation and the second equation of Equation 2.6. The volume integral over the source region produces a vector, $\underline{C}_1(\theta, \phi)$, that depends on the angle coordinates of the spherical coordinate system and:

$$\underline{H} = \underline{C}_1(\theta,\phi) \frac{-jke^{-jkr}}{r} \tag{2.36}$$

The form of this far-field equation is identical to the plane wave solution, with the exception of the $1/r$ reduction of field intensity with distance from the source region. The direction of propagation is everywhere radial from the source region. The $\underline{E}$ and $\underline{H}$ fields are perpendicular to the direction of propagation and to each other. An orthogonal current system in the source region produces a second vector, $\underline{C}_2(\theta, \phi)$, orthogonal to the first to provide two independent constants equivalent to the two vectors set by the boundary conditions for the plane wave. The current systems can be adjusted to produce two orthogonal linearly, circularly, or elliptically polarized waves. The total power of a plane wave field is infinite due to the assumed infinite extent of a plane wave. The total power in the outgoing spherical wave is finite and conserved in a lossless medium.

2.4 *Reflection and refraction*

At large distances from a spatially limited source such as an antenna, the radius of curvature of a constant phase wavefront can be much larger than

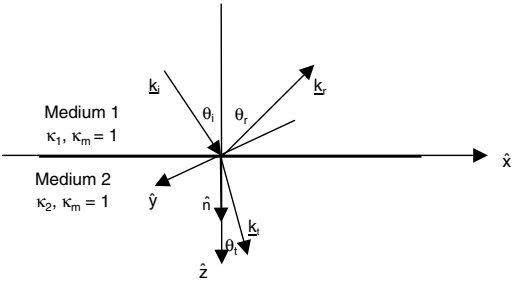

Figure 2.1 Geometry for reflection and refraction at a plane surface.

the spatial extent of a scattering, reflecting, or refracting object. Then the wave when incident on the object can be approximated as a plane wave. The use of plane waves and plane boundaries for scattering problems can reduce the complexity of the analysis.

An infinite plane surface between two media of differing dielectric constants will cause the partial reflection of an incident wave and a change in direction of propagation or a refraction of the wave transmitted through the boundary. Figure 2.1 presents the geometry of the scattering problem. The plane of incidence contains the normal to the boundary surface, $\hat{n}$, and the incident wave vector, $\underline{k}_i$. The complex dielectric constants for the two media are κ_1 and κ_2. The relative permeabilities of both media are equal to 1. The solution requires the use of the boundary conditions specified in Equation 2.4. Solutions are sought for two orthogonal polarizations, linear with $\underline{E}$ perpendicular to the plane of incidence, $E_\perp$, and linear with $\underline{E}$ parallel to the plane of incidence, $E_\parallel$. Any polarization can be decomposed into these two polarization states.

For a bounding surface with no surface currents or charges, the boundary conditions on $\underline{E}_\perp$ are given by the second equation in Equation 2.4. $\underline{E}_\perp$ in medium 1 is the sum of the field intensities for the incident and reflected wave. The boundary conditions then are:

$$\underline{E}^i_\perp e^{-j(\underline{k}_i \cdot \underline{r} - j\omega_i t)} + \underline{E}^r_\perp e^{-j(\underline{k}_r \cdot \underline{r} - j\omega_r t)} = \underline{E}^t_\perp e^{-j(\underline{k}_t \cdot \underline{r} - j\omega_t t)}$$

The exponential functions must match so:

$$\begin{aligned} \omega_i &= \omega_r = \omega_t = \omega \\ \underline{k}_i \cdot \underline{r} &= \underline{k}_r \cdot \underline{r} = \underline{k}_t \cdot \underline{r} \end{aligned} \tag{2.37}$$

where the equalities hold along the boundary surface. The second equation in Equation 2.37 implies that the incident, reflected, and transmitted waves are all in the plane of incidence.[3] Employing a cartesian coordinate system with x along the surface in the plane of incidence, y in the surface and normal

to the plane of incidence, and z along the normal to the surface but directed into medium 2:

$$\underline{k}_i \cdot \hat{x} = n_1 k_0 \sin(\theta_i) \tag{2.38}$$

where θ_i is the incidence angle between the vector wavenumber and the z axis and n_1 is the complex index of refraction in medium 1. Then, equating the real parts of Equation 2.37:

$$n_1' \sin(\theta_i) = n_1' \sin(\theta_r) = n_2' \sin(\theta_t) \tag{2.39}$$

where n' is the real part of the index of refraction. Then:

$$\begin{aligned} \theta_r &= \theta_i \\ \frac{n_2'}{n_1'} &= \frac{\sin(\theta_i)}{\sin(\theta_t)} \end{aligned} \tag{2.40}$$

where the first equation equates the incidence angle to the angle of reflection and the second equation is Snell's law of refraction. The field intensity values are obtained from the first two equations of Equation 2.4.

$$\begin{aligned} & n \times \left(\underline{E}_\perp^i + \underline{E}_\perp^r - \underline{E}_\perp^t \right) = 0 \\ & \therefore E_\perp^i + E_\perp^r - E_\perp^t = 0 \\ & n \times \left(\underline{k}_i \times \underline{E}_\perp^i + \underline{k}_r \times \underline{E}_\perp^r - \underline{k}_t \times \underline{E}_\perp^i \right) = 0 \\ & \therefore n_1 \cos(\theta_i) E_\perp^i - n_1 \cos(\theta_r) E_\perp^r - n_2 \cos(\theta_t) E_\perp^t = 0 \end{aligned} \tag{2.41}$$

Solving for the transmitted and reflected field intensities:

$$\begin{aligned} \tau_\perp &= \frac{E_\perp^t}{E_\perp^i} = \frac{2\cos(\theta_i)}{\cos(\theta_i) + \frac{n_2}{n_1}\cos(\theta_t)} \\ \Gamma_\perp &= \frac{E_\perp^r}{E_\perp^i} = \frac{\cos(\theta_i) - \frac{n_2}{n_1}\cos(\theta_t)}{\cos(\theta_i) + \frac{n_2}{n_1}\cos(\theta_t)} \end{aligned} \tag{2.42}$$

where $\tau_\perp$ is the transmission coefficient and $\Gamma_\perp$ is the reflection coefficient.

For $\underline{E}^i$ in the plane of incidence, the roles of $\underline{E}$ and $\underline{H}$ are reversed because $\underline{H}$ is now perpendicular to the plane of incidence:

$$\tau_{||} = \frac{H_{||}^t}{H_{||}^i} = \frac{2\cos(\theta_i)}{\frac{n_2}{n_1}\cos(\theta_i) + \cos(\theta_t)}$$
$$\Gamma_{||} = \frac{H_{||}^r}{H_{||}^i} = \frac{\frac{n_2}{n_1}\cos(\theta_i) - \cos(\theta_t)}{\frac{n_2}{n_1}\cos(\theta_i) + \cos(\theta_t)} \tag{2.43}$$

Equation 2.42 and Equation 2.43 are the Fresnel transmission and reflection coefficients, respectively. Because the permeability is the same in both media, the ratio of the indices of refraction can be replaced by the inverse ratios of the characteristic impedance:

$$\frac{n_2}{n_1} = \frac{\sqrt{\varepsilon_2}}{\sqrt{\varepsilon_1}} = \frac{\sqrt{\varepsilon_2\mu_0}}{\sqrt{\varepsilon_1\mu_0}} = \frac{\eta_1}{\eta_2} \tag{2.44}$$

Reflection and transmission coefficients for a plane air–water interface are presented in Figure 2.2 and Figure 2.3. The dielectric constant and loss tangent are taken from Figure 1.20. Figure 2.2 gives the magnitude of the coefficients as a function of incidence angle. For a smooth horizontal water surface, parallel polarization corresponds to vertical linear polarization and perpendicular corresponds to horizontal polarization. The angle of incidence is complementary to the grazing angle. For a terrestrial path with a grazing angle at the water surface of only a few degrees (angle of incidence close to 90°), a 180° phase shift occurs on reflection for both polarizations (see Figure 2.3). The minimum in the reflection coefficient for vertical polarization (para) occurs at the pseudo Brewster angle. This angle marks the sign change in the real part of the reflection coefficient for parallel polarization. The sign change produces a reversal in the sense of a reflected circularly polarized wave. For randomly polarized radiation, the pseudo Brewster angle minimum enhances the horizontally polarized component relative to the vertically polarized component.

The incident polarization can be decomposed into linear polarizations perpendicular and parallel to the plane of incidence. For a general linear polarization, all that is needed is a rotation:

$$\begin{pmatrix} E_\perp \\ E_{||} \end{pmatrix} = \begin{pmatrix} \cos(\phi) & -\sin(\phi) \\ \sin(\phi) & \cos(\phi) \end{pmatrix} \begin{pmatrix} E \\ 0 \end{pmatrix} \tag{2.45}$$

where ϕ is the angle between the incident $\underline{E}$ and the horizontal plane.

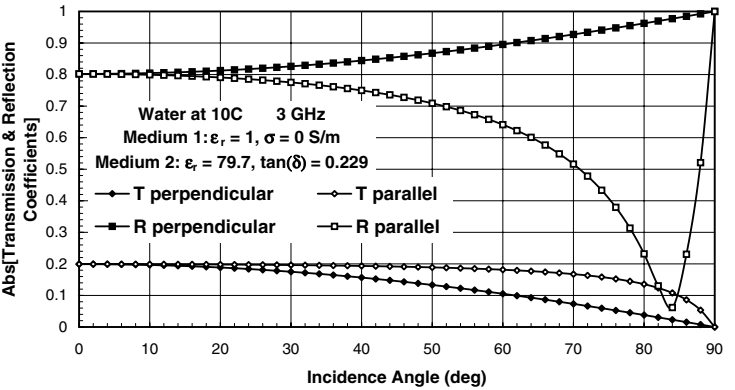

Figure 2.2 Magnitude of transmission and reflection coefficients for an air–water surface.

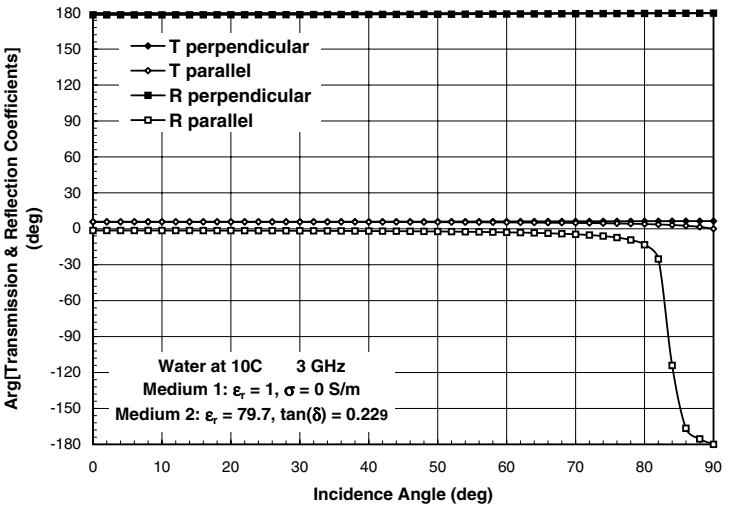

Figure 2.3 Phase of transmission and reflection coefficients for an air–water surface.

The reflection and transmission coefficients describe the change in the magnitude of the field intensity vectors. The relative reflected power and transmitted power values are obtained from the square of the magnitude of the coefficients. The reflectivity, **R**, is the ratio of the reflected to incident power reflected from the medium per unit area on the surface. The transmissivity, **T**, is the ratio of the power transmitted into medium 2 to the power incident on the medium per unit surface area.[4] The transmissivity and reflectivity values are obtained by the ratios of the magnitudes of the Poynting vectors adjusted by the projection of the unit area transverse to the wavefront onto the boundary surface:

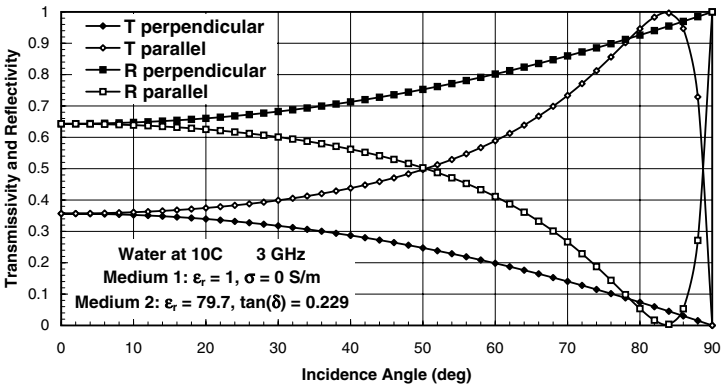

Figure 2.4 Transmissivity and reflectivity for an air–water surface.

$$
\begin{aligned}
\mathbf{R}_{\perp} &= \frac{n_1 \cos(\theta_r)\left|E_{\perp}^{r}\right|^2}{n_1 \cos(\theta_i)\left|E_{\perp}^{i}\right|^2} = \left|G_{\perp}\right|^2 \\
\mathbf{R}_{||} &= \left|G_{||}\right|^2 \\
\mathbf{T}_{\perp} &= \frac{n_2 \cos(\theta_t)\left|E_{\perp}^{t}\right|^2}{n_1 \cos(\theta_i)\left|E_{\perp}^{i}\right|^2} = \frac{n_2 \cos(\theta_t)}{n_1 \cos(\theta_i)}\left|T_{\perp}\right|^2 \\
\mathbf{T}_{||} &= \frac{n_2 \cos(\theta_t)}{n_1 \cos(\theta_i)}\left|T_{||}\right|^2
\end{aligned}
\tag{2.46}
$$

The reflectivity and transmissivity values for the coefficients displayed in Figure 2.2 are shown in Figure 2.4. The transmissivity and reflectivity for a given polarization and incidence angle add to 1 in conformance with the conservation of energy at the boundary surface.

2.5 *Geometrical optics*

The geometrical optics approximation describes wave propagation in the limit of high frequencies. In a homogeneous isotropic medium, the waves propagate in straight lines called rays; in an inhomogeneous isotropic medium, the rays are curved. Geometrical optics describes the ray trajectories in the limit where changes in the properties of the medium are slowly varying in space.[4,5] Starting with the steady-state field equations, Equation 2.8, the plane wave solution, Equation 2.12 is obtained for a homogeneous medium. As a trial solution for an inhomogeneous equation, assume a generalized plane wave solution:[4]

$$\underline{E}(\underline{r},\omega) = \underline{E}_G(\underline{r})e^{-jk_0\mathbf{S}(\underline{r})} \tag{2.47}$$

where $\underline{E}_G$, is a vector function of position and $\mathbf{S}$ is a scalar function of position. The surface $L = \mathrm{Re}[\mathbf{S}]$ equal a constant is a constant phase wavefront. Note L has the dimension of length because $k_0 L$ is the value of phase in radians on the wavefront. By substituting the trial solution into Equation 2.8, the following results are obtained:

$$\begin{aligned}
\nabla\times\left(\underline{H}_G e^{-jk_0\mathbf{S}}\right) &= \left[\nabla\times\underline{H}_G + jk_0\underline{H}_G\times\nabla\mathbf{S}\right]e^{-jk_0\mathbf{S}} = (\sigma + j\omega\varepsilon)\underline{E}_G e^{-jk_0\mathbf{S}} \\
\nabla\times\left(\underline{E}_G e^{-jk_0\mathbf{S}}\right) &= \left[\nabla\times\underline{E}_G + jk_0\underline{E}_G\times\nabla\mathbf{S}\right]e^{-jk_0\mathbf{S}} = -j\omega\mu\underline{H}_G e^{-jk_0\mathbf{S}} \\
\nabla\cdot\left(\varepsilon\underline{E}_G e^{-jk_0\mathbf{S}}\right) &= \left[\varepsilon\nabla\cdot\underline{E}_G + \underline{E}_G\cdot\nabla\varepsilon - jk_0\varepsilon\underline{E}_G\cdot\nabla\mathbf{S}\right]e^{-jk_0\mathbf{S}} = 0 \\
\nabla\cdot\left(\mu\underline{H}_G e^{-jk_0\mathbf{S}}\right) &= \left[\mu\nabla\cdot\underline{H}_G + \underline{H}_G\cdot\nabla\mu - jk_0\mu\underline{H}_G\cdot\nabla\mathbf{S}\right]e^{-jk_0\mathbf{S}} = 0
\end{aligned} \tag{2.48}$$

which may be simplified to:

$$\begin{aligned}
\nabla\mathbf{S}\times\underline{H}_G + \frac{(\sigma + j\omega\varepsilon)}{jk_0}\underline{E}_G &= \frac{1}{jk_0}\nabla\times\underline{H}_G \\
\nabla\mathbf{S}\times\underline{E}_G - \frac{j\omega\mu\underline{H}_G}{jk_0} &= \frac{1}{jk_0}\nabla\times\underline{E}_G \\
\nabla\mathbf{S}\cdot\underline{E}_G &= \frac{1}{jk_0}\left(\nabla\cdot\underline{E}_G + \underline{E}_G\cdot\frac{\nabla\varepsilon}{\varepsilon}\right) \\
\nabla\mathbf{S}\cdot\underline{H}_G &= \frac{1}{jk_0}\left(\nabla\cdot\underline{H}_G + \underline{H}_G\cdot\frac{\nabla\mu}{\mu}\right)
\end{aligned} \tag{2.49}$$

Note that this equation is exact; no approximation has been made.

The geometrical optics approximation holds in the limit $f \to \infty$. In this limit, k_0 also approaches infinity while ω/k_0 is constant and the right-hand side of each equation in Equation 2.49 approaches zero:

$$\begin{aligned}
\nabla\mathbf{S}\times\underline{H}_G + \frac{\varepsilon}{\sqrt{\mu_0\varepsilon_0}}\underline{E}_G &= 0 \\
\nabla\mathbf{S}\times\underline{E}_G - \frac{\mu}{\sqrt{\mu_0\varepsilon_0}}\underline{H}_G &= 0 \\
\nabla\mathbf{S}\cdot\underline{E}_G &= 0 \\
\nabla\mathbf{S}\cdot\underline{H}_G &= 0
\end{aligned} \tag{2.50}$$

where $\nabla\mathbf{S}$ is in the direction normal to the wavefront, and, from the last two equations in Equation 2.50, is perpendicular to the field intensity vectors. The first two equations may be combined to obtain:

$$\nabla\mathbf{S}\times\nabla\mathbf{S}\times\underline{E}_G + n^2\underline{E}_G = 0$$

or

$$(\nabla\mathbf{S}\cdot\nabla\mathbf{S} - n^2)\underline{E}_G = 0 \tag{2.51}$$

and because $\underline{E}_G \neq 0$, $\nabla\mathbf{S}\cdot\nabla\mathbf{S} - n^2 = 0$ and $\nabla L = \mathrm{Re}[\nabla\mathbf{S}]$, the real parts may be combined to yield:

$$(\nabla L)^2 = (n')^2 \tag{2.52}$$

which is called the eikonal equation. This equation is often taken as the starting point for geometrical optics analyses. Note that the eikonal equation, which describes the geometry of the wavefronts, is not a function of the field vectors and, except for propagation through the ionosphere, not explicitly a function of frequency.

The flow of power is given by the time-averaged Poynting vector, $\underline{S}$. For a nonmagnetic medium, $\mu = \mu_0$ and:

$$\underline{S} = \frac{1}{2}\mathrm{Re}\left[\underline{E}_G\times\underline{H}_G^*\right] = \frac{1}{2}\sqrt{\frac{\mu_0}{\varepsilon_0}}\underline{E}_G\times\mathrm{Re}[\nabla\mathbf{S}]\times\underline{E}_G{}^* = \frac{1}{2\eta_0}\left(\underline{E}_G\cdot\underline{E}_G^*\right)\frac{\nabla L}{n'} \tag{2.53}$$

where $\hat{s} = \nabla L/n'$ is a unit vector in the direction of the Poynting vector and is normal to the wavefront. In an isotropic medium, a ray passes from one wavefront surface to the next along the direction of the Poynting vector. The position vector to a point on a ray, $\underline{r}(s)$, describes the trajectory of the ray as a function of position, s, along the ray:

$$\hat{s} = \frac{d\underline{r}(s)}{ds} = \frac{\nabla L(\underline{r}(s))}{n'(\underline{r}(s))} \tag{2.54}$$

or

$$n'\frac{d\underline{r}}{ds} = \nabla L \tag{2.55}$$

The differential equation for the ray is then formed by finding the change in ∇L with s along the ray:[4]

$$\frac{d}{ds}\left(n'\frac{d\underline{r}}{ds}\right)=\frac{d}{ds}\nabla L=\hat{s}\cdot\nabla(\nabla L)=\frac{\nabla L}{n'}\cdot\nabla(\nabla L)=\frac{\nabla(\nabla L\cdot\nabla L)}{2n'}$$

therefore

$$\frac{d}{ds}\left(n'\frac{d\underline{r}}{ds}\right)=\nabla n' \tag{2.56}$$

The optical or electrical path length along a ray is obtained by integrating along the trajectory of the ray:

$$\int_{\text{ray}} n'ds=\int_{\text{ray}}\nabla L\cdot d\underline{s}=\int_{\text{ray}}\frac{dL}{ds}d\underline{s}=L(s_2)-L(s_2)=L_P \tag{2.57}$$

The physical path length is just

$$L_S=\int_{\text{ray}} ds$$

The transit time for a wavefront to move along the path, t_P, is:

$$L_P=\int_{\text{ray}} n'ds=\int_{\text{ray}}\frac{c}{v_P}ds=c\int_{\text{ray}} dt=ct_P \tag{2.58}$$

and the phase delay on the path is

$$t_P=\frac{L_P}{c} \tag{2.59}$$

The theory of geometrical optics can also be derived from Fermat's principle, which states that the transit time between two wavefronts along a ray is a minimum.[4–6] Starting from Fermat's principle:

$$\delta L_P=\delta\int_{\text{ray}} n'ds=0 \tag{2.60}$$

which states that the variation of the integral

$$\int_{\text{ray}} n' ds$$

is stationary (a minimum) along a ray between specified (fixed) points in the medium, and the calculus of variations may be used to derive the differential equation for the path of the ray, $s(\underline{r})$. It is given by Equation 2.56, which is Euler's equation.

The conservation of energy in a source-free, lossless medium requires the net total power flow through a closed surface in that medium to be zero.[4] By the divergence theorem

$$\oint_{\text{Surface}} \underline{S} \cdot dArea = \int_{\text{Volume}} (\nabla \cdot \underline{S}) dVolume = 0, \nabla \cdot \underline{S} = 0$$

Power flows in the direction of the real part of the Poynting vector. A tube of rays directs power along the tube. Power does not flow across the rays or through the sides of the tube. To conserve energy, the power flow into one end of the tube equals the power flow out of the other end. The power flux density at each end of the tube therefore must be inversely proportional to the cross-sectional area of the wavefronts at each end of the tube.

The geometrical optics approximation holds subject to the neglect of the right-hand sides of the equations in Equation 2.49. In general, if changes in the permeability or permittivity are small on scales much larger than a wavelength or the radius of curvature of a wavefront is much larger than a wavelength, the approximations should hold.[4,5] Geometrical optics is not valid at a shadow boundary (i.e., for a diffraction problem), at a focus of rays or at a caustic surface (where neighboring rays cross).

The equation for the ray trajectory simplifies for a spherically symmetrical medium using a spherical coordinate system with its origin at the center of symmetry. The normal to the great circle plane containing the ray direction is given by $\underline{r}(s) \times \hat{s}$ and the change in that plane with s is given by:[4]

$$\frac{d}{ds}\left(\underline{r} \times n' \hat{s}\right) = \frac{d\underline{r}}{ds} \times n' \hat{s} + \underline{r} \times \frac{d}{ds}\left(n' \frac{d\underline{r}}{ds}\right) = \underline{r} \times \nabla L = 0$$

Therefore, $\underline{r} \times n' \hat{s}$ is a constant and the ray trajectory is always in the same great circle plane. This equation can be restated as:

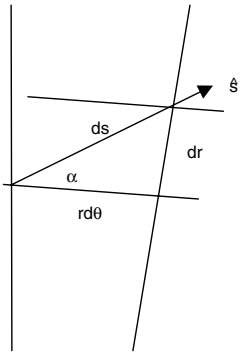

Figure 2.5 Differential ray geometry.

$$\frac{\left|\underline{r}\times n'\hat{s}\right|}{A}=\frac{n'r}{A}\cos(\alpha)=m\cos(\alpha)=K=\text{constant} \tag{2.61}$$

where α is the local elevation angle or the angle the ray direction takes relative to the local horizontal and $m = n'r/A$ is the modified index of refraction. This equation is Snell's law in spherical coordinates (see Section 1.4.2.1).

The differential equation for the ray can be obtained from Equation 2.58 by relating the elevation angle to the local geometry of the ray (Figure 2.5). The angle α is related to the differentials shown in the figure by:

$$\cos(\alpha)=\frac{rd\theta}{\sqrt{(dr)^2+(rd\theta)^2}}=\frac{r}{\sqrt{\left(\frac{dr}{d\theta}\right)^2+r^2}}=\frac{K}{n'r} \tag{2.62}$$

which with a little algebra becomes:

$$d\theta=\frac{Kdr}{r\sqrt{(n'r)^2-K^2}}=\frac{Kdr}{r\sqrt{m^2-K^2}} \tag{2.63}$$

Equation 2.60 can be reduced to quadrature but, to integrate, the dependence of the index of refraction on distance from the origin of the coordinate system must be specified.

The expressions for L_P and L_S may be obtained from the differential equation for the ray by:

$$dL_S=ds=\sqrt{(dr)^2+(rd\theta)^2}=dr\sqrt{1+\frac{r^2K^2}{r^2\left(m^2-K^2\right)}}=\frac{mdr}{\sqrt{m^2-K^2}} \tag{2.64}$$

and

$$dL_P = n' dL_S = \frac{n' m dr}{\sqrt{m^2 - K^2}} = \frac{m^2 dr}{r\sqrt{m^2 - K^2}} \tag{2.65}$$

The change in S along a pyramidal tube of rays emanating from a point source can be obtained by calculating the wavefront area contained in the base of the narrow tube of rays emanating from that source at a distance L_S from the source. The two opposite sides of the tube will be confined between two great circle planes separated by a small azimuthal angle, $\Delta\phi$. The top and bottom sides of the tube will contain rays emitted from the source at angles $\alpha + \Delta\alpha/2$ and $\alpha - \Delta\alpha/2$. For rays propagating in a homogeneous medium, the rays will travel in straight lines and the area will be

$$\Delta\phi\Delta\alpha L_P^2 \text{ and } S_0 \propto \frac{1}{L_P^2}$$

In a spherically symmetrical medium, differential bending of the top and bottom rays will produce an S value different from the result for a homogeneous medium at the same value of L_P. The ratio of S to S_0 is called spreading loss or focusing loss. Because the ray tube is confined between great circle planes passing through the source, there is no change in S due to azimuthal spreading.

2.6 *Ray tracing*

The Earth's atmosphere is often modeled as spherically symmetric with the index of refraction varying with height (see Section 1.4.2.1). The index of refraction varies with time and is generally known only at a number of discrete heights. For computational convenience, the atmosphere is usually broken up into concentric spherical shells between the heights, h_i, where $n'(h_i)$ is known. If $n'(h)$ is assumed to vary linearly with height between the known values (a constant n' gradient layer), the integration of Equation 2.63 in the layer requires the evaluation of an elliptic integral. For the range of index of refraction values expected in the atmosphere, additional approximations will be required to evaluate the integral. If instead, the modified index of refraction $m(h)$ is assumed to vary linearly with height between the known values, Equation 2.63 can be readily integrated.

For the layer between m_i and m_{i+1}, the change in θ, $\Delta\theta_i = \theta_{i+1} - \theta_i$ is given by:

$$\Delta\theta_i = \int_{h_i+A}^{h_{i+1}+A} \frac{Kdr}{r\sqrt{m^2-K^2}} = \int_{h_i+A}^{h_{i+1}+A} \frac{Kdr}{r\sqrt{(ar+b)^2-K^2}}$$

$$= \int_{h_i+A}^{h_{i+1}+A} \frac{Kdr}{r\sqrt{(ar)^2+2abr+(b^2-K^2)}}$$

$$= \int_{h_i+A}^{h_{i+1}+A} \frac{Kdr}{r\sqrt{ur^2+vr+w}}\;;w=b^2-K^2, v=2ab, u=a^2$$

$$= -\frac{K}{\sqrt{w}}\ln\left[\frac{\sqrt{(m^2-K^2)}+\sqrt{w}}{r}+\frac{v}{2\sqrt{w}}\right]_{h_i+A}^{h_{i+1}+A}\;;w>0 \tag{2.66}$$

$$= \frac{K}{\sqrt{-w}}\sin^{-1}\left[\frac{vr+2w}{r\sqrt{v^2-4uw}}\right]_{h_i+A}^{h_{i+1}+A}\;;w<0$$

$$= -\frac{2K}{v}\left[\frac{\sqrt{(m^2-K^2)}}{r}\right]_{h_i+A}^{h_{i+1}+A}\;;w=0$$

where A is the radius of the Earth.

The integral for ΔL_{Si} is:

$$\Delta L_{Si} = \int_{h_i+A}^{h_{i+1}+A} \frac{mdr}{\sqrt{m^2-K^2}} = \frac{1}{a}\left[\sqrt{m^2-K^2}\right]_{h_i+A}^{h_{i+1}+A} \tag{2.67}$$

where a, b, u, v, and w are defined in Equation 2.66. The integral for ΔL_{Pi} is:

$$\Delta L_{Pi} = \int_{h_i+A}^{h_{i+1}+A} \frac{m^2dr}{r\sqrt{m^2-K^2}} \approx \Delta L_{Si}\left(1+\frac{1}{2}\left(N_i'+N_{i+1}'\right)\times 10^{-6}\right)$$

$$= |a|\Delta L_{Si} + \frac{b^2}{K}\Delta\theta_i + b\ln\left[2ur+v+2|a|\sqrt{m^2-K^2}\right]_{h_i+A}^{h_{i+1}+A} \tag{2.68}$$

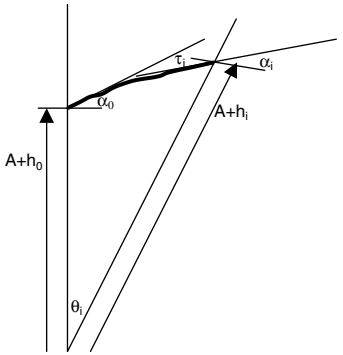

Figure 2.6 Ray geometry.

The ray trajectory results up to level i are then given by (Figure 2.6):

$$\begin{aligned}
\theta_i &= \sum_{j=0}^{i-1} \Delta\theta_j \\
L_{Si} &= \sum_{j=0}^{i-1} \Delta L_{Sj} \\
L_{Pi} &= \sum_{j=0}^{i-1} \Delta L_{Pj} \\
\alpha_i &= \cos^{-1}\left(\frac{K}{m_i}\right)
\end{aligned} \tag{2.69}$$

These ray parameters depend on the index of refraction profile and the initial or apparent elevation angle of the ray, α_0. In practice, the end-points of the ray, (h_0, 0) and (h_i, θ_i) are known and the initial elevation angle is to be determined. This can be done only by iterating through a selection of trial initial elevation angles values until the desired ray trajectory end-point is reached. In radar-tracking applications, the apparent elevation angle and the electrical distance to the target are measured and the geometrical distance, d_i, and the elevation angle error, ε_i, are to be determined. These parameters and the ray bending, τ_i are given by:

$$\begin{aligned}
d_i &= \sqrt{\left(A+h_i\right)^2 + \left(A+h_0\right)^2 - 2\left(A+h_i\right)\left(A+h_0\right)\cos(\theta_i)} \\
\alpha_{Ti} &= \cos^{-1}\left(\frac{\left(A+h_i\right)\sin(\theta_i)}{d_i}\right) \\
\varepsilon_i &= \alpha_0 - \alpha_{Ti} \\
\tau_i &= \alpha_0 + \theta_i - \alpha_i
\end{aligned} \tag{2.70}$$

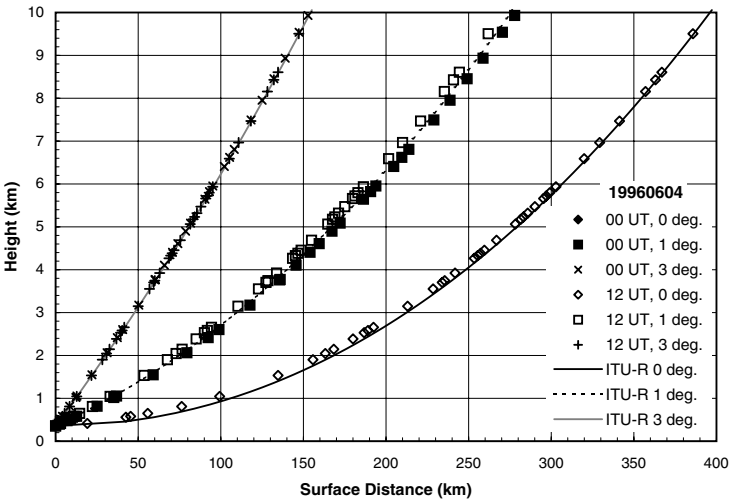

Figure 2.7 Ray trajectories for different index of refraction profiles.

where α_{Ti} is the geometrical or true elevation angle as measured from the initial ray location. Focusing loss may be calculated by comparing the cross-sectional area of a tube of rays originating at the source:

$$A_{Fi} = 4.343 \ln\left(\frac{\alpha_D - \alpha_0 + \tau_{Di} - \tau_0}{\alpha_D - \alpha_0}\right) \text{ dB} \tag{2.71}$$

where A_{Fi} is the focusing loss in dB, α_D is the initial elevation angle for the top of the ray tube offset by a small amount above the initial elevation angle, α_0, and τ_{Di} is the total bending of the offset ray at level *i*.

Sample ray trajectories are displayed in Figure 2.7. They are for the ITU *m*-profile model and rawinsonde soundings (RAOBs) displayed in Figure 1.26. The plotting symbols on the ray trajectories calculated from the RAOBs are at each reported height. Results obtained using the bending and elevation angle error calculations presented in Equation 2.70 are displayed in Figure 1.27 and Figure 1.28.

2.7 *Scalar diffraction theory*

Geometrical optics describes electromagnetic waves in the high frequency limit as the wavelength approaches zero. In this limit, rays incident on an absorbing obstacle produce a shadow region behind the obstacle with a discontinuous boundary between the illuminated and dark sectors. Alternatively, the wave nature of light is explicit in the Huygens wavelet construction procedure used to obtain one wavefront from another.[4,6] Starting with

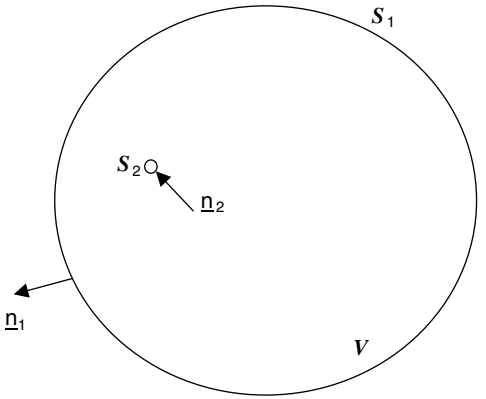

Figure 2.8 Surface and volume geometry for the application of Green's theorem.

the homogeneous scalar wave equation for a source free region, for example, Equation 2.11 for one of the cartesian components of $\underline{E}$:

$$\nabla^2\phi + k^2\phi = 0 \tag{2.72}$$

Green's theorem may be used to relate the field at an observation point inside a volume to the fields at the surfaces surrounding the volume (Figure 2.8):

$$\int_{\mathbf{V}} \left(\psi\nabla^2\phi - \phi\nabla^2\psi\right) d\mathbf{V} = \int_{\mathbf{S_1}} \left(\psi\nabla\phi - \phi\nabla\psi\right)\cdot\hat{n}\, d\mathbf{S} + \int_{\mathbf{S_2}} \left(\psi\nabla\phi - \phi\nabla\psi\right)\cdot\hat{n}\, d\mathbf{S} \tag{2.73}$$

If both ψ and ϕ satisfy Equation 2.72 in the volume and on the surfaces and each function is continuous within the volume and on the surfaces, the volume integral is zero. The free space Green's function (Equation 2.33) satisfies these requirements except at the singularity where $\underline{r} = \underline{r}'$. Let the singularity at $\rho = \underline{r} - \underline{r}'$ be enclosed within surface $\mathbf{S}_2$. The surface normals point out of volume $\mathbf{V}$; therefore, $\hat{n}_2 = -\hat{\rho}$. Equation 2.72 then reduces to:

$$\begin{aligned} \phi(\rho) &= \frac{e^{-jk\rho}}{\rho} \\ \psi(\underline{r}') &= -\frac{1}{4\pi}\int_{\mathbf{S_1}} \left(\psi(\underline{\rho})\nabla\left(\frac{e^{-jk\rho}}{\rho}\right) - \frac{e^{-jk\rho}}{\rho}\nabla\psi(\underline{\rho}) \right)\cdot\hat{n}_1 d\mathbf{S} \end{aligned} \tag{2.74}$$

where the $\mathbf{S}_2$ integral yields $4\pi\psi(\underline{r}')$ as $\rho \to 0$. This equation for ψ is known as the Helmholtz–Kirchhoff integral.[4]

The physical optics solution to the scalar diffraction problem is obtained from the equation for $\psi(\underline{r}')$ when $\psi(\underline{r})$ is specified everywhere on the bounding

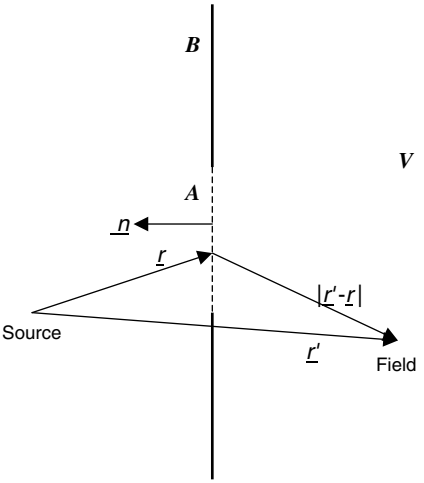

Figure 2.9 An aperture in an infinite absorbing screen.

surface $\mathbf{S}_1$. A knowledge of $\psi(\underline{r})$ everywhere on the surface requires the solution of the wave equation. Kirchhoff introduced the approximation that for an aperture in an infinite absorbing screen, $\psi(\underline{r})$ and its first derivative along the surface normal could be set to zero on the absorbing screen and to the values of the wave incident on the aperture. Then for a spherical wave emanating from a point source incident on the aperture **A** and screen **B**, the diffracted field at the field point behind the screen in volume **V** becomes (Figure 2.9):

$$\psi(\underline{r}) = \psi_0 \frac{e^{-jkr}}{r} \text{ on the aperture } \mathbf{A},\ 0 \text{ otherwise}$$

$$\psi(\underline{r}') = -\frac{\psi_0}{4\pi}\int_{\mathbf{A}} \left(\frac{e^{-jkr}}{r} \nabla\left(\frac{e^{-jk|\underline{r}'-\underline{r}|}}{|\underline{r}'-\underline{r}|} \right) - \frac{e^{-jk|\underline{r}'-\underline{r}|}}{|\underline{r}'-\underline{r}|} \nabla \frac{e^{-jkr}}{r} \right) \cdot \hat{n} d\mathbf{S} \qquad (2.75)$$

$$\psi(\underline{r}') = \frac{jk\psi_0}{4\pi}\int_{\mathbf{A}} \frac{e^{-jkr}}{r}\frac{e^{-jks}}{s}\left(-\hat{s}\cdot\hat{n} - r\cdot\hat{n}\right) d\mathbf{S}$$

where $\underline{s} = \underline{r}' - \underline{r}$ and terms in $1/r^2$ and $1/s^2$ from the gradient operations have been neglected. This is the Fresnel–Kirchhoff diffraction formula. It may be simplified by assuming that for a source far from the aperture, $\underline{r}$ is constant across **A**, and for $\underline{r}$ normal to the aperture, $\hat{r}\cdot\hat{n} = -1$, then:

$$\psi(\underline{r}') = \frac{jk\psi_0}{4\pi r}\int_{\mathbf{A}} \frac{e^{-jkr}e^{-jks}}{s}\left(1 + \hat{r}\cdot\hat{s}\right) dS \qquad (2.76)$$

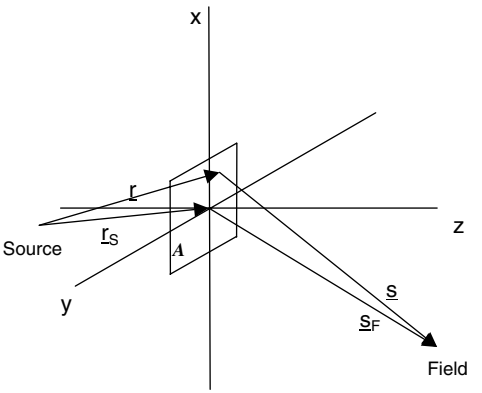

Figure 2.10 Geometry for the derivation of the Fresnel–Kirchhoff diffraction integral.

For the rectangular aperture in an infinite plane-absorbing screen shown in Figure 2.10, Equation 2.76 may be further simplified to yield:

$$\begin{aligned}\psi(\underline{r}') &= \frac{jk\psi_0\left(1+\hat{r}_S\cdot\hat{s}_F\right)}{4\pi r_S s_F}e^{-jk(r_S+s_F)}\int_A e^{-jkf(\xi,\eta)}d\xi d\eta \\ &= K\int_A e^{-jkf(\xi,\eta)}d\xi d\eta\end{aligned} \tag{2.77}$$

where ξ, η are the surface integration coordinates in the aperture with an origin at the end point of $\underline{r}_S$. Then the variation of r across the aperture can be approximated by:

$$\begin{aligned}r &= \sqrt{(x_S-\xi)^2+(y_S-\eta)^2+z_S^2} \\ r-r_S &\approx -\left(\frac{x_S\xi+y_S\eta}{r_S}\right)+\left(\frac{\xi^2+\eta^2}{2r_S}\right)-\frac{\left(x_S\xi+y_S\eta\right)^2}{2r_S^3}-\ldots\end{aligned} \tag{2.78}$$

with a similar approximation for $s - s_F$. The approximate expression for the phase variation in the integrand is

$$\begin{aligned}f(\xi,\eta) = &-\left(\frac{x_S}{r_S}+\frac{x_F}{s_F}\right)\xi-\left(\frac{y_S}{r_S}+\frac{y_F}{s_F}\right)\eta+\left(\frac{1}{r_S}+\frac{1}{s_F}\right)\frac{\xi^2+\eta^2}{2} \\ &-\frac{\left(x_S\xi+y_S\eta\right)^2}{2r_S^3}-\frac{\left(x_F\xi+y_F\eta\right)^2}{2s_F^3}+\ldots\end{aligned} \tag{2.79}$$

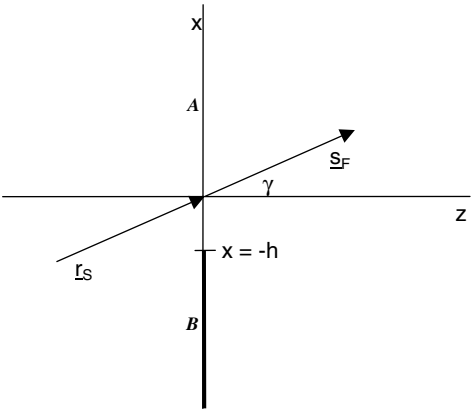

Figure 2.11 Knife-edge diffraction geometry.

If only the first two terms (linear in ξ, η) are needed to describe the phase variation, the approximation is termed Fraunhoffer diffraction, otherwise it is Fresnel diffraction.[4] For Fraunhoffer diffraction, the integral is a two-dimensional Fourier transform. The far-field antenna pattern for an aperture antenna is often calculated using this approximation.

Knife-edge diffraction requires the use of the Fresnel diffraction integral. Consider the knife edge illustrated in Figure 2.11. For this case, the path between the point source and the field point, $\underline{r}_S + \underline{s}_F$ is a straight line in the x, z plane making an angle γ with the z axis. The absorbing screen below the knife edge is the half x, y plane **B** and the aperture is the half x, y plane **A**. Then $f(\xi, \eta)$ becomes:

$$\frac{x_F}{s_F} = -\frac{x_S}{r_S} = \sin(\gamma)$$

$$\frac{y_F}{s_F} = -\frac{y_S}{r_S} = 0 \tag{2.80}$$

$$f(\xi,\eta) = \frac{1}{2}\left(\frac{1}{r_S} + \frac{1}{s_F}\right)\left(\xi^2\cos^2(\gamma) + \eta^2\right)$$

which is quadratic in ξ and η. The integral then can be reduced to Fresnel integrals. Let:

$$u = \sqrt{\frac{2}{\lambda}\left(\frac{r_S + s_F}{r_S s_F}\right)}\xi\cos(\gamma) = w\xi\cos(\gamma)$$

$$v = \sqrt{\frac{2}{\lambda}\left(\frac{r_S + s_F}{r_S s_F}\right)}\eta = w\eta$$

then:

$$\psi(\underline{r}') = K\int_{A} e^{-jkf(\xi,\eta)}\,d\xi d\eta$$
$$= \frac{K}{w^2\cos(\gamma)}\int_{wx}^{\infty}\int_{-\infty}^{\infty} e^{-j\frac{\pi}{2}\left(u^2+v^2\right)}\,dudv \tag{2.81}$$

The Fresnel integrals are defined to be:[7]

$$C(z) = \int_0^z \cos\left(\frac{\pi}{2}w^2\right)dw; \quad S(z) = \int_0^z \sin\left(\frac{\pi}{2}w^2\right)dw$$

where

$$C(\infty) = \frac{1}{2} \text{ and } \quad S(\infty) = \frac{1}{2}$$

Expanding the integral in Equation 2.81,

$$\psi(\underline{r}') = \frac{K}{w^2\cos(\gamma)}\left[\int_{wx}^{\infty}\int_{-\infty}^{\infty}\cos\left(\frac{\pi}{2}\left(u^2+v^2\right)\right)dudv - j\int_{wx}^{\infty}\int_{-\infty}^{\infty}\sin\left(\frac{\pi}{2}\left(u^2+v^2\right)\right)dudv\right]$$

$$= \frac{K}{w^2\cos(\gamma)}\left[\int_{wx}^{\infty}\cos\left(\frac{\pi}{2}u^2\right)du\int_{-\infty}^{\infty}\cos\left(\frac{\pi}{2}v^2\right)dv - \int_{wx}^{\infty}\sin\left(\frac{\pi}{2}u^2\right)du\int_{-\infty}^{\infty}\sin\left(\frac{\pi}{2}v^2\right)dv\right]$$

$$\frac{-jK}{w^2\cos(\gamma)}\left[\int_{wx}^{\infty}\cos\left(\frac{\pi}{2}u^2\right)du\int_{-\infty}^{\infty}\sin\left(\frac{\pi}{2}v^2\right)dv + \int_{wx}^{\infty}\sin\left(\frac{\pi}{2}u^2\right)du\int_{-\infty}^{\infty}\cos\left(\frac{\pi}{2}v^2\right)dv\right]$$

and

$$\psi(\underline{r}') = \frac{K}{w^2\cos(\gamma)}\left[\int_{wx}^{\infty}\cos\left(\frac{\pi}{2}u^2\right)du - \int_{wx}^{\infty}\sin\left(\frac{\pi}{2}u^2\right)du - j\int_{wx}^{\infty}\cos\left(\frac{\pi}{2}u^2\right)du - j\int_{wx}^{\infty}\sin\left(\frac{\pi}{2}u^2\right)du\right]$$

$$= \frac{K}{w^2\cos(\gamma)}\left[S(wx) - C(wx) - j\left(1 - S(wx) - C(wx)\right)\right]$$

The Fresnel integrals may be obtained from math tables or calculated from the following approximation:[7]

$$C(z) = \frac{1}{2} + \mathrm{f}(z)\sin\left(\frac{\pi}{2}z^2\right) - \mathrm{g}(z)\cos\left(\frac{\pi}{2}z^2\right)$$

$$S(z) = \frac{1}{2} - \mathrm{f}(z)\cos\left(\frac{\pi}{2}z^2\right) - \mathrm{g}(z)\sin\left(\frac{\pi}{2}z^2\right)$$

$$\mathrm{f}(x) = \frac{1 + 0.926x}{2 + 1.792x + 3.104x^2}$$

$$\mathrm{g}(x) = \frac{1}{2 + 4.142x + 3.492x^2 + 6.670x^3}$$

with an error of less than 2×10^{-3}.

The ratio of the diffracted to incident power at the knife edge is then given by:

$$\frac{I}{I_0} = \frac{r_S^2}{2\left(r_S + s_F\right)^2}\left[\frac{1}{2} - S(wx)(1 - S(wx)) - C(wx)(1 - C(wx))\right]$$

and the ratio of diffracted power to the power at the field point that would have been incident in the absence of the absorbing screen is:

$$\frac{I}{I_0} = \frac{1}{2}\left[\frac{1}{2} - S(wx)(1 - S(wx)) - C(wx)(1 - C(wx))\right] \tag{2.82}$$

and the Fresnel diffraction parameter (Equation 1.18) is given by $\nu = wx$.

The results presented in Section 1.4.1.7 were generated using these equations.

2.8 *Geometrical theory of diffraction*

The scalar diffraction analysis neglects the vector nature of electromagnetic waves and the requirement that Maxwell's equations be satisfied. The problem of an aperture in a perfectly conducting screen enclosing the volume with the field point requires the inclusion of line currents along the aperture edge caused by the discontinuities in the vector fields across the aperture boundaries. Starting with the vector Green's theorem, the extension to electromagnetic wave diffraction becomes:[8]

$$\phi(\underline{\rho}) = \frac{e^{-jk\rho}}{\rho}$$

$$\underline{E}(\underline{r}') = -\frac{1}{4\pi}\left[\int_{S_1}\left(\underline{E}(\underline{\rho})\hat{n}\cdot\nabla\left(\frac{e^{-jk\rho}}{\rho}\right) - \frac{e^{-jk\rho}}{\rho}\hat{n}\cdot\nabla\underline{E}(\underline{\rho})\right)_1 d\mathbf{S}\right. \tag{2.83}$$

$$\left. -\frac{1}{jwe}\oint_{\text{Edge}}\underline{H}(\underline{\rho})\cdot\hat{n}\nabla\left(\frac{e^{-jk\rho}}{\rho}\right)d\mathbf{l} - \oint_{\text{Edge}}\left(\frac{e^{-jk\rho}}{\rho}\right)\underline{E}(\underline{\rho})\times\hat{n}d\mathbf{l}\right.$$

To compute the field at points interior to the bounding surface, the fields on the conducting screen and aperture must be determined. This is generally done by solving the electromagnetic wave boundary value problem to determine the field incident on the aperture and conducting screen.

The geometrical theory of diffraction (GTD) combines geometrical optics and canonical calculations of electromagnetic diffraction problems available in the literature. For propagation between two points, ray tracing is used to connect the direct ray (if there is one) between the source and field point, reflected rays from surfaces, and diffracted rays from edges and discontinuities in electrical parameters.[2] In the case of reflection, the incident ray is treated locally as a plane wave incident at the point of reflection. The power associated with each ray is calculated from the geometrical spreading of the ray from each point source, additional spreading due to gradients in the index of refraction, added divergence of the rays caused by reflection from a curved surface, and loss due to diffraction.

One of the canonical diffraction problems is diffraction by a wedge. Figure 2.12 describes a wedge in a plane normal to its edge along the z axis. The source is at an angle ϕ_S and the field point is at ϕ_F from the x axis. The wedge has an included angle of $W = (2-n)\pi$ in radians. For oblique

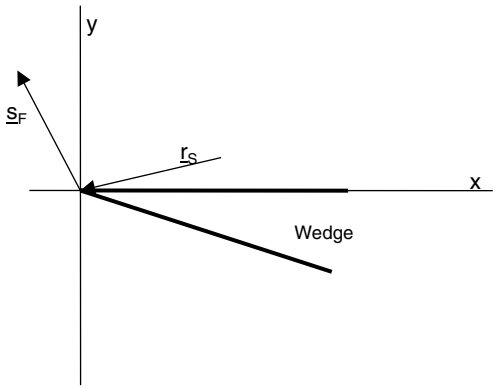

Figure 2.12 Wedge diffraction geometry.

incidence on the wedge, the source is at an angle β_S from the z axis in the plane of incidence and the field point is at β_F from the z axis in the plane of diffraction. Fermat's principle extended to the diffraction problem equates β_S and β_F.[2] The equation for the diffracted wave is:

$$\underline{E}^d(\underline{s}_F) = \underline{\underline{D}}(\beta_S, \phi_S, \phi_F) \cdot \underline{E}^i(\underline{r}_S) A(r_S, s_F) e^{-jks_F} \tag{2.84}$$

or, in matrix form:

$$\begin{pmatrix} E_\perp^d \\ E_{||}^d \end{pmatrix} = \begin{pmatrix} D_\perp & 0 \\ 0 & D_{||} \end{pmatrix} \begin{pmatrix} E_\perp^i \\ E_{||}^i \end{pmatrix} A(r_S, s_F) e^{-jks_F} \tag{2.85}$$

The diffraction coefficients are:

$$\begin{aligned} A &= \sqrt{\frac{r_S}{s_F(r_S + s_F)}} \\ L &= \frac{r_S s_F \sin^2(\beta_S)}{r_S + s_F} \\ D_\perp &= D^i(\phi_F - \phi_S) \frac{2\sqrt{L}}{\sin(\beta_S)} \frac{e^{-jk(r_S - L)}}{\sqrt{r_S}} \\ D_{||} &= D^d(\phi_F + \phi_S) \frac{2\sqrt{L}}{\sin(\beta_S)} \frac{e^{-jk(r_S - L)}}{\sqrt{r_S}} \end{aligned} \tag{2.86}$$

where

$$\begin{aligned} D^i(\phi_F - \phi_S) = & -\frac{e^{-j\frac{\pi}{4}}}{2n\sqrt{2\pi k}} \left[\cot\left(\frac{\pi + \phi_F - \phi_S}{2n} \right) F^+(\phi_F - \phi_S) \right. \\ & \left. + \cot\left(\frac{\pi - (\phi_F - \phi_S)}{2n} \right) F^-(\phi_F - \phi_S) \right] \\ D^d(\phi_F - \phi_S) = & -\frac{e^{-j\frac{\pi}{4}}}{2n\sqrt{2\pi k}} \left[\cot\left(\frac{\pi + \phi_F + \phi_S}{2n} \right) F^+(\phi_F + \phi_S) \right. \\ & \left. + \cot\left(\frac{\pi - (\phi_F + \phi_S)}{2n} \right) F^-(\phi_F + \phi_S) \right] \end{aligned} \tag{2.87}$$

for $N^{\pm}$ the positive, negative or 0 integer closest to the solution of the following:

$$2n\pi N^{+} - \left(\phi_F \pm \phi_S\right) = \pi$$

$$2n\pi N^{-} - \left(\phi_F \pm \phi_S\right) = -\pi$$

$F^{\pm}$ may be found from:

$$B^{+}(\phi_F \pm \phi_S) = \sqrt{kr_S\left(1 + \cos(\phi_F \pm \phi_S) - 2\pi n N^{+}\right)}$$

$$B^{-}(\phi_F \pm \phi_S) = \sqrt{kr_S\left(1 + \cos(\phi_F \pm \phi_S) + 2\pi n N^{-}\right)}$$

$$F^{+}(\phi_F \pm \phi_S) = j2B^{+}(\phi_F \pm \phi_S)e^{j\left(B^{+}(\phi_F \pm \phi_S)\right)^2} \int_{B^{+}(\phi_F \pm \phi_S)}^{\infty} e^{-jt^2}dt \tag{2.88}$$

$$F^{-}(\phi_F \pm \phi_S) = j2B^{-}(\phi_F \pm \phi_S)e^{j\left(B^{-}(\phi_F \pm \phi_S)\right)^2} \int_{B^{-}(\phi_F \pm \phi_S)}^{\infty} e^{-jt^2}dt$$

where the integral may be evaluated using Fresnel integrals. Balanis[2] has provided a Fortran program to compute the diffraction coefficients given in Equation 2.87 in Chapter 11 of his text.

The diffracted wave generates only one of the rays to be considered in the geometrical optics analysis of diffraction from a wedge. A direct ray may propagate from the source to the observer. A reflected ray may also be present with reflection on the side of the wedge illuminated by the source. Other scattering obstacles may be present that produce additional reflected or diffracted rays. Note that in contrast to the solution for Fresnel diffraction by a knife-edge absorbing screen, where the complete field in the interference region ($n < 0$ in Figure 1.23) is obtained from Equation 2.82, in GTD, the interference between the direct ray and the diffracted ray must be evaluated explicitly. By breaking the problem into its component rays and evaluating the vector field produced by each ray, the effects of varying the transmitter and receiver antenna patterns on the transmission loss between the source and receiver may be readily evaluated.

2.9 List of symbols

Symbol	Quantity	Units	Equation
$\underline{H}$	Magnetic field intensity (vector)	A/m	2.1
$\underline{E}$	Electric field intensity (vector)	V/m	2.1
$\underline{D}$	Electric flux density (vector)	C/m^2	2.1
$\underline{B}$	Magnetic flux density (vector)	T or Wb/m^2	2.1
J	Current density (vector)	A/m^2	2.1
$\underline{r}$	Position vector	m	2.1
$\underline{\underline{\varepsilon}}$	Permittivity tensor	F/m = C/V/m	2.4
$\underline{\underline{\mu}}$	Permeability tensor	H/m = Vs/m	2.4
$\underline{\underline{\sigma}}$	Conductivity tensor	S/m	2.4
$\underline{u}$	Velocity of the free charges	m/s	2.4
$\hat{n}$	Unit vector normal to a surface		2.3
$\underline{H}$	Steady state magnetic field intensity (vector)	A/m	2.6
$\underline{E}$	Steady state electric field intensity (vector)	V/m	2.6
$\underline{D}$	Steady state electric flux density (vector)	C/m^2	2.6
$\underline{B}$	Steady state magnetic flux density (vector)	T or Wb/m^2	2.6
$\underline{J}$	Steady state current density (vector)	A/m^2	2.6
$\underline{A}$	Vector potential		2.25
c	Speed of light in free space = 3×10^8 m/s	m/s	2.14
$\underline{E}_{\mathrm{L}}$	Complex $\underline{E}$ for left hand circular polarization	V/m	2.22
$\underline{E}_{\mathrm{R}}$	Complex $\underline{E}$ for right hand circular polarization	V/m	2.22
$\underline{E}_{\xi}$	Complex $\underline{E}$ for linear polarization	V/m	2.22
$\underline{E}_{\psi}$	Complex $\underline{E}$ for linear polarization	V/m	2.22
$\underline{E}_{\perp}$	Comples $\underline{E}$ perpendicular to plane of incidence		2.41
$\underline{E}_{\shortparallel}$	Comples $\underline{E}$ parallel with the plane of incidence		2.45
f	Frequency	Hz	2.5
$G(\underline{r};\underline{r}')$	Free space Green's function		2.32
k	Wavenumber	1/m	2.11
k_0	Free space wavenumber	1/m	2.12
L	Electrical path length	m	2.51
L_{P}	Phase path length	m	2.56
L_{S}	Physical path length	m	2.56
n	Complex index of refraction		2.14
R	Reflectivity		2.46
$\underline{S}$	Poynting vector	W/m^2	2.19
S	Position along a ray		2.54
S	Complex scalar function of position	m	2.47
t	Time	s	2.1
T	Transmissivity		2.46
t_{P}	Phase delay	s	2.58
v_{P}	Phase velocity	m/s	2.12

(continued)

2.9 List of symbols (continued)

Symbol	Quantity	Units	Equation
$\Gamma_\perp$, $\Gamma_\parallel$	Plane wave reflection coefficients		2.41, 2.42
a	Elevation angle		2.61
α_0	Initial elevation angle		2.70
α_T	True elevation angle		2.70
ε_o	Permittivity of free space = $1/36\pi \times 10^{-9}$ F/m	F/m	2.12
ε_r	Complex dielectric constant		2.14
ϕ_E	Electric scalar potential		2.26
h	Characteristic impedance of the medium	W	2.18
η_0	Free space impedance = 377 Ω	W	2.18
κ_m	Relative permeability		2.14
l	Wavelength	m	2.12
λ_0	Free space wavelength	m	2.12
μ_o	Permeability of free space = $4\pi \times 10^{-7}$ H/m	H/m	2.12
r	Charge density	C/m^3	2.1
r	Steady state charge density	C/m^3	2.6
$\tau_\perp$, $\tau_\parallel$	Plane wave transmission coefficients		2.41, 2.42
w	Radian frequency	rad/s	2.5
q	Central angle	r	2.63
d	Geometrical distance	μm	2.70
e	Elevation angle error	r	2.70
t	Ray bending	r	2.70
A_F	Focusing loss	dB	2.71
f	Scalar functions of position		2.74
y	Scalar functions of position		2.74
S,C	Fresnel integrals		2.82
D	Diffraction coefficients		2.86

References

1. Miner, G.F., *Lines and Electromagnetic Fields for Engineers*, Oxford University Press, New York, 1996.
2. Balanis, C.A., *Antenna Theory Analysis and Design*, Harper & Row, New York, 1982.
3. Panofsky, W.K.H. and Phillips, M., *Classical Electricity and Magnetism*, Addison-Wesley, Reading, MA, 1962.
4. Born, M. and Wolf, E., *Principles of Optics*, 4th ed., Pergamon Press, New York, 1970.
5. Freehafer, J.E., Geometrical optics, in *Propagation of Short Radio Waves*, D.E. Kerr, Ed., Dover, New York, 1965.
6. Silver, S., Wavefronts and rays, in *Microwave Antenna Theory and Design*, S. Silver, Ed., Dover, New York, 1965.
7. Abramowitz, M. and Stegun, I.A., *Handbook of Mathematical Functions*, Dover, New York, 1965.
8. Stratton, J.A., *Electromagnetic Theory*, McGraw-Hill, New York, 1941.

chapter three

Absorption

3.1 Molecular absorption

Oxygen and water vapor molecules in the lower atmosphere interact with electromagnetic waves propagating through the atmosphere to produce both attenuation and phase delay relative to propagation in free space. The oxygen molecule has a permanent magnetic dipole moment, and the water vapor molecule has a permanent electric dipole moment. Each has a resonant interaction with the electromagnetic field, absorbing and emitting photons at microwave frequencies in response to quantum changes in rotational energy.[1] The frequency of each photon depends on the energy change between allowable quantum states. These frequencies are the absorption or emission lines. The lines are broadened by collisions between molecules at the higher pressures near the ground (often called pressure broadening), Doppler broadening at lower pressures much higher in the atmosphere, and Zeeman splitting for molecules with a permanent magnetic dipole moment at even higher altitudes in the presence of the Earth's magnetic field. In addition, quantum interference effects in the wings between closely spaced lines in frequency can increase broadening.

3.1.1 Complex index of refraction

The complex index of refraction of the atmosphere is related to the radio refractivity, N', and specific attenuation, α, by:[2]

$$\begin{aligned} n-1 &= N\times 10^{-6} = \left(N' - jN''\right)\times 10^{-6} \\ N'(f) &= N_0 + N'_D(f) + N'_W(f) \\ \alpha &= 0.182 f N''(f) = 0.182 f\left(N''_D(f) + N''_W(f)\right) \end{aligned} \tag{3.1}$$

where f is frequency (GHz), N' the refractivity (ppm or N units), N_0 the average radio refractivity, N'_D the deviation from N_0 due to dry gases, N'_W the deviation from N_0 due to water vapor, and α the specific attenuation

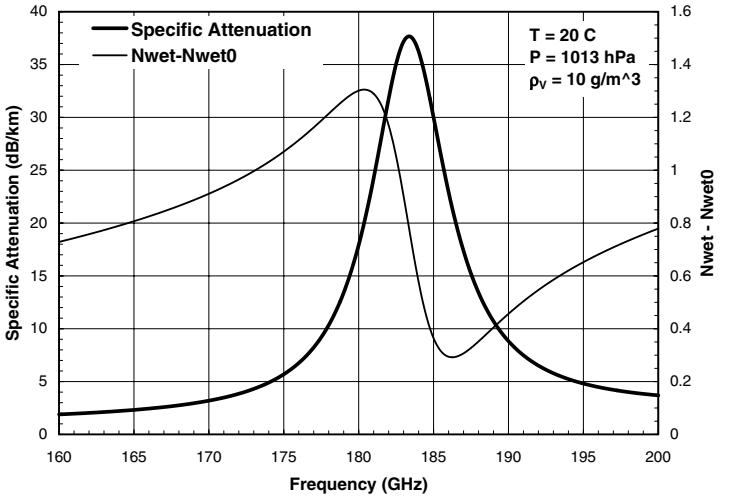

Figure 3.1 Water vapor line shape near 183 GHz.

(dB/km). In addition, trace constituents may contribute to the complex index of refraction in the 0.3 to 300 GHz frequency range, but their effect is negligible in comparison to the effects of molecular oxygen and water vapor.

3.1.1.1 *Water vapor*

Absorption and refraction by water vapor have the absorption line shape and anomalous dispersion characteristics presented in Figure 3.1. The broadened water vapor line at 183.3 GHz is an isolated line. The wings of the absorption line, the region away from the line center and above the apparent baseline level between 160 and 200 GHz, are in evidence. The dispersion curve, labeled Nwet – Nwet0, continues to show line-broadening effects over the entire displayed range of frequencies. The real and imaginary parts of the complex index of refraction are obtained by summing the contributions of the far wings of a large number of lines at different frequencies. The equations for the refractivity (ppm or N units) caused by water vapor are:[2]

$$
\begin{aligned}
N'_W &= N'_b + \sum_{i=1}^{n_b} S_i^b F_i'^b \\
N'_b &= 0.998 f^2 P_V \theta^{2.7} (1 - 0.2\theta) \times 10^{-6} \\
S_i^b &= b_{1i} \times 10^{-1} P_V \theta^{3.5} e^{b_{2i}(1-\theta)} \\
F_i'^b &= \frac{\nu_{0i} - f}{(\nu_{0i} - f)^2 + \gamma_i^2} + \frac{\nu_{0i} + f}{(\nu_{0i} + f)^2 + \gamma_i^2} - \frac{2}{\nu_{0i}} \\
\gamma_i &= b_{3i} \times 10^{-4} \left(p\theta^{b_{4i}} + b_{5i} P_V \theta^{b_{6i}} \right)
\end{aligned}
\tag{3.2}
$$

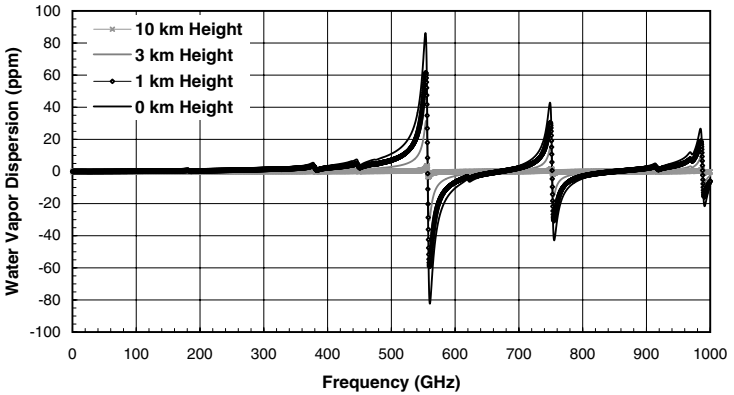

Figure 3.2 Anomalous dispersion about water vapor lines below 1000 GHz.

where p is dry gas pressure (hPa); P_V the water vapor pressure (hPa); $P = p + P_V$ the total pressure; $\theta = {}^{300}/_{T}$, where T is temperature (K); n_b the number of absorption lines used in the summation; ν_{0i} the center frequency for line i; and b_{1i} to b_{6i} the parameters for line i (see Table 3.2). The line parameters were obtained experimentally for the assumed line shape. N_b is the continuum term that represents the additional contributions from lines at frequencies above 1000 GHz. It was also obtained experimentally.[2] Figure 3.2 presents the dispersion curves for the frequency range from 0.25 to 1000 GHz for four heights in the ITU-R model atmosphere (Table 3.1). The anomalous dispersion extremes about the three strongest lines amount to up to one quarter of the total radio refractivity at each height.

The specific attenuation for water vapor is found from:

$$\begin{aligned}
\alpha_W &= 0.1820 f N''_W(f) \\
N''_W &= N''_b + \sum_{i=1}^{n_b} S_i^b F_i''^b \\
N''_b &= f P_V \theta^3 \left(3.53 P_V \theta^{7.5} + 0.113 p\right) \times 10^{-7} \\
F_i''^b &= \frac{f}{\nu_{0i}} \left(\frac{\gamma_i}{\left(\nu_{0i} - f\right)^2 + \gamma_i^2} + \frac{\gamma_i}{\left(\nu_{0i} + f\right)^2 + \gamma_i^2} \right)
\end{aligned} \tag{3.3}$$

where the line strength and line width values are given in Equation 3.2 and the line parameters are given in Table 3.2. The line strengths are proportional to the b_1 line parameter. Figure 3.3 presents the water vapor absorption spectrum for frequencies below 1000 GHz. The three strongest lines produce attenuations well in excess of 1000 dB/km at heights lower than 3 km and

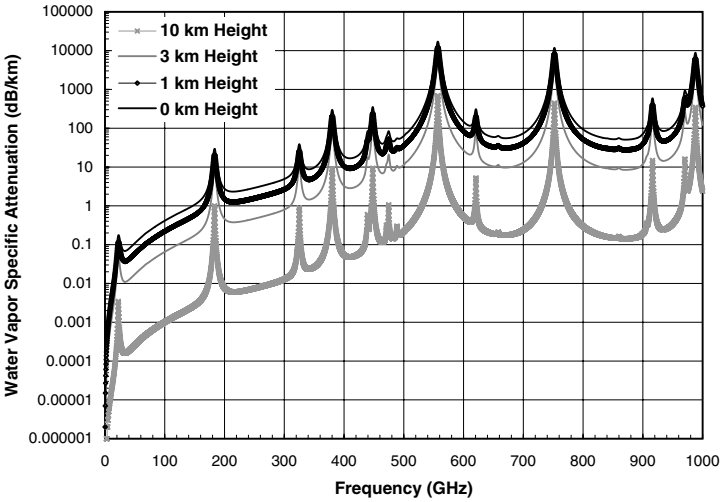

Figure 3.3 Water vapor absorption below 1000 GHz.

Table 3.1 ITU-R Model Atmosphere

Height (km)	Pressure (hPa)	Temperature (°C)	Water vapor density (g/m^3)	N_0 (ppm)
0	1013.2	15.0	7.5	318
1	898.7	8.9	4.6	275
3	701.0	–4.5	1.7	213
10	264.3	–50.0	0.05	92

water vapor densities above 4 g/m^3. Strong lines, which produce extreme specific attenuation values, are needed to produce significant dispersion.[1]

A large number of even stronger lines occur at frequencies above 1000 GHz.[3] These lines give rise to the continuum region between the lines obvious in Figure 3.2. The specific attenuation due to water vapor approaches zero at zero frequency. The lowest frequency water vapor line at 22.235 GHz produces an attenuation lower than 0.2 dB/km for standard conditions at the surface (Table 3.1).

3.1.1.2 Molecular oxygen

Molecular oxygen has more than 44 absorption lines in the 0- to 1000-GHz frequency range. Table 3.3 lists 37 of the stronger lines within the 50- to 70-GHz frequency band and 7 more above 100 GHz. The closely packed lines in the 50- to 70-GHz band require a correction to the line shape employed for water vapor absorption to account for line overlap. The equations for refractivity (ppm or N units) caused by molecular oxygen are:[2]

$$
\begin{aligned}
N'_D &= N'_a + \sum_{i=1}^{n_a} S_i^a F_i'^a \\
N'_a &= -6.14 p\theta^2 \left(\frac{f^2}{f^2 + d^2} \right) \times 10^{-5} \\
d &= 5.6 \times 10^{-4} \left(p + 1.1 P_V \right) \theta \\
S_i^a &= a_{1i} \times 10^{-7} p \theta^3 e^{a_{2i}(1-\theta)} \\
F_i'^a &= \frac{\left(\nu_{0i} - f \right) + \delta\gamma_i \left(\frac{f}{\nu_{0i}} \right)}{\left(\nu_{0i} - f \right)^2 + \gamma_i^2} + \frac{\left(\nu_{0i} + f \right) - \delta\gamma_i \left(\frac{f}{\nu_{0i}} \right)}{\left(\nu_{0i} + f \right)^2 + \gamma_i^2} - \frac{2}{\nu_{0i}} \\
\gamma_i &= a_{3i} \times 10^{-4} \left(p\theta^{(0.8 - a_{4i})} + 1.1 P_V \theta \right) \\
\delta &= \left(a_{5i} + a_{6i} \right) \times 10^{-4} p \theta^{0.8}
\end{aligned}
\tag{3.4}
$$

where d is the width frequency (Debye width) in the Debye formula for the complex index of refraction of nonresonant dry gases and δ is the correction for interference effects due to line overlap. The line parameters, a_{1i} to a_{6i}, are listed in Table 3.3. The anomalous dispersion produced by an isolated absorption line is displayed in Figure 3.4. The dispersion for frequencies up to 1000 GHz is shown in Figure 3.5 for the heights in the ITU-R model atmosphere listed in Table 3.1.

The specific attenuation produced by nonresonant absorption and by the absorption lines is given by:

$$
\begin{aligned}
\alpha_D &= 0.1820 f N''_D(f) \\
N''_D &= N''_a + \sum_{i=1}^{n_a} S_i^a F_i''^a \\
N''_a &= f p \theta^2 \left(6.14 \times 10^{-5} \left(\frac{d}{f^2 + d^2} \right) + 1.4 \times 10^{-12} \left(1 - 1.2 \times 10^{-5} f^{1.5} \right) p \theta^{1.5} \right) \\
F_i''^b &= \frac{f}{\nu_{0i}} \left(\frac{\gamma_i - \delta\left(\nu_{0i} - f \right)}{\left(\nu_{0i} - f \right)^2 + \gamma_i^2} + \frac{\gamma_i - \delta\left(\nu_{0i} + f \right)}{\left(\nu_{0i} + f \right)^2 + \gamma_i^2} \right)
\end{aligned}
\tag{3.5}
$$

where the line strength, line width, Debye width, and interference correction are given in Equation 3.4. The absorption spectrum is presented in Figure 3.6.

Table 3.2 Empirical Line Parameters for Water Vapor

Line frequency (GHz)	b_1	b_2	b_3	b_4	b_5	b_6
22.235080	0.1090	2.143	28.11	0.69	4.80	1.00
67.813960	0.0011	8.735	28.58	0.69	4.93	0.82
119.995941	0.0007	8.356	29.48	0.70	4.78	0.79
183.310074	2.3000	0.668	28.13	0.64	5.30	0.85
321.225644	0.0464	6.181	23.03	0.67	4.69	0.54
325.152919	1.5400	1.540	27.83	0.68	4.85	0.74
336.187000	0.0010	9.829	26.93	0.69	4.74	0.61
380.197372	11.9000	1.048	28.73	0.69	5.38	0.84
390.134508	0.0044	7.350	21.52	0.63	4.81	0.55
437.346667	0.0637	5.050	18.45	0.60	4.23	0.48
439.150812	0.9210	3.596	21.00	0.63	4.29	0.52
443.018295	0.1940	5.050	18.60	0.60	4.23	0.50
448.001075	10.6000	1.405	26.32	0.66	4.84	0.67
470.888947	0.3300	3.599	21.52	0.66	4.57	0.65
474.689127	1.2800	2.381	23.55	0.65	4.65	0.64
488.491133	0.2530	2.853	26.02	0.69	5.04	0.72
503.568532	0.0374	6.733	16.12	0.61	3.98	0.43
504.482692	0.0125	6.733	16.12	0.61	4.01	0.45
556.936002	510.0000	0.159	32.10	0.69	4.11	1.00
620.700807	5.0900	2.200	24.38	0.71	4.68	0.68
658.006500	0.2740	7.820	32.10	0.69	4.14	1.00
752.033227	250.0000	0.396	30.60	0.68	4.09	0.84
841.073593	0.0130	8.180	15.90	0.33	5.76	0.45
859.865000	0.1330	7.989	30.60	0.68	4.09	0.84
899.407000	0.0550	7.917	29.85	0.68	4.53	0.90
902.555000	0.0380	8.432	28.65	0.70	5.10	0.95
906.205524	0.1830	5.111	24.08	0.70	4.70	0.53
916.171582	8.5600	1.442	26.70	0.70	4.78	0.78
970.315022	9.1600	1.920	25.50	0.64	4.94	0.67
987.926764	138.0000	0.258	29.85	0.68	4.55	0.90

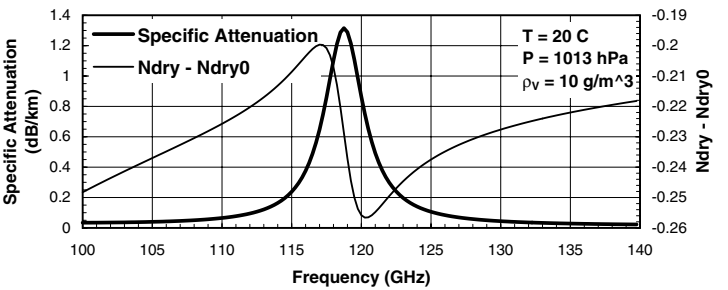

Figure 3.4 Molecular oxygen line shape near 118 GHz.

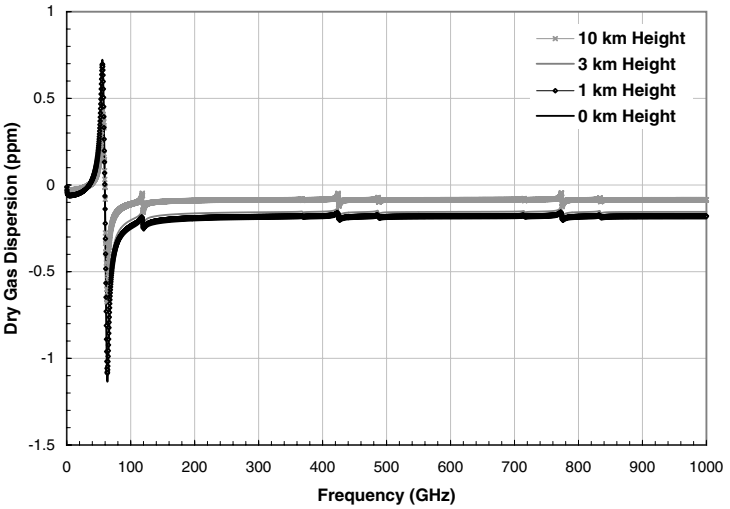

Figure 3.5 Anomalous dispersion about oxygen lines below 1000 GHz.

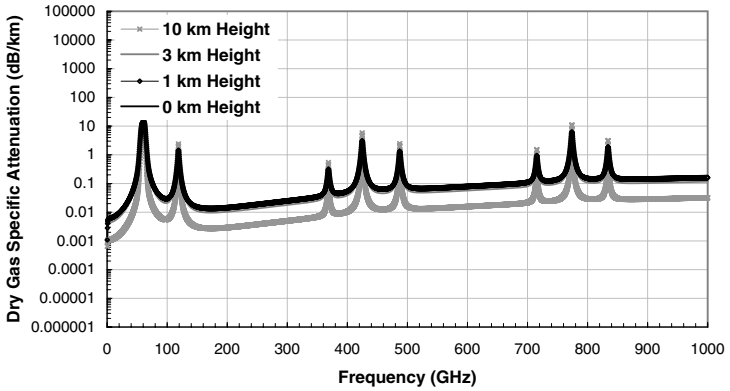

Figure 3.6 Oxygen absorption below 1000 GHz.

The 50- to 70-GHz band of absorption lines is displayed in Figure 3.7. Pressure broadening has smoothed out the contributions of the individual lines at heights below 10 km or pressures higher than 260 hPa (see Table 3.1). A specific attenuation of more than 2 dB/km is still present at the line centers between 57 and 63 GHz at a height of 30 km.

3.1.2 *Approximate models*

3.1.2.1 *ITU-R model*

Approximate models that provide for easier calculation of surface conditions are available. The ITU-R provides a means to obtain the specific attenuation

Table 3.3 Empirical Line Parameters for Dry Gases

Line frequency (GHz)	a_1	a_2	a_3	a_4	a_5	a_6
50.474238	0.94	9.694	8.60	0	1.600	5.520
50.987749	2.46	8.694	8.70	0	1.400	5.520
51.503350	6.08	7.744	8.90	0	1.165	5.520
52.021410	14.14	6.844	9.20	0	0.883	5.520
52.542394	31.02	6.004	9.40	0	0.579	5.520
53.066907	64.10	5.224	9.70	0	0.252	5.520
53.595749	124.70	4.484	10.00	0	–0.066	5.520
54.130000	228.00	3.814	10.20	0	–0.314	5.520
54.671159	391.80	3.194	10.50	0	–0.706	5.520
55.221367	631.60	2.624	10.79	0	1.151	5.514
55.783802	953.50	2.119	11.10	0	–0.920	5.025
56.264775	548.90	0.015	16.46	0	2.881	–0.069
56.363389	1344.00	1.660	11.44	0	–0.596	4.750
56.968206	1763.00	1.260	11.81	0	–0.556	4.104
57.612484	2141.00	0.915	12.21	0	–2.414	3.536
58.323877	2386.00	0.626	12.66	0	–2.635	2.686
58.446590	1457.00	0.084	14.49	0	6.848	–0.647
59.164207	2404.00	0.391	13.19	0	–6.032	1.858
59.590983	2112.00	0.212	13.60	0	8.266	1.413
60.306061	2124.00	0.212	13.82	0	–7.170	0.916
60.434776	2461.00	0.391	12.97	0	5.664	–2.323
61.150560	2504.00	0.626	12.48	0	1.731	–3.039
61.800154	2298.00	0.915	12.07	0	1.738	–3.797
62.411215	1933.00	1.260	11.71	0	–0.048	–-4.277
62.486260	1517.00	0.083	14.68	0	–4.290	0.238
62.997977	1503.00	1.665	11.39	0	0.134	–4.860
63.568518	1087.00	2.115	11.08	0	0.541	–-5.079
64.127767	733.50	2.620	10.78	0	0.814	–5.525
64.678903	463.50	3.195	10.50	0	0.415	–5.520
65.224071	274.80	3.815	10.20	0	0.069	–5.520
65.764772	153.00	4.485	10.00	0	–0.143	–5.520
66.302091	80.09	5.225	9.70	0	–0.428	–5.520
66.836830	39.46	6.005	9.40	0	–0.726	–5.520
67.369598	18.32	6.845	9.20	0	–1.002	–5.520
67.900867	8.01	7.745	8.90	0	–1.255	–5.520
68.431005	3.30	8.695	8.70	0	–1.500	–5.520
68.960311	1.28	9.695	8.60	0	–1.700	–5.520
118.750343	945.00	0.009	16.30	0	–0.247	0.003
368.498350	67.90	0.049	19.20	0.6	0	0
424.763124	638.00	0.044	19.16	0.6	0	0
487.249370	235.00	0.049	19.20	0.6	0	0
715.393150	99.60	0.145	18.10	0.6	0	0
773.839675	671.00	0.130	18.10	0.6	0	0
834.145330	180.00	0.147	18.20	0.6	0	0

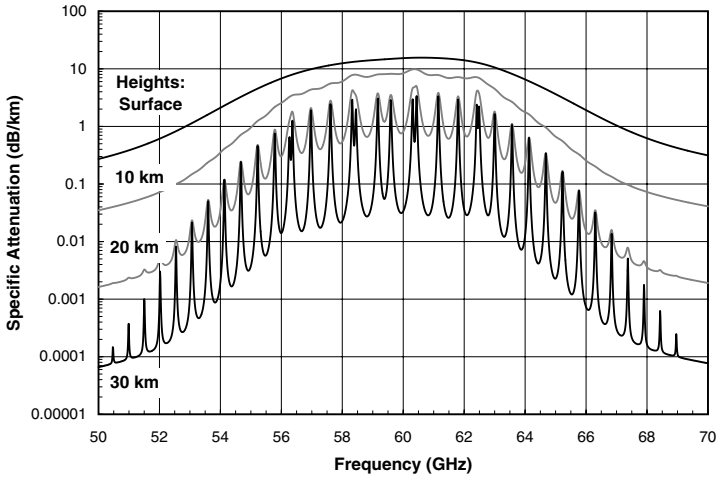

Figure 3.7 Oxygen line fine structure between 50 and 70 GHz.

in the window regions and at isolated lines.[4] It was obtained by fitting curves to the line summation model calculation procedure presented previously. The expression for the specific attenuation due to water vapor for surface temperature and pressure as listed in Table 3.1 is given, as a function of water vapor density, ρ_V, by:[4]

$$\alpha_W = f^2 \rho_V \times 10^{-4} \left(0.05 + 0.0021\rho_V + \frac{3.6}{(f-22.2)^2 + 8.5} + \frac{10.6}{(f-183.3)^2 + 9.0} + \frac{8.9}{(f-325.4)^2 + 23.6} \right) \tag{3.6}$$

for frequencies less than 350 GHz. The specific attenuation due to oxygen is given by:

$$\alpha_D = f^2 \times 10^{-3} \left(7.19 \times 10^{-3} + \frac{6.09}{f^2 + 0.227} + \frac{4.81}{(f-57)^2 + 1.5} \right) \tag{3.7a}$$

for $f < 57$ GHz and by:

$$\alpha_D = (f+198)^2 \times 10^{-3} \left(3.79 \times 10^{-7} f + \frac{0.265}{(f-63)^2 + 1.59} + \frac{0.028}{(f-118)^2 + 1.47} \right) \tag{3.7b}$$

for frequencies above 63 GHz. The total specific attenuation for surface conditions is given by $\alpha = \alpha_W + \alpha_D$ (dB/km).

3.1.2.2 *Regression model*

An alternative approach is to calculate the specific attenuation for the expected range of atmospheric variables and perform a multivariate regression analysis of the calculations on relevant atmospheric variables. Radiosonde data have been collected globally for many years. To represent global meteorological conditions, 220 profiles were selected from the large collection of available observations subject to the constraint that the reduced sample set have the same means and standard deviations as the full data set at the mandatory pressure reporting levels. The regression analysis produced the model:

$$\alpha = a + b\rho_V - cT \tag{3.8}$$

for each of the frequencies in Table 3.4. For this simplified model, ρ_V is surface water vapor density (g/m^3), T the surface temperature (°C), and α the result (dB/km).

The results of using both the linear regression model and the simplified ITU-R model are presented in Figure 3.8 for the standard surface conditions of 15°C, 7.5 g/m^3, and an implied surface pressure of 1013 hPa. The figure also presents the full line summation results described previously and the regression coefficients from Table 3.4. The regression model values closely match the ITU-R model results. The largest differences between the simplified model predictions and the full line calculations are in the atmospheric window between the complex of oxygen lines near 60 GHz and the isolated oxygen line at 119 GHz. At 94 GHz, the regression model predicts too high a specific attenuation by 24%; the ITU-R model predicts too high a value by 21%. The regression values were obtained using an earlier version of the line summation model, which employed a different line shape for water vapor and different empirically developed continuum corrections.[5] The earlier model matched the reported observations available through the late 1960s.[6] The newer line summation model developed by Liebe provides a better match to the larger set of measurements available through the late 1980s.[2]

The linear regression model provides a ready means to calculate the sensitivity of specific attenuation estimates to changes in surface temperature or surface water vapor density. An examination of Figure 3.8 or Table 3.4 reveals that the variation in specific attenuation with temperature is less than 0.1 dB/km for the entire expected –40°C to +40°C range of mid-latitude surface temperature values. Water vapor variations produce significant variations, accounting for nearly all the attenuation at frequencies above 10 GHz and below 50 GHz, frequencies in the window between 70 and 115 GHz, and frequencies above 120 GHz (see Figure 1.11 and Figure 1.12). The ITU-R model neglects any dependence on surface pressure and temperature while

Table 3.4 Global 220-Profile Regression Model for Surface-Specific Attenuation

Frequency (GHz)	a(f) (dB/km)	b(f) (dB/km/(g/m^3))	c(f) (dB/km/°C)	ITU-R model (dB/km)
1	5.8783E–03	1.7757E–05	5.1713E–05	5.2358E–03
4	8.0208E–03	1.4115E–04	8.5030E–05	7.8040E–03
6	8.2424E–03	3.0012E–04	8.9553E–05	9.1500E–03
12	8.9761E–03	1.3681E–03	1.0802E–04	1.7617E–02
15	9.5298E–03	2.6865E–03	1.2540E–04	2.7798E–02
16	9.7615E–03	3.4499E–03	1.3302E–04	3.3640E–02
20	1.2492E–02	1.2478E–02	1.0142E–04	1.0456E–01
22	1.8076E-02	2.2078E–02	1.2963E–04	1.8172E–01
24	1.6155E–02	2.0274E–02	5.6312E–05	1.6737E–01
30	1.7869E–02	1.0019E–02	2.8032E–04	8.8807E–02
35	2.6386E–02	1.0067E–02	3.6935E–04	9.6348E–02
41	4.9874E–02	1.2104E–02	6.2036E–04	1.3135E–01
45	8.9245E–02	1.4038E–02	1.0183E–03	1.7926E–01
50	2.6656E–01	1.7100E–02	2.5108E–03	3.5715E–01
70	4.4894E–01	3.1895E–02	4.4260E–03	6.2176E–01
80	1.6011E–01	3.9123E–02	1.2984E–03	4.3406E–01
90	1.1318E–01	4.9472E–02	7.4397E–04	4.7306E–01
94	1.0650E–01	5.4034E–02	6.4083E–04	5.0214E–01
110	1.1598E–01	7.4860E–02	6.4432E–04	6.6777E–01
115	2.0575E–01	8.2626E–02	1.8530E–03	7.9765E–01
140	1.2318E–01	1.2932E–01	3.7151E–04	1.0875E+00
160	1.5263E–01	2.0618E–01	7.8427E–04	1.6872E+00
200	2.2599E–01	3.6578E–01	1.6717E–03	2.9443E+00
220	2.2720E–01	3.1566E–01	1.7359E–04	2.5920E+00
240	2.5803E–01	3.5654E–01	–1.1886E–04	2.9339E+00
280	3.3657E–01	4.9670E–01	-6.6397E–05	4.0628E+00
300	3.7908E–01	6.2912E–01	8.0767E–04	5.0854E+00

considering only variations in water vapor density. Note that the allowable water vapor density is a function of air temperature because the saturation vapor pressure is a function of temperature (see Figure 1.44).

3.2 Absorption on a slant path

3.2.1 Attenuation

Absorption on a slant path may be calculated from the specific attenuation values obtained as a function of height from the temperature, pressure, and water vapor density values along the path. Calculations for a vertical path through the atmosphere from sea level are presented in Figure 3.9. The ITU-R

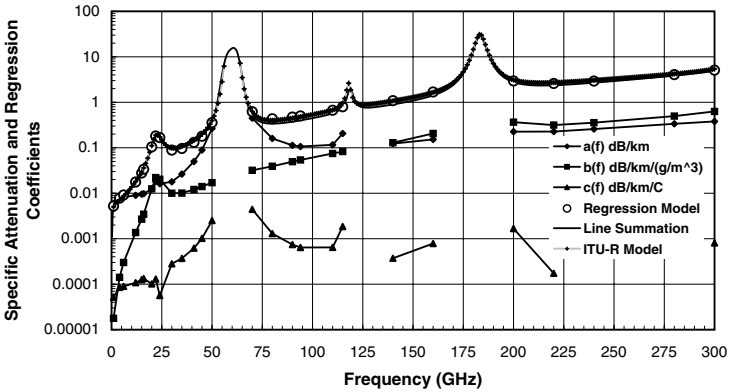

Figure 3.8 Specific attenuation models and regression coefficients.

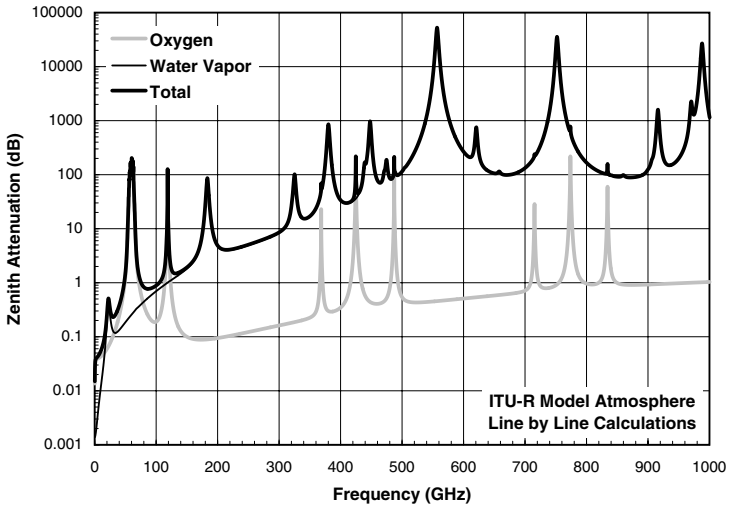

Figure 3.9 Zenith attenuation below 1000 GHz.

model atmosphere was used to provide pressure, temperature, and water vapor density as a function of height. The specific attenuation values at four different heights were presented in Figure 3.3 and Figure 3.6. The separate contributions of oxygen and water vapor are shown in Figure 3.9 together with the total attenuation for a zenith path.

Slant path attenuation can be calculated for elevation angles above 5° by using the cosecant law for propagation above a plane Earth:

$$A(\alpha) = \frac{A_Z}{\sin(\alpha)} \tag{3.9}$$

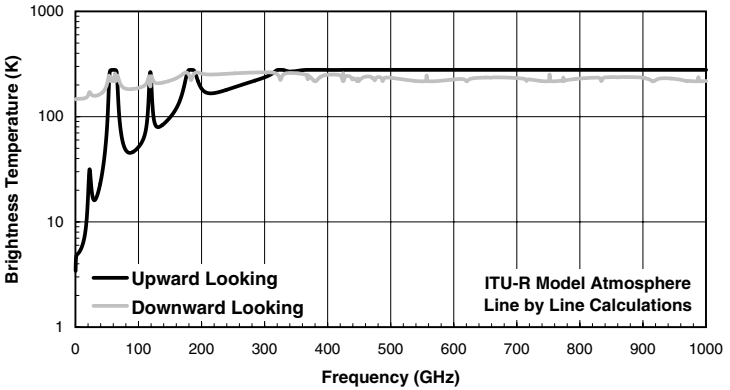

Figure 3.10 Brightness temperature below 1000 GHz.

where A is attenuation and α the elevation angle. At lower elevation angles, the slant path distance above a spherical Earth must be calculated. At elevation angles below about 2°, adjustment must be made for refraction. For elevation angles below 5°, the vertical variation of specific attenuation must also be considered (see Equation 3.11).

3.2.2 *Brightness temperature*

The brightness temperature is calculated using the radiative transfer equation (see Section 1.4.2.5). Calculations for a zenith path using the ITU-R model atmosphere are presented in Figure 3.10. Both the upward-looking sky brightness temperature and the downward-looking Earth brightness temperature values are presented. The emissivity of the Earth's surface for the downward-looking calculations was assumed to have the value 0.5 independent of frequency.

3.2.3 *Approximate models*

3.2.3.1 *ITU-R model*

The ITU-R model employs the approximate models for the specific attenuation of the dry gases and for water vapor at the surface times an effective path length through the atmosphere at an elevation angle, α, above 5°:[4]

$$A(\alpha) = \frac{\alpha_D h_D e^{-h/h_D} + \alpha_W h_W e^{-h/h_W}}{\sin(\alpha)} \tag{3.10}$$

where h is the height of the terminal above ground or surface level, the specific attenuation is given by Equation 3.6 and Equation 3.7, and the effective zenith path lengths for attenuation, h_W and h_D are given by:

$$h_W = h_{W0}\left(1 + \frac{3}{(f-22.3)^2+5} + \frac{5}{(f-183.3)^2+6} + \frac{2.5}{(f-325.4)^2+4}\right)$$

$$h_D = 6 \qquad ; f < 57 \text{ GHz} \tag{3.11}$$

$$h_D = 6 + \frac{40}{(f-118.7)^2+1} \qquad ; f > 63 \text{ GHz}$$

with h_W and h_D in kilometers, h_{W0} is 1.6 km for clear sky conditions and 2.1 km in rain. At lower elevation angles, the slant path distance above a spherical Earth must be calculated.

3.2.3.2 *Regression model*

An alternative approach is to calculate the zenith attenuation for the expected range of atmospheric variables and perform a multivariate regression analysis of the calculations on the relevant atmospheric variables measured at the surface. The 220-profile radiosonde database was used to calculate the regression coefficients (see Section 3.1.2.2). The regression analysis produced the model:

$$A_Z = a + b\rho_V - cT \tag{3.12}$$

for each of the frequencies in Table 3.5. For this simplified model, ρ_V is surface water vapor density (g/m^3), T the surface temperature (°C), and the result A_Z the zenith attenuation (dB).

The results of using the line-by-line summation calculations described in Section 3.2.1 and the approximate models presented in this section are shown in Figure 3.11.

3.2.3.3 *ACTS model*

The regression model presented previously employed a 220-profile data set drawn from a wide range of mid-latitude and tropical climates. The second-order statistics for the reduced data set matched the statistics obtained from a much larger data set that contained a decade of radiosonde data obtained by weather services globally. Regression analyses can also be tailored to a specific location by using a set of radiosonde observations from that location. As an aid for the calibration of the ACTS propagation experiment attenuation measurements, 106 clear-weather radiosonde profiles were selected from the twice-daily radiosonde ascents made during the first two years of the ACTS measurement program by the National Weather Service in Norman, OK. These profiles were used to calculate the medium temperature, the sky brightness temperature, and the gaseous absorption at the two frequencies employed for the ACTS beacon measurements of path attenuation.

Table 3.5 Global 220-Profile Regression Model Zenith Attenuation

Frequency (GHz)	a(f) (dB)	b(f) (dB/(g/m^3))	c(f) (dB/°C)	ITU-R model (dB)
1	3.3446E–02	2.7551E–06	1.1189E–04	2.9922E–02
4	3.9669E–02	2.7599E–04	1.7620E–04	3.8371E–02
6	4.0448E–02	6.5086E–04	1.9645E–04	4.1735E–02
12	4.3596E–02	3.1786E–03	3.1470E–04	6.2183E–02
15	4.6138E–02	6.3384E–03	4.5527E–04	8.5676E–02
16	4.7195E–02	8.2112E–03	5.3568E–04	9.8887E–02
20	5.6047E–02	3.4557E–02	1.5508E–03	2.7275E–01
22	7.5989E–02	7.8251E–02	3.0978E–03	5.2081E–01
24	6.9102E–02	5.9116E–02	2.4950E–03	4.2827E–01
30	8.5021E–02	2.3728E–02	1.3300E–03	2.4444E–01
35	1.2487E–01	2.3681E–02	1.4860E–03	2.9273E–01
41	2.3683E–01	2.8402E–02	2.1127E–03	4.5276E–01
45	4.2567E–01	3.2766E–02	2.9945E–03	7.0457E–01
50	1.2671E+00	3.9155E–02	5.7239E–03	1.7872E+00
70	2.1403E+00	7.3246E–02	1.0436E–02	2.6826E+00
80	7.0496E–01	9.5860E–02	5.8635E–03	9.7060E–01
90	4.5760E–01	1.2185E–01	5.7369E–03	8.7788E–01
94	4.1668E–01	1.3320E–01	5.9439E–03	9.0717E–01
110	4.3053E–01	1.8465E–01	7.8499E–03	1.3588E+00
115	8.9351E–01	2.0292E–01	1.1297E–02	3.4972E+00
140	3.6788E–01	3.1894E–01	1.1941E–02	1.8040E+00
160	4.1446E–01	5.0635E–01	1.9078E–02	2.7310E+00
200	5.6172E–01	8.9655E–01	3.3943E–02	5.1337E+00
220	5.4358E–01	7.7720E–01	2.7580E–02	4.4434E+00
240	6.0124E–01	8.7887E–01	3.0693E–02	4.9874E+00
280	7.5941E–01	1.2220E+00	4.2753E–02	6.8652E+00
300	8.5290E–01	1.5400E+00	5.5148E–02	8.8358E+00

The regression equations for medium temperature are:

$$\begin{aligned} Tmed_{20.2} &= 261 + 1.68\rho_V + 0.18T \\ Tmed_{27.5} &= 258 + 1.80\rho_V + 0.17T \end{aligned} \tag{3.13}$$

where $Tmed$ is the effective medium temperature (K), with T the surface air temperature (°C) and ρ_V the surface water vapor density (g/m^3). The equations for sky brightness temperature are:

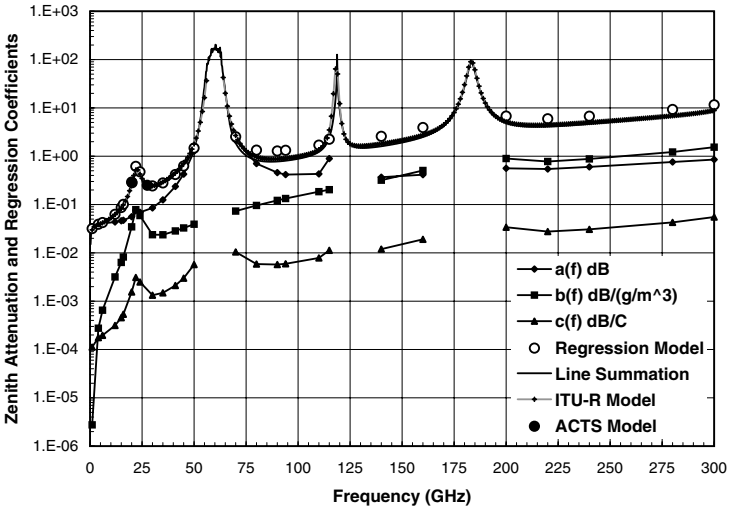

Figure 3.11 Zenith attenuation models and regression coefficients.

$$T_{B20.2} = \left(7.6\frac{P}{974} + 2.32\rho_V + 0.046T - 0.68\right)\frac{\sin(\alpha_N)}{\sin(\alpha)}$$
$$T_{B27.5} = \left(8.8\frac{P}{974} + 1.80\rho_V + 0.025T - 0.37\right)\frac{\sin(\alpha_N)}{\sin(\alpha)} \quad (3.14)$$

where P is the surface pressure (total) (hPa), α the elevation angle for the path, and α_N is 49.1°, the elevation angle to ACTS in Norman, OK. The path attenuation is obtained from Equation 1.49.

Figure 3.12 presents the model estimates for slant path attenuation for average mid-latitude conditions at the surface. For frequencies below 70 GHz, the models agree. At higher frequencies, the regression model predicts higher window attenuation values than do the other models. This difference is caused because of using an earlier version of line shape for the water vapor absorption lines and an earlier estimate of the continuum contributions.[5] The local regression model developed for the ACTS propagation experiment matched the other models at 20.2 and 27.8 GHz.

3.2.4 Specific attenuation profiles

3.2.4.1 June 4, 1996

An estimate of slant path attenuation requires an estimate of specific attenuation along the path. The line-by-line calculations presented in Figure 3.12 used the ITU-R model atmosphere to provide an estimate of the temperature, pressure, and water vapor density as a function of height along the path. The ITU-R model assumed exponential decreases in water vapor density

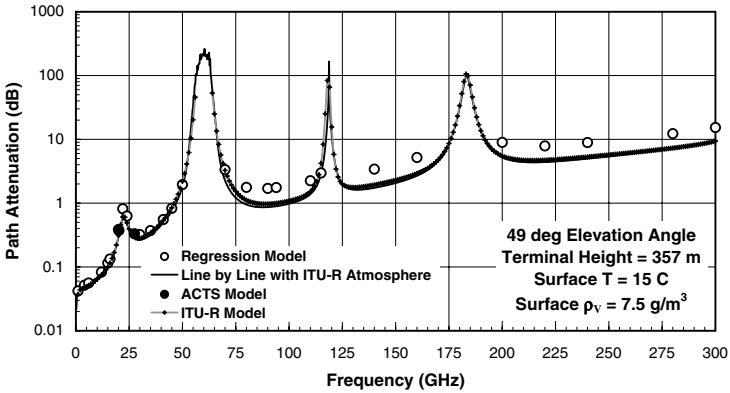

Figure 3.12 Path attenuation model predictions.

and dry gas density with height. The ACTS model and the regression model used different collections of radiosonde data to provide measured values of temperature, pressure, and water vapor density as a function of height. Figure 1.41 gives water vapor density measurements as a function of height obtained from two radiosonde soundings made in Norman, OK, on June 4, 1996, at 00:00 and 12:00 UT. The corresponding air temperature values are shown in Figure 1.45. Given air temperature and water vapor density as a function of height, the air pressure may be estimated by using the hydrostatic equation (Equation 1.26).

The specific attenuation profiles due to the dry gases (oxygen), water vapor, and their sum (total) are presented in Figure 3.13 for June 4, 1996, and for June 5, 1996, at 00:00 UT. A radiosonde balloon rises at about 300 m/min, so the soundings are not instantaneous observations but represent measurements made over several tens of minutes. The observations are usually started before the indicated hour. The measured path attenuation values for this day are displayed in Figure 3.14. The path attenuation values calculated from the specific attenuation profiles in Figure 3.13 are indicated by the symbol identified as RAOB (for radiosonde observation). The slant path from Norman, OK, to ACTS was at a 49.1° elevation angle during the data collection phase of the ACTS propagation experiment.

The several path attenuation model estimates are indicated in the figure. The ITU-R model atmosphere presents a single mid-latitude average value and is therefore shown as a horizontal line. The ITU-R model depends only on the surface value of water vapor density at ground or terminal height. The surface values were hourly recordings provided by the National Weather Service (NWS) for the airport in Norman, OK. The path attenuation estimates for the model were calculated for each hour and are shown as horizontal lines for that hour. The meteorological observations made at the airport were separated from the ACTS Propagation Terminal (APT) by about 7 km in the horizontal and 70 m in the vertical. The ACTS model estimates were also

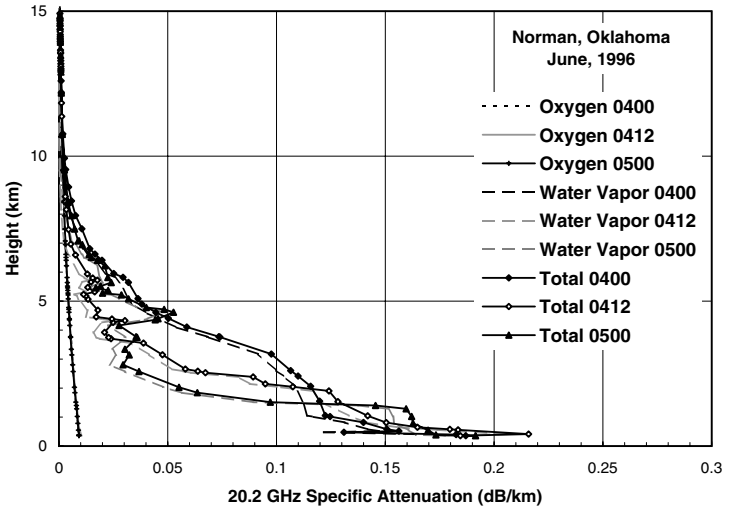

Figure 3.13 Specific attenuation profiles for Norman, OK, for June 4, 1996.

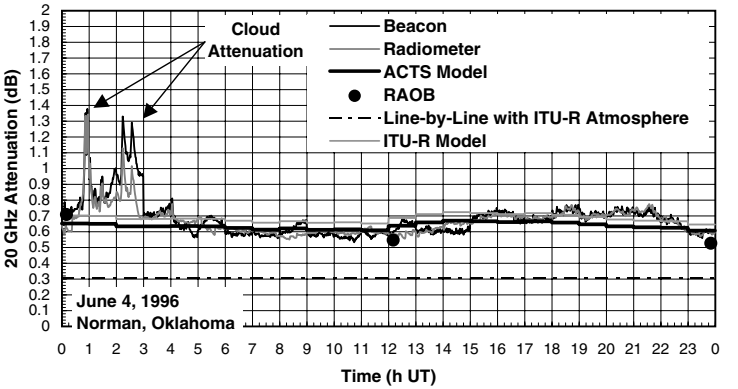

Figure 3.14 Path attenuation time series for Norman, OK, for June 4, 1996.

calculated from the hourly data by using pressure and temperature as well as water vapor density.

The APT also provided meteorological data at the terminal location. Computations based on measurements made at the terminal produced nearly identical results to the hourly observations made at the closest NWS site but were abandoned during the experiment because of calibration problems at some of the APT sites.

The 1-min path attenuation average time series is displayed in Figure 3.14. The radiometer measurements were obtained from a total power radiometer with a center frequency at the beacon frequency. The radiometer used the same antenna employed for the beacon measurements.[7] The antenna

pattern for the radiometer was coaxial with the angle of arrival of the beacon signal. The radiometer sky brightness temperature measurements were converted to total attenuation (relative to free space) estimates by using Equation 1.49. The total power radiometer was calibrated every 15 min.

The beacon attenuation measurements were made with a separate beacon receiver.[7] The beacon- and radiometer-derived path attenuation estimates tracked within 0.1 dB, except for observations made within the clouds. Within the cloud observations between 02:00 and 03:00 UT, the average difference was 0.25 dB; outside the clouds, the meteorologically based model predictions were within 0.1 dB of the measurements. The ACTS model and ITU-R model predictions differed by less than 0.1 dB.

The water vapor attenuation profiles showed a drying of the atmosphere between heights of 1 and 4 km above the surface and a moistening in the very lowest levels above the ground, at heights below a few hundred meters. The variability was caused by changes in water vapor concentration; the oxygen contributions shown in Figure 3.13 showed no change in time over the day. After 03:00 UT, variations in path attenuation were all caused by water vapor variations along the path.

3.2.4.2 June 5, 1996

The specific attenuation profiles for June 5, 1996, are shown in Figure 3.15. The path attenuation time series is displayed in Figure 3.16. For this day, the changes in path attenuation were caused by water vapor variations along the path. The path attenuation ranged over 0.4 dB from 0.5 to 0.9 dB. Again, the path attenuation derived from radiometer and beacon measurements differed by less than 0.1 dB. The attenuation values computed from the RAOBs differed from the path measurements by less than 0.1 dB. The predictions based on surface measurements differed from the observations on the path by as much as 0.2 dB. The variations in water vapor with height relative to the assumed exponential decrease of the ITU-R model or the average structure represented by the ACTS regression model produced these differences. The ACTS model provided a better match to the observations.

3.2.4.3 June 6, 1996

June 6, 1996, was a day with rain. The specific attenuation profiles are given in Figure 3.17 and the path attenuation time series presented in Figure 3.18 and Figure 3.19. Figure 3.18 addresses the path attenuation in the periods between the rain events and Figure 3.19 shows the much higher path attenuation values produced by the rain. For this day, the ITU-R model employed the 2.1-km rain scale height for rain. The ITU-R model predicted too large a value by about 0.4 dB (60% too high) during the clear periods between the rain showers. The ACTS model was constructed from clear weather (no rain or cloud) soundings. This model performed better in the intervals between showers. The 00:00 UT soundings on June 7 showed a better agreement between the RAOB value and the ITU-R model for rainy conditions than the

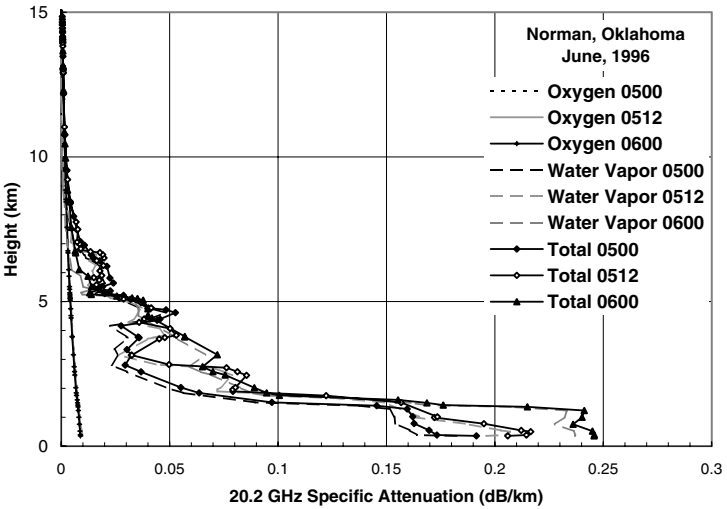

Figure 3.15 Specific attenuation profiles for Norman, OK, for June 5, 1996.

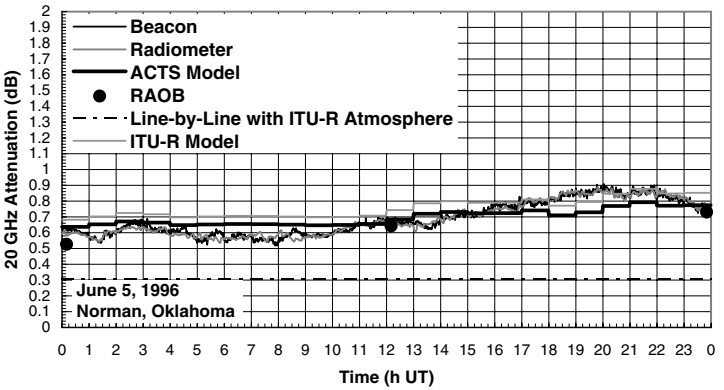

Figure 3.16 Path attenuation time series for Norman, OK, for June 5, 1996.

ACTS clear weather model. The specific attenuation profile for this sounding showed a better match to the 2.1-km scale height.

The 1-min average sky brightness temperature time series for June 6 is presented in Figure 3.20. These data were used to generate the radiometer-derived path attenuation measurements. The ACTS model starts with the estimation of the medium temperature required to calculate attenuation, given a radiometer measurement of brightness temperature (see Equation 1.49, Equation 3.13, and Equation 3.14). The ACTS model sky brightness temperature prediction is also displayed. The sky brightness temperature estimates from the RAOBs are also shown. The 00:00 and 12:00 UT RAOBs for June 6 differed from the ACTS model prediction by less than 4 K. The

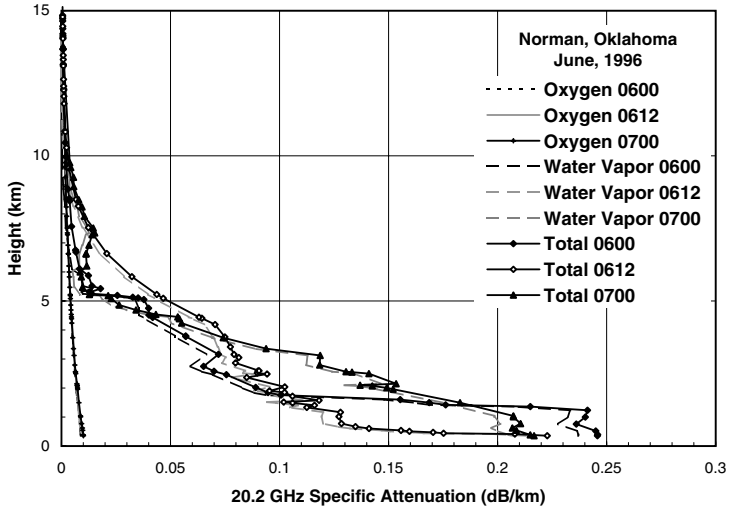

Figure 3.17 Specific attenuation profiles for Norman, OK, for June 6, 1996.

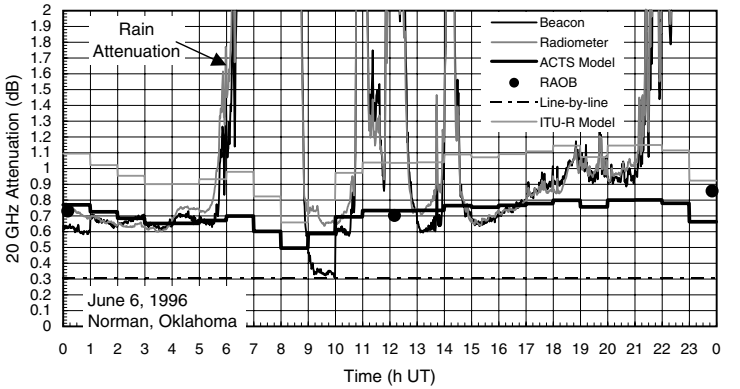

Figure 3.18 Path attenuation time series for Norman, OK, for June 6, 1996.

00:00 UT RAOB obtained during rain for June 7 differed by 9 K. Note that as the measured brightness temperature approaches the medium temperature, the uncertainty in the estimate of path attenuation calculated using Equation 1.49 increases. Generally, radiometric measurements should not be used to estimate path attenuation if the resulting attenuation value is more than 6 to 8 dB.

The radiative transfer equation describes the emission from a nonscattering atmosphere, gaseous emission, or cloud particle emission (see Equation 1.46). The absorption cross section per unit volume is proportional to the specific attenuation. Restating the radiative transfer equation, the

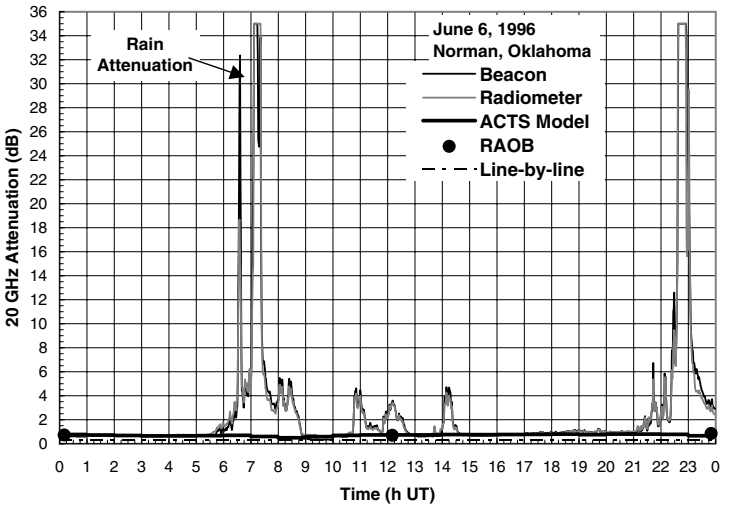

Figure 3.19 Path attenuation time series for Norman, OK, for June 6, 1996.

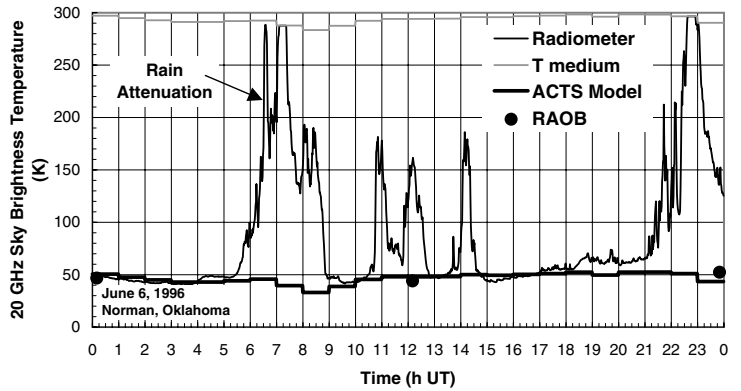

Figure 3.20 Sky brightness temperature time series for Norman, OK, for June 6, 1996.

brightness temperature is proportional to the integral of the specific attenuation times the temperature (K) of the gas or cloud times the reduction in emitted energy between the emitter and the receiver due to attenuation along the path. If the dominant source of attenuation is higher in the atmosphere at a colder temperature, the brightness temperature is lower for the same specific attenuation than if it is lower in the atmosphere at a warmer temperature. The medium temperature (see Equation 1.47) is the value of temperature that produces the same brightness temperature when factored outside the integral. For emission by water vapor in the atmosphere, the medium temperature is near the temperature at the surface because the dominant source of emission is near the ground. For emission

dominated by clouds higher in the atmosphere, the medium temperature is lower because the physical temperature of the cloud is lower.

If the medium temperature is in error because the location of the dominant source of emission is at the wrong temperature, the estimate of attenuation by Equation 1.49 is in error. The ACTS model is biased toward higher medium temperatures because it addresses the prediction of absorption by atmospheric gases low in the clear atmosphere. The use of the model-predicted medium temperature might produce errors in the estimation of attenuation from radiometric measurements if the dominant rain or clouds are distant from the terminal. This source of error may become significant if the path attenuation is above about 10 dB. The estimation error may also be significant if the specific attenuation profile is markedly different from the profiles in the data set used for the regression analysis.

3.3 *ACTS statistics*

The ACTS propagation experiment obtained 5 years of path attenuation measurements at seven locations in the United States and Canada. Path attenuation and sky brightness temperature measurements were collected for each second of observation. To aid in system calibration, radiometric sky brightness temperature observations were separately recorded twice daily at radiosonde sounding times.

3.3.1 *Twice-daily sky brightness temperature*

3.3.1.1 *Norman, OK*

The twice-daily brightness temperature measurements for Norman, OK, are presented in Figure 3.21. The majority of the measured brightness temperature values are in a band between 0 and 60 K. Within this band, a seasonal variation is evident, with a peak during the summer months and a minimum during the winter. This band corresponds to clear weather conditions. The values between this band and about 300 K are produced by absorption in clouds or attenuation by rain (see Figure 3.20, in which two of the RAOB time samples are for cloudy or rainy conditions with brightness temperatures above 60 K).

Brightness temperature values estimated by the ACTS model were recorded for the same sample times. A comparison between measured and modeled values is presented in Figure 3.22. The majority of the observations lie about the equality line, with the rain or cloud contaminated observations well above the line. A maximum of 60 K for summertime clear weather conditions indicates that the maximum path attenuation values associated with gaseous absorption on a 49° elevation angle path at 20.2 GHz is 1 dB.

The spread of measured values about the equality line can be used to estimate the prediction uncertainty for the ACTS model and the measurement uncertainty of the ACTS propagation experiment measurement system.

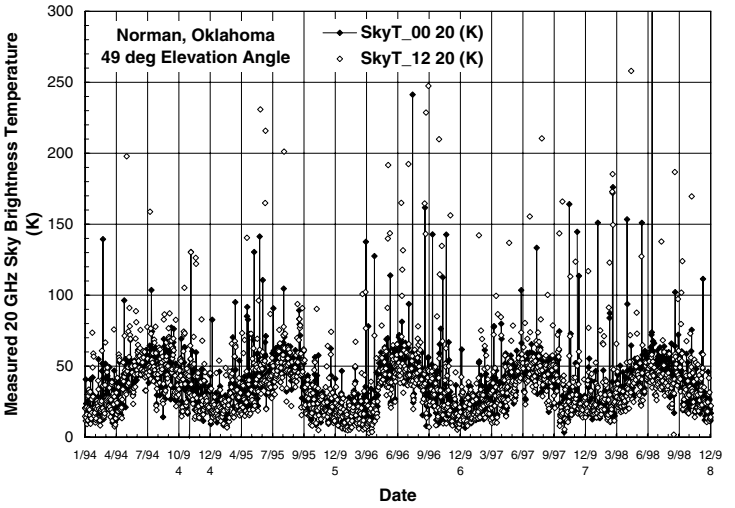

Figure 3.21 Five-year sky brightness time series for Norman, OK.

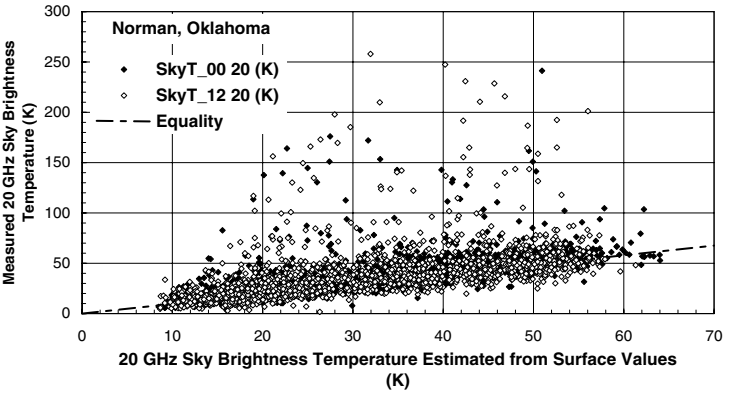

Figure 3.22 Scattergram-measured vs. modeled sky brightness temperatures.

Based on an assumed normal distribution for measurement and modeling errors, the one standard deviation error is the order of 10 K. This value translates to 0.11 dB.

3.3.1.2 Fairbanks, AK

The twice-daily sky brightness temperature measurements for Fairbanks, AK, are presented in Figure 3.23. The low elevation angle path from Fairbanks to ACTS produced a higher path attenuation and corresponding sky brightness temperature. The measurements showed fewer brightness temperature increases due to rain or clouds relative to the seasonal variations due to gaseous absorption than indicated in the Oklahoma data.

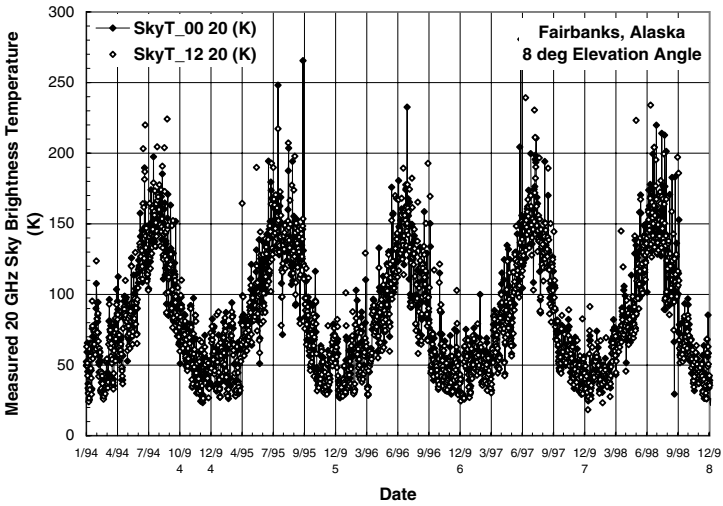

Figure 3.23 Five-year sky brightness time series for Fairbanks, AK.

3.3.1.3 Vancouver, British Columbia

The twice-daily sky brightness temperature measurements for Vancouver, British Columbia, are presented in Figure 3.24. The seasonal variations in gaseous absorption produced about the same variations in brightness temperature as evident in the Oklahoma data even with the lower elevation angle to ACTS. The measurements showed more brightness temperature increases due to rain or clouds relative to the seasonal variations than indicated in the Oklahoma data, but the maximum increases were lower. The maximum attenuation values observed during the entire experiment at the radiosonde launch times were lower than for Oklahoma.

3.3.1.4 Greeley, CO

The twice-daily sky brightness temperature measurements for Greeley, CO, are presented in Figure 3.25. The seasonal variations in gaseous absorption did not show the wider swings of the Oklahoma observations. The lack of cloud or rain increased during the winter months, suggesting that snow dominated precipitation occurrences in winter and few attenuation events occurred. The break in the observations in May 1997 occurred when the site was not operational.

3.3.1.5 Tampa, FL

The twice-daily sky brightness temperature measurements for Tampa, FL, are presented in Figure 3.26. The seasonal variations in gaseous absorption showed a widening of the range of brightness temperatures and absorption values during the winter and spring months. The increased occurrences of cloud or rain increases during the year show that rain events can occur

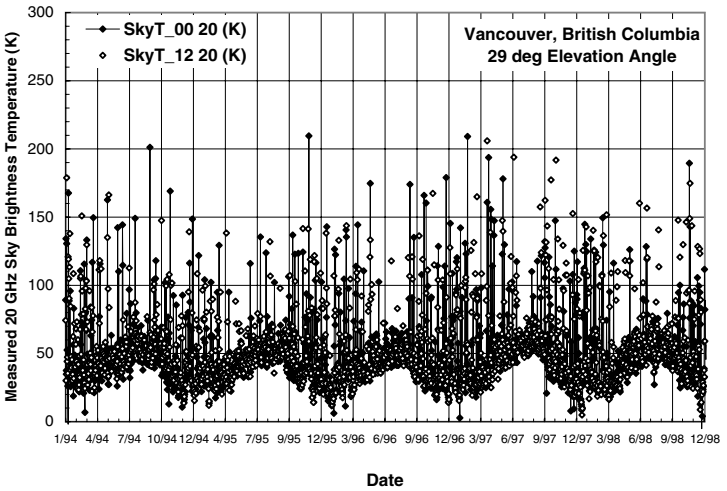

Figure 3.24 Five-year sky brightness time series for Vancouver, British Columbia.

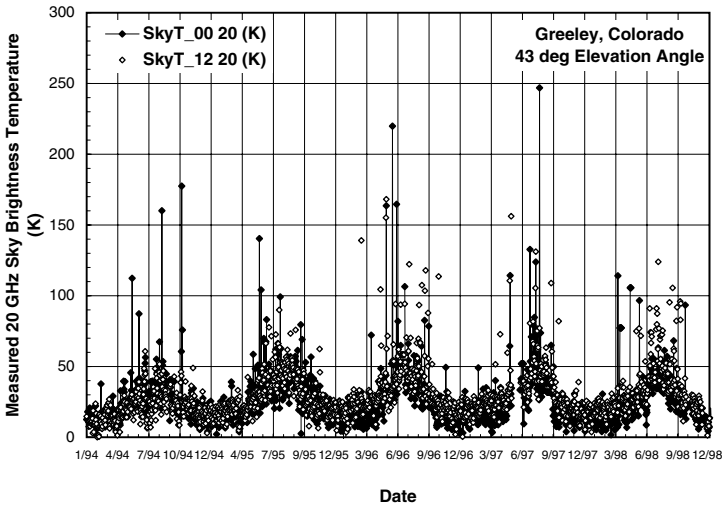

Figure 3.25 Five-year sky brightness time series for Greeley, CO.

during all seasons. The break in the observations in October 1997 occurred when the site was not operational.

3.3.1.6 White Sands, NM

The twice-daily sky brightness temperature measurements for White Sands, NM, are presented in Figure 3.27. The seasonal variations in gaseous absorption showed a small increase in the brightness temperatures and absorption values during the summer months. The decreased occurrences of cloud or

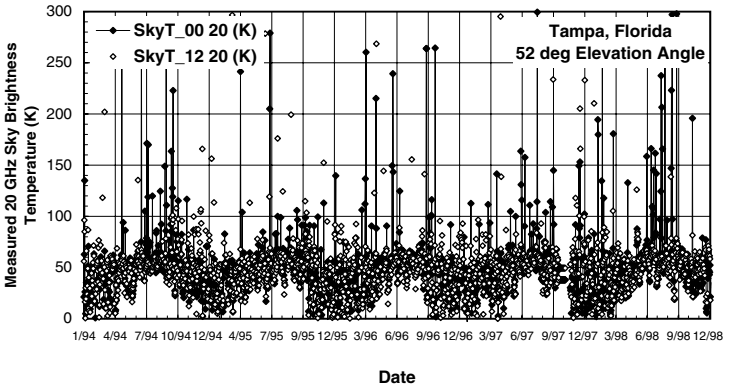

Figure 3.26 Five-year sky brightness time series for Tampa, FL.

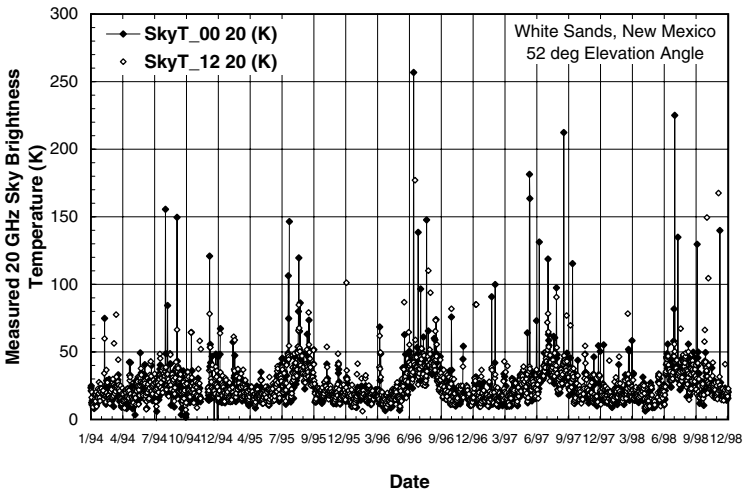

Figure 3.27 Five-year sky brightness time series for White Sands, NM.

rain increases during the year show that only a few rain events can occur during any season but mainly in the summer. The break in the observations in November 1994 occurred when the site was not operational.

3.3.1.7 Reston, VA

The twice-daily sky brightness temperature measurements for Reston, VA, are presented in Figure 3.28. The seasonal variations in gaseous absorption showed a wider range of gaseous absorption values than those recorded in Oklahoma. The data also show a significant number of rain and cloud attenuation events spread throughout the year. For this site, the start of the data collection period was delayed for three months.

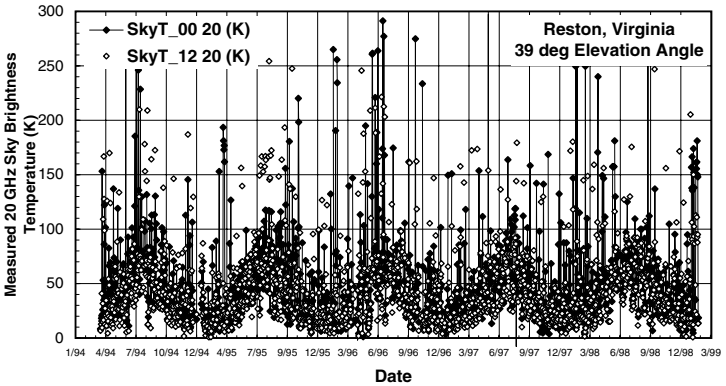

Figure 3.28 Five-year sky brightness time series for Reston, VA.

3.3.2 Gaseous absorption distributions

Empirical distribution functions (EDFs or cumulative distributions of observed values) were compiled from the 1-sec average beacon and radiometer estimates of attenuation. The attenuation values are total attenuation relative to free space. They have not been corrected for the effects of water on the APT antenna either due to rain rate or dew. The entire 5 years of observations were used.

3.3.2.1 Norman, OK

EDFs for the 20.2-GHz observations at the Oklahoma site are presented in Figure 3.29. In this figure, the range of attenuation values was limited from –0.5 to 2.0 dB. The data used to compile the distributions represent all the attenuation mechanisms that can affect a path in Oklahoma, with the exception of snow events. Attenuation due to wet snow on the antenna has been edited from the data set. Gaseous absorption is responsible for attenuation values in the 0 to 1 dB range. Scintillation can produce signal level increases (a negative attenuation) and decreases. Both the beacon attenuation and attenuation values derived from radiometer measurements are treated separately. Scintillation does not affect the radiometer results.

EDFs were prepared for each season and for the full year. The seasons are defined meteorologically. Winter includes the months of December, January, and February. The other seasons follow three months at a time. Only the summer data showed a difference between the radiometer and beacon data and only for attenuation values 1 dB or greater. This difference could be caused by the more intense scintillation events.

The full attenuation EDFs are shown in Figure 3.30. In this figure, the differences between the radiometer estimates of attenuation and the beacon measurements are significant for attenuation values above 6 dB. In this case, the uncertainty in medium temperature is important.

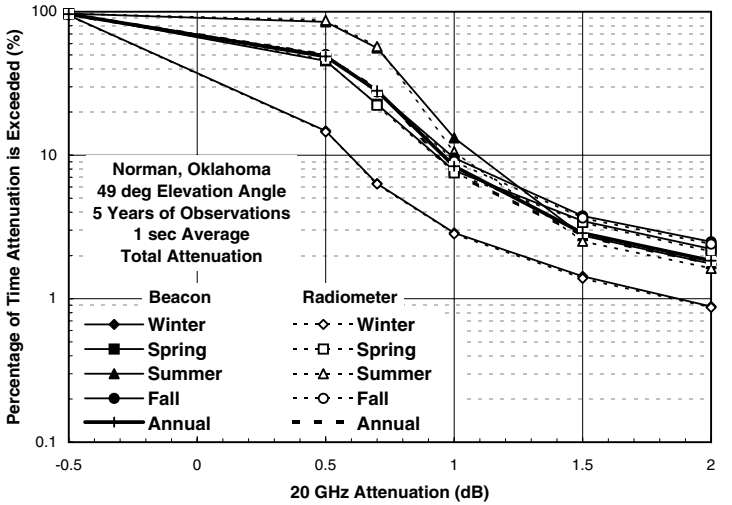

Figure 3.29 20-GHz Attenuation EDFs for Norman, OK.

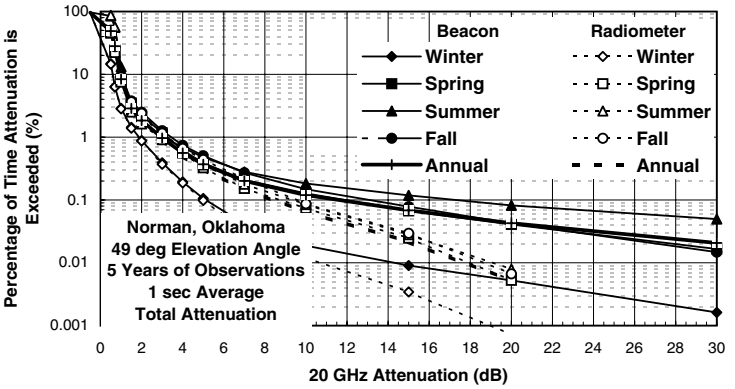

Figure 3.30 20-GHz Attenuation EDFs for Norman, OK.

The seasonal variations showed that the path attenuation due to gaseous absorption (radiometer EDFs between 0.5 and 1.0 dB) is less than 1 dB 90% of the summer period and less than 1 dB 97% of the winter period. On average, gaseous absorption is less than 1 dB 92% of the time. This result was also obtained for the fall and spring periods.

3.3.2.2 Fairbanks, AK

EDFs for the 20.2-GHz observations at the Alaska site are presented in Figure 3.31. For this site, EDFs for the summer period showed that 2 dB of attenuation was exceeded 89% of the time. When 4 dB is used as the upper limit for gaseous absorption events, the attenuation is less than 4 dB 90% of the

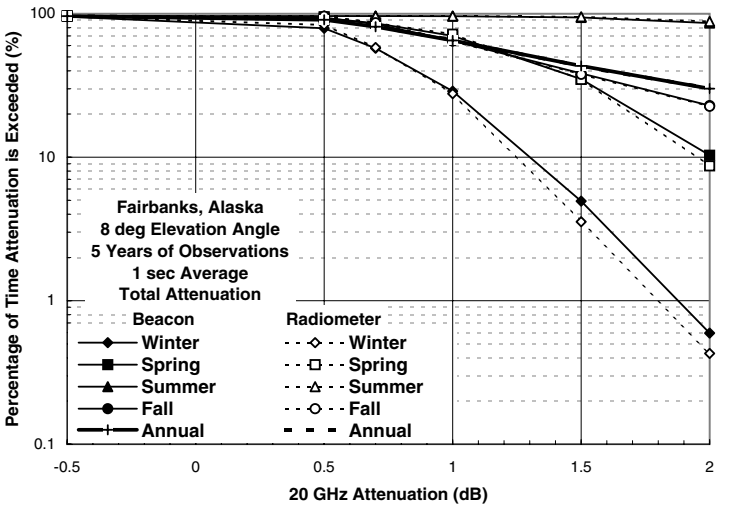

Figure 3.31 20-GHz Attenuation EDFs for Fairbanks, AK.

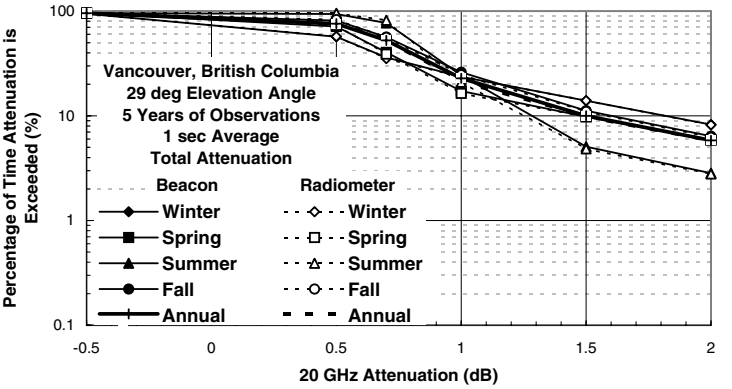

Figure 3.32 20-GHz Attenuation EDFs for Vancouver, British Columbia.

time in summer and 99.999% of the time in winter. On average, the attenuation is less than the 4-dB threshold 97% of a year. The 4-dB value corresponds to a sky brightness temperature of about 170 K.

3.3.2.3 Vancouver, British Columbia

EDFs for the 20.2-GHz observations at the British Columbia site are presented in Figure 3.32. For this site, the gaseous absorption was less than 1 dB 75% of the time, with little variation by season. At higher attenuation values, the probability of exceeding the attenuation value is lowest during the summer months.

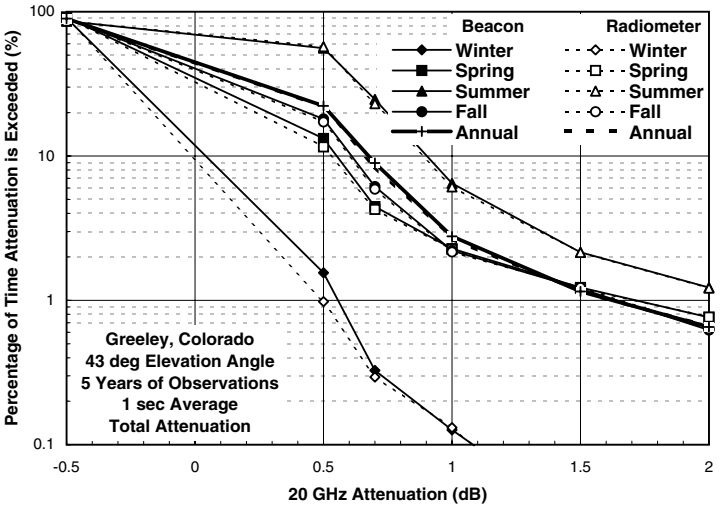

Figure 3.33 20-GHz Attenuation EDFs for Greeley, CO.

3.3.2.4 Greeley, CO

EDFs for the 20.2-GHz observations at the Colorado site are presented in Figure 3.33. For this site, EDFs for the summer period showed that less than 1 dB of attenuation occurred 94% of the time and for the winter period less than 1 dB of attenuation occurred 99.96% of the time. On average, the absorption was less than 1 dB 97% of a year.

3.3.2.5 Tampa, FL

EDFs for the 20.2-GHz observations at the Florida site are presented in Figure 3.34. For this site, EDFs for the summer period showed that less than 1 dB of attenuation occurred 73% of the time and for the winter and spring periods less than 1 dB of attenuation occurred 90% of the time. On average, the absorption was less than 1 dB 83% of a year.

3.3.2.6 White Sands, NM

EDFs for the 20.2-GHz observations at the New Mexico site are presented in Figure 3.35. For this site, the EDFs for the summer period showed that less than 1 dB of attenuation occurred 96.6% of the time and for the spring period less than 1 dB of attenuation occurred 99.3% of the time. On average, the absorption was less than 1 dB 98% of a year.

3.3.2.7 Reston, VA

EDFs for the 20.2-GHz observations at the Virginia site are presented in Figure 3.36. For this site, EDFs for the summer period showed that less than 1 dB of attenuation occurred 65% of the time and for the winter period less than 1 dB of attenuation occurred 91% of the time. On average, the absorption was less than 1 dB 80% of a year.

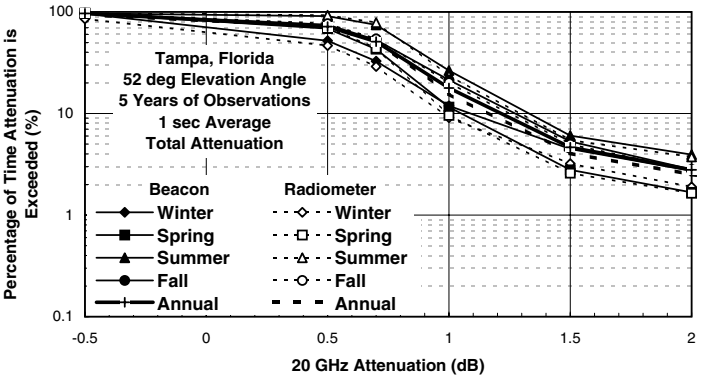

Figure 3.34 20-GHz Attenuation EDFs for Tampa, FL.

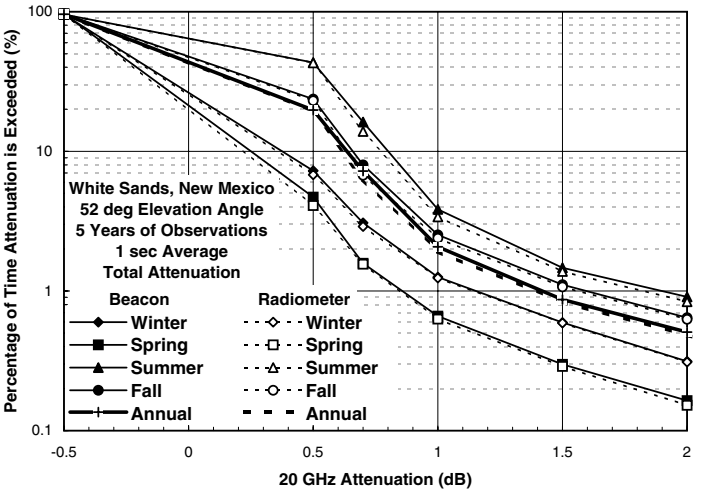

Figure 3.35 20-GHz Attenuation EDFs for White Sands, NM.

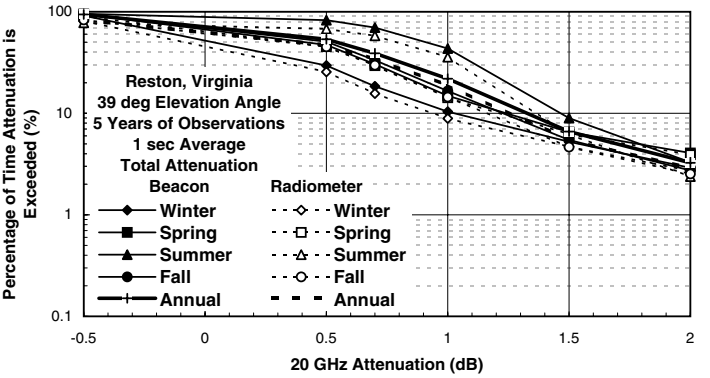

Figure 3.36 20-GHz Attenuation EDFs for Reston, VA.

3.4 List of symbols

Symbol	Quantity	Units	Equation
S_i^b	Line strength	GHz	3.2
$F_i'^b$	Line-shape factor	GHz^{-1}	3.2
S_i^a	Line strength	GHz	3.4
$F_i'^a$	Line-shape factor	GHz^{-1}	3.4
a_{1i} to a_{6i}	Empirical oxygen line parameters	dB/km	3.4
A_Z	Zenith attenuation	dB	3.9
b_{1i} to b_{6i}	Empirical water vapor line parameters	dB/km	3.2
d	Debye width	GHz	3.4
f	Frequency	GHz	3.1
h	Slant path terminal height	km	3.10
h_D	Dry gas scale height	g/m^3	3.2
h_W	Water vapor scale height	km	3.10
N	Complex radio refractivity	ppm	3.1
N′	Refractivity	N units	3.1
N'_D	Refractivity deviation caused by dry gases	N units	3.1
N'_W	Refractivity deviation caused by water vapor	N units	3.1
N_0	Average radio refractivity	N units	3.1
N_a	Oxygen continuum	ppm	3.4
N_a	Number of oxygen lines used in summation		3.4
N_b	Water vapor continuum	ppm	3.2
n_b	Number of water vapor lines used in summation		3.2
p	Dry gas pressure	hPa	3.2
P	Total pressure = $P_V + p$	hPa	3.2
P	Total pressure	hPa	3.14
P_V	Water vapor pressure	hPa	3.2
T	Absolute temperature	K	3.2
T	Temperature	C	3.8
Θ	Inverse temperature = 300/T		3.2
α	Specific attenuation	dB/km	3.1
α	Elevation angle	r	3.10
$\alpha_{D\_}$	Specific attenuation due to dry gases	dB/km	3.5
$\alpha_{W\_}$	Specific attenuation due to water vapor	dB/km	3.3
δ	Interference parameter for line overlap		3.4
γ_i	Line width	GHz	3.2
ν_{oi}	Line frequency	GHz	3.2
ρ_V	Water vapor density	g/m^3	3.6

References

1. Van Vleck, J.H., Theory of absorption by uncondensed gases, in *Microwave Antenna Theory and Design*, S. Silver, Ed., Dover, New York, 1965.
2. Liebe, H.J., MPM — An atmospheric millimetre-wave propagation model, *Int. J. Infra. Mm. Waves*, 10(4), 631, 1989.
3. Liou, K.N., *Radiation and Cloud Processes in the Atmosphere*, Oxford University Press, New York, 1992.
4. ITU-R, Recommendation ITU-R P.676–2, Attenuation by Atmospheric Gases, International Telecommunications Union, Geneva, 1995.
5. Waters, J.W., Absorption and emission by atmospheric gases, in *Methods of Experimental Physics*, M.L. Meeks, Ed., Academic Press, New York, 1976, Vol. 12B, Chap. 2.3.
6. Crane, R.K., Fundamental limitations caused by RF propagation, *Proc. IEEE*, 69(3), 196, 1981.
7. Crane, R.K., Wang, X., Westenhaver, D.B., and Vogel, W.J., ACTS propagation experiment: Design, calibration, and data preparation and archival, *Proc. IEEE*, 85(7), 863, 1997.

chapter four

Refraction

4.1 Ray bending

Refraction effects were summarized in Section 1.4.2. The ray tracing procedures needed to analyze refraction effects were developed in Section 2.5 and Section 2.6. Figure 2.7 provides sample ray trajectories for the ITU-R model atmosphere and for radio refractivity profiles obtained from rawinsonde observations (RAOBs) made on June 4, 1996, in Norman, OK. The trajectories calculated by using the RAOB data differed little from the model trajectory for rays launched at an initial elevation angle of 3°. At a 1° initial elevation angle, the trajectories calculated for the 00:00 UT and 12:00 UT RAOBs differed from each other and from the model prediction. For a 0° initial elevation angle, the ray for the 00:00 UT RAOB was trapped below 57 m (0.414 km msl) above the surface (at 0.357 km msl). For these calculations, the Earth's surface was assumed to be a sphere concentric with the center of the Earth at the height of the meteorological instrument used to make the surface observations (about 1 m above the physical surface).

An expanded view of ray trajectories calculated for the 12:00 UT RAOB is presented in Figure 4.1 for a family of five rays with initial elevation angles separated by 0.1°. The modified radio refractivity profile, $M(z)$, is also displayed in this figure. Each trajectory gives the ray height above mean sea level (msl) vs. surface distance from the ray launch location for propagation above the spherical Earth. In general, the vertical gradient in radio refractivity is negative, producing a downward bending of the rays, but, for this figure, the gradient is positive, producing an upward bending at heights below 0.55 km msl (see Figure 1.42 and Figure 1.47) followed by downward bending at higher altitudes. Figure 4.2 displays ray trajectories calculated for the 00:00 UT RAOB M-profile. For this profile, the downward bending of rays launched with an initial elevation angle less than 0.24° is great enough to return the ray to the Earth's surface. The rays returned to the initial ray height are trapped rays with a turning point at the height where the local elevation angle is zero.

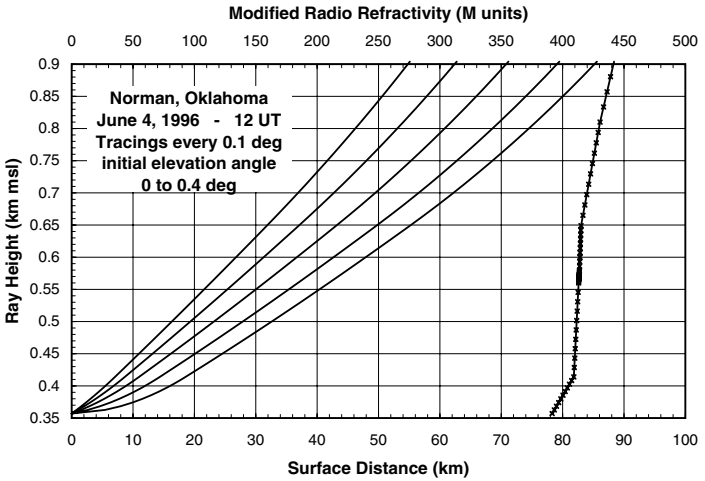

Figure 4.1 Low elevation angle ray trajectories for Norman, OK, for June 4, 1996, at 12:00 UT.

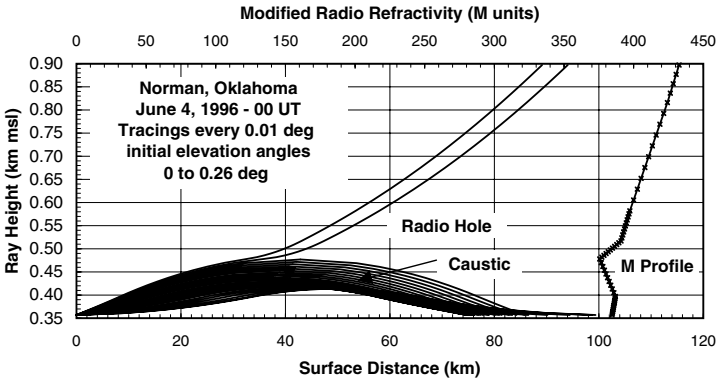

Figure 4.2 Low elevation angle ray trajectories for Norman, OK, for June 4, 1996, at 00:00 UT.

The ray trajectories for both the 00:00 UT and 12:00 UT RAOBs show regions of space where, by geometrical optics calculations, electromagnetic energy will not reach. For each figure, rays at initial elevation angles from the highest angle shown to a zenith ray will propagate out through the atmosphere. Assuming the radio horizon is at a 0° initial elevation angle, rays do not propagate below that horizon but electromagnetic energy will propagate below the radio horizon by diffraction (using physical optics), by surface waves (at lower frequencies, which are not considered in this handbook), by transhorizon scatter, and, at sufficiently low frequencies, by ionospheric refraction (not considered in this handbook). Likewise, geometrical optics predicts a radio hole (region of reduced electromagnetic energy)

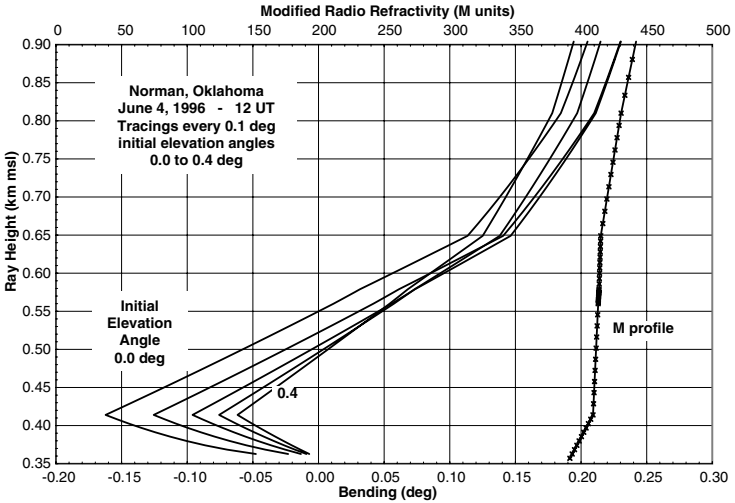

Figure 4.3 Bending profiles for Norman, OK, for June 4, 1996, at 12:00 UT.

between the trapped rays and the ray with the lowest initial elevation angle that propagates up and out of the atmosphere. Energy is propagated into the radio hole by diffraction but at reduced power levels.

4.1.1 Bending and focusing

Ray bending is computed for a given *M*-profile by using Equation 2.69 and Equation 2.70. Downward ray bending is positive. The bending profiles for the ray trajectories depicted in Figure 4.1 are shown in Figure 4.3. At a 0° initial elevation angle, the bending is negative (upward) for ray heights below 0.55 km msl. At higher initial elevation angles, the magnitude of the bending is less. As a result, these rays tend to converge, producing an increased power flux density or a focusing gain (negative loss) as displayed in Figure 4.4. Refractivity profiles that have a positive vertical gradient and produce focusing gain are called subrefractive.[1]

In the height intervals with a negative radio refractivity gradient but a gradient not strong enough to produce trapping or ducting, the decrease in ray bending with height produces a divergence in elevation between adjacent rays. In the geometrical optics limit, electromagnetic energy is confined to a tube of rays and cannot cross the rays that form the tube boundaries. The power flux density therefore decreases relative to the normal spreading from a point source in a medium with constant radio refractivity, leading to a focusing loss along the tube of rays. If the refractive index gradients are strong enough to cause trapping, $dN/dz < -157$ N units/km, adjacent rays may cross over one another near the turning point. In this case, geometrical optics predicts an infinite power flux density at the point of crossing and the geometrical optics approximation is not valid. The surface containing

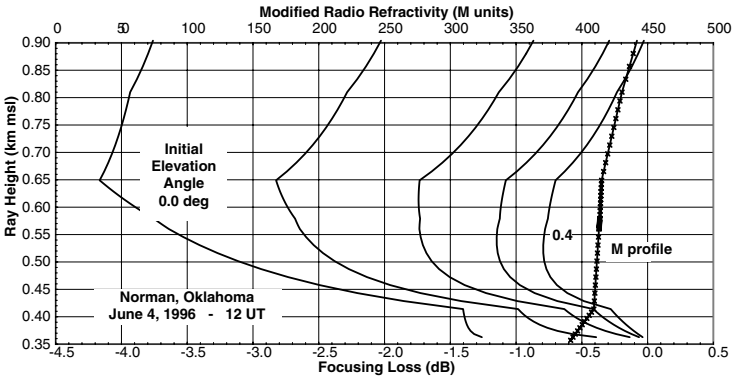

Figure 4.4 Focusing loss profiles for Norman, OK, for June 4, 1996, at 12:00 UT.

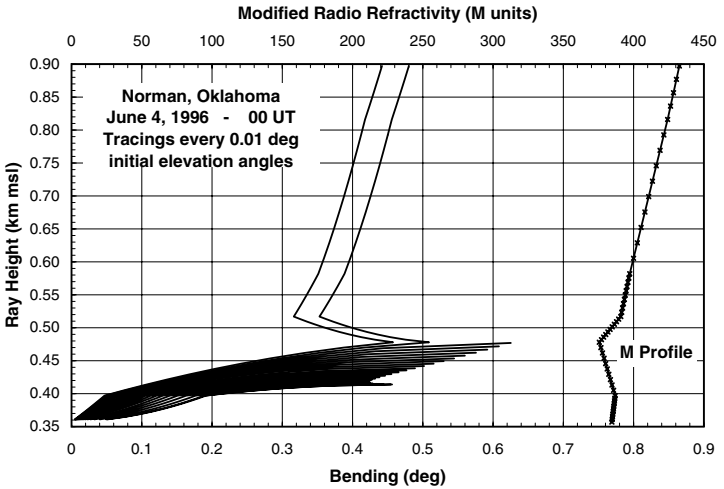

Figure 4.5 Bending profiles for Norman, OK, for June 4, 1996, at 00:00 UT.

the ray crossings is called a caustic surface or caustic. Figure 4.5 displays the bending profiles for the radio duct illustrated in Figure 4.2. The bending is downward but gets larger as the initial elevation angle increases for initial elevation angles between 0° and 0.12°, producing crossing rays and a caustic surface. The resulting focusing loss profiles are shown in Figure 4.6. Within the duct, the focusing loss calculation is made only from the start of the ray to the turning point.

The bending and focusing loss profiles for initial elevation angles near zero (Figure 4.3 and Figure 4.4) are for the first 550 m of height above the ground. The bending went positive within the first 100 m. Although the bending went positive, the initial ray convergence dominated the ray tracing all the way to one Earth's radius above the ground. The focusing and bending

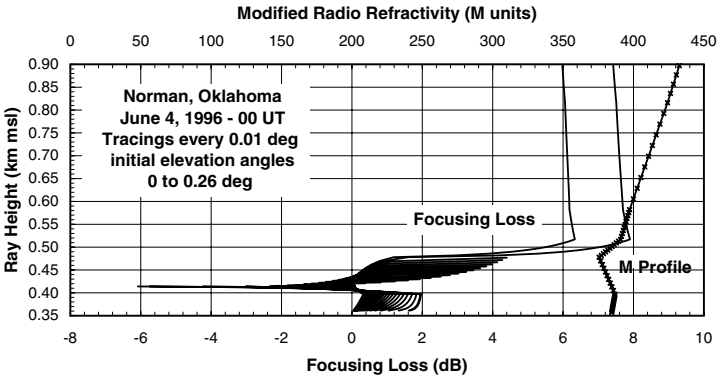

Figure 4.6 Focusing loss profiles for Norman, OK, for June 4, 1996, at 00:00 UT.

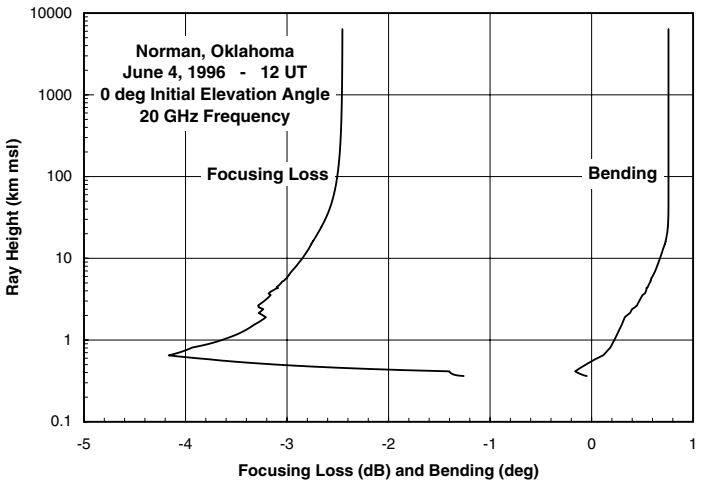

Figure 4.7 Focusing loss and bending profiles for 0° initial elevation angle for Norman, OK, for June 4, 1996, at 12:00 UT.

profiles for the 0° initial elevation angle ray are shown in Figure 4.7. The bending did not change with height for heights above 20 km (see Figure 1.27). In contrast, the focusing loss or gain values continued to change up to a height of 300 km.

Figure 4.8 and Figure 4.9 present ray bending and focusing loss values, respectively, for propagation through the atmosphere as a function of initial elevation angle. These figures are for two days when surface ducts were evident in two of the RAOB radio refractivity profiles. For rays with initial elevation angles high enough to escape the duct, large values of bending and focusing loss were evident for the lowest elevation angle ray. For these days, by an initial elevation angle of 1°, the effects of the surface ducts or surface subrefractive layers could be neglected.

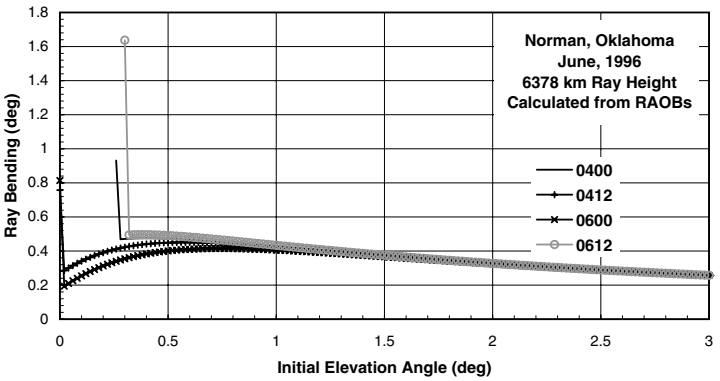

Figure 4.8 Ray bending at a height of one Earth radius as a function of initial elevation angle for Norman, OK, for two days in June 1996.

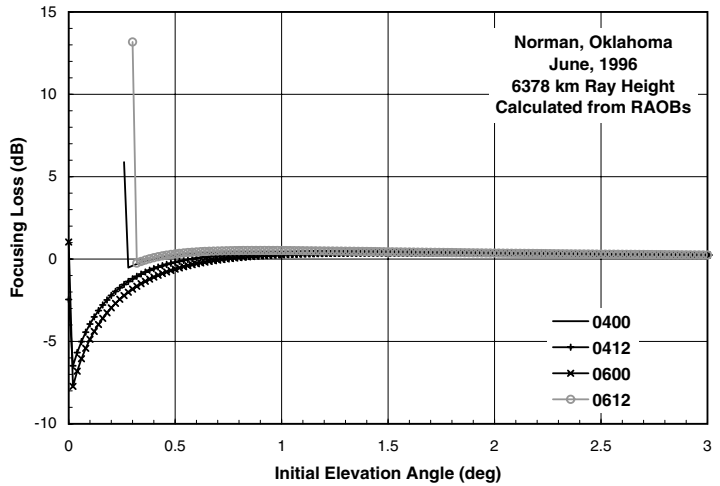

Figure 4.9 Focusing loss at a height of one Earth radius as a function of initial elevation angle for Norman, OK, for two days in June 1996.

Figure 4.10 displays the focusing loss for a 49° initial elevation angle ray for each of the three RAOBs. The focusing gain observed in the first 100 m of the atmosphere is evident in this figure, but is very small. At this elevation angle, focusing effects may be neglected. No adjustment for focusing is necessary for the attenuation values reported in Figure 3.14.

The variations in radio refractivity in the ionosphere can affect focusing at frequencies below 1 GHz. Figure 4.11 shows the maximum effect as a function frequency and of target height (upper end of ray). Figure 4.12 provides an expanded scale with the minimum and maximum expected effects due to the ionosphere. Again, focusing effects due to the ionosphere

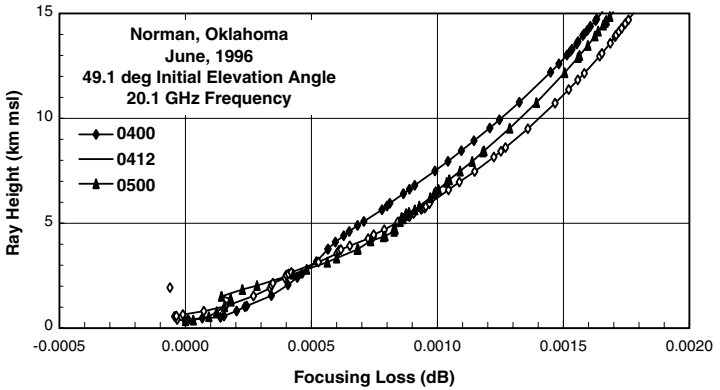

Figure 4.10 Focusing loss profiles for 49° initial elevation angle for Norman, OK, for June 4, 1996, at 00:00 and 12:00 UT and June 5, 1996, at 00:00 UT.

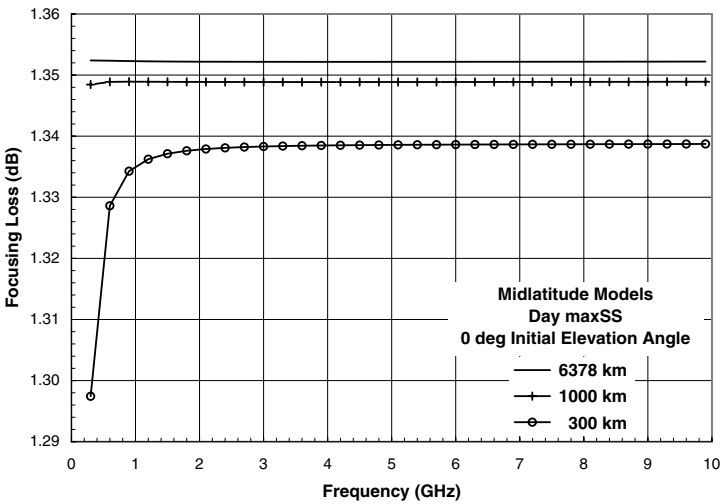

Figure 4.11 Focusing loss at 0° initial elevation angle as a function of frequency at several heights for the mid-latitude daytime maximum ionosphere model.

can be neglected for rays starting at the surface of the Earth for all elevation angles and frequencies above 0.3 GHz (see also Figure 1.31 and Figure 1.32). The very small change in focusing loss with frequency evident in Figure 4.12 is a result of the dispersion produced by the water vapor and oxygen lines evident in Figure 3.2 and Figure 3.5.

4.1.2 *Elevation angle error*

Bending produces both focusing effects and initial elevation angle pointing errors relative to the actual direction to the target or ray end point. Elevation

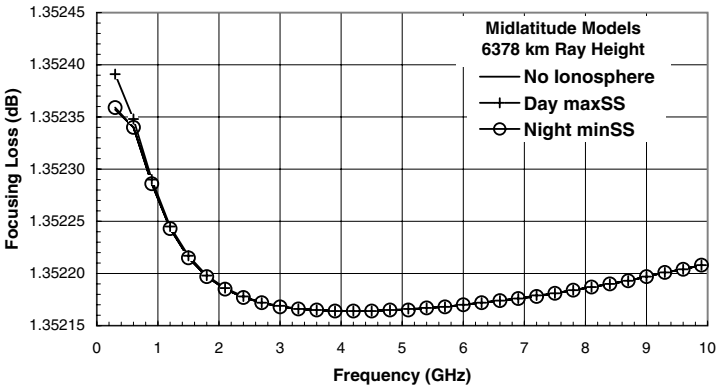

Figure 4.12 Focusing loss at 0° initial elevation angle as a function of frequency at one Earth radius height for the mid-latitude daytime maximum and nighttime minimum ionosphere model.

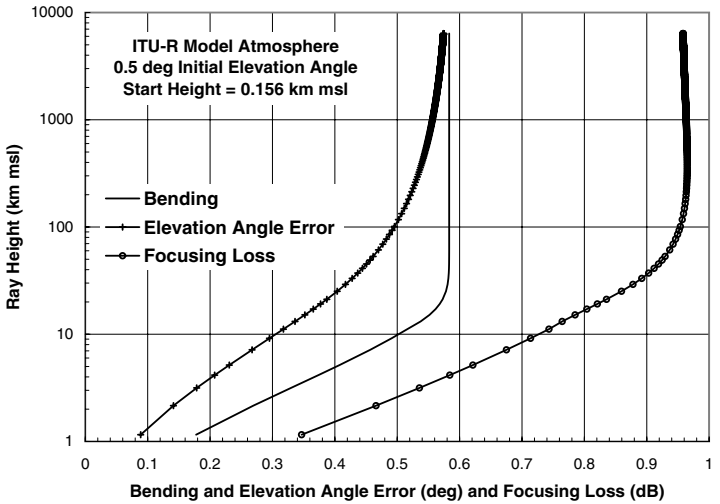

Figure 4.13 Focusing loss, elevation angle error, and bending profiles for 0.5° initial elevation angle for the ITU-R model atmosphere

angle error for the ITU-R model atmosphere is highest at 0° initial elevation angle and decreases with increasing elevation angle as shown in Figure 1.34. The elevation angle error changes with changes in the radio refractivity profile and the height of the target as shown in Figure 4.13 for a model atmosphere and Figure 4.14 for the Norman, OK, RAOB for June 4, 1996, at 12:00 UT.

Elevation angle errors are generally not important to communication system design except at low elevation angles when the expected variation in initial elevation angle with changes in the radio refractivity profile

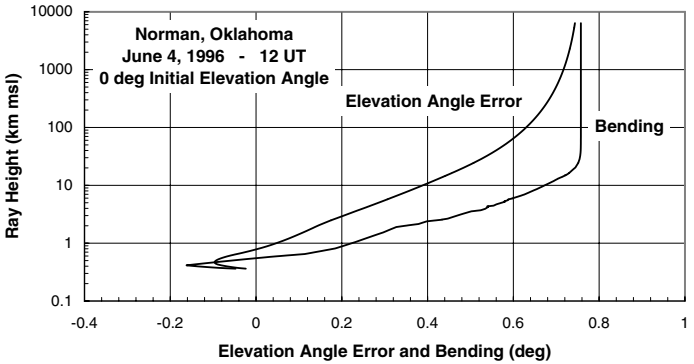

Figure 4.14 Elevation angle error and bending profiles for 0° initial elevation angle for Norman, OK, for June 4, 1996, at 12:00 UT.

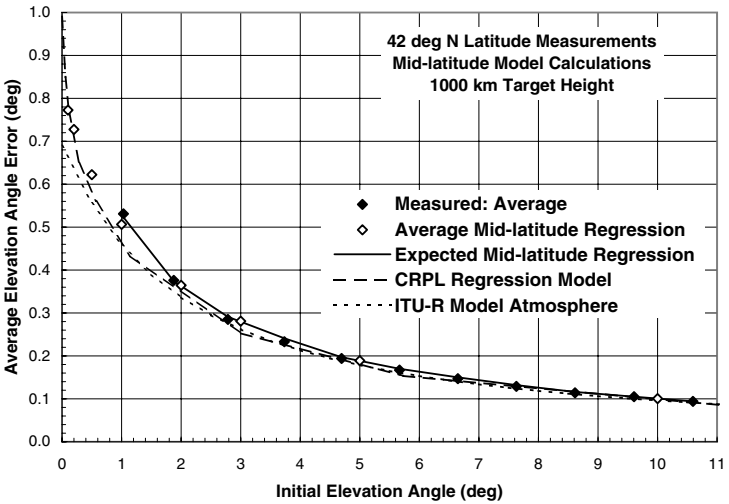

Figure 4.15 Average elevation angle error for a 42° N latitude site.

approaches more than a few tenths of the antenna beamwidth. For precision-tracking radars, elevation angle errors at low elevation angles become significant. Long-range radar height finders are not used in air traffic control because of the large aircraft height determination errors that can result from elevation angle errors.

High-power radar observations of calibration spheres in 1000-km-height orbits were employed to observe elevation angle errors.[2,3] The resulting average and root-mean-square deviations (RMSDs) about the average elevation angle error are displayed in Figure 4.15 and Figure 4.16, respectively. The measurements were made in the northeastern United States. The regression analysis results were obtained from ray tracings. The mid-latitude

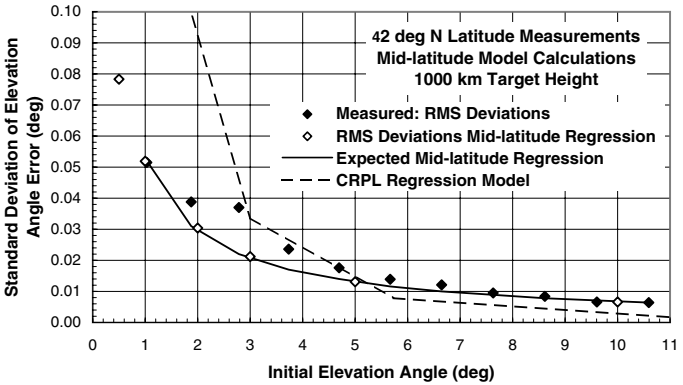

Figure 4.16 Standard deviation of elevation angle error for a 42° N latitude site.

regression was performed using 273 RAOBs from Albany, NY, for February and August 1966 through 1968. All the twice-daily soundings that reached an altitude of 25 km were used. The analysis was performed to determine the correlation between the computed elevation angle error for propagation through the atmosphere and the surface value of radio refractivity. The intent was to develop a simple elevation angle error prediction procedure based on the use of surface measurements of radio refractivity.[3,4] The CRPL model employed 77 RAOBs that were selected to span the expected global range of radio refractivity profiles.[1] The CRPL regression coefficients and statistics were for a target height of 70 km.

The mid-latitude and CRPL model regression coefficients are available for selected initial elevation angles:

$$\tau = A + BN_S \tag{4.1}$$

Table 4.1 presents the mid-latitude model values for bending. The CRPL regression coefficients are listed in the reference. The elevation angle error for propagation through the entire atmosphere is taken to be the bending value. Figure 4.13 shows that the elevation angle error approaches the bending value as height increases. For initial elevation angles higher than 1°, the difference between bending and elevation angle error at a 1000-km height was less than 1% of the bending value for the profiles in the mid-latitude collection.

The measured average and RMSD values are for more than 1500 elevation angle determinations made during two 5-day tracking sessions during September 1974. The elevation error measurements were spread over the range of initial elevation angle shown in Figure 4.15 and Figure 4.16. The number of observations in each 1° analysis interval ranged from 23 to 200. The estimated elevation angle measurement error due to receiver noise, calibration uncertainty, and orbit determination errors was less than

Table 4.1 Mid-Latitude Regression Model for Bending

Initial elevation angle (°)	*A* (°)	*B* (°/N)	Mean bending (°)	RMSD bending (°)	Correlation coefficient	Expected residual error (°)
0.1	–1.1128	0.005778	0.7726	0.152	0.81	0.0893
0.2	–0.8892	0.004951	0.7276	0.123	0.85	0.0639
0.5	–0.5123	0.003473	0.6222	0.0783	0.94	0.0265
1	–0.2683	0.002372	0.5064	0.0519	0.97	0.0123
2	–0.09591	0.0014094	0.3645	0.0304	0.99	0.005
3	–0.04098	0.0009854	0.2809	0.0212	0.99	0.0031
5	–0.010232	0.0009096	0.1889	0.0131	0.99	0.0019
10	–0.000305	0.0003086	0.1005	0.0066	0.99	0.00099

0.003° rms. The average elevation error for each 1° interval is presented in Figure 4.15. The standard deviation or RMSD from the average is presented in Figure 4.16. In the highest two angle intervals, the RMSD is about twice the estimated measurement error.

The average and RMSD values for the mid-latitude regression model are for the 273 RAOB calculations. The expected mid-latitude values are from the regression model for the surface radio refractivity values at the times of the calibration sphere pass. The average values are at the initial elevation angle values used in the regression analysis. The regression coefficients were interpolated to the initial elevation angles of the observations within each 1° analysis interval and converted to elevation angle error estimates for the measured value of surface radio refractivity, N_S. Differences between the average and expected values arise from the variations in N_S with observation time relative to the average for the RAOB set. The average CRPL model values were estimated by using the average N_S values for all the radar observations. Above 5°, the measurements and models generally agree. At lower elevation angles, closer agreement is found between the measurements and the mid-latitude regression values.

The measured and modeled RMSD values are shown in Figure 4.16. The RMSDs for the mid-latitude data set were obtained from the regression analysis of the 273 RAOBs. The expected values for the mid-latitude model were calculated for the N_S values at the times of radar measurements. The standard deviation estimates for the CRPL model are for the expected variations of N_S during the experiment combined with the estimated residual error relative to the estimate, given an N_S value. The measured RMSD values are higher than the model predictions at initial elevation angles above 3°. They approach the expected values from the mid-latitude regression model at higher initial elevation angles. The CRPL model overestimates the variations and underestimates the average value at elevation angles below 3°. This result follows from the use of similar climate data for the mid-latitude model whereas the CRPL model employed a wide range of climates in its development.

The residual errors after correction by using the surface radio refractivity values are presented in Figure 4.17. In precision radar tracking operations, correction for elevation angle errors is generally required. Correction procedures based on the use of linear regression analyses of calculated elevation angle error on surface radio refractivity values are often tried. This figure presents the results of using such a procedure. The expected results of using either the CRPL or mid-latitude model are displayed together with the observed residuals relative to the mid-latitude model predictions. At the lowest initial elevation angle where the elevation angle errors are greatest, the correction procedure worked as expected. At the highest initial elevation angles shown, the residual error approaches the elevation angle measurement error of the radar system. In the intermediate initial elevation angle range, the measured residual errors are higher than expected. The residual

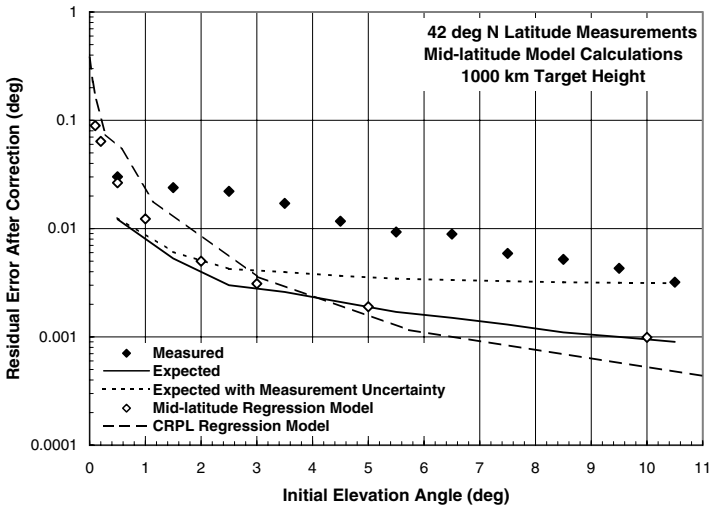

Figure 4.17 Residual elevation angle error after correction for a 42° N latitude site.

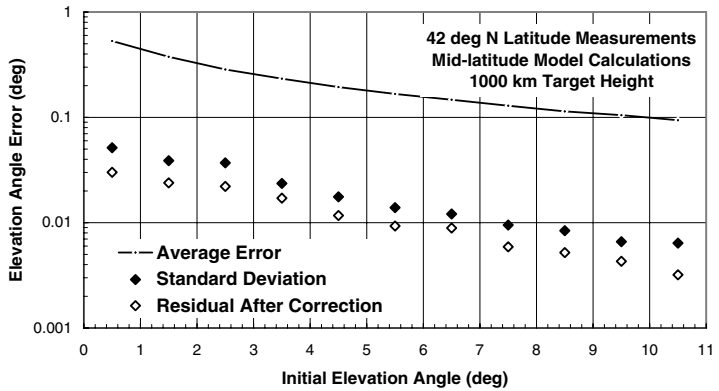

Figure 4.18 Elevation angle error for a 42° N latitude site.

errors were not correlated with surface values of radio refractivity. The sources of the increased elevation angle error were angle of arrival scintillation due to turbulence and larger but still small-scale fluctuations in the vertical gradients of radio refractivity.

The relative magnitudes of the average elevation angle error, the RMSDs in error about the average value, and the residual errors relative to a surface correction model are shown in Figure 4.18. Employing a simple correction of just using the expected value of the elevation angle error reduces the pointing error by about an order of magnitude. The surface value correction procedure decreases the pointing error by only an additional factor of 1.7.

4.1.3 *Trapping or ducting*

Trapping occurs when ray bending is sufficient to turn an upward-propagating wave back toward the ground. The height of the turning point marks the upper limit of the duct for the initial elevation angle and start height of the ray. Assuming horizontal or spherical symmetry, a ray trapped within a duct will return to its initial launch height, and then, if launched with a positive initial elevation angle, propagate down to a second turning point or down to a reflecting surface. On reflection or turning, the ray continues on between the upper turning height and the lower turning or reflecting height. The trapped ray will lose energy by absorption and scattering on reflection. At turning, the geometrical optics approximation is violated and energy can be lost via diffraction, scattering by turbulence, or other physical processes.

The *M*-profile provides a ready means to establish the layers that may trap electromagnetic waves. Figure 4.19 presents an illustration of an elevated ducting layer. A ray launched at a 0° elevation angle at height z_B will propagate upward with an increasing local elevation angle as required by Snell's law until reaching height z_0. At heights between z_0 and z_T, the local elevation angle decreases with increasing height until the ray reaches the upper turning point with a local elevation angle of 0° at z_T. At this turning point, the ray may bifurcate and some energy propagate or tunnel upward to start another ascending ray at a 0° elevation angle. The remaining energy will propagate back downward.

The initial height of the 0° ray is at its lower turning point for the downward directed ray in the duct. Rays launched at heights between z_B and z_0 with a 0° initial elevation angle (at a lower turning point for the ray) will reach an upper turning point at the height between z_0 and z_T where the *M*-value matches the *M*-value at the launch point. Rays launched at heights between z_0 and z_T with a 0° initial elevation angle (at an upper turning point

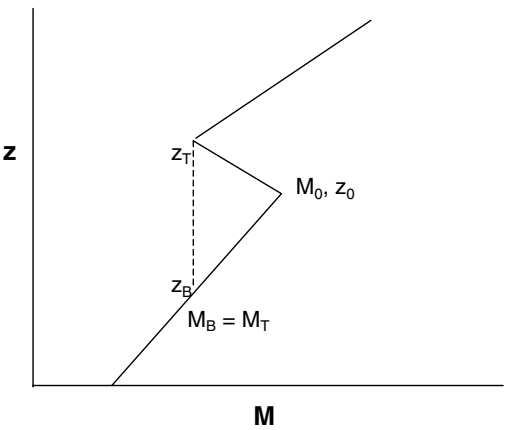

Figure 4.19 *M*-profile for an elevated duct.

for the ray) will reach a lower turning point at the height between z_B and z_0 where the M-value matches the M-value at the launch point.

All that is needed to cause a duct is a layer having a decrease in M-value with height. If the M-values at heights below the layer with decreasing M are always above the lowest M-value in the region of decrease, the duct is a ground-based duct. Referring again to Figure 4.19, if the Earth's surface were at a height between z_0 and z_T, the duct would be identified as a ground-based duct.

For efficient trapping, the duct thickness must be large compared to the wavelength of the electromagnetic radiation. This thickness requirement is necessitated for the application of geometrical optics. The possibility of propagation in thin ducts may be analyzed using physical optics,[5] a full wave solution,[6,7] or the parabolic approximation to the wave equation.[8] If the duct is too thin, trapping might not occur. If the duct is thick enough or the frequency high enough, ray tracing in the duct is sufficient. A number of model analyses have been published that provide guidance for the use of the geometric optics solution.[1,5,9] Figure 4.20 presents the predictions of several of the models. Kerr[5] and Dougherty and Hart (D&H)[9] present results that do not depend on the change in M, $\Delta M = M_0 - M_T$, within the duct. Bean and Dutton (B&D)[1] provide results that include the effects of a change in M. The critical frequency is an approximation to the lowest frequency for efficient trapping. Ducts may still affect propagation at frequencies lower than the critical frequency, but the losses for propagation along the duct may be high.

Rays trapped within a duct are confined within the ducting layer. Ray tubes can expand in the horizontal but not in the vertical. Path loss for propagation in ducts is therefore characterized by an inverse distance dependence instead of the usual inverse distance squared dependence for propagation in free space.

Figure 4.21 presents an example of ray trajectories in a ground-based duct. Note that the trapped rays were traced only through a single up-and-down cycle. If the initial elevation angle was greater than 0°, the ray

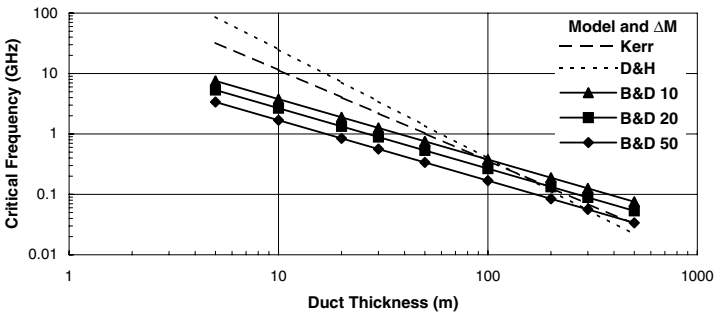

Figure 4.20 Critical minimum frequency for a duct.

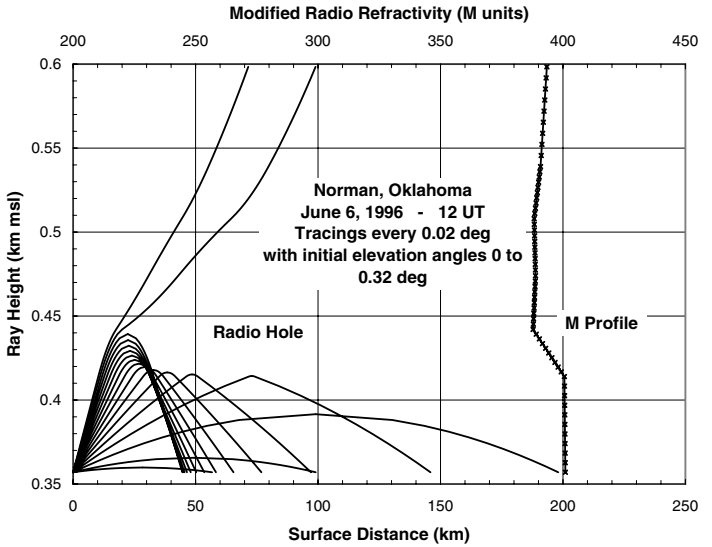

Figure 4.21 Ray trajectories in a ground-based duct.

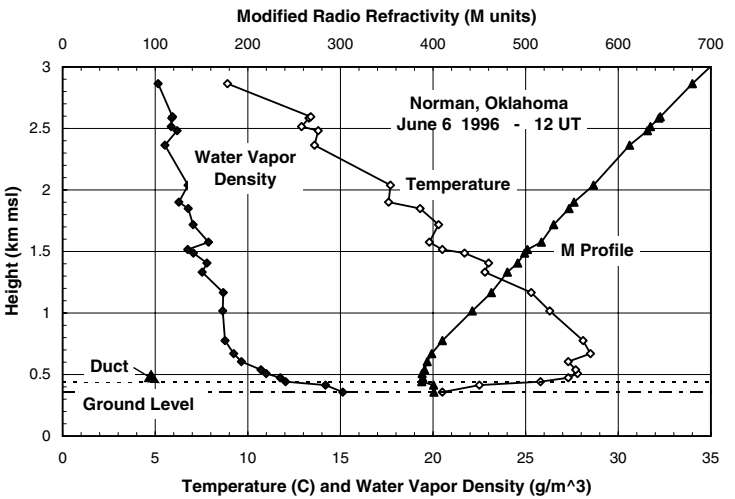

Figure 4.22 Temperature and water vapor density profiles for a ground-based duct.

was assumed to reach a reflecting surface when it propagated back down its initial height. The critical frequency computed by the B&D model for the *M*-profile shown in the figure was 0.39 GHz. The temperature and water vapor density profiles that produced the ground-based duct are presented in Figure 4.22. At the time of the RAOB sounding, the temperature near the surface had cooled by over 10°C, producing a temperature inversion. The water vapor density profile also showed a rapid drying above the surface

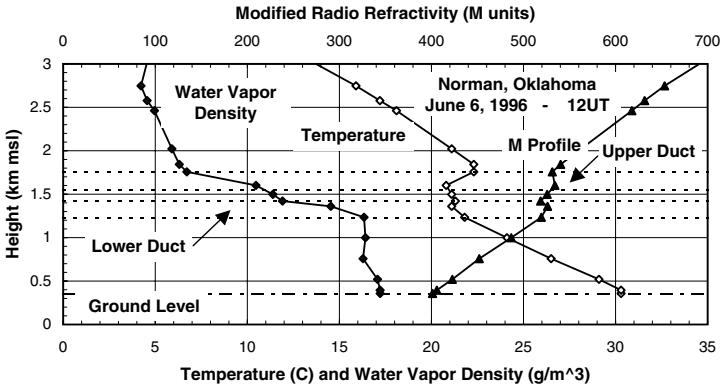

Figure 4.23 Temperature and water vapor density profiles for elevated ducts.

(see Figure 4.23 for the 12-h earlier sounding). These conditions combined to produce a ground-based duct. Similar temperature and humidity profiles occur over water,[10] where they cause an evaporation duct. Over land, these conditions often follow the occurrence of a thundershower. They can occur in coastal regions when warm dry air from the land flows out over cooler moist air in contact with the water.[5,11] Nocturnal radiation cooling of the Earth's surface can also produce strong temperature inversions and ground-based ducts.[11]

The RAOB obtained 12 h earlier showed the typical decrease in temperature with height throughout the planetary boundary layer (Figure 4.23), that is, up to a height of 0.9 km above ground level (1.2 km msl). Two temperature inversions are evident at higher altitudes in the figure, with significant drying occurring in each. The resulting *M*-profile indicates the occurrence of two elevated ducts. Ray trajectories for transmitters within each duct are shown in Figure 4.24. The critical frequency for the lower duct is 0.23 GHz and that for the upper duct is 0.34 GHz. Efficient coupling into these ducts is possible only for transmitters and receivers within the duct.

Figure 3.18 and Figure 3.19 display the 20-GHz attenuation time series for June 6, 1996, for Norman, OK. The attenuation data show the occurrence of two rainy periods, 05:00 to 10:00 UT (midnight to 5 a.m. local time) and from 21:00 UT into the next UT day. The time series for surface temperature and water vapor density are shown in Figure 4.25. The surface temperature cooled only a few degrees until a front moved by at 06:00 UT, followed by further surface cooling in rain at 07:00 UT. Surface water vapor density decreased abruptly after the first rainy period and then increased to the value at the surface shown in the 12:00 UT RAOB. From 12:00 UT on, the surface temperature increased due to afternoon heating until a second frontal passage with heavy rain, abrupt cooling, and drying at the surface.

A comparison of the temperature and water vapor profiles at 00:00 and 12:00 UT and 00:00 UT on the next day is presented in Figure 4.26. The profiles for 00:00 UT on June 6 show a capping inversion between 1.4 and

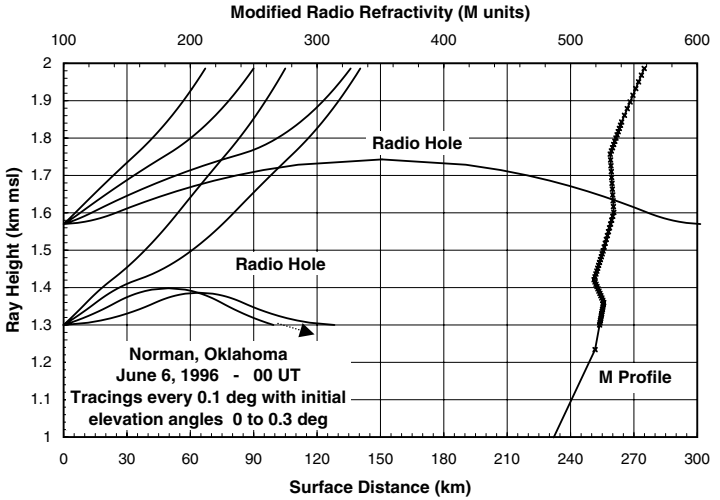

Figure 4.24 Ray trajectories in elevated ducts.

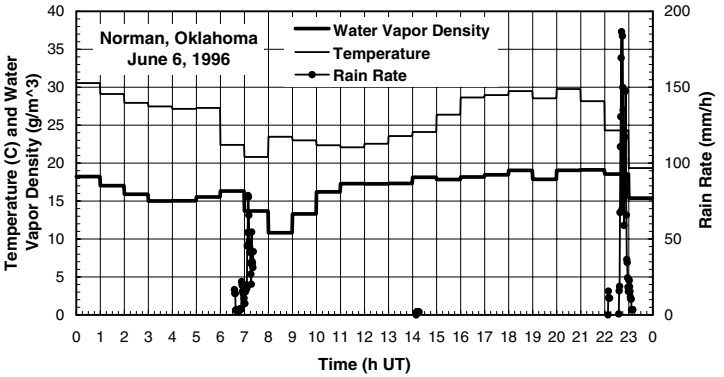

Figure 4.25 Time series of surface meteorological parameters for Norman, OK, for June 6, 1996.

1.8 km msl, with a reduction of nearly 10 g/m^3 in water vapor density between the moist air below and the dryer air above. The temperature profile for 12:00 UT reveals a strong temperature inversion at the surface and a sequence of minor temperature inversions in the 1.4- to 2.6-km height range. The final sounding for the day (local time) was in rain. The *M*-profiles showed the ducts described above and near standard refractive conditions in rain.

Figure 4.27 displays the potential temperature and specific humidity profiles for the times presented in Figure 4.27. Potential temperature is conserved in an unsaturated, well-mixed atmosphere with neutral stability.[12] A positive vertical gradient in potential temperature indicates a stable region

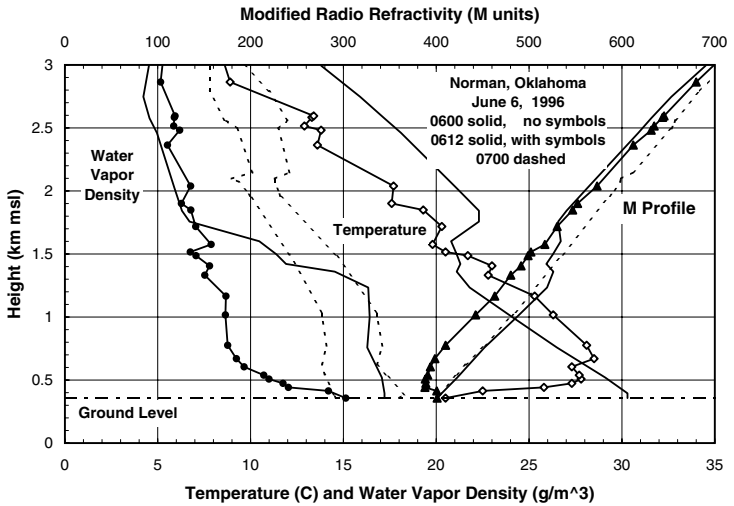

Figure 4.26 Temperature and water vapor density profiles for Norman, OK, for June 6, 1996.

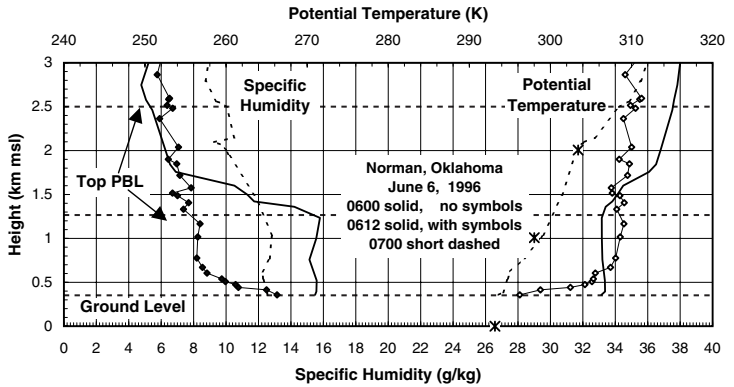

Figure 4.27 Potential temperature and specific humidity profiles for Norman, OK, for June 6, 1996.

of the atmosphere, whereas a negative gradient is unstable, allowing rising thermals when the sun heats the ground. The parcel theory describes the motion of a parcel of air relative to its environment when displaced adiabatically (without exchange of heat with its environment).[12,13] In an environment in hydrostatic equilibrium (see Equation 1.24), the vertical motion of a parcel of air is given by:

$$\frac{Dw}{Dt} = -g - \frac{1}{\rho}\frac{\partial p}{\partial z} = \frac{D^2(\delta z)}{Dt^2} \tag{4.2}$$

where w is the vertical component of the velocity, $\underline{v}$, of the parcel and $D/Dt = \partial/\partial t + \underline{v} \cdot \nabla$ the total derivative, p, ρ are the pressure and density of the air in the parcel, respectively, and δz the displacement of the parcel from its initial position. The pressure inside the parcel is assumed to take on the pressure of the environment:

$$\frac{\partial p}{\partial z} = \frac{dP_0}{dz} = -g\rho_0 \tag{4.3}$$

where P_0, ρ_0 are the environmental values. Then:

$$\frac{d^2(\delta z)}{dt^2} = -g\left(\frac{\rho - \rho_0}{\rho}\right) = -g\left(\frac{\theta_0(z) - \theta}{\theta_0(z)}\right) = -\frac{g}{\theta_0}\frac{d\theta_0}{dz}\delta z = -\mathbf{N}^2\delta z \tag{4.4}$$

where

$$\theta = \theta_0(z) - \frac{d\theta_0(z)}{dz}\delta z$$

because θ does not change with δz due to the assumed adiabatic displacement of the parcel.

Equation 4.4 is the equation for a simple harmonic oscillator with solution $\delta z = Ce^{-j\mathbf{N}t}$ with $\mathbf{N}$ the radian Brunt–Vaisalla frequency for buoyancy oscillations. For $d\theta_0/dz > 0$ the atmospheric layer is stable with the buoyancy force $g(\rho - \rho_0/\rho_0)$ opposing the motion of the parcel; for $d\theta_0/dz = 0$ neutral stability obtains and the atmospheric layer is well mixed with no buoyancy force produced to oppose parcel motion; and $d\theta_0/dz > 0$ for the layer is unstable with the buoyancy force acting to accelerate the parcel away from its initial position.

The 00:00 UT potential temperature profile in Figure 4.27 reveals an unstable layer between 0.4 and 1.2 km msl, indicative of solar heating of the ground, with thermals rising to the height of the strongly stable layer from 1.2 to 1.8 km msl. The strongly stable region is a capping inversion that stops the upward motion and provides a barrier to further upward transport of water vapor. The result is a layer that can produce one or more elevated ducts. The thermals displace the stable layer, producing buoyancy oscillations. Such oscillations can produce a wavelike motion of isopleths of radio refractivity, destroying the presumed spherical symmetry of the radio refractivity profile. These oscillations can launch internal gravity or buoyancy waves that propagate along the strongly stable layer.[13,14] The two-layer ducting structure evident in Figure 4.26 could be a single wavy layer that was sampled at several locations in the horizontal as the sounding balloon drifted through the layer as it rose.[15]

The 12:00 UT sounding in Figure 4.26 shows the effects of surface cooling. At heights above the surface layer, the sounding is close to neutral stability, with little change in specific humidity. The surface layer produced a ground-based duct. By 00:00 UT on June 7 (local time 7 p.m. on June 6), the atmosphere was nearly saturated after the heavy rain. For heights between 0.8 and 2 km msl, the relative humidity was above 97%. The symbols on the potential temperature curve are for a moist adiabatic profile, with the latent heat of condensation added to the parcel of air as it rises.[12] It is noted that in this case, no ducts are formed.

The planetary boundary layer (PBL) is a turbulent transition region between air motion at the surface of the Earth and the horizontal flow of air higher in the lower troposphere. Solar heating of the surface produces convective turbulence with rising thermals that generate a well-mixed layer of neutral stability capped by an inversion layer.[13] Under these conditions, the top of the PBL is taken at the height of the inversion. Sometimes in deep moist convection, a second, higher inversion forms that is then the top of the PBL. The variation or shear of the horizontal wind with height produces mechanical turbulence that effects a momentum transfer between the horizontal flow higher in the lower troposphere and the surface. When mechanical turbulence provides the transition region, the top of the PBL is taken at the height where the wind direction approaches a constant over a thicker layer of the atmosphere (Figure 4.28). The range of heights for the tops of the PBLs in the potential temperature and wind profiles for June 6, 1996, in Norman, OK, are indicated in Figure 4.27 and Figure 4.28. The thickness of the PBL can range from less than 0.1 km to more than 3 km. During the daytime in mid-latitude over land climates, the PBL thickness is of the order of a kilometer.

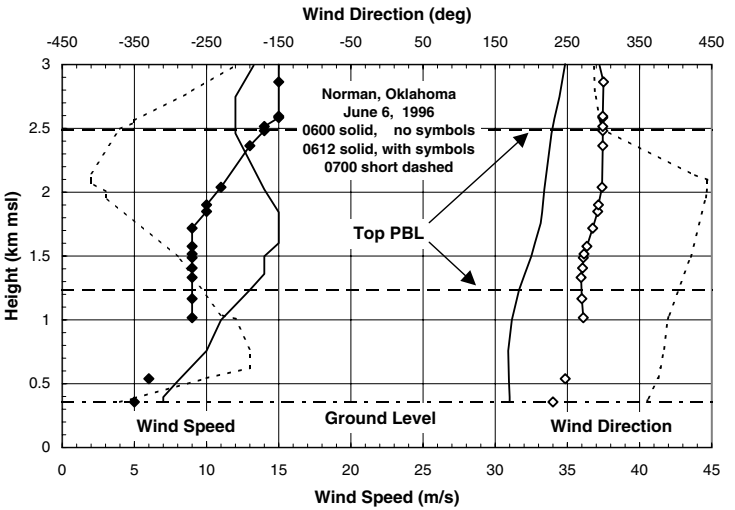

Figure 4.28 Wind speed and direction profiles for Norman, OK, for June 6, 1996.

The horizontal motions of air from different air masses at different heights in the troposphere are often in different directions. Internal horizontal boundary layers form between the streams of air from different source regions. These boundary layers are characterized by an increase in stability and a concentration of wind shear across the layer. Sometimes they produce elevated ducts that affect the performance or airborne search radars or air-to-air communication systems.

Although the horizontal layer assumption was made for the ray tracings within ducts, the atmospheric stability associated with the inversion layers that produced the ducts often leads to oscillations in layer height and internal gravity or buoyancy waves that perturb the ducts. The initial elevation angles for trapping were all less than 0.3° for the tracings displayed in Figure 4.21 and Figure 4.24. Buoyancy waves periodically change the local elevation angles at the duct needed for efficient coupling into the duct. These changes affect the initial elevation angles at the transmitter and receiver locations needed for coupling to the duct. Observations of simultaneously occurring initial elevation angles ranging from –0.5° to + 0.5° have been reported on a 31.5-km link at a frequency of 16.7 GHz.[16] Elevated duct coupling between ground-based terminals and nongeostationary orbiting satellites has also been reported.[17] In both cases, buoyancy wave perturbations of the elevated layer geometry were required to produce efficient, low-loss coupling into and out of the duct.

Propagation within a duct and coupling into and out of a duct can be modeled by using geometrical optics, physical optics, or other approximations to a multimode, full wave solution to the electromagnetic wave equation. Comparisons between model predictions and observations have not been satisfactory because of the difficulties entailed in determining the precise structure of the radio refractivity fields in space and time. Bean et al. produced a statistical analysis for the prediction of duct occurrences based on analyses of a collection of 5 years of RAOBs from 268 sites worldwide.[18,19] The limited response times of the temperature and humidity sensors on the balloons then available reduced the magnitudes of the derived gradients of radio refractivity. As a consequence, the negative *M*-gradients required for ducting were rarely observed and small positive gradients are often used to determine duct occurrence statistics. In a study of duct occurrence along the eastern coast of New Jersey during two weeks in August 1966, ground-based ducts were observed 40% of the time, were forecast to be less than 5% of the time by the Bean et al. statistics, and were forecast from simultaneous collocated RAOBs 25% of the time.[17] If an *N*-gradient of –100 N units/km were employed for duct prediction, the forecast occurrences would be 10% of the month of August from the Bean et al. predictions and nearly 60% of the time from the collocated RAOBs.[19] However, the false alarm rate would have been 38% for the collocated RAOBs.

4.2 *Path delay*

Propagation along a ray path would produce time delays relative to propagation between the ray end-points if no atmosphere were present. The equations for the physical ray path length, L_S, and electrical phase path length, L_P, are given in Section 2.5 and Section 2.6. The range error is a measure of propagation delay. It is the excess distance or range to a target that a radar would report if the observed time delay were converted to distance by using the speed of light in a vacuum. The range error is composed of two parts: (1) the excess physical path length over the straight line between the ray end-points that would occur in a vacuum and (2) the change in propagation delay due to the difference between the propagation velocity along the ray in the atmosphere and the speed of light in a vacuum but along the same physical ray path. It is noted that for propagation through a dispersive medium such as the ionosphere, the group velocity should be used to calculate the range error (see Figure 1.38).

4.2.1 *Range error*

Range errors for the ray trajectories presented in Figure 4.1 are displayed in Figure 4.29. For initial elevation angles between 0° and 0.4°, the range errors for a target at a height of 0.9 km msl from a radar at a height of 0.357 km msl are less than 28 m. These results are for the *M*-profile displayed in the figure. For propagation through the entire atmosphere up to a height of one Earth radius, the range errors are shown in Figure 4.30 as a function of frequency for mid-latitude models with maximum and minimum ionospheric effects. The range errors as a function of the initial elevation angle are shown in Figure 4.31 for a frequency of 0.3 GHz and the same mid-latitude models. Figure 4.32 presents range error as a function of height for a

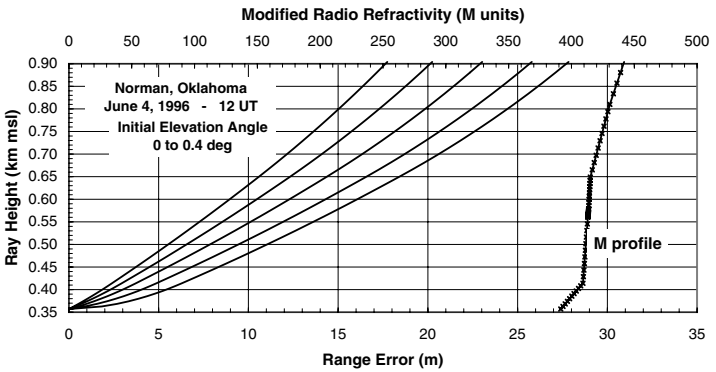

Figure 4.29 Low initial elevation angle range error profiles trajectories for Norman, OK, for June 4, 1996, at 12:00 UT.

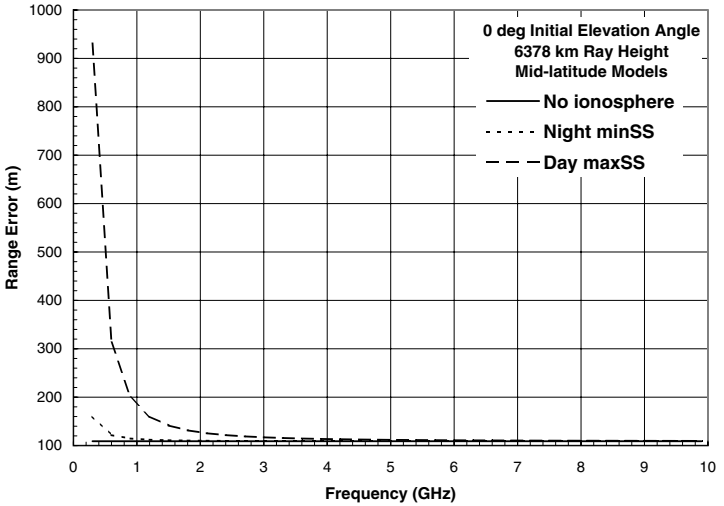

Figure 4.30 Range error at 0° initial elevation angle as a function of frequency at one Earth radius height for the mid-latitude daytime maximum and nighttime minimum ionosphere model.

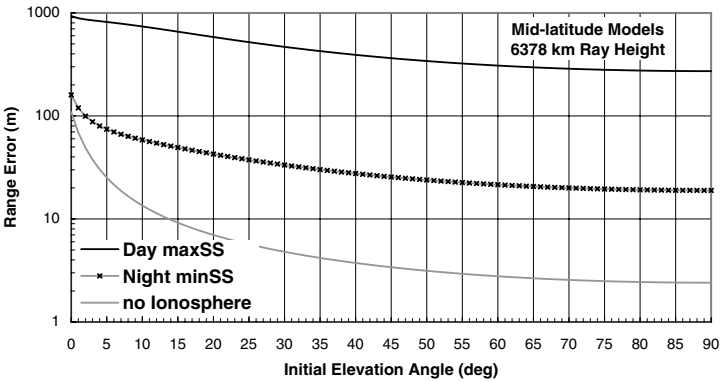

Figure 4.31 Range error as a function of initial elevation angle for 0.3 GHz at one Earth radius height for the mid-latitude daytime maximum and nighttime minimum ionosphere model.

0° initial elevation angle ray launched at a height of 0 km msl. Roughly 37% of the range error for propagation through the atmosphere occurs by a height of 1 km and 97% by a height of 26 km.

Range error statistics were calculated for the mid-latitude RAOB data set used to generate the average and RMSD mid-latitude regression statistics for elevation angle error presented in Figure 4.15 and Figure 4.16. The average and standard deviation of the range errors are displayed in Figure 4.33 as a function of initial elevation angle. On average, the standard deviation

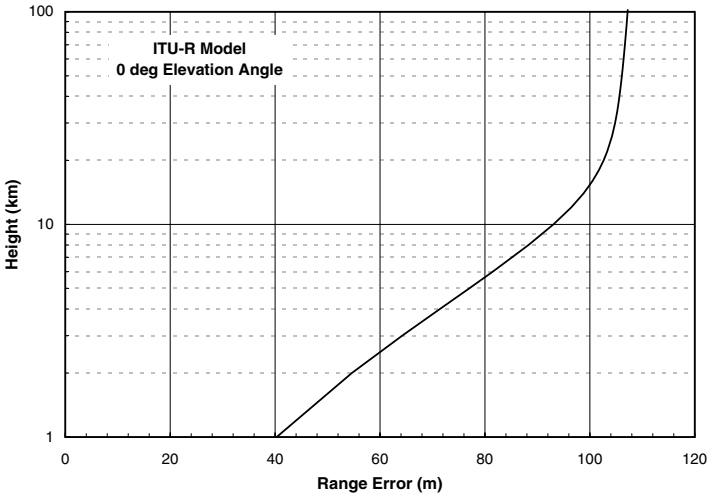

Figure 4.32 Range error as a function of ray height for a 0° initial elevation angle calculated for the ITU-R model atmosphere.

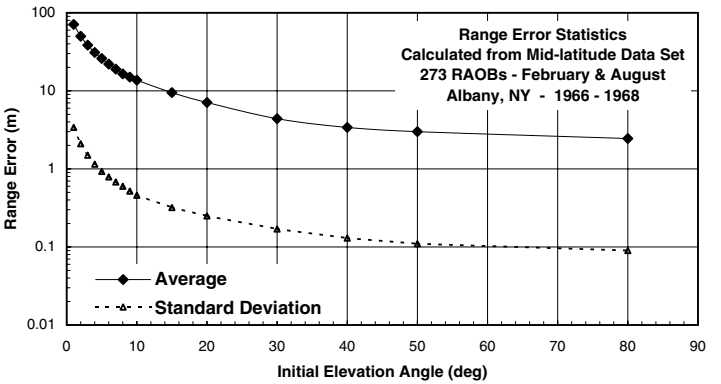

Figure 4.33 Range error statistics for a mid-latitude site.

of range error is less than 4% of the average value. The variations in range error, $\mathbf{e}_R$, along a path are primarily due to the path-integrated variations in water vapor concentration along the path.

$$\mathbf{e}_R \approx L_P - L_S = \int_{ray} (n' - 1) ds = \int_{ray} N \cdot 10^{-6} ds = \int_{ray} \left(N_D + N_W \right) \cdot 10^{-6} ds \qquad (4.5)$$

where N_D = 77.6 (P/T) and N_W = 3.75 × 10^5 $(PV/T)$are the dry and wet components of the radio refractivity, respectively. For propagation through the atmosphere, the integral over the dry term can be related to surface pressure by using Equation 1.26:

$$\int_{\text{ray}} N_D \cdot 10^{-6} ds \approx \left(\frac{0.0776}{\sin(\alpha_0)} \right) \int_z^{\infty} \frac{P(h)}{T(h)} dh = \left(\frac{K_D P(z)}{\sin(\alpha_0)} \right); \quad \alpha_0 > 10^\circ \tag{4.6}$$

where $K_D = 0.00227$ when h is in kilometers, range error in meters, and surface pressure in hPa. The restriction on initial elevation angle is required to enable the use a straight ray over a flat Earth approximation.

The wet term is more complex because that component of radio refractivity is proportional to the ratio of water vapor density to absolute temperature. The wet term can be approximated using the mean value theorem:

$$\int_{\text{ray}} N_W \cdot 10^{-6} ds \approx \frac{373}{\sin(\alpha_0)} \int_z^{\infty} \frac{P_V}{T^2} dh = \frac{1.72}{\overline{T} \sin(\alpha_0)} \int_z^{\infty} \rho_V(h) dh = \frac{K_V}{\overline{T} \sin(\alpha_0)} W \tag{4.7}$$

where $\overline{T}$ is the mean value for absolute temperature in the surface layer where the water vapor is concentrated, W the total precipitable water (g/cm^2 or cm), and $K_V = 17.2$. The approximations in Equation 4.6 and Equation 4.7 are compared with the exact calculations in Figure 4.34. For this figure, the surface value of absolute temperature was used to approximate the mean value in the surface layer. Multifrequency radiometer observations are sometimes used to estimate total precipitable water, especially when clouds are absent.[20]

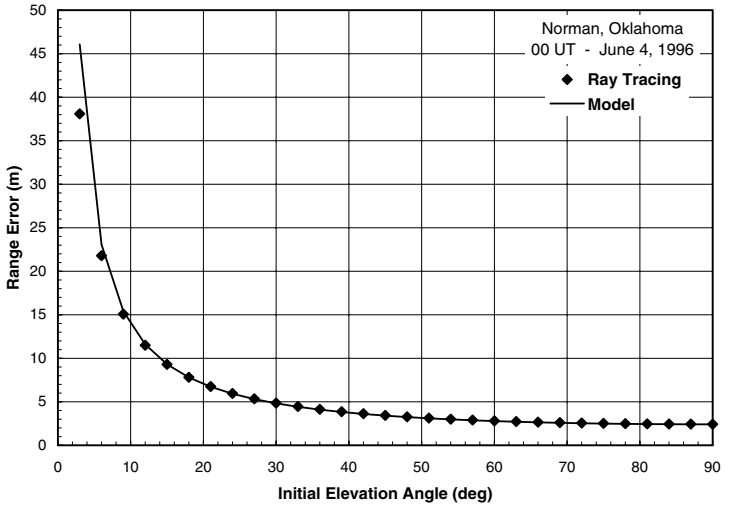

Figure 4.34 Range errors calculated from ray tracings for Norman, OK, for June 4, 1996, at 12:00 UT compared with the model using surface data and a precipitable water estimate.

Uncertainties in the estimate of phase shifts or range errors on propagation paths affect the measurement accuracies of long baseline interferometers and position estimates made by using global positioning satellites (GPS). GPS observations use two frequency observations on a path to remove ionospheric phase shifts. The phase-correction procedure makes use of the dispersion relationship for propagation through the ionosphere (see Equation 1.21).[21] Currently, GPS phase shift observations are used to map water vapor changes in the troposphere. One application of interest is the use of GPS to estimate vertical profiles of radio refractivity in over-water ducts.[22]

4.2.2 *Multipath*

The range errors for the ray trajectories presented in Figure 4.2 are displayed in Figure 4.34 and Figure 4.35. Within the duct, rays were traced only to the first turning point. The range errors varied from 12.1 to 16.1 m for the trapped rays. The trapped rays had initial elevation angles ranging from 0° to 0.24°. Internal atmospheric multipath was possible where trapped rays crossed. Figure 4.36 illustrates a case of crossing rays. In this case, the upper ray has a smaller path delay because the radio refractivity values were lower along the upper path. From the initial location of the two rays to the second crossing point, the difference in electrical path length was 0.5 m or many wavelengths at 20 GHz. The differences of the local elevation angles were 0.16° at the initial end of the paths and 0.18° at the other end. Waves transmitted over both paths would interfere at the receiving end.

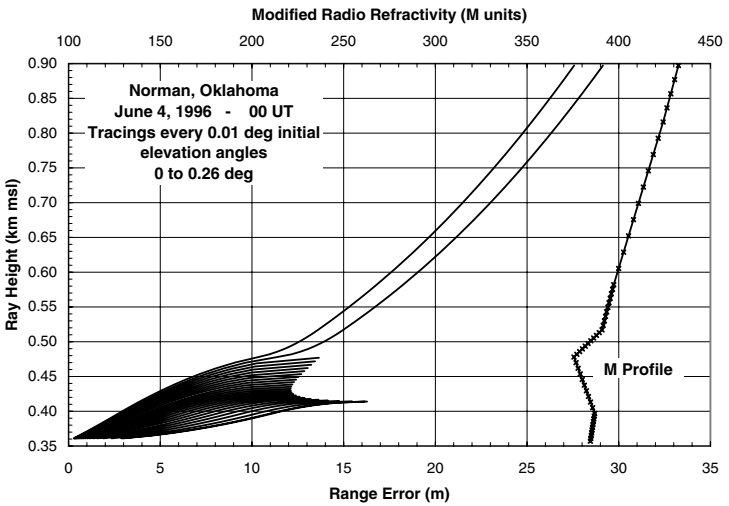

Figure 4.35 Range error calculations within a duct for Norman, OK, for June 4, 1996, at 00:00 UT.

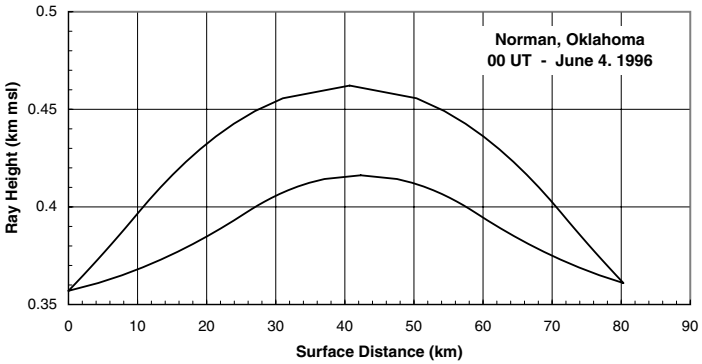

Figure 4.36 Multipath ray trajectories within a duct for Norman, OK, for June 4, 1996, at 00:00 UT.

Slight variations in radio refractivity along either path could cause a switch from constructive to destructive interference. Depending on the beamwidths of the transmitting and receiving antennas, the resultant signal could vary over a wide range of values. For identical antenna gains in the directions of each ray and no gaseous absorption, the signal levels could vary from + 5.7 to –22.2 dB relative to the signal on the upper path. However, at 20 GHz, the difference in gaseous absorption on the two paths would reduce the variation to +3.3, –5.3 dB relative to the signal on the upper path. If additional multipath due to ground or obstacle reflections were present, the signal levels could vary over a wider range.

Webster and Scott reported internal atmospheric multipath observations on a 31.5-km path at 16.7 GHz.[16] They show several multipath events when the angles of arrival on the individual rays showed variations with periods ranging from 2 to 5 min.. The expected periods for buoyancy oscillations on thin stable layers are of the same order of magnitude. The calculated minimum periods for the rays in Figure 4.36 were 4 min for the lower ray and 5 min for the upper ray. The resulting multipath fading would have shorter intervals between signal level minima. The signal amplitude data that Webster and Scott presented showed fades with times between minima on the order of the angle-of-arrival periods to shorter intervals. The figures they presented showed intervals with strong fading that would last for an hour or more.

The buoyancy oscillations that perturbed the ducting layers provided time-varying geometries that could produce three or more resolvable rays. In addition, ground-reflected rays within the duct could increase the count by several more. The time delay between the two rays depicted in Figure 4.36 was of the order of 1.7 ns (for a 0.5-m path length difference). For the shorter path reported by Webster and Scott, the time delay differences could be closer to a nanosecond. For path length differences of the order of 0.5 m, the path length difference is 33 wavelengths at 20 GHz. Small fluctuations in path length due to wave-induced changes in geometry and radio refractivity

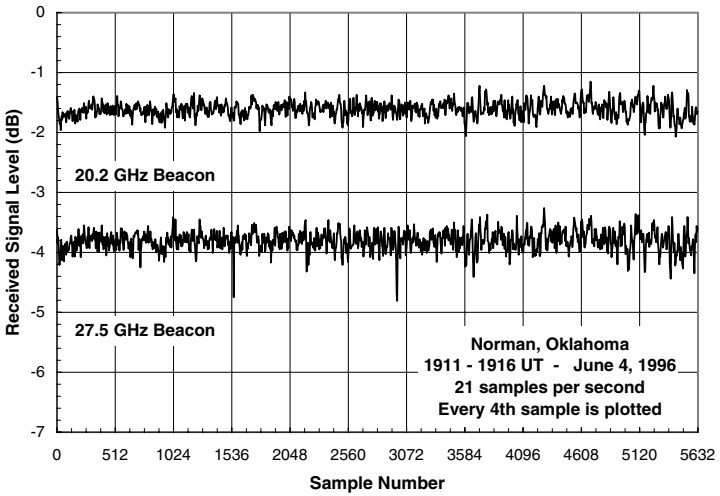

Figure 4.37 High data rate time series for Norman, OK, for June 4, 1996, at 19:00 UT.

differences caused by water vapor density variations would, over time, create a uniform distribution of phase difference between the two ray paths. Simulations of amplitude statistics for the combination of five or more paths, each with an uncorrelated uniform random distribution of phase over the range 0 to 2π radians, result in a Rayleigh distribution. Observations of internal atmospheric multipath amplitude statistics often result in a Rayleigh distribution.

4.3 Scintillation

Scintillation is usually identified as the cause of rapid fluctuations in signal amplitude, phase, and angle or arrival that are evident on propagation paths through the ionosphere and lower atmosphere. Figure 4.37 displays a short time series of the received signal level in decibels from the Advanced Communications Technology Satellite (ACTS) observed between 19:10 and 19:16 UT on June 4, 1996, at Norman, OK. The 1-min average 20-GHz attenuation time series for this day is given in Figure 3.14. Attenuation by clouds was identified as the cause of attenuation in the first few hours UT. The beacon attenuation time series showed both rapid and slower variations, with the signal remaining within a 0.2-dB range of values over the rest of the day. Scintillation events during times with clouds and rain are introduced in Section 1.4.2.5.2 and illustrated in Figure 1.65 through Figure 1.68.

4.3.1 ACTS observations

The time series displayed in Figure 4.37 was obtained by using the high data rate recording mode available at the ACTS Propagation Terminal (APT).[23] Ten minutes of observations were collected each hour for several of the ACTS

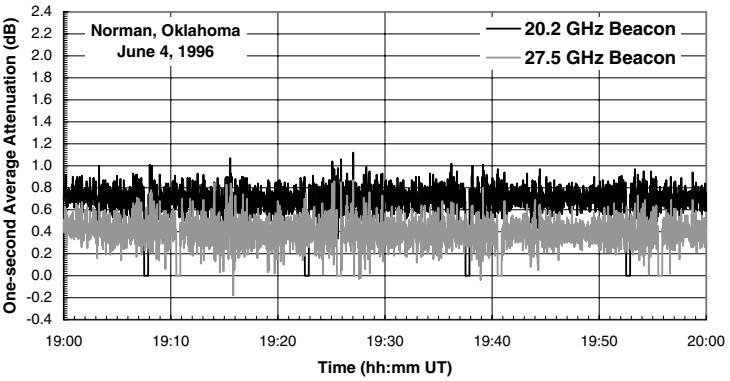

Figure 4.38 One-second average time series for Norman, OK, for June 4, 1996, at 19:00 UT.

sites for several of the years of data collection. The sampling rate was 21 per/second for both beacons. The collected data were received signal level in decibels, with an arbitrary reference level. Calibration could be made by comparing the high data rate observations with the calibrated 1-sec average attenuation observations presented in Figure 4.38. The observations displayed in this figure show the periodic radiometer calibrations by 23-sec duration 0-attenuation events spaced by 15 min. During radiometer calibration, the receiver input for that frequency was switched to a dummy load preventing the beacon receiver from making signal level observations. The times for calibration at the two frequencies were staggered, and therefore observations could be made continuously at least at one of the two frequencies. The high data rate collection interval was fit between calibration periods.

The time series presented in Figure 4.37 and Figure 4.38 were relatively quiet, with rapid fluctuations that spanned a range of up to 0.6 dB at the high data rate with a reduction in the range of attenuation values to about 0.3 dB with 1-sec integration. These time series were from the 19:00 to 20:00 UT time when the radiometer-derived attenuation values showed no indication of cloudiness. Figure 4.39 and Figure 4.40 show the 60-sec average attenuation time series for the entire day. The 60-sec attenuation standard deviation values calculated from the 1-sec average values collected within a minute are also given. Two types of scintillation are shown: wet scintillation caused by the presence of clouds during the 00:00 to 04:00 UT time interval, the 13:00 to 15:00 UT interval and again between 18:00 and 19:00 UT; and clear-air scintillation during the intervals when no increases relative to receiver noise are evident in the radiometer standard deviation values. The clear-air scintillation is caused by random phase changes produced by radio refractivity fluctuations in turbulence along the path. This form of scintillation is a result of diffraction by phase changes in a plane perpendicular to the propagation path (a phase changing screen).[24,25] Wet scintillation is

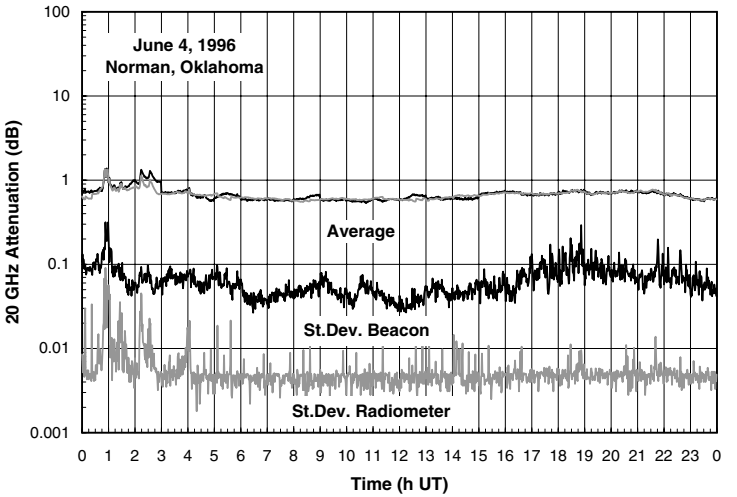

Figure 4.39 One-minute average and standard deviation time series at 20.2 GHz for Norman, OK, for June 4, 1996.

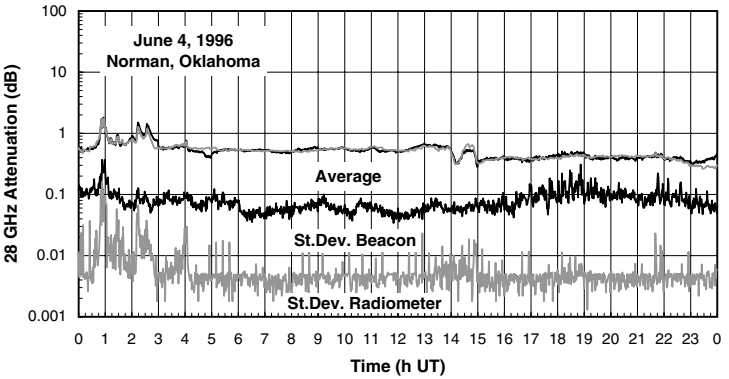

Figure 4.40 One-minute average and standard deviation time series at 27.5 GHz for Norman, OK, for June 4, 1996.

caused by random variations in absorption by cloud droplets or rain drops. The latter is detectable by a radiometer whereas the former is not.

Scintillation is usually represented by second-order fluctuation statistics for the path: by the variance, autocorrelation function, or power spectrum. The square root of the variance is plotted in Figure 4.39 and Figure 4.40. The average power spectra are plotted in Figure 4.41 and Figure 4.42. The spectra labeled HDR are from the high data rate observations. Each spectrum was calculated by averaging 11 contiguous 512-point FFTs. Each averaged spectrum is for 4.4 min of observations. The 1-sec spectrum is the average of 7 contiguous 512-point FFTs that each span 8.5 min of observations. The spectra

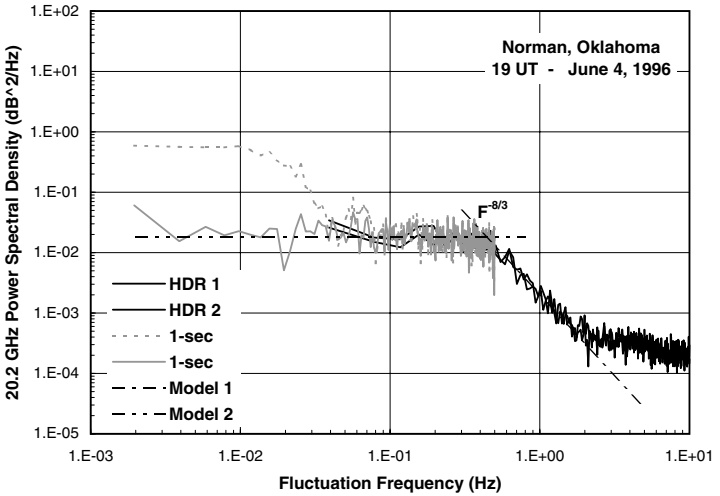

Figure 4.41 Scintillation spectra for the 20.2-GHz beacon for Norman, OK, for June 4, 1996, at 19:00 UT.

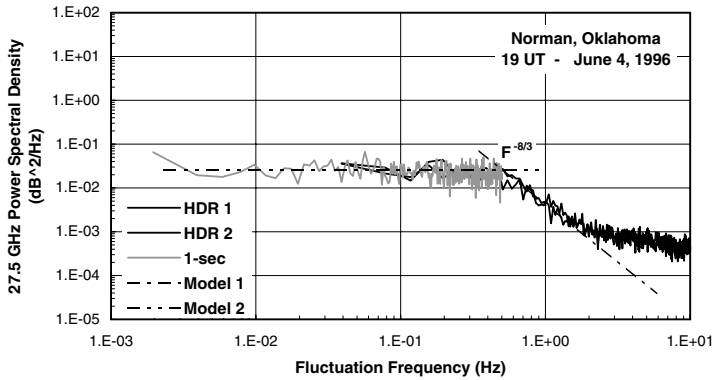

Figure 4.42 Scintillation spectra for the 27.5-GHz beacon for Norman, OK, for June 4, 1996, at 19:00 UT.

were computed without the use of windowing to better preserve their shape. Figure 4.41 shows two 1-sec spectra, one for the raw data with the calibration intervals at 0-dB attenuation (the dashed curve) and the other with the calibration intervals filled in by scaling observations from the other frequency channel. Data collected for 30 sec prior to each calibration interval were used to calculate the scaling ratio.

The expected shape of the spectrum for scintillation produced by clear-air radio refractivity fluctuations has a flat low fluctuation-frequency, F, asymptote (Model 2) and an $F^{-8/3}$ power law high fluctuation frequency asymptote (Model 1).[24,26] These model curves were fit to the spectra in

Figure 4.41 by eye. At fluctuation frequencies greater than 2 Hz, the high data rate spectra tail off into receiver noise. The second-order statistics were stationary for the 1-h period considered in Figure 4.37 through Figure 4.42. The three-dimensional spatial fluctuation spectrum for specific humidity variations in turbulence, the variations of a passive additive in the flow that contribute to radio refractivity variations, is often modeled by a k^{-p} segment in the inertial subrange, where k is the spatial wavenumber and $p = 11/3$.[24,27] The temporal fluctuation spectrum then has a high-frequency asymptote of $F^{-(p-1)}$ when the spatial fluctuations in radio refractivity that contribute to F are still in the inertial subrange. The Rytov approximation used to calculate the spectrum in the limit of weak scintillation employs integration along the path, with the result that only the cross path phase fluctuations contribute to the signal amplitude spectra. For turbulent fluctuations confined to a thin layer, the corner fluctuation frequency, F_C, at the intersection of Model 1 and Model 2, corresponds approximately to the flushing rate for the first Fresnel zone on the propagation path, that is,

$$F_C \propto \frac{v\sqrt{f}}{\sqrt{D}}$$

where v is the drift velocity of the irregularity structure, f is the carrier frequency, and D the distance to the irregularity layer.[25, 26]

The model curves in Figure 4.42 were scaled from the model curves in Figure 4.41, using the predictions of clear-air scintillation theory. The expression for the variance of the logarithm of the amplitude fluctuations is given by: [24, 28]

$$\sigma_\chi^2 = \left(\frac{20}{\ln(10)}\right)^2 0.56\left(\frac{2\pi f}{c}\right)^{7/6} G(A) \int_{\text{layer}} C_n^2(x) x^{5/6} dx \qquad (4.8)$$

where $C_n^2(x)$ is the refractive index structure constant that describes the intensity of the index of refraction fluctuations; x the distance from the closest terminal; G the aperture-averaging factor, which is a function of aperture area, σ_χ is in decibels, and the integral is over the extent of the turbulent layer that crosses the propagation path. In this equation, the transmitted wave is assumed to be a plane wave incident on the turbulence and, if the receive aperture is small in comparison to the size of the first Fresnel zone at the turbulent layer, that is, a point receiver with an isotropic antenna pattern, $G = 1$. For a thin elevated layer on an Earth-space path, the equation may be simplified to:

$$\sigma_\chi^2 = 4.65 \cdot 10^8 f^{7/6} C_n^2 D^{5/6} LG \qquad (\text{dB}^2) \qquad (4.9)$$

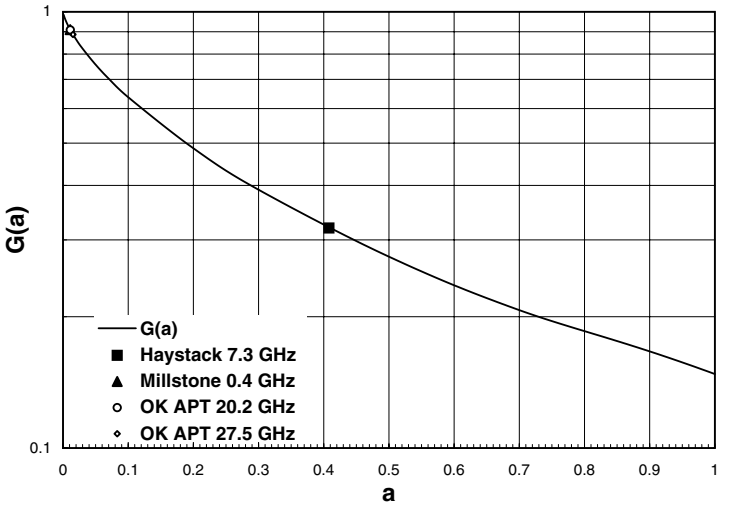

Figure 4.43 Aperture-averaging function.

where f is in gigahertz, L is the length of the turbulent layer along the path (km), D the distance to the turbulent layer (km), C_n^2 the intensity of the refractivity turbulence in the layer ($m^{-2/3}$) and $G(A,f,D)$ is the aperture-averaging factor. G may be approximated by:[26]

$$G(a) = 3.8637(a^2+1)^{11/12}\sin\left(\frac{11}{6}\tan^{-1}\left(\frac{1}{a}\right)\right) - 7.0835a^{5/6} \qquad (4.10)$$

where

$$a = 1.557\cdot 10^{-3}\frac{A\eta_A f}{D}$$

with A the antenna aperture area(m^2), η_A the aperture efficiency, and f and D as given in Equation 4.9.

The aperture-averaging factor is presented in Figure 4.43. The symbols give the averaging function values for the Oklahoma APT and for much larger aperture antennas that were used in a study of tropospheric scintillation at low elevation angles. The calculations for the different antennas were for a turbulent layer at a height of 1 km above ground level. The results for the Haystack and Millstone antennas will be considered in Section 4.3.2. The observed standard deviations of the attenuation values for the hour of measurements used to generate the spectra in Figure 4.41 and Figure 4.42 were 0.097 dB at 20.2 GHz and 0.111 dB at 27.5 dB. When the frequency-dependent factors in Equation 4.9 are used to scale from 20.2 to 27.5 GHz, the predicted

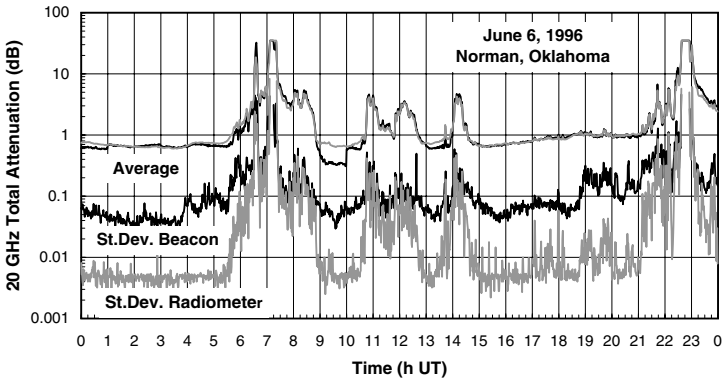

Figure 4.44 One-minute average and standard deviation time series at 20.2 GHz for Norman, OK, for June 6, 1996.

value at 27.5 GHz is 0.114. This scaling procedure was used to determine the model curves in Figure 4.42. The corner frequency was also increased by $\sqrt{27.5/20.2}$ in accordance with the definition of corner frequency. The observed spectra are consistent with the theoretical predictions, including the use of frequency scaling to derive the model curves for Figure 4.42.

Scintillation observations made on June 6 included periods with clouds and rain. Figure 4.44 presents the scintillation data for 20.2 GHz together with the attenuation data for the same period. The standard deviation of the attenuation values derived from the radiometer observations show receiver noise between 00:00 and 05:00 UT, that is, clear-air scintillation during that time period. Clouds producing up to 1 dB of attenuation were evident during each of the hours during the 15:00 to 21:00 UT period. Rain affected the path during the rest of the day. Time series for the 19:00 UT hour with clouds is presented in Figure 4.45 and Figure 4.46. The high data rate observations show wider ranges of received signal levels than do the data for clear-air conditions (see Figure 4.37). The 1-sec average samples for the entire hour also show wider ranges of attenuation values with small changes in the average level from one 10-min interval to the next.

The 20-GHz beacon scintillation spectra are given in Figure 4.47. The model curves for clear-air scintillation were fit to the 20.2 GHz data by eye and scaled to 27.5 GHz for Figure 4.48. At fluctuation frequencies below about 0.02 Hz, an increase in power spectral density is observed with a slope of $F^{-5/3}$. The low frequency segment of the spectrum displayed in Figure 4.48 also has the same slope. Power law spectra with an $F^{-5/3}$ slope are often seen in terrestrial and Earth-space line-of-sight observations of attenuation by clouds or by rain. The time series of receiver power level fluctuations observed during the 12:00 UT hour with rain are presented in Figure 4.49 and Figure 4.50.

The high data rate time series show rapid fluctuations riding on much slower signal level changes. The 1-sec average samples also show the rapid

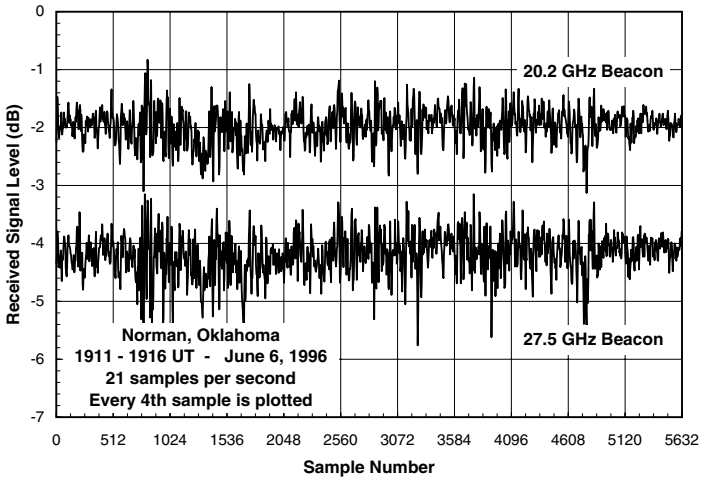

Figure 4.45 High data rate time series for Norman, OK, for June 6, 1996, at 19:00 UT.

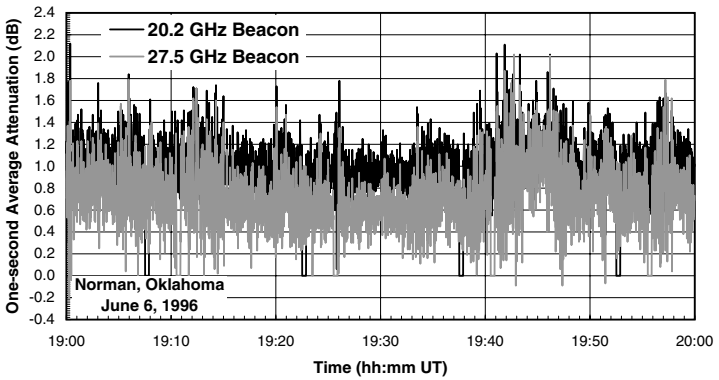

Figure 4.46 One-second average time series for Norman, OK, for June 6, 1996, at 19:00 UT.

fluctuations riding on the much larger changes in attenuation level that occurred within the hour. Although the data appear locally stationary in the variance, the mean value changes widely over the 1-h period. As before, the calibration intervals were filled in using frequency scaling from the attenuation observations from the other frequency channel. The time series was broken into seven consecutive blocks of 512 sec and the power spectra calculated for each block were averaged to produce the spectra displayed in Figure 4.51 and Figure 4.52. The low-frequency asymptote for these spectra is again $F^{-5/3}$. In this case, the model was scaled from the 20.2-GHz spectrum to the 27.5-GHz spectrum by using the ratio of attenuations for light rain and the Fresnel zone size scaling employed for a corner frequency. The model

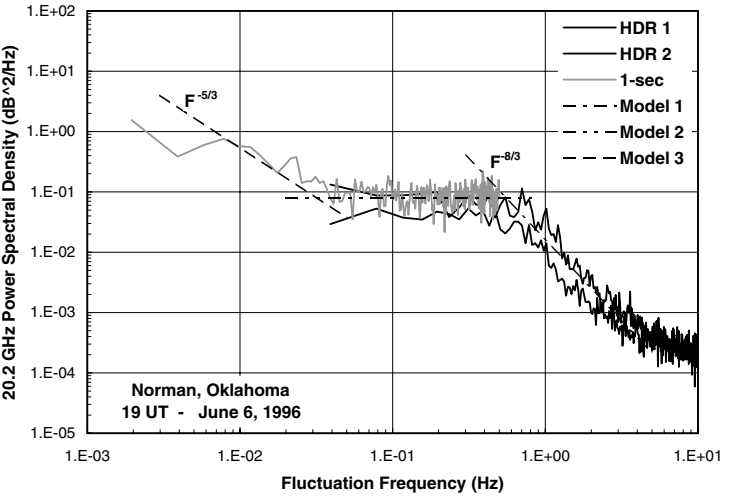

Figure 4.47 Scintillation spectra for the 20.2-GHz beacon for Norman, OK, for June 6, 1996, at 19:00 UT.

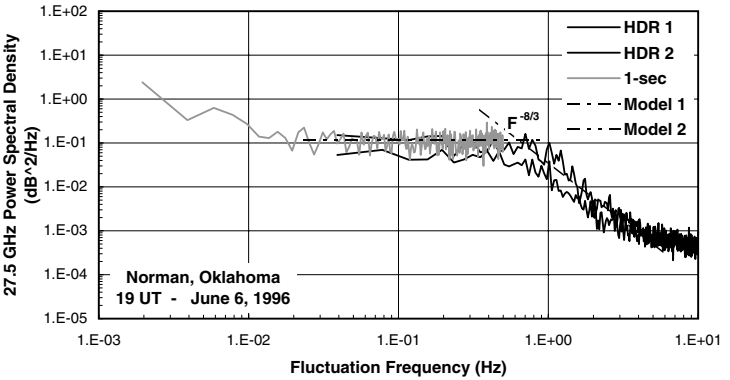

Figure 4.48 Scintillation spectra for the 27.5-GHz beacon for Norman, OK, for June 6, 1996, at 19:00 UT.

matches the spectrum at each frequency. The high data rate spectra are consistent with a high frequency extension of the 1-sec spectra and show little change from one 5-min set to the next. Figure 4.53 and Figure 4.54 display spectra for another hour with rain. Again, the $F^{-5/3}$ low frequency asymptote is evident.

Theoretical analyses of clear-air scintillation suggest that the probability density function for signal level during a scintillation event is lognormal when the random process is stationary.[29] The attenuation histogram for the time series for clear-air scintillation is presented in Figure 4.55. The model distributions are lognormal (normal for values in decibels) with the mean

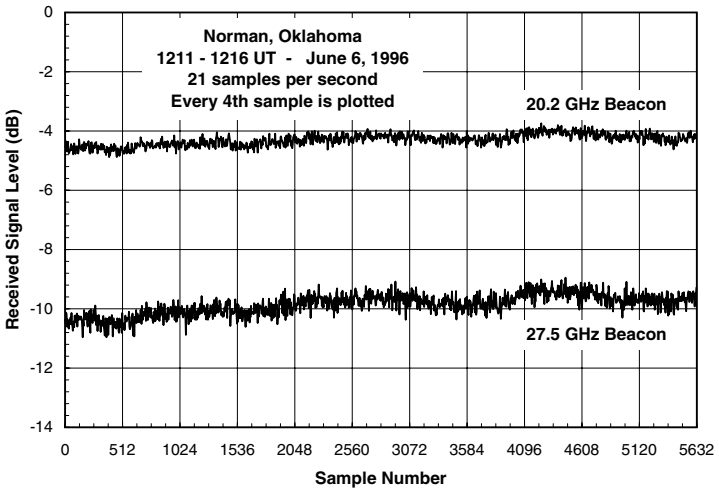

Figure 4.49 High data rate time series for Norman, OK, for June 6, 1996, at 12:00 UT.

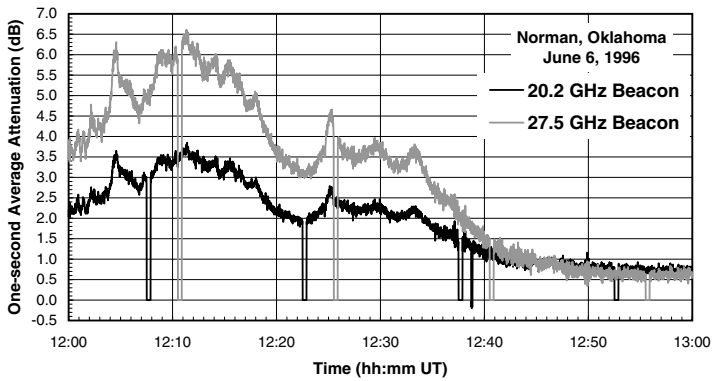

Figure 4.50 One-second average time series for Norman, OK, for June 6, 1996, at 12:00 UT.

and standard deviation parameters computed from the time series after frequency scaling by using data from the other frequency channel to fill in the calibration intervals. The theoretical model and observations are in agreement. The probability density for the hour with cloud and clear-air scintillation were also consistent with a lognormal distribution as shown in Figure 4.56. In both examples, the spectra displayed the $F^{-8/3}$ high fluctuation frequency asymptote. The two hours with rain did not produce stationary distributions or distributions that were lognormal. The histograms for the rain cases are presented in Figure 4.57 and Figure 4.58.

The long-term signal level distributions for clear-air scintillation may be constructed from the lognormal distribution for each stationary interval

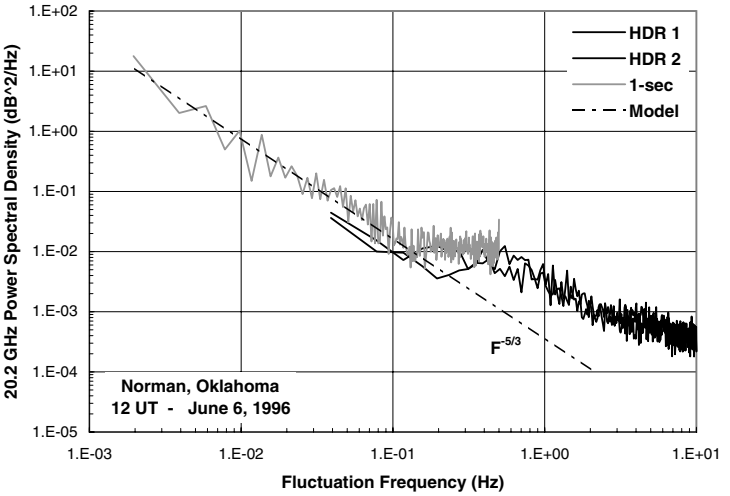

Figure 4.51 Scintillation spectra for the 20.2-GHz beacon for Norman, OK, for June 6, 1996, at 12:00 UT.

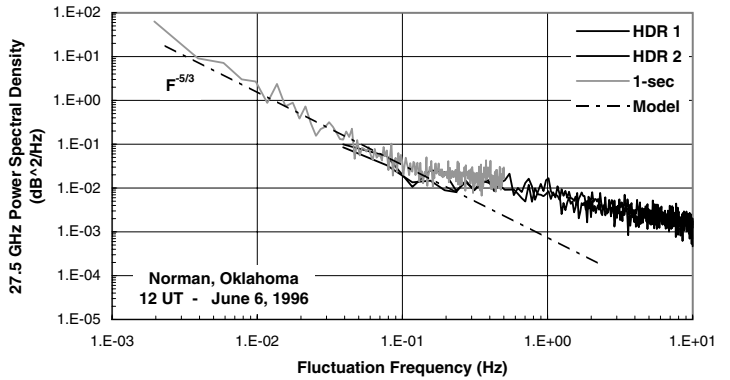

Figure 4.52 Scintillation spectra for the 27.5-GHz beacon for Norman, OK, for June 6, 1996, at 12:00 UT.

conditioned on the standard deviation value for that interval combined with the probability distribution for the standard deviation values.[29,30] Such a procedure is also conditioned on the requirement that the fluctuations are caused by clear-air scintillation. Figure 1.71 presented the annual empirical cumulative distribution functions (EDFs) for the observed standard deviation values at 20.2 and 27.5 GHz at the Norman, OK, ACTS site. These EDFs result from all possible causes of fluctuations. The plotted EDFs are for attenuation standard deviation values obtained from the beacon observations and for the standard deviations obtained from radiometer observations. The radiometer data provide statistics for fluctuations produced by absorption on the path:

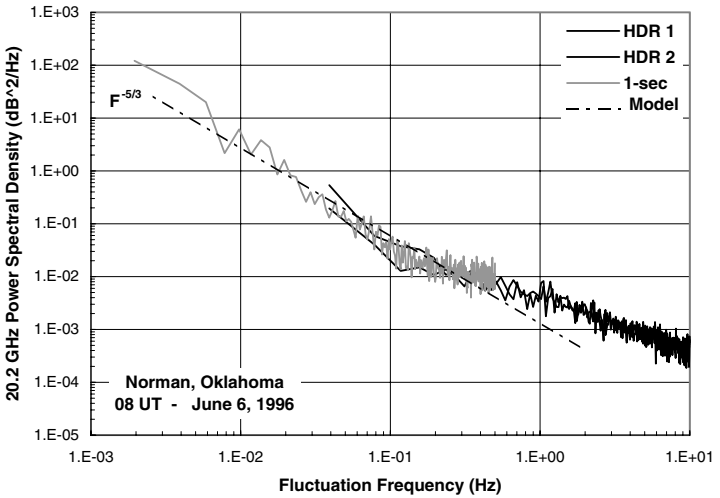

Figure 4.53 Scintillation spectra for the 20.2-GHz beacon for Norman, OK, for June 6, 1996, at 08:00 UT.

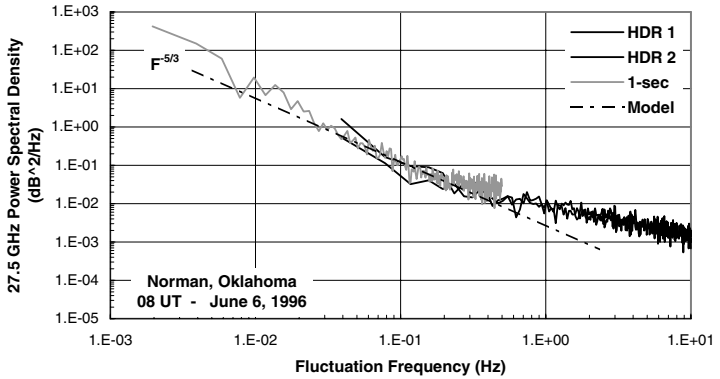

Figure 4.54 Scintillation spectra for the 27.5-GHz beacon for Norman, OK, for June 6, 1996, at 08:00 UT.

rain, clouds, water layer on a radome, or gaseous absorption. The beacon EDFs show higher standard deviation values at a given probability level than the radiometer EDFs for that probability level except perhaps at attenuation standard deviations higher than 3 dB when the uncertainties in the radiative transfer function approximations used to convert sky brightness temperature to attenuation become important.

The logarithmic scales used to present the EDFs in Figure 1.71 emphasize the low probabilities of exceedence and high standard deviation values to be associated with scintillation produced by rain and clouds. In Oklahoma, clear-air conditions occur for more than 10% of the year (or for total

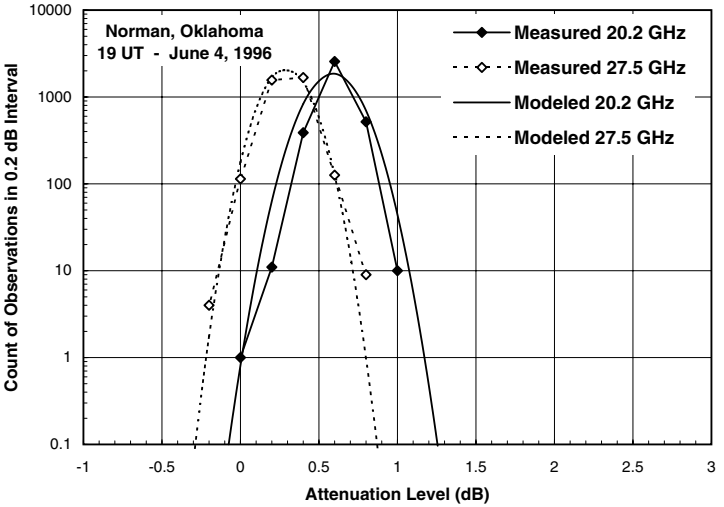

Figure 4.55 Measured and modeled signal level histograms for Norman, OK, for June 4, 1996, at 19:00 UT.

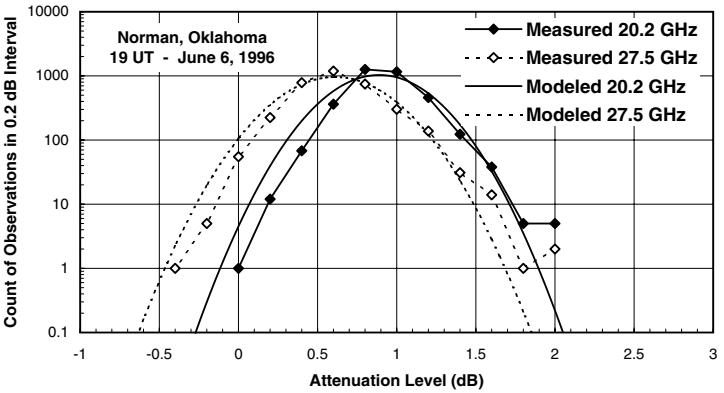

Figure 4.56 Measured and modeled signal level histograms for Norman, OK, for June 6, 1996, at 19:00 UT.

attenuation values less than about 1 dB) and rain only occurs less than 5% of a typical year (see Figure 1.101). The 1-sec average and 1-min average EDFs for Oklahoma are presented in Figure 4.59 and Figure 4.60, respectively. They are displayed to emphasize clear-air conditions. The 1-min averages show no difference between the beacon and radiometer observations. By 1-min averaging, any effect of clear-air scintillation on the signal level distribution is removed, but at a 1-sec averaging time small differences are evident.

The seasonal EDFs for the 1-min standard deviation values for Norman, OK, are presented in Figure 4.61 through Figure 4.64. The plotting scales

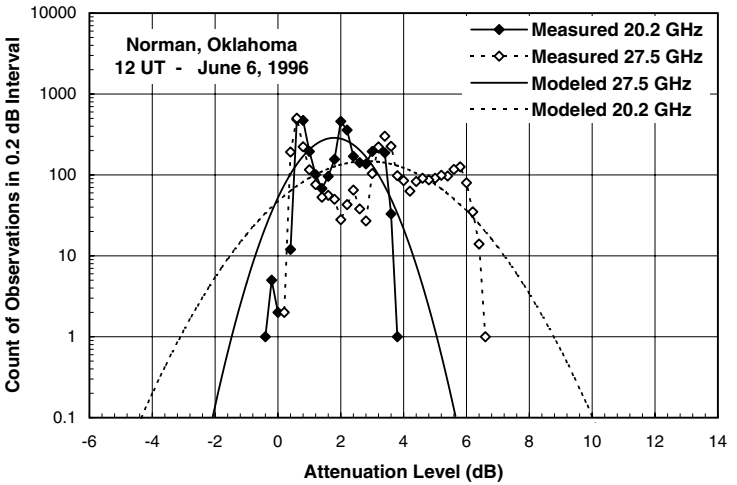

Figure 4.57 Measured and modeled signal level histograms for Norman, OK, for June 6, 1996, at 12:00 UT.

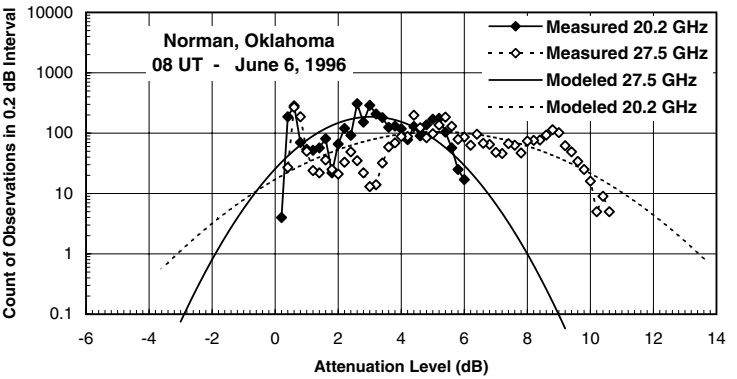

Figure 4.58 Measured and modeled signal level histograms for Norman, OK, for June 6, 1996, at 08:00 UT.

were selected to emphasize the clear-air scintillation part of the distributions. Two model computations are presented. They were calculated by using Equation 4.9 for a single 0.2-km-thick turbulent layer at a 1-km height above the ground terminal antenna. The models assumed two turbulent intensity values: $C_n^2 = 10^{-13}$ and $C_n^2 = 10^{-12}$. They span the observed range of clear-air scintillation standard deviation values for all the seasons but summer. The higher temperature and water vapor density values that occur in the northern mid-latitude summertime produce more intense refractive index fluctuations. These intensity values are typical of those observed with radar.[11,31] The median (50%) values are also indicated in each figure.

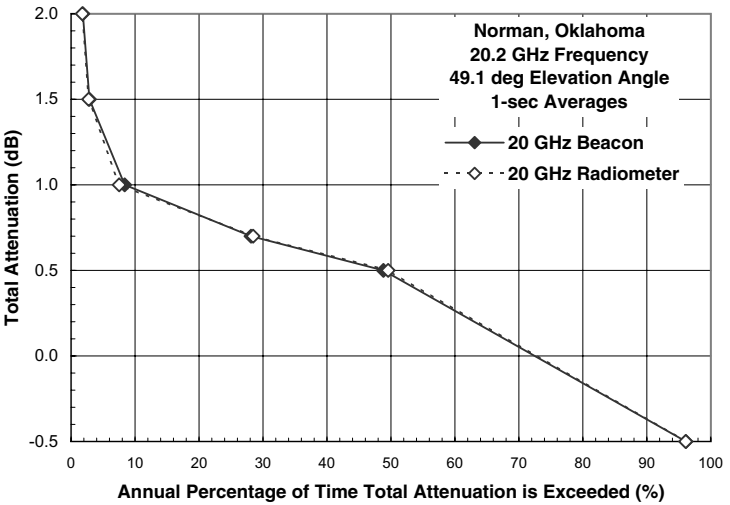

Figure 4.59 Empirical 5-year, 1-sec average total attenuation distributions at 20.2 GHz for Norman, OK.

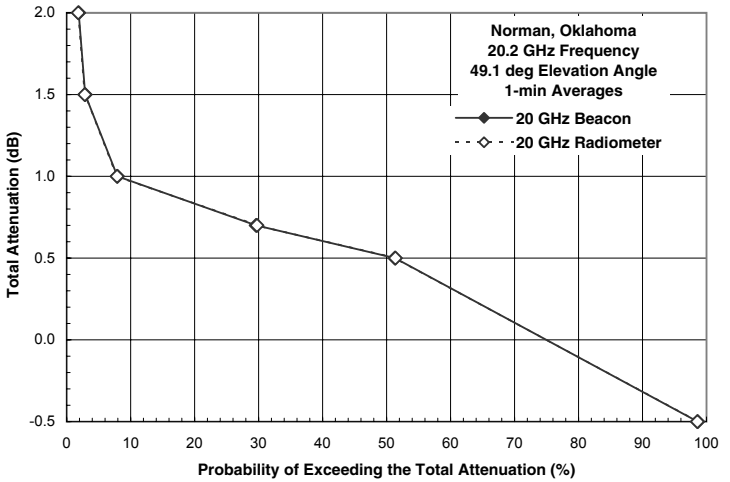

Figure 4.60 Empirical 5-year, 1-min average total attenuation distributions at 20.2 GHz for Norman, OK.

The bounding model curves for the seven sites in the ACTS propagation study are presented in Figure 4.65 and Figure 4.66, together with the median values from the seasonal EDFs for each site. The model equation predicts a strong dependence on elevation angle (Equation 4.9). The higher median value for summertime at the Alaska site is consistent with this prediction. The elevation angles ranged from 8° in Alaska (AK) to 50° for Florida (FL),

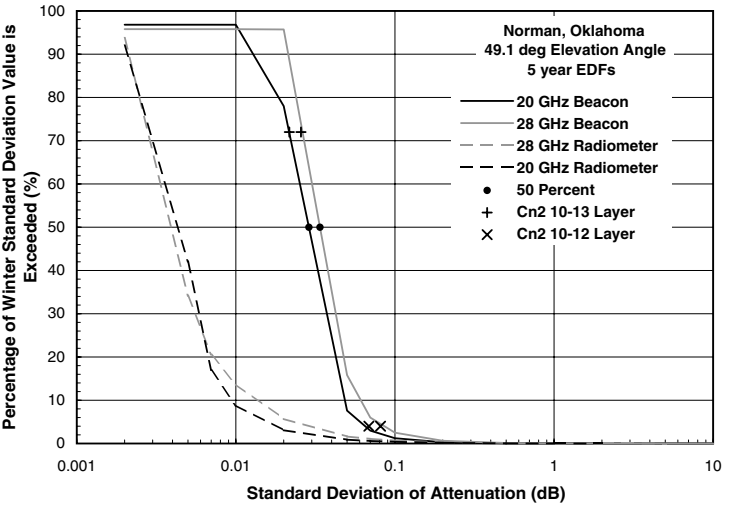

Figure 4.61 Empirical 1-min standard deviation distributions for the winter season for Norman, OK.

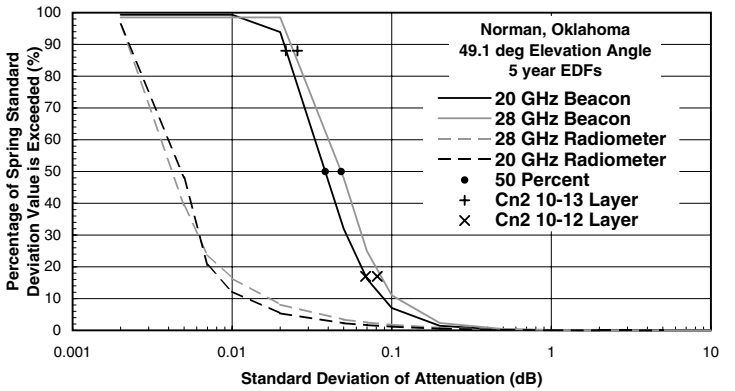

Figure 4.62 Empirical 1-min standard deviation distributions for the spring season for Norman, OK.

New Mexico (NM), and Oklahoma (OK). The southern U.S. sites, FL, OK and VA, are in locations of high humidity in the summer. The median summertime standard deviation values fore these locations lie at or above the predictions for a 0.2-km-thick layer with $C_n^2 = 10^{-12}$. The Colorado (CO) and NM sites are high above sea level (1.5 km msl) with low average humidity. As a result, the summertime values are lower than the bounding model predictions.

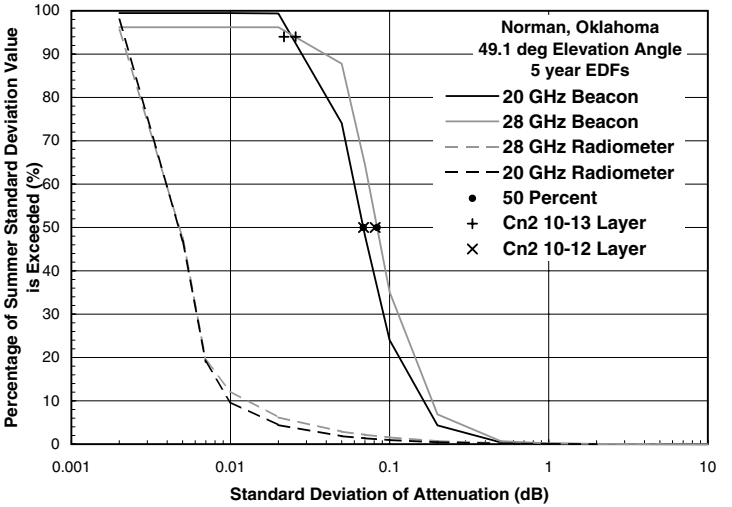

Figure 4.63 Empirical 1-min standard deviation distributions for the summer season for Norman, OK.

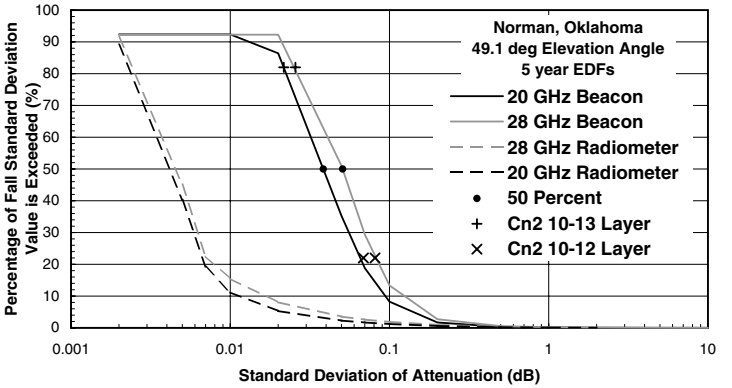

Figure 4.64 Empirical 1-min standard deviation distributions for the fall season for Norman, OK.

4.3.2 Low elevation angle observations

A low elevation angle study of signal level and angle of arrival scintillation was made in northeastern Massachusetts in 1975.[28] Two-frequency observations were made using the Interim Defense Communication Satellite Program (IDCSP) satellites after they were decommissioned. The satellites were in 14-day orbits providing slow, typically 1°/h rises and sets relative to the large aperture antennas at the Haystack Radio Astronomy Observatory and the Millstone tracking radar in Westford, MA. The antennas were equipped

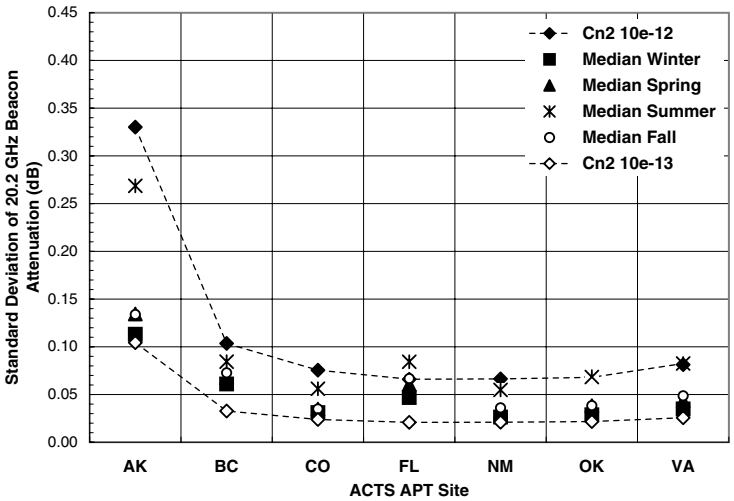

Figure 4.65 Median 1-min standard deviation values at 20.2-GHz ACTS APT sites.

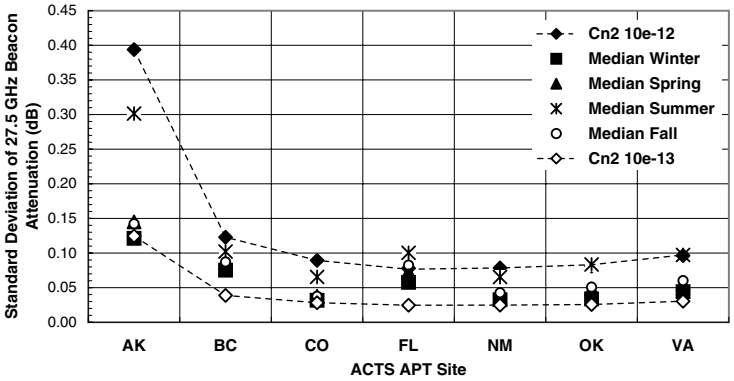

Figure 4.66 Median 1-min standard deviation values at 27.5-GHz ACTS APT sites.

with monopulse beacon or telemetry tracking systems that allowed precision signal level and angle of arrival measurements. An example of the median signal level standard deviation observations made during a two-day tracking session is given in Figure 4.67.

Predictions by a simple, single turbulent layer scintillation model are presented for each frequency. The parameters for the model are listed in the figure. The aperture-averaging factors for this model are displayed in Figure 4.43 for a 6.5° elevation angle. The observed standard deviations are higher than predicted by the model at the lower elevation angles, especially at 0.4 GHz. For these large-aperture antennas, any multipath due to terrain reflection is negligible at the indicated initial elevation angles because antenna-pointing angles to terrain features are well down on the side of the antenna patterns. The observed scintillation is caused by either diffraction

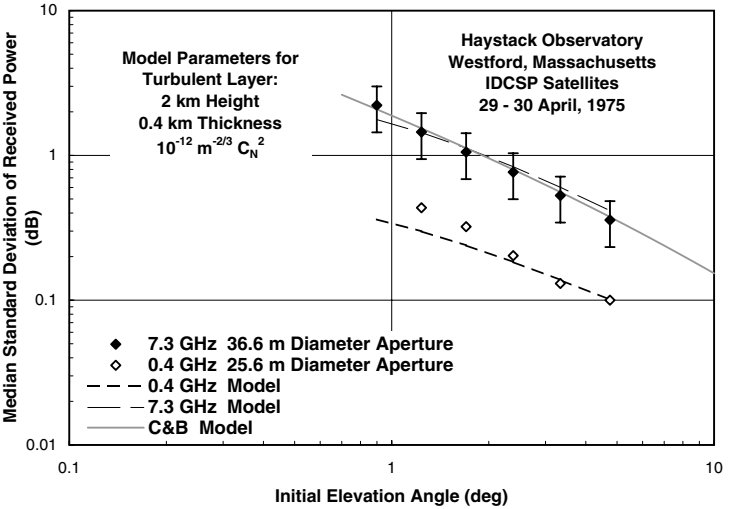

Figure 4.67 Median standard deviation of received signal level as a function of initial elevation angle at 7.3 and 0.4 GHz at Haystack Observatory.

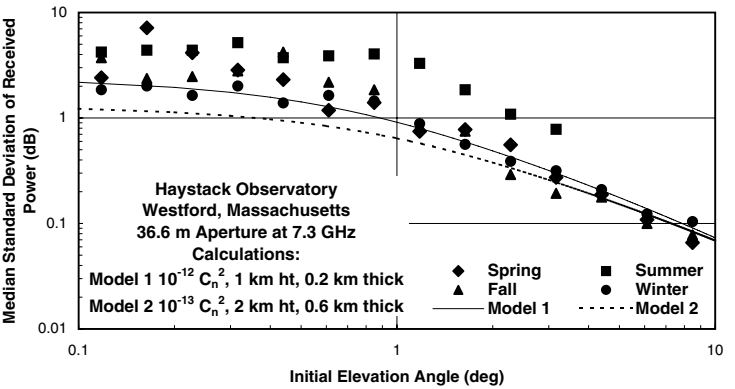

Figure 4.68 Median standard deviation of received signal level as a function of initial elevation angle for different seasons at 7.3 GHz at Haystack Observatory.

by index of refraction fluctuations or by internal atmospheric multipath from coupling into an elevated duct perturbed by buoyancy waves.

One of the earliest scintillation prediction models recommended by the ITU-R (then CCIR) was based on a curve fit to the 7.3-GHz median values shown in Figure 4.67 (the C&B Model).[32,33] Seasonal statistics were also presented for the year-long sampling of scintillation statistics.[28] They are presented in Figure 4.68. The predictions of two thin turbulent layer models are also displayed. The observed median values roughly follow the model predictions over the full range of elevation angles shown in the figure for winter, spring, and fall.

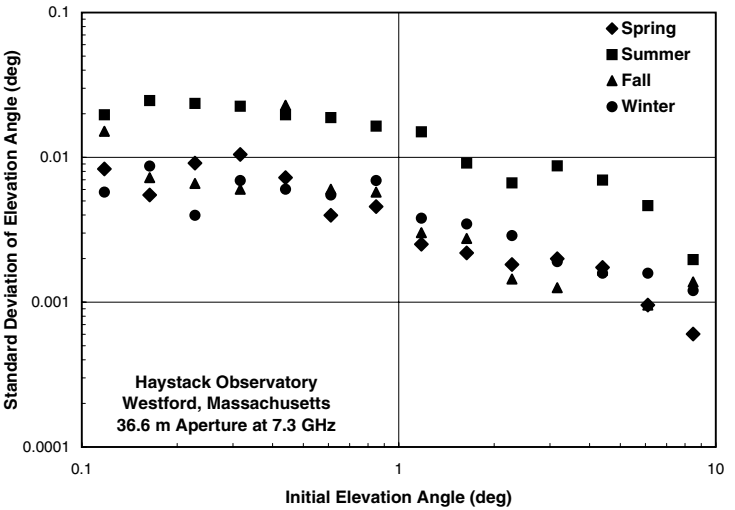

Figure 4.69 Median standard deviation of elevation angle values as a function of initial elevation angle for different seasons at 7.3 GHz at Haystack Observatory.

The simultaneously observed median values for the elevation angle fluctuations are shown in Figure 4.69.[28,34] The seasonal dependence in the standard deviation values for angle of arrival is the same as for signal level. The three-dimensional spatial spectrum of index of refraction fluctuations has a $k^{-11/3}$ power law shape in the inertial subrange.[27] At smaller wavenumbers (larger spatial scales), the spatial spectrum flattens. The fluctuation frequency spectrum produced by index of refraction variations drifting through the first Fresnel zone flattens at the corner frequency because of Fresnel zone filtering. If the flattening of the spatial spectrum happened to occur at the Fresnel filtering scale, the low-frequency asymptote to the fluctuation frequency spectrum would have a negative slope, resulting in smaller fluctuations at lower frequencies. The phase fluctuations spectrum has both $F^{-8/3}$ high-frequency and low-frequency asymptotes if the inertial subrange extends to frequencies above and below the corner frequency.[25] The angle-of-arrival spectrum then has $F^{-5/3}$ high- and low-frequency asymptotes.[34] As a result, the angle of arrival standard deviation values will change as a function of length of time used to collect samples for the calculation of the standard deviation estimates. The observations at Haystack and Millstone used 8-sec data collection intervals for processing.

4.3.3 *Standard deviation prediction models*

The C&B model presented in Figure 4.67 was based on a limited set of observations. It did not provide estimates of seasonal variations. Karasawa et al. extended the prediction model to include seasonal variations, better estimates of scintillation intensity based on a full year of observations at a single location, and empirically derived exponents for the expected frequency and elevation

angle dependence.[35] The original C&B model was derived from the simple weak scintillation layer diffraction model (see Equation 4.9):[28]

$$\sigma_\chi = \sqrt{\sigma_R^2 \left(\frac{f}{f_R}\right)^{2a} \left(\frac{\csc(\alpha)}{\csc(\alpha_R)}\right)^{2b} \frac{G}{G_R}} = \sigma_R \left(\frac{f}{f_R}\right)^{a} \left(\frac{\csc(\alpha)}{\csc(\alpha_R)}\right)^{b} \sqrt{\frac{G}{G_R}} \quad \text{(dB)} \quad (4.11)$$

where $\sigma_R = 1.88$ was the value observed at the reference frequency, $f_R = 7.3$ GHz, and the reference elevation angle $\alpha_R = 1°$ The exponent $a = 7/12$ is the frequency dependence given in Equation 4.9, but $b = 0.85$ was a departure from Equation 4.9 that was selected to match the points plotted in Figure 4.67 after adjustment by the aperture-averaging factor. The reference value of G was computed for the Haystack 36.6-m antenna at 7.3 GHz for an elevation angle of 1° and a turbulent layer height of 1 km. The layer thickness was assumed to equal the layer height; that is, the exponent b would equal 11/12 if the elevation angle were greater than 5°.

Karasawa et al. picked new values for σ_R, f_R, α_R, a, and b to best match their observations.[35] They placed limits on their model to restrict the elevation angles to values above and frequencies to the 6- to 20-GHz range. To extend the model to locations other than the receiver site, they performed a regression analysis of σ_R on the wet component of radio refractivity. For $f_R = 11.5$ GHz, $\alpha_R = 6.5°$, an antenna aperture diameter of 7.6 m, $a = 0.45$, and $b = 1.3$, they found:

$$\sigma_R = 0.15 + 0.0052\overline{N}_{\text{wet}} \quad (4.12)$$

where $\overline{N}_{\text{wet}}$ is the monthly average value for the location of interest. The predictions of this model are presented in Figure 4.70 (labeled KYA) together with the median seasonal observations from Figure 4.68. The shape of the model prediction curves provides a good match to the observations for initial elevation angles in the 3° to 10° range. The magnitudes of the predictions within this initial elevation angle range are in good agreement with the observations given the limited duration of the sample observations.

Significant departures from the model are evident at elevation angles below 1°. The underlying prediction model, Equation 4.9, is based on the Rytov approximation for weak scattering.[36] As the intensity or extent of the index of refraction turbulence increases along the propagation path, the weak scintillation model breaks down and the result is strong scintillation. In the limit of strong scintillation, the signal level probability distribution approaches a Rayleigh distribution. The signal level probability distribution in the transition region from weak to strong scintillation is often modeled by a Nakagami-m distribution.[36] The simplest representation of the standard deviation values in this transition region is an abrupt change from the weak model to the constant value of 5.6 dB for a Rayleigh distribution. This limit is shown in Figure 4.70.

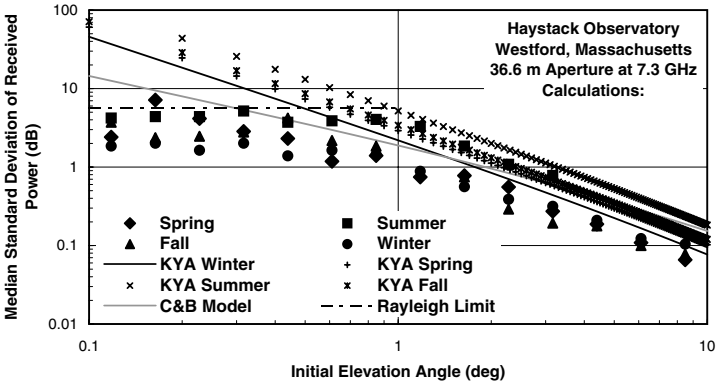

Figure 4.70 Comparison of measured and modeled standard deviation of received signal level as a function of initial elevation angle for different seasons at 7.3 GHz at Haystack Observatory.

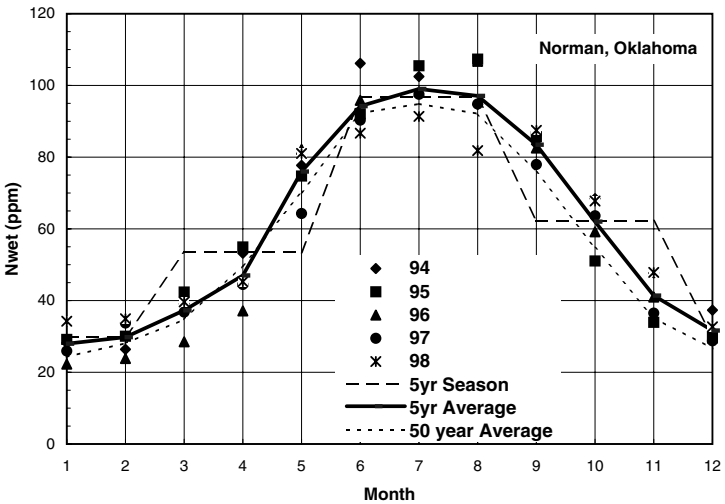

Figure 4.71 Monthly average N_{wet} by year for Norman, OK.

Scintillation model predictions were made using the Karasawa et al. model for the full 5-year ACTS propagation experiment observations. The starting point for applying the model is the determination of the monthly or seasonally averaged N_{wet} values. Figure 4.71 presents the monthly averaged values for each year and the full 5 years of observations at the site in Norman, OK. The 50-year seasonal averages are for the central month in each meteorological season. They were compiled from the hourly aviation weather statistics for Oklahoma City (the closest airport with a long record of observations) obtained from the US National Climate Data Center (NCDC). Note that the meteorological climate seasons are three months long with winter spanning December, January, and February.

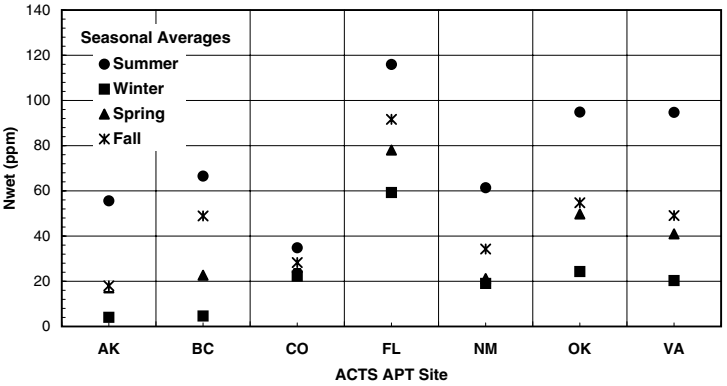

Figure 4.72 Five-year season average N_{wet} for ACTS APT sites.

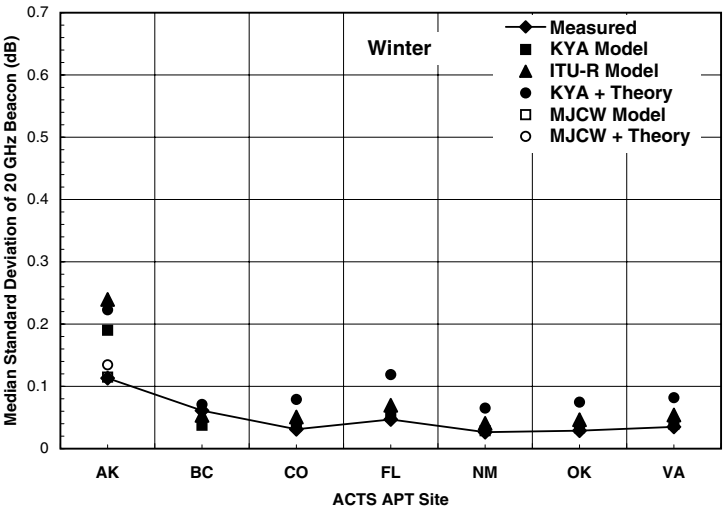

Figure 4.73 Measured and modeled median received signal standard deviations at 20.2 GHz for winter season at ACTS APT sites.

The seasonal N_{wet} averages for each of the ACTS APT sites are displayed in Figure 4.72. For each site, the closest airport with a long data record was used to compile the statistics. Most of the sites experienced a wide range of average seasonal values over the year. In contrast, the Colorado site displayed little variation. As with the median seasonal standard deviation values (Figure 4.65 and Figure 4.66), the southern sites (except NM) showed the highest summertime average N_{wet} values. The seasonal median standard deviation value predictions of the Karasawa et al. model are presented in Figure 4.73 through Figure 4.76 (identified by KYA + Model). Several other model predictions are also displayed in each of the figures.

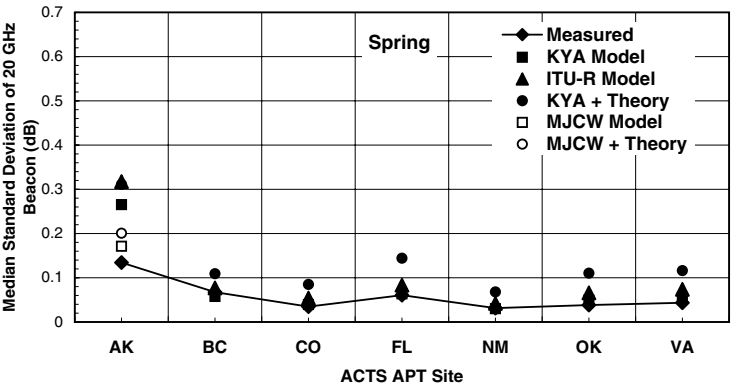

Figure 4.74 Measured and modeled median received signal standard deviations at 20.2 GHz for spring season at ACTS APT sites.

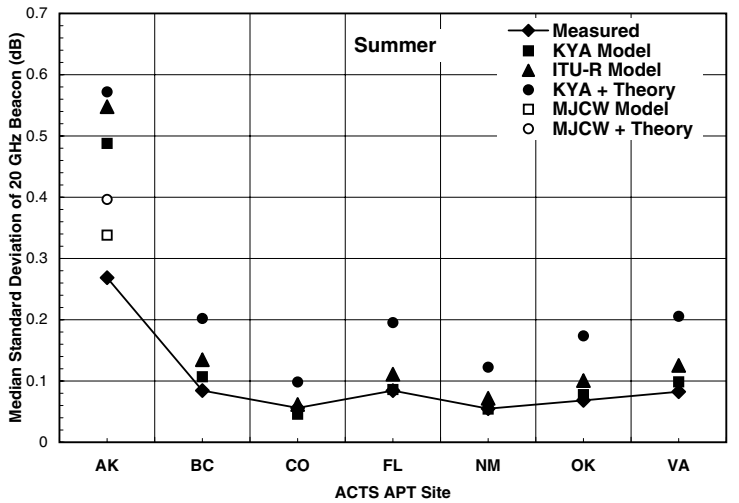

Figure 4.75 Measured and modeled median received signal standard deviations at 20.2 GHz for summer season at ACTS APT sites.

The several models are variations on the basic structure of the Karasawa et al. model (Equation 4.11 and Equation 4.12). Using a further simplification of these equations:

$$\sigma_{\chi} = \sigma_{\mathrm{Ref}} f^{a} \left(\csc(\alpha)\right)^{b} \sqrt{G} \qquad \text{(dB)}$$
$$\sigma_{\mathrm{Ref}} = c + d\overline{N}_{\mathrm{wet}} \tag{4.13}$$

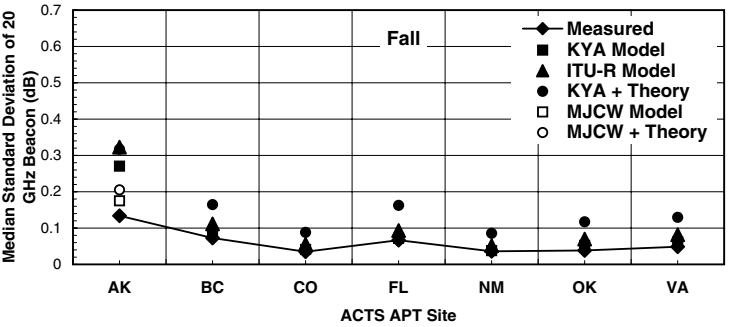

Figure 4.76 Measured and modeled median received signal standard deviations at 20.2 GHz for fall season at ACTS APT sites.

Table 4.2 Model Parameters and Performance Results at ACTS Sites

Model	*a*	*b*	*c*	*d*	Location	RMSD 20 GHz	RMSD 28 GHz
C&B	7/12	0.85	0.0227	0	All	1.38	1.46
KYA[a]	0.45	1.3	0.0034	0.0012	All	0.29	0.31
KYA + T	7/12	11/12	0.0034	0.0012	All	0.86	0.86
ITU-R[b]	7/12	1.2	0.0036	0.0001	All	0.48	0.50
MJWC[c]	0.45	1.3	0.0020	0.000089	AK[d]	0.19[d]	0.18[d]
MJWC + T	7/12	11/12	0.0020	0.000089	AK[d]	0.82[d]	0.82[d]

[a] Karasawa, Y., Yamada, M., and Allnutt, J.E., *IEEE Trans. Ant. Propag.* AP-36(11), 1608, 1988.

[b] ITU-R, Recommendation ITU-R P.618–4, International Telecommunications Union, Geneva, 1995.

[c] Mayer, C.E. et al., *Proc. IEEE*, 85(7), 936, 1997.

[d] RMSD values computed for MJWC at AK site and KYA at the rest of the sites.

with all the parameters for the reference path being included in σ_{Ref}. The *a* and *b* exponents and the *c* and *d* coefficients are listed for the several models in Table 4.2.

The RMSD values provide a measure of model performance. They are constructed using the assumption that the seasonal deviations of the median standard deviations were lognormally distributed about the predicted values. The computed statistics are based on the natural logarithm of the ratio of the observed to modeled values. The Karasawa et al.[35] model provided the best fit to the ACTS observations. The modification to that model recommended by Mayer et al. (labeled MJCW).[38] for application in Alaska provided a marked improvement for the high-latitude site. The improved clear-air scintillation model recommended for use by the ITU-R[37] based on European observations did not perform well against the 5-year ACTS propagation experiment data set.

Revisions of the models using the theoretically derived exponents given in Equation 4.9 (identified as + T in the table and + Theory in the figures) produced significantly poorer results. The problem lies in the assumed

vertical structure of index of refraction turbulence in the lower atmosphere. The original model (C&B) assumed a single layer of limited thickness at a height of 1 km agl. This assumption did not fit the low elevation angle Haystack observations and a revised exponent was proposed to provide an improved fit for a very limited set of observations. Karasawa et al. provided best-fit coefficients for a 1-year set of observations. They assumed a single turbulent layer at a height of 2 km agl (see Figure 4.68 for a comparison of single-layer predictions for layers at heights of 1 and 2 km agl). Their best-fit exponents and regression coefficients provided adjustments for variations in layer height, thickness, and intensity of turbulence that worked well for mid-latitude sites. A modification of the regression coefficients for the Alaska site provided an additional improvement in model behavior. Similar improvements may be expected for applications in tropical regions. They await the availability of long-term data from tropical sites.

4.4 *List of symbols*

Symbol	Quantity	Units	Equation
$\underline{v}$	Vector air velocity	m/s	4.2
$\frac{D}{Dt}$	Total derivative	s^{-1}	4.2
T	Layer average absolute temperature	K	4.7
σ_χ^2	Variance of the received signal in dB	dB^2	4.8
C_N^2	Refractive index structure constant	$m^{-2/3}$	4.8
$\overline{N}_{wet}$	Average wet component of radio refractivity	N units	4.12
A	Aperture area	m^2	4.8
A, B	Regression coefficients		4.1
c	Speed of light in free space	m/s	4.8
$\mathbf{e}_R$	Range error	m	4.5
f	Frequency	GHz	4.8
g	Acceleration due to gravity	m/s^2	4.2
$G(A)$	Aperture averaging factor		4.8
K_D, K_W	Scaling constants		4.6, 4.7
$\mathbf{N}$	Brunt-Vaisalla frequency	s^{-1}	4.4
N_D	Dry component of radio refractivity	N units	4.5
N_S	Surface radio refractivity	N units	4.1
N_W	Wet component of radio refractivity	N units	4.5
p, P	Pressure	hPa	4.2
t	Time	s	4.2
w	Vertical air velocity	m/s	4.2
W	Total precipitable water	g/cm^2	4.7
x	Distance from closest terminal	m	4.8
z	Vertical coordinate	m	4.2
α_0	Initial elevation angle	r	4.6
δz	Vertical parcel displacement	m	4.2
θ	Potential temperature	K	4.4
ρ	Density	Kg/m^3	4.2
σ_R	Reference scintillation intensity	dB	4.11
τ	Ray bending	deg	4.1

References

1. Bean, B.R. and Dutton, E.J., *Radio Meteorology*, National Bureau of Standards Monograph No. 92, Washington, D.C., 1966.
2. Crane, R.K., Fundamental limitations caused by RF propagation, *Proc. IEEE*, 89(3), 196, 1981.
3. Crane, R.K., Analysis of Tropospheric Effects at Low Elevation Angles, Rome Air Development Center, Griffiss Air Force Base, NY, RADC-TR-78–252, 1978.
4. Crane, R.K., Refraction effects in the neutral atmosphere, *Methods of Experimental Physics*, in Meeks, M.L., Ed., Academic Press, New York, 1976, Vol. 12, Part B, Section 2.5.
5. Kerr, D.E., Ed., *Propagation of Short Radio Waves*, McGraw-Hill, New York, 1951.
6. Budden, K.G., *The Waveguide Mode Theory of Wave Propagation*, Logos Press, London, 1961.
7. Brekhovskikh, L.M., *Waves in Layered Media*, 2nd ed., Academic Press, New York, 1980.
8. Kuttler, J.R. and Dockery, G.D., Theoretical description of the parabolic approximation/Fourier split-step method of representing electromagnetic propagation in the troposphere, *Radio Sci.*, 26(2), 381, 1991.
9. Dougherty, H.T. and Hart, B.A., Recent progress in duct propagation predictions, *IEEE Trans. Ant. Propag.*, AP-27(4), 542, 1979.
10. Hitney, H.V., Pappert, R.A., Hattan, C.P., and Goodhart, C.L., Evaporation duct influences on beyond-the-horizon high altitude signals, *Radio Sci.*, 13(4), 669, 1978.
11. Gossard, E.E., Clear weather meteorological effects on propagation at frequencies above 1 GHz, *Radio Sci.*, 16(5), 589, 1981.
12. Holton, J.R., *An Introduction to Dynamic Meteorology*, 2nd ed., Academic Press, New York, 1979.
13. Houze, R.A., Jr., *Cloud Dynamics*, Academic Press, New York, 1993.
14. Gossard, E.E. and Hooke, W., *Waves in the Atmosphere*, Elsevier, New York, 1975.
15. Gossard, E.E., Neff, W.D., Zamora, R.J., and Gaynor, J.E., The fine structure of elevated refractive layers: Implications for over-the-horizon propagation and radar sounding systems, *Radio Sci.*, 19(6), 1523, 1984.
16. Webster, A.R. and Scott, A.M., Angles-of-arrival and tropospheric multipath microwave propagation, *IEEE Trans. Ant. Propag.*, AP-35(1), 94, 1987.
17. Crane, R.K., A review of transhorizon propagation phenomena, *Radio Sci.*, 16(5), 649, 1981.
18. Bean, B.R., Cahoon, B.A., Sampson, C.A., and Thayer, G.D., *A World Atlas of Atmospheric Radio Refractivity*, ESSA Monograph, U.S. Dept. Commerce, Washington, D.C., 1996.
19. ITU-R, Recommendation ITU-R P.453–5, The Radio Refractive Index: Its Formula and Refractivity Data, International Telecommunications Union, Geneva, 1995.
20. Westwater, E.R., The accuracy of water vapor and cloud liquid determination by dual-frequency ground-based microwave radiometry, *Radio Sci.*, 13(4), 677, 1978.
21. Prag, A.B. and Brinkman, D.G., An ionospheric error model for time difference of arrival applications, *Radio Sci.*, 37(3), 10-1, 2002.

22. Lowry, A.R., Rocken, C., Sokolovskiy, S.V., and Anderson, K.A., Vertical profiling of atmospheric refractivity from ground-based GPS, *Radio Sci.*, 37(3), 13-1, 2002.
23. Crane, R.K., Wang, X., Westenhaver, D.B., and Vogel, W.J., ACTS Propagation Experiment: Experiment design, calibration, and data preparation and archival, *Proc. IEEE*, 85(7), 863, 1997.
24. Tatarski, V.I., *The Effects of the Turbulent Atmosphere on Wave Propagation*, National Technical Information Service, U.S. Dept. Commerce, Springfield, VA, 1971.
25. Crane, R.K., Spectra of ionospheric scintillation, *J. Geophys. Res.*, 81(13), 2041, 1976.
26. Haddon, J. and Vilar, E., Scattering induced microwave scintillations from clear air and rain on earth space paths and the influence of antenna aperture, *IEEE Trans Ant. Propag.*, AP-34(5), 646, 1986.
27. Monin, A.S. and Yaglom, A.M., *Statistical Fluid Mechanics*, Lumley, J.L., Ed. and Trans., The MIT Press, Cambridge, MA, 1975, Vol. 2.
28. Crane, R.K., Low elevation angle measurement limitations imposed by the troposphere: An analysis of scintillation observations made at Haystack and Millstone, Technical Report 518, MIT Lincoln Laboratory, Lexington, MA, 1976.
29. Moulsley, T.J. and Vilar, E., Experimental and theoretical statistics of microwave amplitude scintillation on satellite down-links, *IEEE Trans. Ant. Propag.*, AP-30(6), 1099, 1982.
30. Allnutt, J.L., *Satellite-to-Ground Radiowave Propagation*, Peter Peregrinus, London, 1989.
31. Crane, R.K., A review of transhorizon propagation phenomena, *Radio Sci.*, 16(5), 649, 1981.
32. Crane, R.K. and Blood, D.W., Handbook for the Estimation of Microwave Propagation Effects — Link Calculations for Earth-Space Paths, ERT Report P-7376-TR1, Environmental Research & Technology, Inc., Concord, MA.
33. CCIR, Report 718–2, Effects of Tropospheric Refraction on Radiowave Propagation, International Telecommunications Union, Geneva, 1986.
34. Crane, R.K., Variance and spectra of angle-of-arrival and Doppler fluctuations caused by ionospheric scintillation, *J. Geophys. Res.*, 83(A5), 2019, 1978.
35. Karasawa, Y., Yamada, M., and Allnutt, J.E., A new prediction method for tropospheric scintillation on earth-space paths, *IEEE Trans. Ant. Propag.* AP-36(11), 1608, 1988.
36. Crane, R.K., Ionospheric scintillation, *Proc. IEEE*, 65(2), 180, 1977.
37. ITU-R, Recommendation ITU-R P.618–4, Propagation Data and Prediction Methods Required for the Design of Earth-Space Telecommunication Systems, International Telecommunications Union, Geneva, 1995.
38. Mayer, C.E., Jaeger, B.E., Cranke, R.K., and Wang, X., Ka-band scintillations: measurements and model predictions, *Proc. IEEE*, 85(7), 936, 1997.

chapter five

Attenuation by clouds and rain

5.1 Rain

Rain affects propagation through the lower troposphere, where liquid raindrops attenuate electromagnetic waves. Path attenuation can be important on terrestrial and Earth-space links at frequencies above about 6 GHz (see Figure 1.16). The link margin needed to combat multipath fading on a terrestrial link works to protect the same path against rain fades. Depending on link design, rain attenuation on a terrestrial path may not be important at frequencies above 15 or 20 GHz. Multipath is generally not a problem on Earth-space paths, and rain may limit system availability at frequencies as low as 7 or 8 GHz, depending again on link design.

Rain attenuation statistics prediction models have been developed to provide guidance to system designers in their attempts to balance availability requirements and cost. Rain attenuation prediction models are of two general types: (1) regression models that use measured rain-rate and path-attenuation statistics to generate a model for a single location and hopefully for other locations as well and (2) physical models that use statistical information on the rain occurrence and rain-scattering processes to provide predictions that should be valid everywhere. The latter type of model may still be limited by an imperfect understanding of the rain process. Our knowledge of the rain attenuation process has advanced to the point that path attenuation can be computed if the detailed structure of rain — the drop size, shape, orientation, temperature, and physical state distributions of the hydrometeors along the path are known. However, such information is not available, and statistical prediction models are necessary.

In terms of relative importance in predicting attenuation statistics, knowledge of the rain-rate statistics is critical, followed by the statistics of rain extent along the path. The differences caused by changes in the drop parameter distributions are generally small and overshadowed by the yearly variability of the rain occurrence statistics (e.g., see Figure 1.91, Figure 1.100, and Figure 1.101).

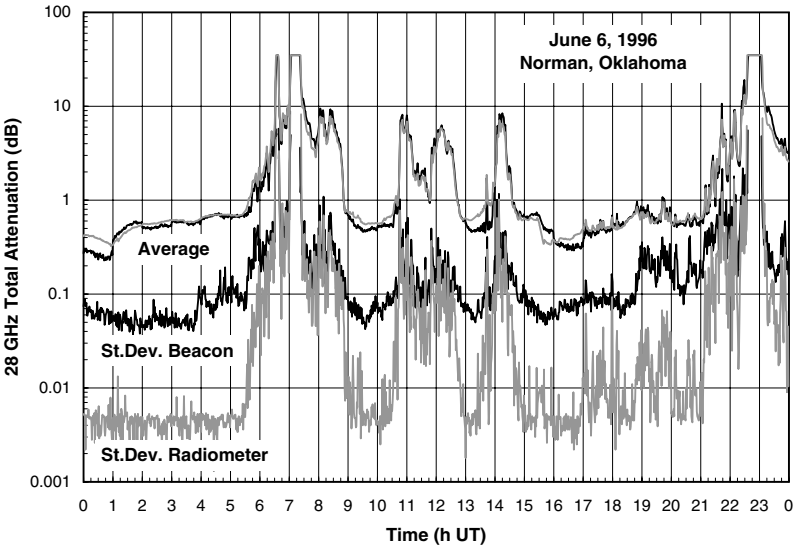

Figure 5.1 One-minute average and standard deviations of total 27.5-GHz beacon attenuation for Norman, OK, for June 6, 1996.

5.2 *Rain attenuation*

Figure 3.18 through Figure 3.20 and Figure 4.46 present time series of observed total attenuation (due to rain, clouds, gaseous absorption, and water on the antenna) at 20.2 GHz, and Figure 4.25 presents collocated and simultaneously measured rain rates at the ACTS APT site in Norman, OK, on June 6, 1996. Figure 5.1 displays the measured total attenuation values at 27.5 GHz for the same day and Figure 5.2 displays the excess attenuation due to clouds and rain at the two frequencies. The dynamic range of the ACTS APTs limited the observations to total attenuation values below 30 dB. Loss-of-signal conditions were identified by scintillation values characteristic of receiver noise alone. The attenuation values for intervals with a complete loss of signal were arbitrarily set to 35 dB.

Two loss-of-signal events are evident in the figures. Rain with a peak rate greater than 78 mm/h occurred at the ACTS propagation terminal (APT) during the first event and rain with a peak rate greater than 180 mm/h occurred during the second event. The excess rain attenuation was consistently higher at 27.5 GHz than at 20.2 GHz during periods with rain. Excess rain attenuation was calculated by subtracting the gaseous absorption estimated for the minute from the attenuation obtained from the recorded surface meteorological observations (see Section 3.2.3.3). The excess attenuation was produced by rain, clouds, and water on the antenna. Figure 5.3 presents a comparison between 1-min averaged excess attenuation values at 20.2 and 27.5 GHz. A loss of signal at 27.5 GHz was observed over a 16- to 23-dB range of attenuation values at 20.2 GHz. At lower attenuation values,

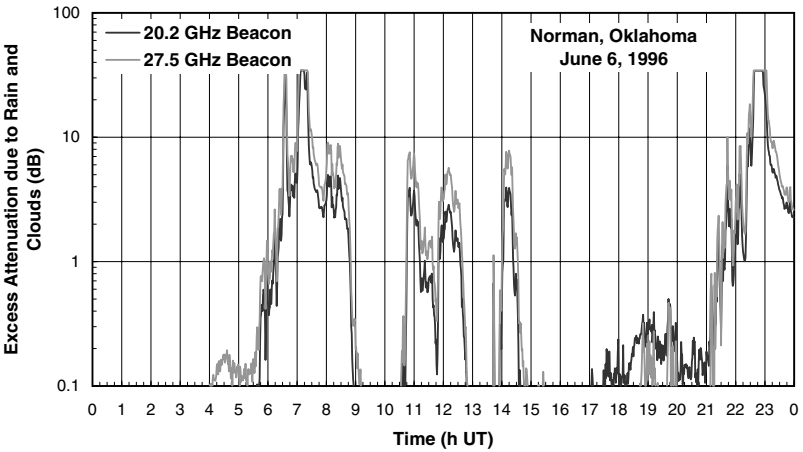

Figure 5.2 Excess one-minute average attenuation for Norman, OK, for June 6, 1996.

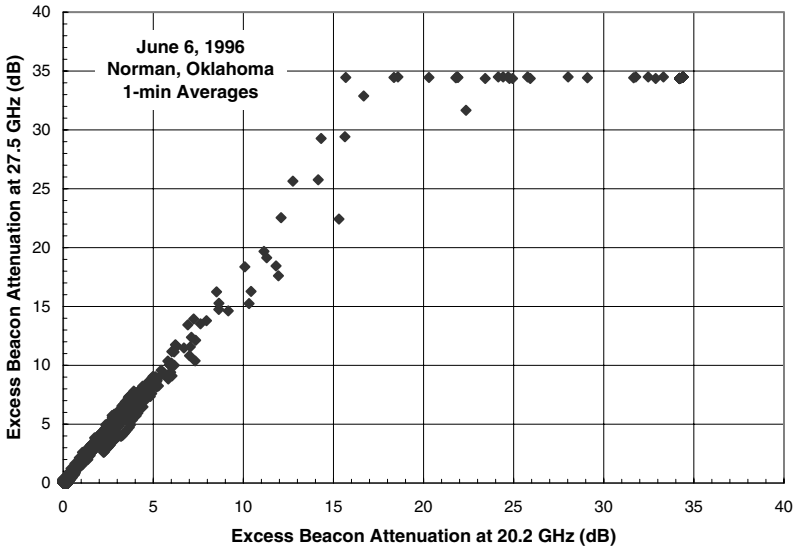

Figure 5.3 Scattergram excess 1-min average attenuation at 20.2 and 27.5 GHz for Norman, OK, for June 6, 1996.

requency for a given attenuation value at the lower frequency.

The standard deviation plots (Figure 4.44 and Figure 5.1) provide a means to identify the dominant physical process producing the attenuation. If the standard deviations of the attenuation estimates derived from the radiometers (radiometer attenuation) are not detectable in the receiver noise, clear-air scintillation is the cause of the observed attenuation. If the standard

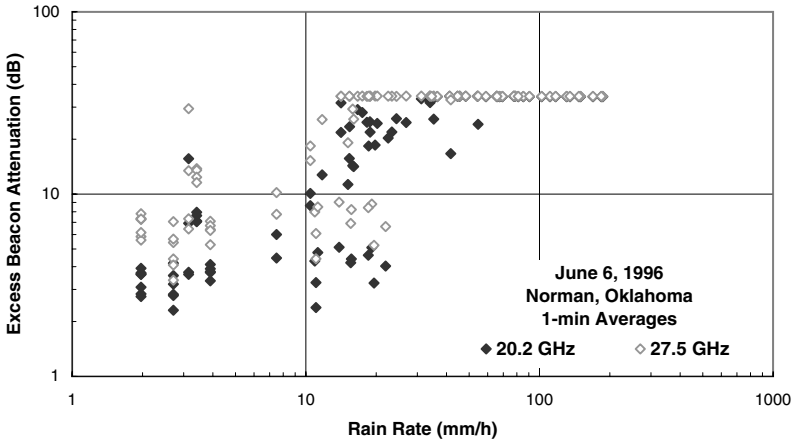

Figure 5.4 Scattergram excess 1-min average attenuation at 20.2 GHz and rain rate for Norman, OK, for June 6, 1996.

deviations of radiometer attenuation are less than the standard deviations of the beacon signals, clouds are the dominant cause of the attenuation. If the standard deviations of radiometer attenuation are the same as the standard deviations of beacon attenuation, rain is the cause.

Attenuation produced by rain can be caused by rain anywhere along the path where the air temperature is warm enough to maintain liquid raindrops. Rain can occur over the rain gauge at the APT but not cover the rest of the path or, conversely, be over most of the path but not over the rain gauge. Figure 5.4 presents the results of a minute-by-minute comparison of excess path attenuation and simultaneous rain-rate measurements. Occurrences of rain over the path but not the gauge are excluded. Only a statistical relationship between rain rate and attenuation is possible.

Two types of rain gauges were used in the ACTS propagation experiment: a capacitor gauge and a tipping bucket gauge. They had different dynamic ranges, integration times, and calibration problems. Four years of data were collected with the tipping bucket gauge at the APT. Figure 5.5 and Figure 5.6 present joint attenuation and rain-rate occurrence statistics. These statistics have been corrected for the occurrence of water on the antenna reflector and feed window.[1] The attenuation is due to gaseous absorption, rain, and clouds on the path. More occurrences of attenuation without rain over the APT are evident than in the approximately logarithmically spaced rain-rate intervals. Except for rain rates above about 15 mm/h, more occurrences of the lowest attenuation values are evident with the occurrence of measurable rain than in the other approximately logarithmically spaced attenuation intervals. For attenuation values above about 2 dB (rain dominant), the mode attenuation value increases with rain rate.

Joint attenuation statistics were compiled for the two beacon frequencies. Figure 5.7 and Figure 5.8 present the empirical joint density functions for

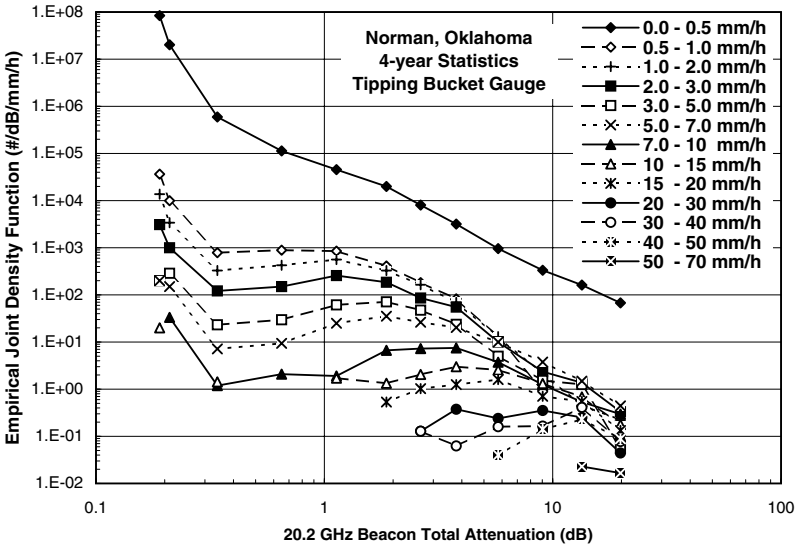

Figure 5.5 Joint 20.2-GHz attenuation and rain-rate distribution for Norman, OK.

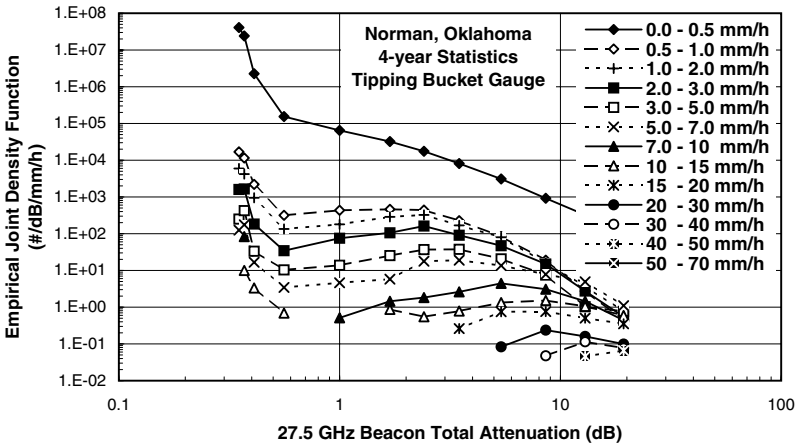

Figure 5.6 Joint 27.5-GHz attenuation and rain-rate distribution for Norman, OK.

5 years of observations at the Norman, OK, APT. These results are for total beacon attenuation. They have been corrected for water on the antenna. Figure 5.7 gives statistics for 1-sec averages. The attenuation values include the signal loss occurrences during clear-air scintillation as well as the effects of rain, clouds, and gaseous absorption. Figure 5.8 shows the 1-min averages. The effects of the more rapid scintillation have been removed by averaging. As a result, for attenuation values above 0.6 dB, the breadths of the empirical density functions about each peak are narrower for the 1-min averages than

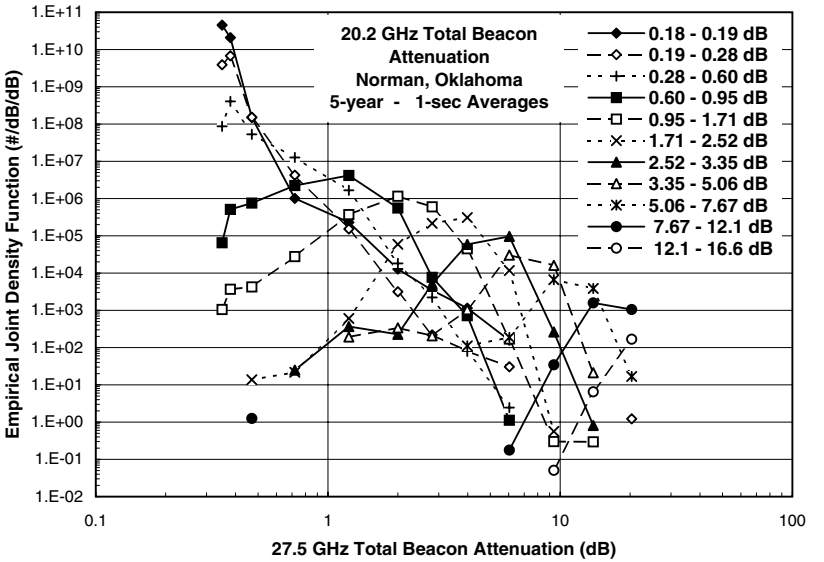

Figure 5.7 Joint 20.2-GHz attenuation and 27.5-GHz attenuation for 1-sec averages distribution for Norman, OK.

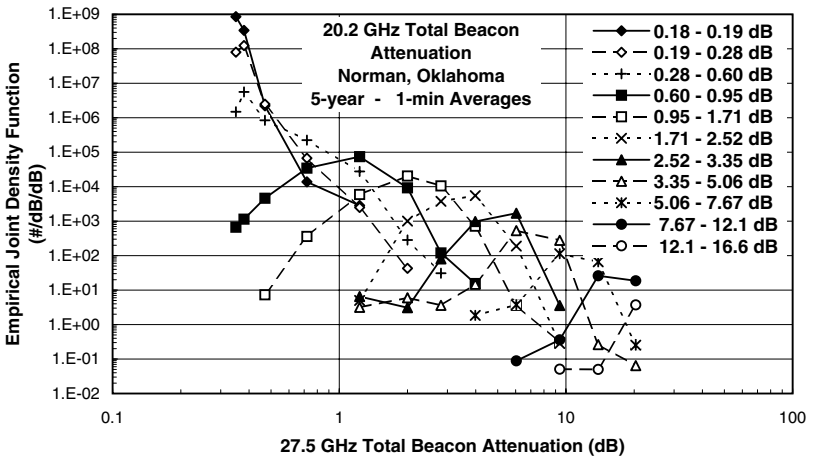

Figure 5.8 Joint 20.2-GHz attenuation and 27.5-GHz attenuation for 1-min averages distribution for Norman, OK.

for the 1-sec averages. The 1-sec average plots are also skewed toward lower attenuation values. These distributions show a wide range of attenuation values at 27.5 GHz for a given attentuation value at 20.2 GHz

The average values of attenuation vs. rain rate are shown in Figure 5.9 for the four years of observations summarized in Figure 5.5 and Figure 5.6. The average attenuation values at the higher frequency given the value at

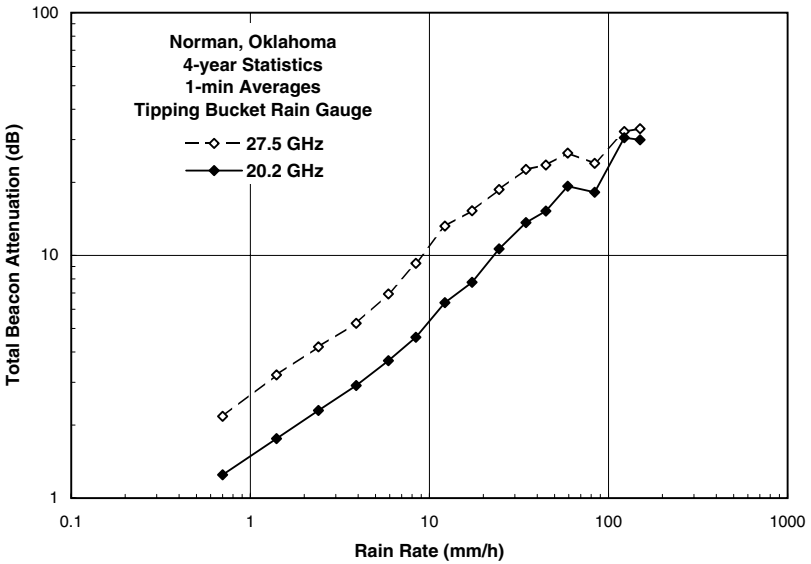

Figure 5.9 Total 20.2-GHz attenuation vs. rain rate for 4-year averages for Norman, OK.

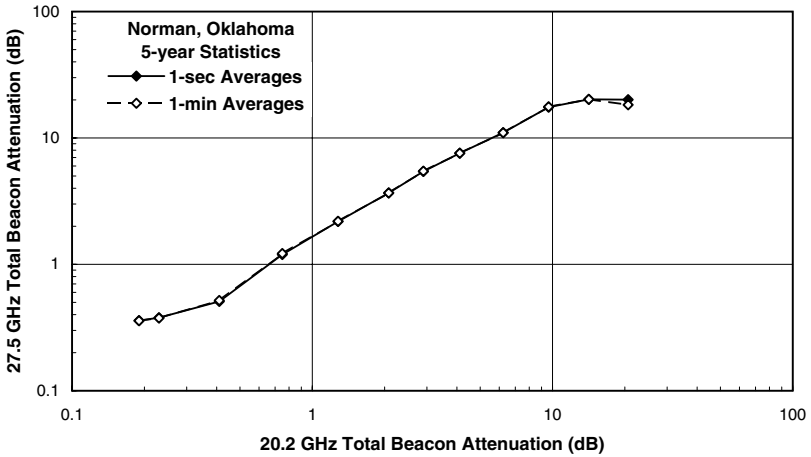

Figure 5.10 Total 20.2-GHz attenuation vs. 27.5-GHz attenuation for 5-year averages for Norman, OK.

the lower frequency are shown in Figure 5.10 for the entire 5-year observation period. The results for both 1-sec and 1-min averages are shown. With averaging, the differences between the distributions vanish. Summary statistics such as those shown in Figure 5.9 and Figure 5.10 were prepared for each of the seven ACTS APT sites. The resulting attenuation vs. rain-rate averages are shown in Figure 5.11. Some of the sites employed the capacitor

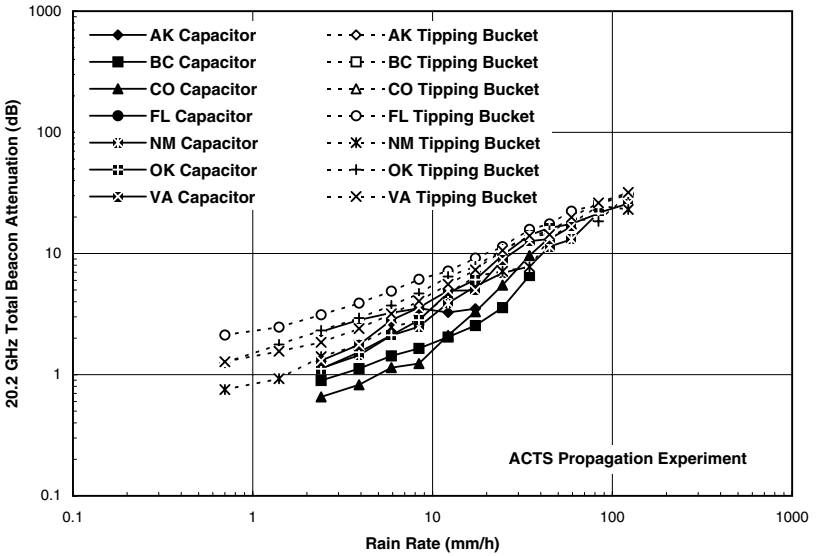

Figure 5.11 Total 20.2-GHz attenuation vs. rain rate for experiment average for ACTS APT sites.

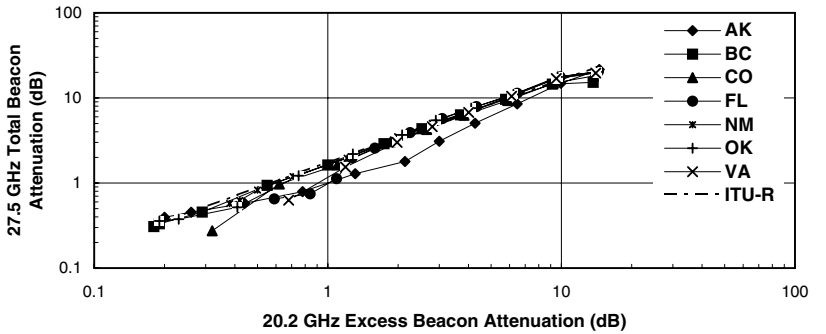

Figure 5.12 Excess 20.2-GHz attenuation vs. 27.5-GHz attenuation for experiment average for ACTS APT sites.

gauges and the rest used tipping bucket gauges. The site in New Mexico recorded data with both gauges. The first year of measurements in Oklahoma were made with the capacitor gauge.[2] At the lower rain rates, the average relationship between attenuation and rain rate varied from one site to the next. Differences between gauges were also evident, but most of the differences were between sites and years at a single site. The only results for observations that used the two gauges for the same measurement period are those for New Mexico. For this site, the gauge-to-gauge differences were small.

The summary statistics for attenuation at one frequency given the attenuation at the other are presented in Figure 5.12 for the seven ACTS sites.

Also shown is the long-term frequency scaling model recommended by the ITU-R:[3]

$$A_{F2} = A_{F1}\left(\frac{\phi_2}{\phi_2}\right)^{1-H(A_{F1})}$$

$$\phi_i = \left(\frac{f_i^2}{1-0.0001f_i^2}\right) \tag{5.1}$$

$$H(A_{F1}) = 1.12\cdot 10^{-3}\sqrt{\frac{\phi_2}{\phi_2}}(\phi_1 A_{F1})^{0.55}$$

where f_i is carrier frequency (GHz) and the A_{Fi} are equiprobable path attenuation values (dB). This model is the result of curve fitting to observations in the ITU-R data bank. The ITU-R model provides a good match to the summary statistics for attenuation values above 2 dB at 20.2 GHz for all the sites but the low-elevation-angle site in Alaska.

5.3 Seasonal rain attenuation statistics

5.3.1 Monthly statistics

The rain attenuation statistics vary with month and year. The 5-year data set was employed to characterize the seasonal variations at each of the ACTS APT sites. The percentage of a month or season that exceeded a 2-dB path attenuation at 20.2 GHz was used as the threshold for rain attenuation. This threshold works well for isolating rain event statistics for sites below a 50° N latitude, but includes a significant number of cloud events on the low, 8.1° elevation angle path in Fairbanks, AK. The monthly occurrence statistics for 2-dB excess attenuation events are shown in Figure 5.13 for the Alaska site. The annual statistics are displayed along with the 5-year averages. Rain attenuation for this site occurs only in the spring, summer, and fall. The seasonal average statistics are also shown. High yearly variations in the monthly statistics are evident February through April and in September and October. In contrast to Alaska, the monthly statistics for Vancouver, British Columbia (Figure 5.14), show rain as predominantly a winter phenomenon, with a reduced occurrence in the summer relative to the other months.

The occurrence statistics for Colorado show rain attenuation to be a spring, summer, and fall phenomenon (Figure 5.15) whereas the rest of the sites can have rain attenuation events during any month (Figure 5.16 through Figure 5.19). Figure 5.20 through Figure 5.22 display the 5-year average empirical exceedence probabilities for all the ACTS APT sites for 2-, 5-, and 10-dB thresholds, respectively. Although rain occurrence is mainly a wintertime phenomena in the Pacific northwest, the Vancouver statistics show that the higher attenuation events are a summertime

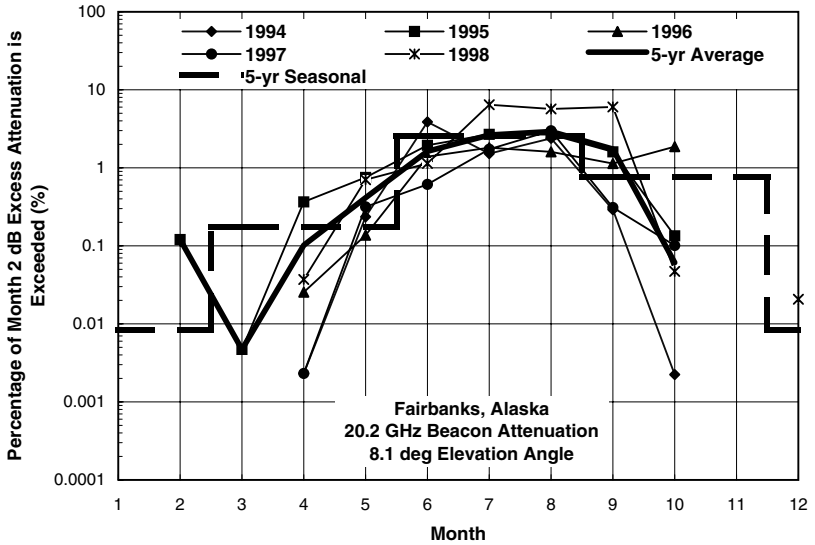

Figure 5.13 Monthly occurrences of 2 dB or higher excess attenuation at 20.2 GHz for Fairbanks, AK.

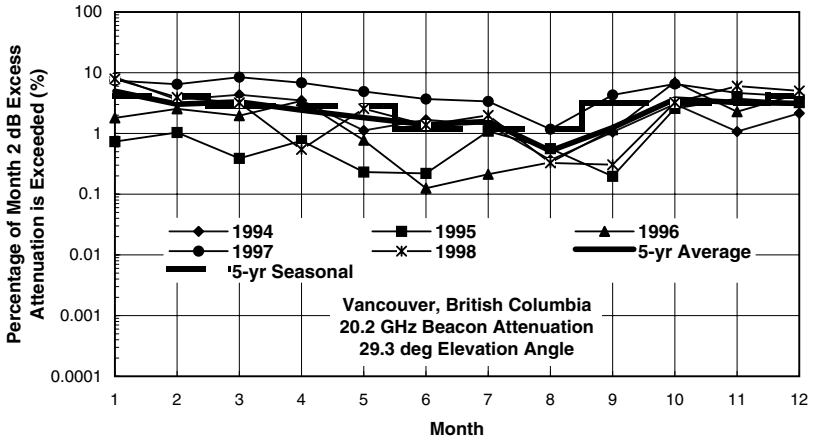

Figure 5.14 Monthly occurrences of 2 dB or higher excess attenuation at 20.2 GHz for Vancouver, British Columbia.

occurrence. The empirical probabilities used to generate these figures are listed in Table 5.1 through Table 5.3.

5.3.2 *Worst-month statistics*

The radiocommunication link design procedure recommended by the ITU-R is to design for the "worst-month" propagation effects. The monthly statistics

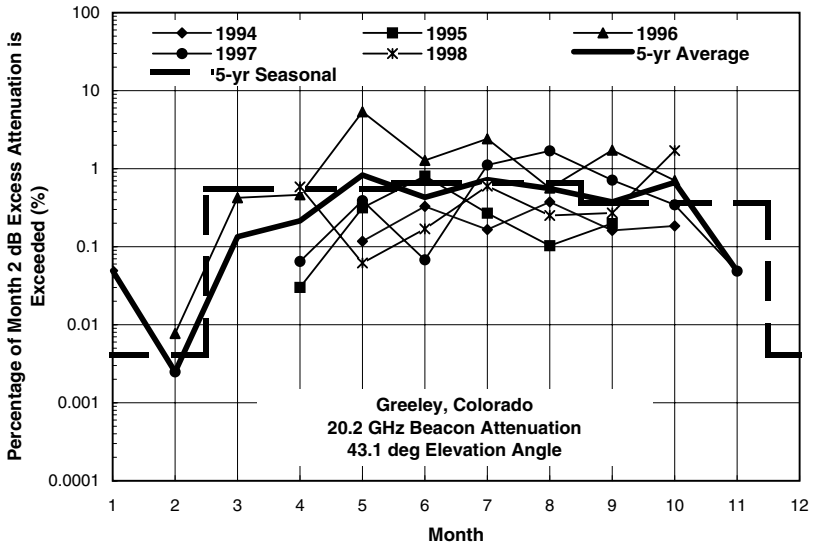

Figure 5.15 Monthly occurrences of 2 dB or higher excess attenuation at 20.2 GHz for Greeley, CO.

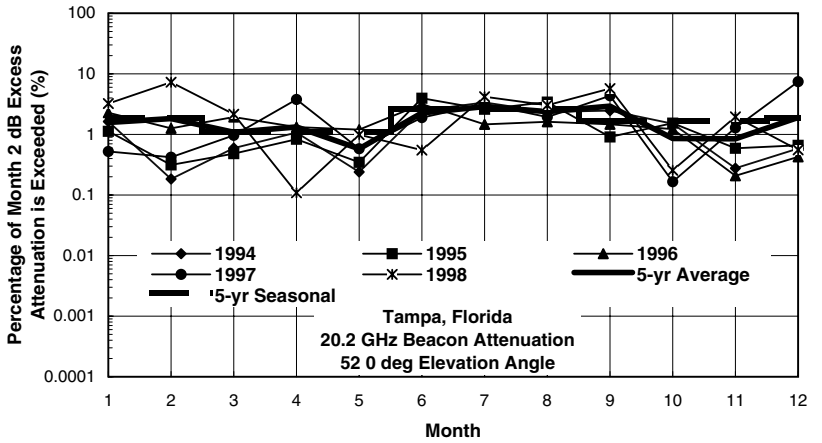

Figure 5.16 Monthly occurrences of 2 dB or higher excess attenuation at 20.2 GHz for Tampa, FL.

given in Table 5.1 through Table 5.3 provide information on the average worst-month occurrence statistics for rain attenuation at the specified thresholds. The average worst month for the 5-year period of the ACTS propagation experiment is defined to be the average of the highest monthly percentage of time value for each year.[4,5] The month that contributes the highest value for a particular threshold will change from year to year (see Figure 5.15 to Figure 5.19 for the 2-dB threshold).

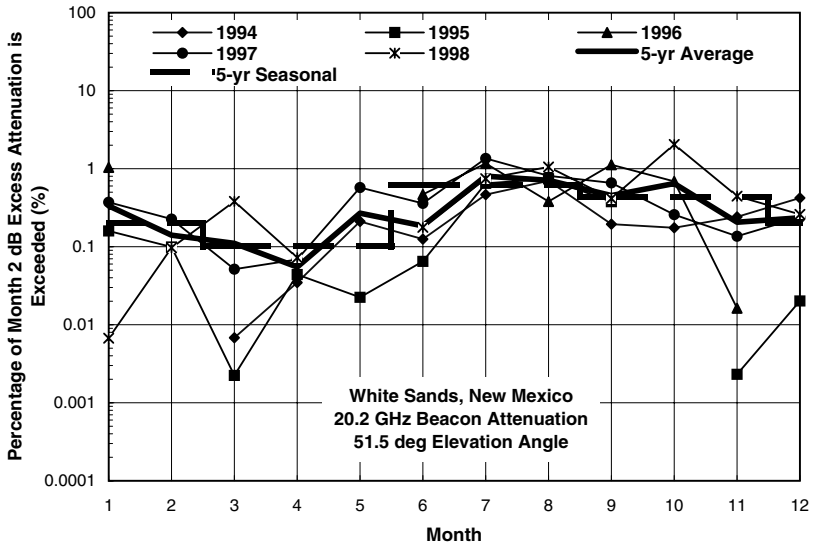

Figure 5.17 Monthly occurrences of 2 dB or higher excess attenuation at 20.2 GHz for White Sands, NM.

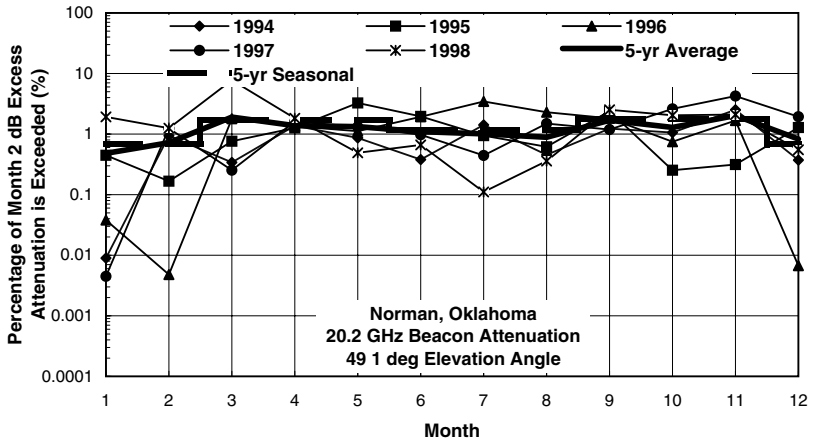

Figure 5.18 Monthly occurrences of 2 dB or higher excess attenuation at 20.2 GHz for Norman, OK.

The *Q* ratio is the average of the 5-year worst-month values divided by the 5-year annual empirical exceedence percentage for the specified threshold. It provides a means to go from the annual to the worst-month statistic. This relationship is needed because most of the data in the databases and most of the available attenuation prediction models are estimates of the annual distributions. The ITU-R recommends the following model, which was curve fit to a number of observation sets:[6]

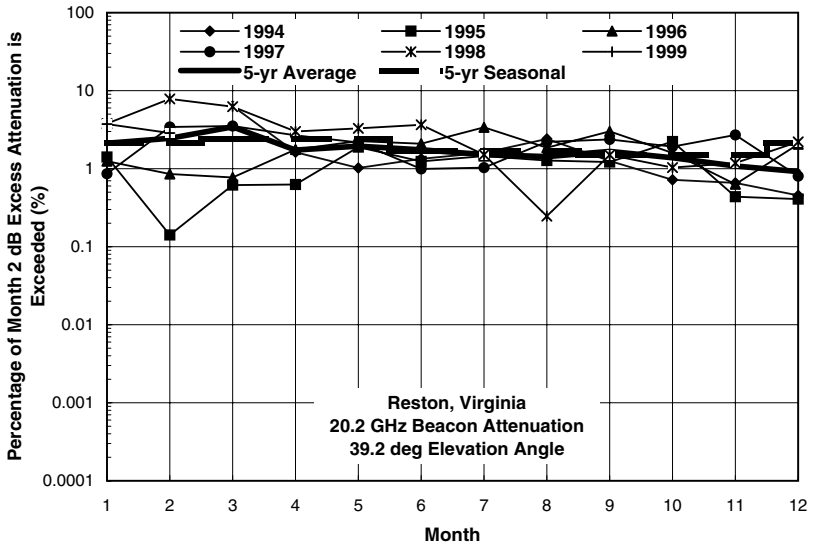

Figure 5.19 Monthly occurrences of 2 dB or higher excess attenuation at 20.2 GHz for Reston, VA.

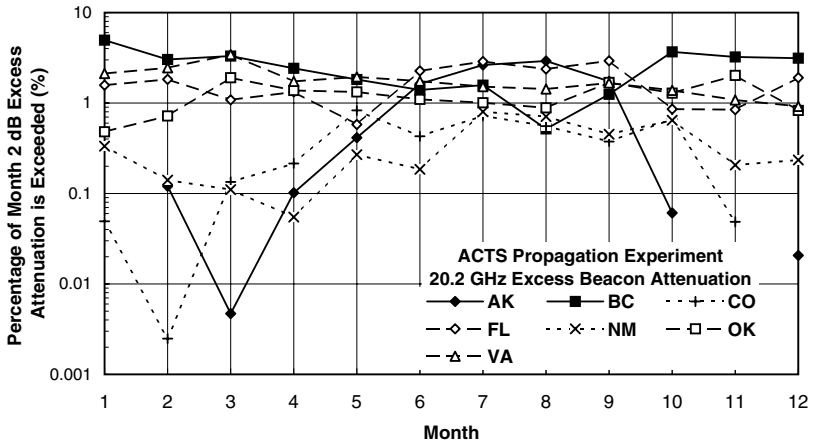

Figure 5.20 Five-year average monthly occurrences of 2 dB or higher excess attenuation at 20.2 GHz for ACTS APT sites.

$$
\begin{aligned}
p_W &= Q p_A \\
Q(p_A) &= Q_1 p_A^{-\beta} \\
\beta &= \ln\left(Q(p_1)/Q(p_2)\right)\ln\left(p_2/p_1\right) \\
Q_1 &= Q(p_1)p_1^{\beta}
\end{aligned}
\tag{5.2}
$$

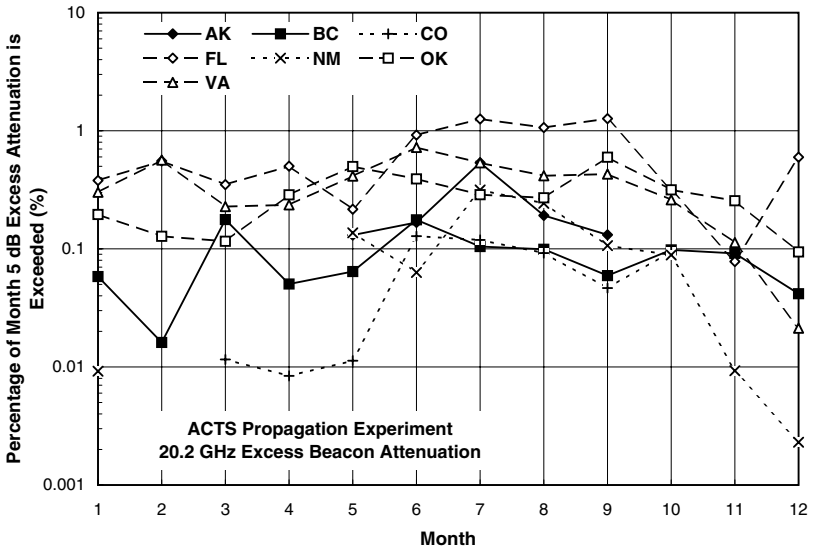

Figure 5.21 Five-year average monthly occurrences of 5 dB or higher excess attenuation at 20.2 GHz for ACTS APT sites.

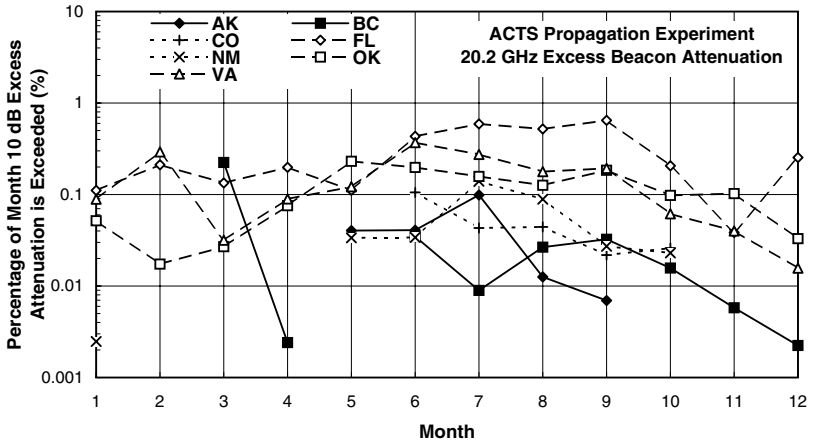

Figure 5.22 Five-year average monthly occurrences of 10 dB or higher excess attenuation at 20.2 GHz for ACTS APT sites.

where p_W and p_A are the worst-month and annual probability values (%), respectively, for the same threshold, the $Q(p_i)$ ratio is calculated at two thresholds, and the annual p_i values (%) are obtained from the long-term annual probability of exceeding each threshold. The results for the ACTS observations obtained by using the 5- and 10-dB excess attenuation value thresholds at 20.2 GHz are given in Table 5.4.

Table 5.1 Percentage of Time the 2-dB Excess 20.2-GHz Rain Attenuation[a] is Exceeded

Month	AK	BC	CO	FL	NM	OK	VA
1		4.958	0.049	1.576	0.334	0.481	2.12
2	0.120	3.030	0.002	1.827	0.141	0.720	2.452
3	0.005	3.308	0.134	1.084	0.110	1.906	3.436
4	0.102	2.421	0.215	1.328	0.055	1.377	1.735
5	0.414	1.820	0.829	0.580	0.269	1.326	1.945
6	1.630	1.396	0.429	2.266	0.185	1.098	1.746
7	2.634	1.577	0.724	2.880	0.802	1.008	1.518
8	2.916	0.518	0.556	2.377	0.709	0.886	1.429
9	1.741	1.248	0.375	2.931	0.452	1.688	1.666
10	0.061	3.679	0.666	0.857	0.645	1.287	1.381
11		3.231	0.049	0.846	0.206	2.021	1.082
12	0.021	3.132		1.906	0.235	0.828	0.918
Annual	0.882	2.848	0.392	1.823	0.339	1.332	1.929
Winter	0.008	4.210	0.004	1.875	0.204	0.675	2.138
Spring	0.174	2.846	0.546	1.113	0.101	1.692	2.421
Summer	2.571	1.198	0.655	2.620	0.614	1.176	1.687
Fall	0.766	3.155	0.364	1.664	0.438	1.775	1.510
Q ratio	4.048	2.498	5.071	2.765	3.538	3.188	2.704

[a] Corrected for water on the antenna.

The intent of this model is to (1) extend the $Q(p)$ estimates to other thresholds and empirical probability values and (2) provide a means to extend the model to locations where sufficient data are not available to generate the β and Q_1 values. The ITU-R recommended values are $\beta = 0.13$ and $Q_1 = 2.85$ if no information is available about the location of the intended link. For Virginia for attenuation by rain on a slant path, the recommended values are $\beta = 0.15$ and $Q_1 = 2.7$. The values obtained from the ACTS experiment are quite different. The Q ratios for 5 years of observations at the ACTS APT sites are displayed in Figure 5.23. The Q_{max} curve presents Q ratios obtained from the empirical distributions. Q_{mod} is obtained from the interpolation formula given in Equation 5.2. The β and Q_1 values are from Table 5.4. QITU and QVA use the ITU-R recommended β and Q_1 values for an unknown location or Virginia, respectively. The results show that the interpolation formula worked well for six of the seven sites. The predicted Q ratios obtained from the ITU-R recommended parameters matched the observations only for the Florida site.

5.4 *Fade duration*

The monthly, seasonal, and annual EDFs provide long-term statistics on the probability of the occurrence of rain attenuation. They do not provide information about the durations of rain events. The time series in Figure 5.2

Table 5.2 Percentage of Time the 5-dB Excess 20.2-GHz Rain Attenuation[a] is Exceeded

Mo	AK	BC	CO	FL	NM	OK	VA
1		0.058		0.379	0.009	0.195	0.302
2		0.016		0.554		0.128	0.565
3		0.177	0.012	0.350		0.116	0.228
4		0.050	0.008	0.501		0.287	0.236
5	0.131	0.064	0.011	0.216	0.137	0.498	0.413
6	0.167	0.176	0.128	0.920	0.063	0.391	0.722
7	0.536	0.105	0.119	1.258	0.315	0.287	0.535
8	0.192	0.099	0.092	1.064	0.243	0.271	0.416
9	0.131	0.059	0.047	1.266	0.106	0.597	0.430
10		0.098	0.095	0.316	0.089	0.316	0.26
11		0.091		0.078	0.009	0.255	0.113
12		0.042		0.597	0.002	0.094	0.021
Annual	0.097	0.025	0.049	0.677	0.081	0.301	0.363
Winter		0.004		0.544	0.026	0.085	0.218
Spring	0.027	0.050	0.021	0.397	0.019	0.323	0.326
Summer	0.326	0.027	0.133	1.139	0.212	0.378	0.585
Fall	0.035	0.020	0.043	0.614	0.065	0.416	0.312
Q ratio	5.866	13.17	4.390	3.032	4.777	2.785	2.465

[a] Corrected for water on the antenna.

illustrates the varying durations of such events. At a 10-dB threshold, the rain events lasted from 10 to 45 min, depending on frequency. At a 2-dB threshold, one of the events lasted for more than 2 h. Fade duration statistics were compiled for each of the ACTS APT sites by month, season, and year. The 1-sec average time series was used to calculate the fade durations. The calibration intervals were filled in by frequency scaling, using the observations at the other frequency and a scaling ratio derived from the prior 30 sec of observations. In contrast to other analyses, no low-pass filtering was used to separate scintillation effects from rain effects.[7]

Figure 5.24 presents the number of fades observed during the 5-year measurement period that exceed specified durations. This figure is for the 20.2-GHz beacon, using a 3-dB total attenuation threshold. Many more fades of shorter duration were also observed. Rain events are expected to produce fading durations longer than a few minutes. As expected, some of the fades lasted longer than an hour. The fading distribution is not presented as a cumulative distribution, because the many very short-term fades that contribute to the observed distribution are the results of scintillation or receiver noise variations above and below the threshold value. Low-pass filtering suppresses the short-term fluctuations, but can also change the fade duration statistics.[7] Several different model distributions have been proposed to represent fade duration statistics, chief among them being the lognormal distribution, the gamma distribution including the exponential, and the Weibull

Table 5.3 Percentage of Time the 10-dB Excess 20.2-GHz Rain Attenuation[a] is Exceeded

Mo	AK	BC	CO	FL	NM	OK	VA
1				0.111	0.002	0.052	0.089
2				0.211		0.017	0.292
3		0.224		0.134		0.027	0.032
4		0.002		0.198		0.076	0.089
5	0.040			0.111	0.034	0.231	0.122
6	0.041	0.035	0.106	0.432	0.034	0.198	0.369
7	0.099	0.009	0.043	0.591	0.140	0.158	0.274
8	0.013	0.027	0.044	0.520	0.089	0.126	0.178
9	0.007	0.032	0.022	0.647	0.027	0.184	0.193
10		0.016	0.026	0.206	0.023	0.098	0.062
11		0.006		0.038		0.102	0.040
12		0.002		0.254		0.033	0.016
Annual	0.015	0.005	0.017	0.305	0.028	0.111	0.142
Winter				0.178	2E-04	0.017	0.069
Spring	0.005	0.016	2E-04	0.171	0.005	0.119	0.090
Summer	0.052	0.003	0.052	0.550	0.093	0.170	0.291
Fall	9E-04	0.002	0.016	0.315	0.014	0.136	0.111
Q ratio	7.885	19.49	5.516	3.226	6.241	3.064	3.261

[a] Corrected for water on the antenna.

Table 5.4 Worst-Month Model Parameters

	AK	BC	CO	FL	NM	OK	VA
β	0.154	0.250	0.215	0.078	0.253	0.095	0.298
Q_1	4.100	5.235	2.299	2.942	2.528	2.483	1.822

distribution (see Section 1.7.2). Segmented distributions have also been employed, in which each segment relates to perhaps a different phenomenon. Each model can be made to fit segments of an observed fade duration distribution.

Figure 5.25 and Figure 5.26 present observed fade duration distributions on lognormal plotting scales. The distributions in Figure 5.25 were obtained from the data presented in Figure 5.24 by the appropriate normalization to become a probability distribution. The reduced variate is for a normal distribution whereas the abscissa is a logarithmic scale. A lognormal distribution would produce a straight line in this figure. The distributions are conditioned both on the attenuation threshold and on a 30-sec minimum duration for a rain event. At duration values higher than 30 sec, the distributions have the straight-line behavior expected for a lognormal process. Different seasons produce identical distributions. If each entire distribution were lognormal, the measured distribution would continue to lower duration values along the model curve.

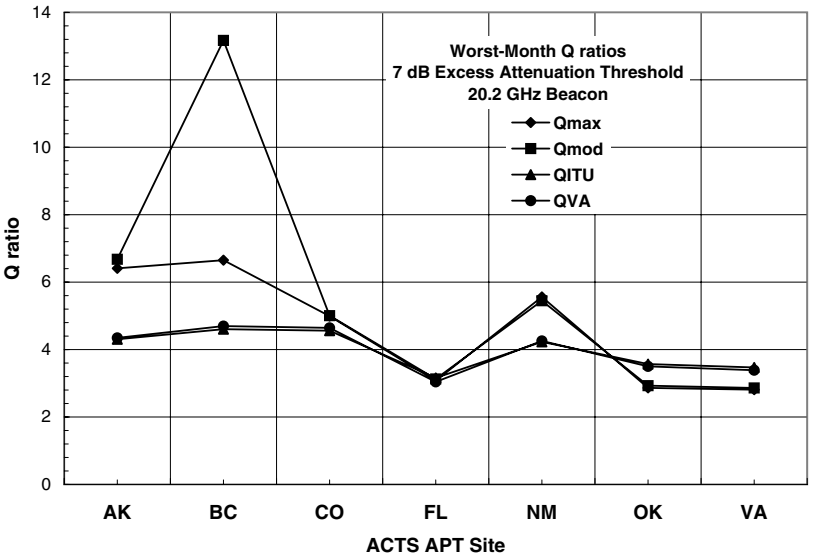

Figure 5.23 Worst-month *Q* ratios for a 7-dB excess attenuation threshold at 20.2 GHz for ACTS APT sites.

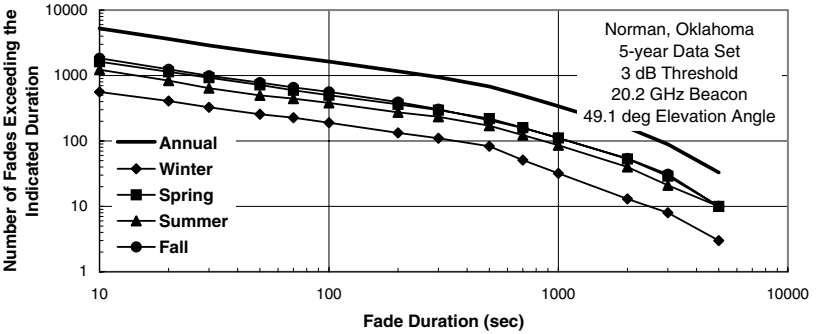

Figure 5.24 Annual and seasonal fade duration for 5-year statistics for a 3-dB threshold at 20.2 GHz for Norman, OK.

The time series used to compile the fade duration distributions were the result of all the processes that can contribute to attenuation. The 3-dB threshold limited those processes to rain and cloud attenuation and to the wet scintillation and receiver noise fluctuations that can accompany the attenuation. Both receiver noise and wet scintillation affect the data at the short time interval scales. The time scales of importance to wet scintillation can easily extend to 30 sec and longer intervals (see the spectra in Figure 4.51 to Figure 4.54). Although the plotted values for the 30-sec duration observations are well off the model curve, the differences represent only 17% of all the fades with durations greater than or equal to 30 sec.

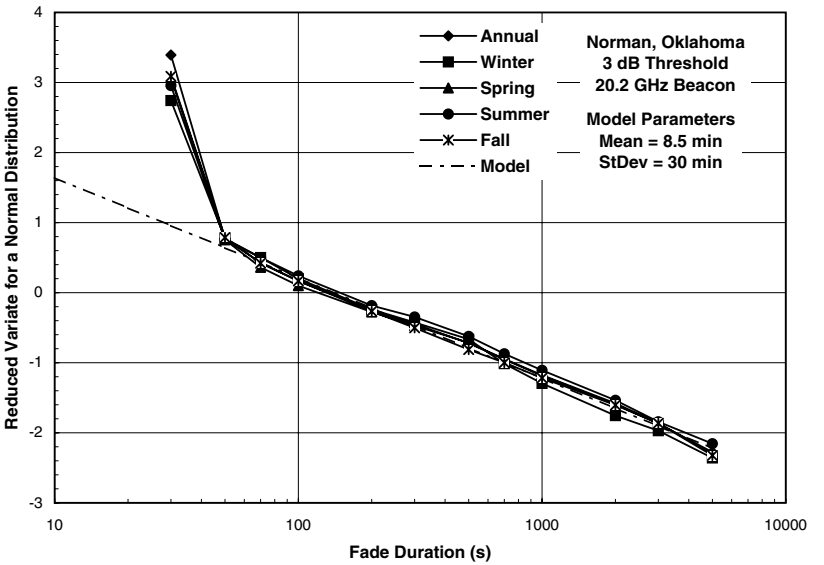

Figure 5.25 Annual and seasonal fade duration for 5-year distributions for a 3-dB threshold at 20.2 GHz for Norman, OK.

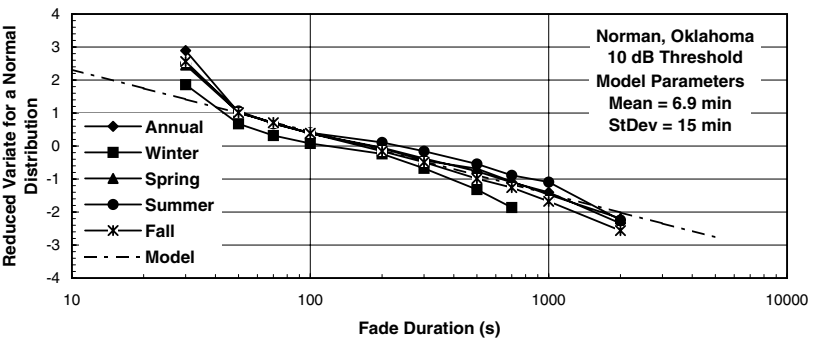

Figure 5.26 Annual and seasonal fade duration for 5-year distributions for a 10-dB threshold at 20.2 GHz for Norman, OK.

Small rain cells have an average size of less than a kilometer and, with a typical translation velocity of 10 m/s, traverse a point in 100 sec and a slant path to a satellite in about 2 min.[8] These small cells are defined relative to their peak intensity. Rain cells may also be defined as areas above a rate threshold (as observed above constant reflectivity thresholds on weather radar displays). Using the latter definition, the cell size is much larger, of the order of 10 km. Simple translation will move a threshold cell across a point in 1000 sec and a slant path in about 20 min. Cell development in time may shorten the observed duration. The parameters of the lognormal distribution are listed in the figure. The mean duration was 8.5 min, well within

the expected range. The median value was only 2.3 min, suggesting that the variations due to the small cells contribute to most of the fades.

Figure 5.26 presents the seasonal fade distributions for a higher, 10-dB, threshold. The annual distribution followed the lognormal model over most of the truncated range of duration values. At 30 sec, only 8% of the observed fades produced the difference from the model prediction. The annual and spring distributions were fit by the model; the winter distribution was below the model curve. Referring to Figure 5.18, most of the rain occurred in the spring followed by fall and the least amount occurred in the winter. The problem could be the limited number of observations used to generate the empirical distributions. Only 31 fades longer than 30 sec and deeper than 10 dB were recorded during the winter over the 5-year observation period.

The fading behavior changed little between the two beacon frequencies. The equiprobable fade threshold at 27.5 GHz, which corresponds to the 3-dB threshold at 20.2 GHz, is 5.2 dB. The fading distributions for a 5-dB threshold at the higher frequency are shown in Figure 5.27. The model fit to the distributions and the 20.2-GHz model for the 3-dB threshold is shown in the figure. The differences between the two models are minor. The annual distributions at four attenuation thresholds and both beacon frequencies are presented in Figure 5.28. In this figure, the 30-sec values were omitted. The observed 20-GHz, 3-dB and 28-GHz, 5-dB distributions are close matches as are the 20-GHz, 5-dB and 28-GHz, 10-dB distributions. Within the statistical uncertainty of the observed distributions, a single distribution could be generated that would fit all the observations. This result supports the conclusion presented by Helmken et al. that their "results support a common log-normal distribution of the fade duration at any fade depth exceeding 2–4 dB, where hydrometeor effects predominate."[7] The model distribution parameters that fit the individual observations in Figure 5.28 are listed in Table 5.5.

The fade duration analysis was extended to the other ACTS APT sites. Figure 5.29 presents the results, including model fits for 20.2-GHz observations at the 3-dB threshold. The solid curves represent the observed distributions and the dashed curves the model distributions. The results show nearly parallel distributions, implying the same model standard deviation values for the logarithm of duration. The median values shifted with location, increasing as the sites move south (or the elevation angle increases). The distribution for Alaska did not provide a good match to a lognormal distribution. As before, the distributions are conditioned on fade durations longer than 30 sec and the 30-sec value is not plotted. The model parameters for the fits as shown in the figure are presented in Figure 5.30 and Table 5.6.

5.5 *Fade rate*

Fade rate statistics were compiled for each ACTS APT site, using the 1-sec average time series. As before, the calibration intervals were filled in by frequency scaling from the time series for the other frequency. The

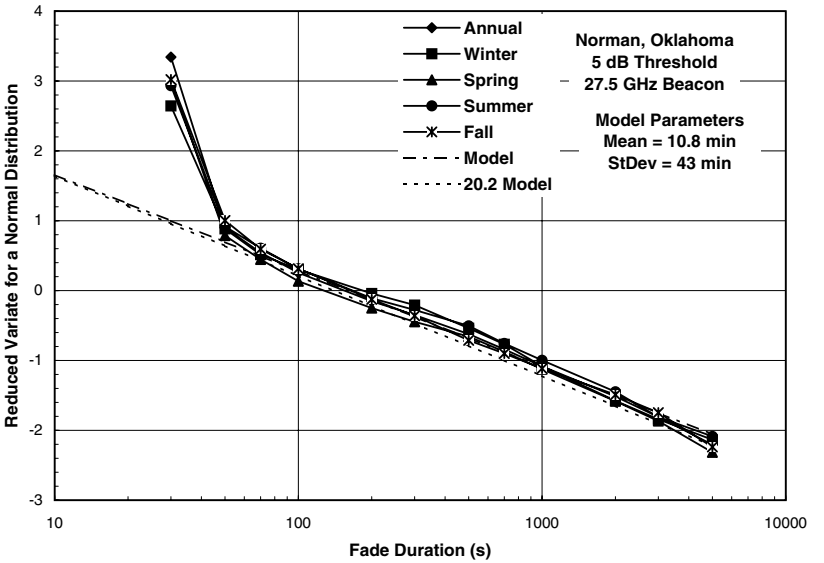

Figure 5.27 Annual and seasonal fade duration for 5-year distributions for a 5-dB threshold at 27.5 GHz for Norman, OK.

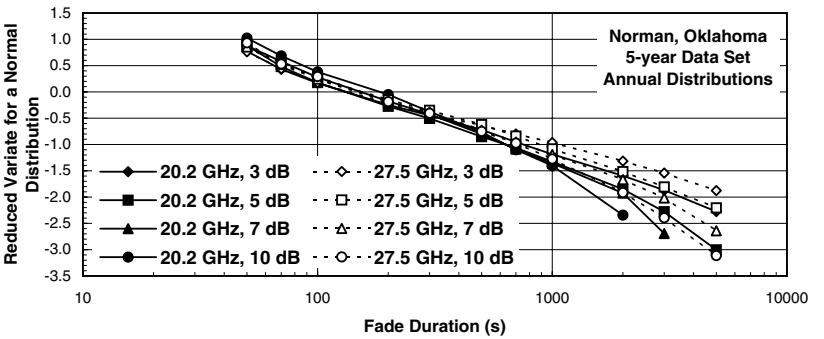

Figure 5.28 Annual fade duration for 5-year distributions for a range of attenuation thresholds at 20.2 and 27.5 GHz for Norman, OK.

Table 5.5 Lognormal Model Parameters for Norman, OK

Threshold (dB)	20.2 GHz Median (min)	20.2 GHz Mean (min)	Standard deviation (min)	27.5 GHz Median (min)	27.5 GHz Mean (min)	Standard deviation (min)
3	2.3	8.5	30	2.7	15.0	82
5	2.3	6.6	18	2.7	10.8	43
7	2.5	6.9	18	2.3	8.5	30
10	2.8	6.0	11	2.4	7.2	20

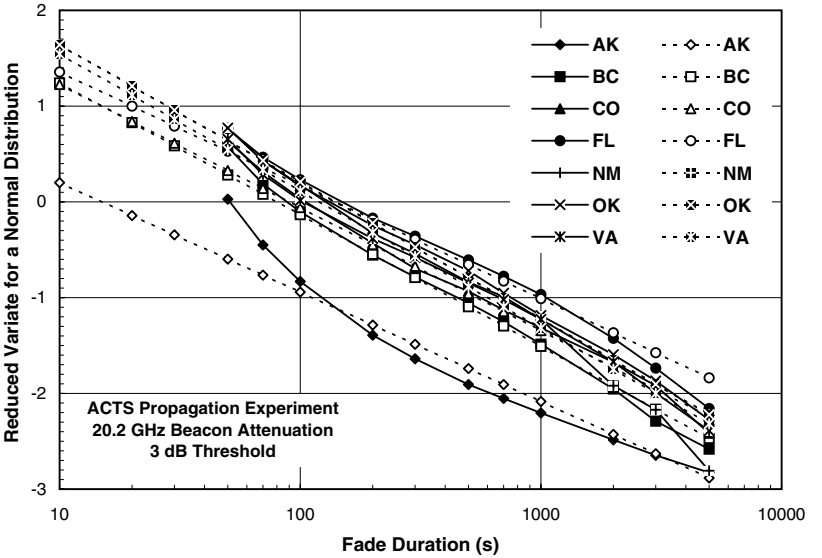

Figure 5.29 Annual fade duration for 5-year distributions for a 3-dB threshold at 20.2 GHz for ACTS APT sites.

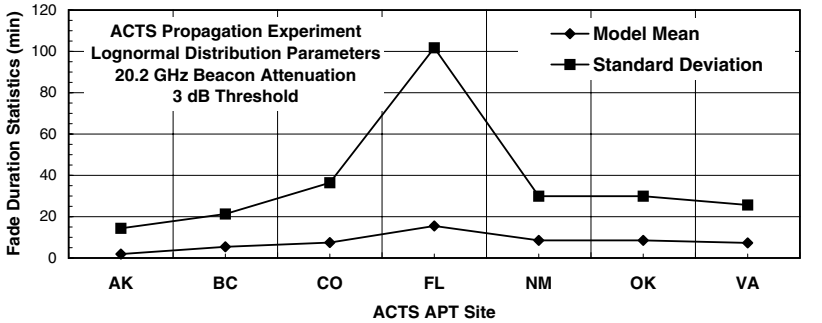

Figure 5.30 Lognormal distribution parameters for annual fade duration for 5-year distributions for a 3-dB threshold at 20.2 GHz for ACTS APT sites.

frequency-scaling factor was determined from the 30 sec of observation prior to a calibration. The empirical joint attenuation, fade rate density function for the Norman, OK, site is given in Figure 5.31. Note that these functions have not been normalized to a joint probability density. No low-pass filtering beyond the 1-sec averaging was used. Fade rates as high as ±2.5 dB/s were observed The attenuation bin boundaries are scaled to correct for water on the antenna. No corrections were made to the time series prior to collecting the joint histograms. A sample segment of a time series prior to calibration adjustment obtained during a period with rain is shown in Figure 4.50; a time series segment in rain after adjustment is shown in Figure 5.32. The

Table 5.6 Model Parameters for ACTS APT Sites for a 3-dB threshold at 20.2 GHz

	Median (min)	Mean (min)	Standard deviation (min)
AK	0.3	1.9	14
BC	1.3	5.4	21
CO	1.5	7.5	36
FL	2.3	15.5	102
NM	2.3	8.5	30
OK	2.3	8.5	30
VA	2.0	7.3	26

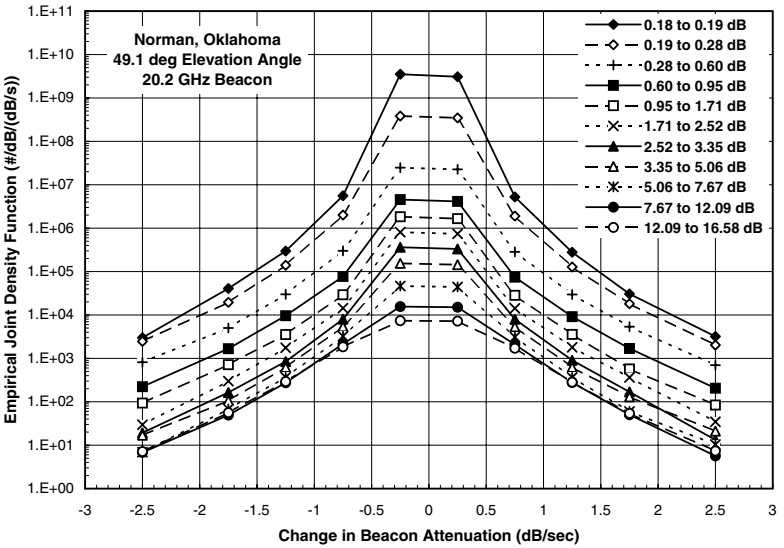

Figure 5.31 Joint fade rate for 20.2-GHz attenuation distribution for Norman, OK.

prior segment shows a short dropout of the beacon in the 12:38 min interval. This dropout contributed both –1.45 dB/s and +1.1 dB/s events. These short dropouts are included in the statistics. The beacon data were calibrated to represent attenuation relative to free space.[9]

The cumulative empirical distribution functions for each of the ACTS APT sites are presented in Figure 5.33 and Figure 5.34. Figure 5.33 presents the distributions for all the 1-sec change observations collected at each site over a 5-year period. Figure 5.34 presents distributions conditioned on attenuation observations higher than 2 dB. The latter is for rain conditions at all sites but Alaska. The short dropout illustrated for the Oklahoma site and others recorded at several other sites mainly affected the entire data set distribution (Figure 5.33) but not the rain and cloud distribution (Figure 5.34). In rain, the sites with more occurrences of convective rain

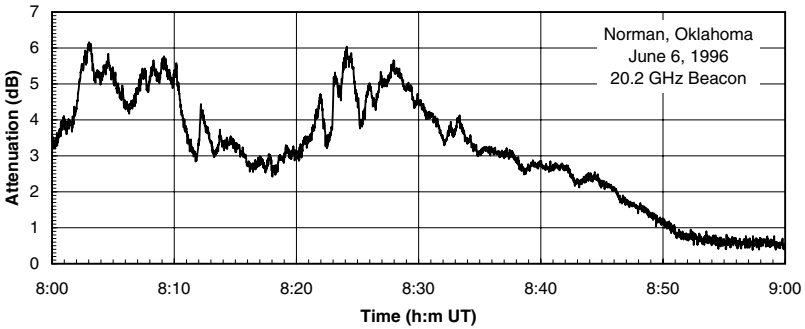

Figure 5.32 Total 20.2-GHz beacon attenuation time series 8:00 to 9:00 UT for June 6, 1996, for Norman, OK.

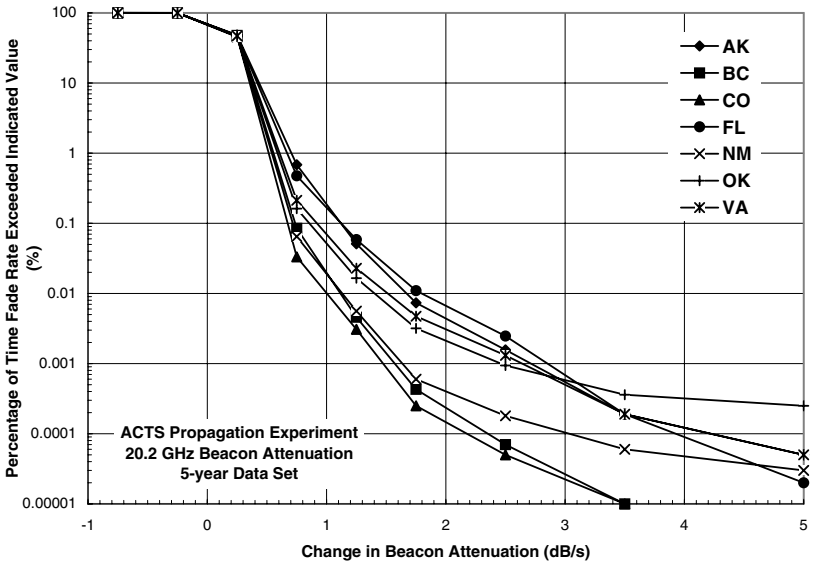

Figure 5.33 Fade rate distributions for all 20.2-GHz attenuation levels for ACTS APT sites.

produced the highest occurrences of high fade rates. The Vancouver site, with extended periods of low rain rates during the winter months, produced the lowest fade rates.

5.6 *Rain attenuation models*

Rain attenuation statistics are needed for radio communication system design and remote sensing system design at the frequencies considered in this book. Historically, annual distribution data have been available from selected locations around the globe, but predominantly in North America and Europe. In

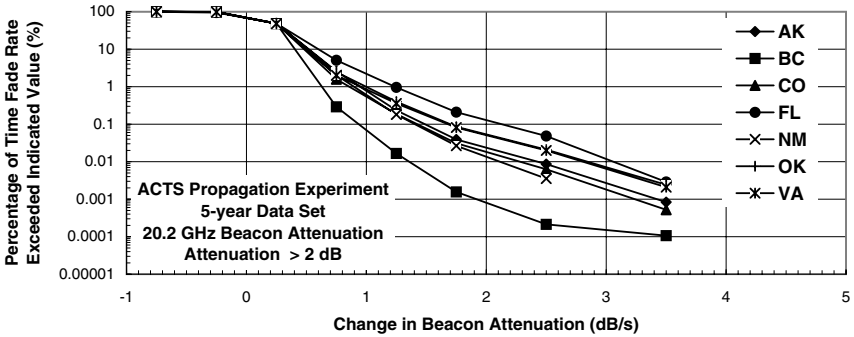

Figure 5.34 Fade rate distributions for 20.2-GHz attenuation levels above 2 dB for ACTS APT sites.

the early days, observations at one location were used to model possible occurrences at another. The ITU-R hosts an extensive database of annual empirical attenuation distributions that can be used for extrapolation to other locations if the rain climates are similar. Over the past few decades, a number of models have been published that either expand on these measured distributions, or the underlying physics of rain attenuation, or both, and automate the prediction process for a location of interest. Crane considered the rain attenuation prediction problem in depth.[8] Here, we summarize the use of only two of the models: the ITU-R recommended model and the latest revisions to the Crane two-component model. The ITU-R model is included because it provides a statistical summary of the data in the databases and because it is the basis for a number of recommendations that affect international agreements on system design and deployment. The Crane model is included because it goes beyond the other available models by presenting a consistent view of the physics of the rain attenuation process as it effects annual, seasonal, monthly, and worst-month occurrence statistics, the statistics of site diversity improvements, and cross-polarization statistics.

Predictions of rain attenuation statistics start with the prediction of rain-rate statistics. These statistics describe the rain climate for the path of interest. Early models used the idea of a rain climate zone or region of the globe where the rain-rate statistics should be similar. These models are gradually becoming replaced by procedures to generate the local statistics from (1) available long-term climate data that can be manipulated to provide the desired rain-rate distribution or (2) from numerical model reanalyses that generate statistics from numerical model output constrained by long time series of global observations on a synoptic scale.

5.6.1 Rain rate models

5.6.1.1 Crane local model

The two-component model combines two rain-rate distributions: (1) an exponential distribution to describe the contributions of small or volume cells

and (2) a lognormal distribution to describe the rates produced in the rain debris region surrounding the small cells.

The revised two-component distribution is approximated by:[8,10]

$$P(r \geq R) \approx P_V(r \geq R) + P_W(r \geq R)$$

$$P_V(r \geq R) = 4.585 R_C^{-0.004} E_1\left(\frac{R}{R_C}\right) \approx P_C e^{-\frac{R}{R_C}} \tag{5.3}$$

$$P_W(r \geq R) = P_D Q\left(\frac{\ln R - \ln R_D}{S_D}\right)$$

where P_V is the volume cell component; P_W the debris component; Q the upper tail of the normal distribution (lognormal because of the explicit use of the natural logarithms and the use of natural logarithms in the calculation of S_D); P_C, R_C, P_D, R_D, and S_D are distribution parameters; and E_1 the exponential integral of order 1. The local model provides the procedures needed to estimate these parameters from available long-term climate data.

The cell parameters, P_C and R_C, may be obtained from excessive 5-min precipitation data and short-duration 5-min maximum precipitation data available from the National Climate Data Center (NCDC) for sites in the United States and its possessions. The two data sets are needed to construct a period of record of at least 20 years. The parameters are extracted from the data by using the extreme value theory.[11] The ordered extreme value distribution is used to extract both parameters. In Figure 5.35, the ordered values

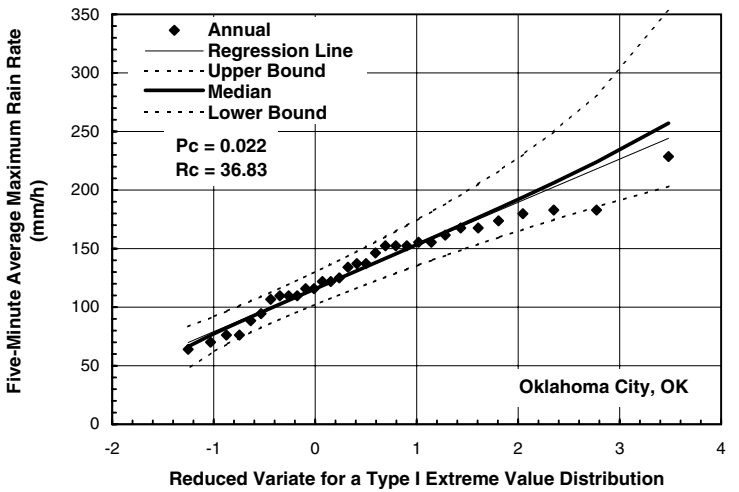

Figure 5.35 Ordered annual 5-min maximum rain-rate distribution for Oklahoma City, OK.

of the highest 5-min rain accumulation for each year of a 32-year record are plotted against the reduced variate for a Type I extreme value distribution. The rain accumulation is expressed as a 5-min average rain rate. The reduced variate is given by:

$$z_i = -\ln\left(-\ln\left(\frac{i}{n+1}\right)\right) \tag{5.4}$$

where z_i is the reduced variate, n the number of samples in the ordered distribution, and i the number of the ordered sample from $i = 1$ for the smallest to $i = n$ for the largest value.

The ordered observations from a type I extreme value distribution should lie along a straight line. P_C and R_C parameters are obtained from the intercept and slope of the line best fit to the distribution. The slope = σ_E = R_C = 36.83 is from the regression line in the figure. The expected annual number of independent samples in the exponential distribution, N, is obtained from the intercept of the regression line. The intercept = μ_E = $\sigma_E \ln(N)$ = 115.9. Then:

$$N = e^{\left(\mu_E / \sigma_E\right)} = 23.3 \text{ five-minute intervals per year} \tag{5.5}$$

and

$$P_C = N \cdot 100 / 12 / 24 / 365 = 0.022\% \tag{5.6}$$

The debris parameters are obtained from a full set of hourly rain accumulation values for the site closest to the proposed radio link. A minimum 30-year period of record is recommended. The hourly data are available from NCDC for more than 7000 sites in the United States. Three parameters are needed from the hourly data: the average annual rain accumulation, M; the average of the natural logarithm of each nonzero hourly sample, m_H; and the standard deviation of the natural logarithm of the nonzero hourly values, s_H. The parameters for the debris distribution are obtained from these values by:

$$\begin{aligned} S_D &= s_H \\ R_D &= e^{2m_H} \\ M &= M_V + M_W \\ &= P_V(0.254)R_C H_T + P_W(0.254)R_D e^{0.5S_D^2} H_T \end{aligned} \tag{5.7}$$

where H_T is the number of hours in a year (or month). This equation may be solved for P_D. The two probability calculations are for the lowest rain accumulation possible in 1 h, 0.254 mm, which is the collection of one tip by a standard tipping bucket gauge.

The two-component prediction model, Equation 5.3, generates the median rain-rate probability distribution. To calculate the expected distribution values, the yearly variation must be modeled. Available observations of the interannual variability of rain-rate and rain-attenuation distributions imply a lognormal distribution of annual values at fixed occurrence values or at fixed rate or attenuation values.[8] Two additional parameters must be obtained from the hourly rain data to model interannual variability and provide a distribution of the expected variations in annual distributions: the yearly standard deviation of the logarithm of the total number of hours with rain and the standard deviation of the natural logarithm of the annual rain accumulation, s_P and s_R, respectively. For the Oklahoma City site, a 46-year record of hourly rain accumulations produced the following set of parameters: M = 845 mm, R_D = 1.85 mm/h, S_D = 1.21, P_D = 1.62%, s_P = 0.22 and s_R = 0.18.

The expected probability value is found from the median distribution by:

$$\begin{aligned} m_P &= \ln(P) \\ P_\mu &= e^{m_P + 0.5 s_P^2} = P e^{0.5 s_P^2} \end{aligned} \tag{5.8}$$

where P_μ is the expected probability distribution. The lognormal interannual variation model can also be used to estimate the yearly occurrence statistics for the distribution. The statistical variability in the distributions affects both the occurrence probability and the rain rate. Both the s_P and s_R values are used to estimate the expected statistical variation (or bounds) on the distribution. The distribution expected to occur once in Y years (with a Y-year return period[11]) is given by:

$$\begin{aligned} \frac{\Delta P}{\Delta R} &= \frac{P(r \geq R + 0.5\Delta R) - P(r \geq R - 0.5\Delta R)}{\Delta R} \\ s_U^2 &= s_P^2 + \frac{\Delta P}{\Delta R} s_R^2 \\ u &= Q^{-1}\left(\frac{1}{Y}\right) \\ P_Y &= P(r \geq R) e^{u s_U^2} \end{aligned} \tag{5.9}$$

where P_Y is the rain-rate distribution expected to occur once every Y years on average.

The bounding curves shown in Figure 5.35 were computed by using the procedure expressed in Equation 5.9, with the following differences: (1) the theoretical distribution for the interannual variation in an Type 1 extreme value was used in place of the normal distribution, Q, and (2) the uncertainty in the distribution order was assumed to be zero that is, $s_R = 0$. The vertical spread between the upper and lower bounding curves in the figure then depends only on the number of samples in the extreme value distribution. The upper bounding curve is for a 20-year return period (5% of the distributions will be above the curve). The expectation is that for a random selection of ordered distributions, 90% of the distributions will lie between the bounding curves and 5% below the lower bounding curve. The bounds are computed at each z_i. The ordered distribution values at neighboring reduced variate values are not independent.[11] A graphical test of consistency with the extreme value distribution hypothesis can be made by counting the fraction of ordered values that lie outside the bounding curves. Because of the statistical dependence between neighboring values, the fraction of values outside the bounds will always be higher than expected by chance.

The procedure used to establish the parameters for the annual local model can be employed for observations for a month or for a season. For application to attenuation prediction, monthly statistics are most important because the rain height used to establish the length of the propagation path in rain varies from one month to the next. The parameters for a monthly volume cell distribution were obtained from the excessive and short-term precipitation data for that month. Results for the spring months that produced the highest rain occurrence values (see Figure 5.18) are shown in Figure 5.36. The ordered distribution of the highest values in the month of interest for each year of data collection were fit to a line with the same slope as the annual distribution. Only the intercept value changed from one month to the next. The volume cell component was modeled as having the same

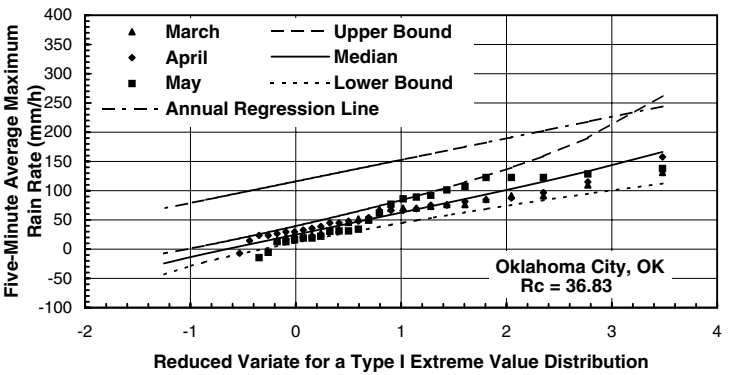

Figure 5.36 Ordered spring 5-min maximum rain-rate distributions for Oklahoma City, OK.

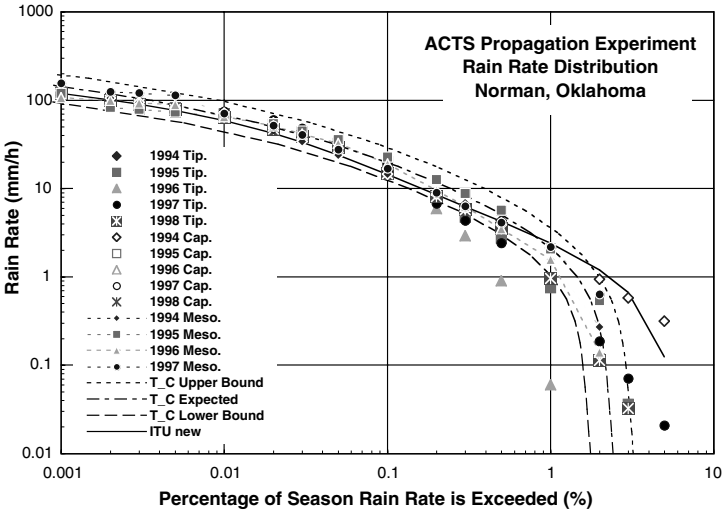

Figure 5.37 Annual empirical rain-rate distributions and model predictions for Norman, OK.

R_C value as the annual distribution, but the P_C value varied from one month to the next. For display and comparison with the bounding curves, each intercept value was shifted to match the intercept for March. With this adjustment prior to plotting, all three monthly distributions were within the expected bounds for 32 years of observations and were consistent with the exponential distribution model.

The debris distributions were also consistent with the use of same R_D and S_D values as the annual distribution for each month. Therefore, three of the seven distribution parameters were set equal to the annual distribution parameters and the rest were varied from one month to the next to best fit the climate data.

The annual local model rain-rate predictions were compared to the 5-year ACTS propagation experiment observations in Figure 5.37 for gauges at the APT and on the airport in Norman, OK. The bounding distributions enclose all the annual distributions labeled Meso. in the figure. These observations were made at ground level on the edge of the airport in Norman, OK, a site about 7 km from the APT. The capacitor gauge (Cap.) was used for the first year of observations and the tipping bucket gauge (Tip.) was used for the last four years of observations. The latter gauges were mounted beside the APT on the roof of a 15-story building. Wind flow across the building affected rates lower than about 10 mm/h. As a result, the occurrences at low rates were fewer than expected. A comparison between the EDFs and the model bounds shows fewer occurrences than expected for three of four years. Overall, the measurements were consistent with the model.

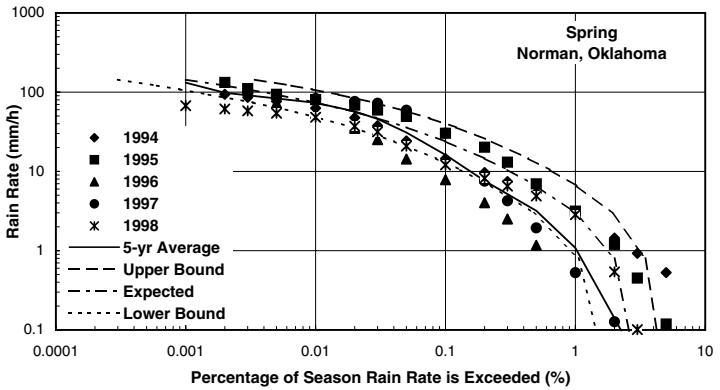

Figure 5.38 Spring season empirical rain-rate distributions and model predictions for Norman, OK.

The spring-month distributions were compiled from the observations shown in Figure 5.36 and the hourly data for the same three months. They were combined to generate the expected distributions for the spring months. The comparison between the observed distributions for each year and the model distributions is presented in Figure 5.38. Only gauge data from the rooftop gauges are shown in this figure. The 1996 distributions were lower than expected for the year and for the spring season. The other years were consistent with the predictions.

5.6.1.2 New ITU-R model

The ITU-R has recommended the use of a new rain-rate distribution prediction model based on the output from a reanalysis of 15 years of numerical model analysis data by the European Centre of Medium-Range Weather Forecast (ECMWF).[12,13] The model output did not provide rain-rate statistics, but produced parameters that were employed in a regression analysis with rain-rate distribution data available in the ITU-R databases to produce a prediction method. The ECMWF output used in this prediction method was the annual rainfall amount for convective type rain, the annual rainfall amount for stratiform rain, and the probability of a rainy 6-h period. These output values were available on a worldwide 1.5° by 1.5° latitude by longitude grid. The output values are interpolated to the location of interest. The model is available from the ITU-R for use on a personal computer.

The disadvantages for this model are (1) uncertainties in the output parameters that arise from a lack of adequate water substance input data, (2) large-scale smoothing that results from the coarse computational grid, and (3) lack of rain-rate statistics on a worldwide grid for use in the regression analysis. The model generates annual predictions, but, in its present state, cannot provide monthly statistics. A problem in extending this model to monthly or seasonal distributions is the lack of available empirical statistics for a month or season.

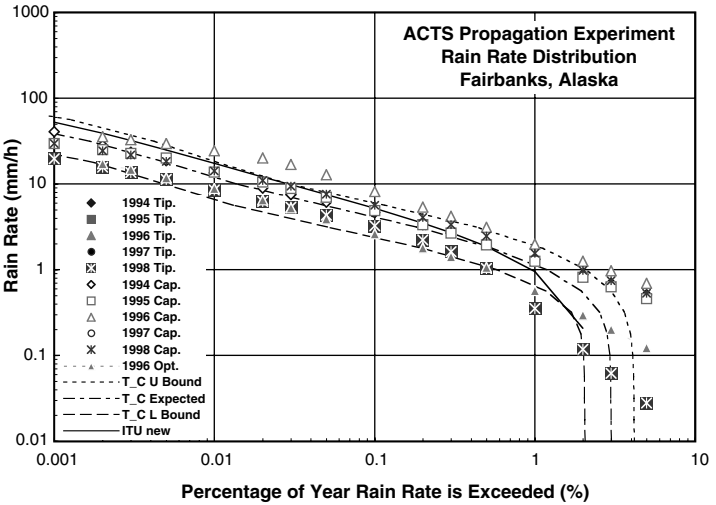

Figure 5.39 Annual empirical rain-rate distributions and model predictions for Fairbanks, AK.

Figure 5.37 includes the new ITU-R model predictions for the Norman, OK, site. The model provides a good match to the data at rates above about 2 mm/h. It predicts more rain at lower rates than was observed at the well-sited Meso. gauge.

5.6.1.3 Comparison to ACTS observations

The empirical annual and dominant seasonal distributions and model predictions are presented in Figure 5.39 through Figure 5.50 for the rest of the ACTS APT sites. Several types of rain gauges were used during the 5-year measurement program. At the Oklahoma site, two different tipping bucket gauges were used, one on the top of a building and the other on a well-placed gauge at ground level in a flat area with no obstructions. The type of gauge used for each year is indicated by the plotted symbols. At the New Mexico site, both the capacitor and tipping bucket gauges were in service. At the Alaska site, both a tipping bucket and capacitor gauge were used for one year and both an optical and capacitor gauge were used for another. At several sites, several years went by without measurements. The gauges used for the seasonal measurements were the gauges employed for the same year. When a choice of gauges was possible, the tipping bucket was employed for comparing with model predictions. At several of the sites, the gauges were mounted on rooftops, sometimes near the roof edge where wind flow could affect the gauge catch.

The seasonal model provided a good match to the observations at the Alaska site except for one of the years. The annual distribution for that year was also above the upper bound. At the British Columbia site, both the annual and winter observations were within the expected bounds. The

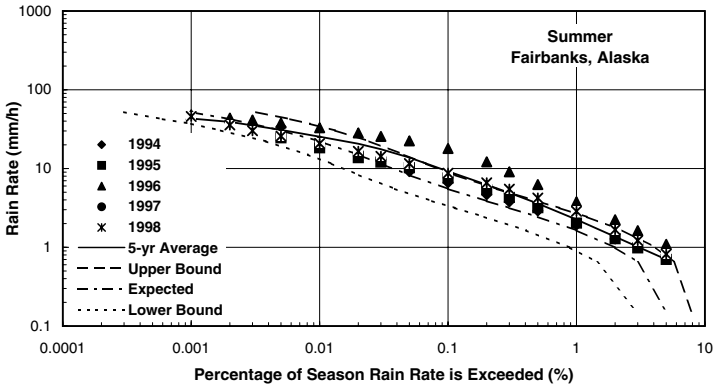

Figure 5.40 Summer season empirical rain-rate distributions and model predictions for Fairbanks, AK.

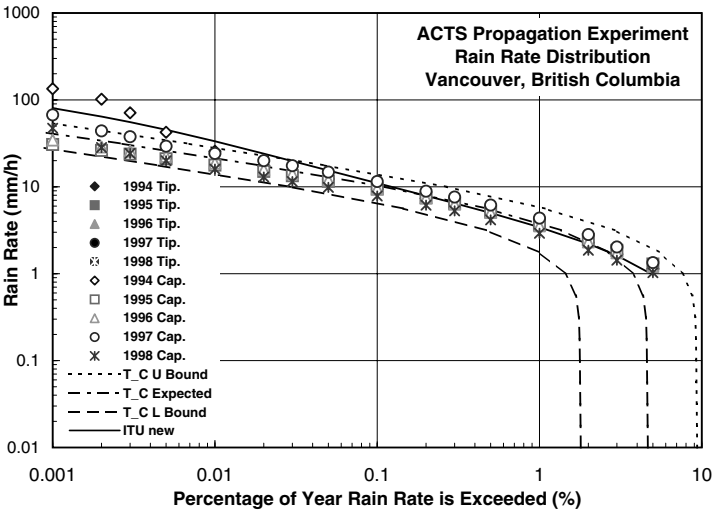

Figure 5.41 Annual empirical rain-rate distributions and model predictions for Vancouver, British Columbia.

Colorado site provided only two years with observations. The match between measurements and predictions was good. At the Florida site, the annual distributions were within the expected bounds. Three of the summer distributions showed fewer occurrences than predicted at rates lower than 10 mm/h. The New Mexico data provided annual observations from two closely spaced gauges. The distributions for each gauge were different but generally within the expected bounds, except for rates below 1 mm/h. At the very low rates, the tipping bucket gauge recorded up to an order of magnitude fewer rain-rate occurrences than the capacitance gauge. For the

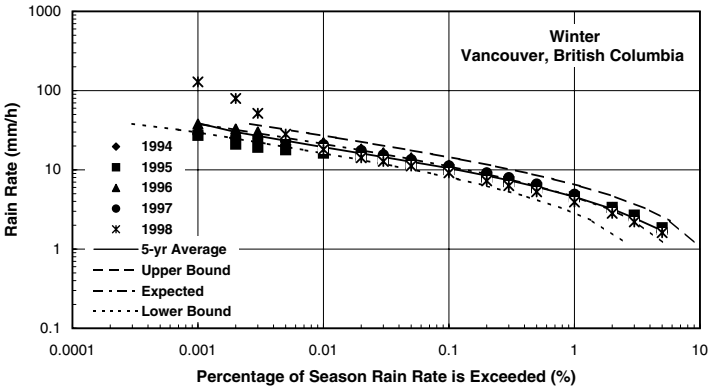

Figure 5.42 Winter season empirical rain-rate distributions and model predictions for Vancouver, British Columbia.

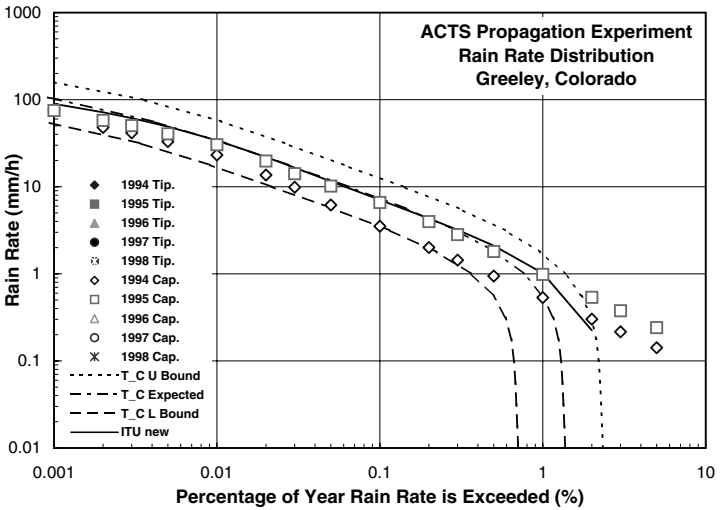

Figure 5.43 Annual empirical rain-rate distributions and model predictions for Greeley, CO.

summer season, only the tipping bucket data are shown. In this case, at the higher rates, the observations had higher than predicted occurrences whereas the lower rates had fewer occurrences than predicted. At the Virginia site, the tipping bucket measurements produced fewer than expected occurrences of rates lower than 10 mm/h, both for the annual distributions and the spring distributions.

Predictions of the new ITU-R model are shown on each of the annual distribution plots. In general, the ITU-R model was within the bounds predicted by the local model predictions, and for two of the sites the ITU-R

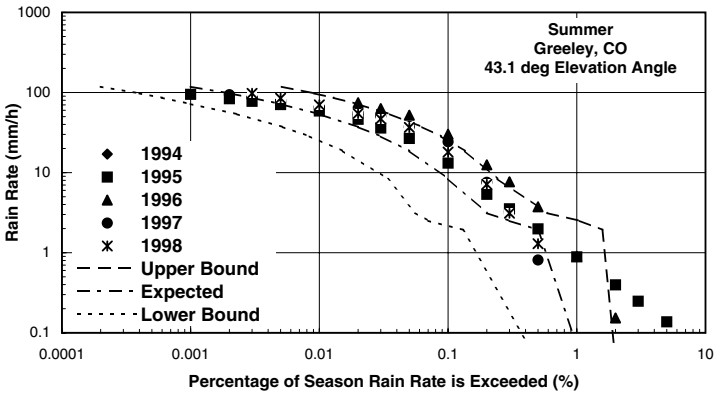

Figure 5.44 Summer season empirical rain-rate distributions and model predictions for Greeley, CO.

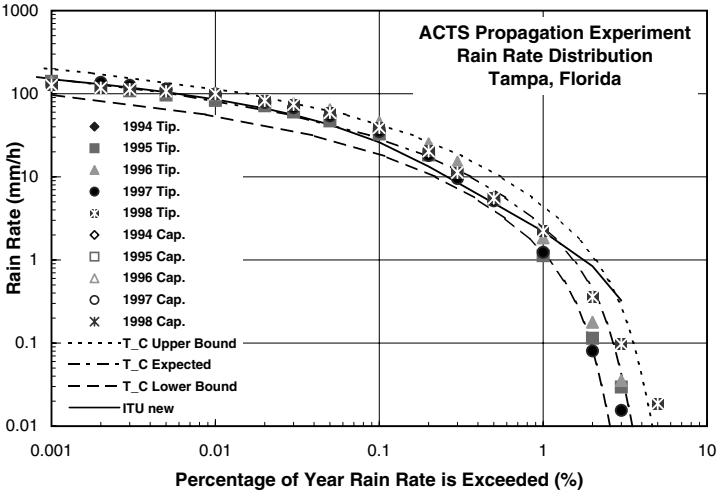

Figure 5.45 Annual empirical rain-rate distributions and model predictions for Tampa, FL.

model matched the expected distribution predicted by the local model. For several of the sites, the shape of the ITU-R model predictions did not match the local model predictions or the observations.

In general, the local model fit the observations within the expected variability of the measurements. For the 30 site-years of empirical distributions, 3 were outside the expected bounds by nearly an order of magnitude along the percentage of time scale at rain rate above 1 mm/h. The annual results match expectations. The seasonal empirical distributions showed more yearly variability than expected, especially at low rain rates. Some of the seasonal differences between observations and predictions could be due

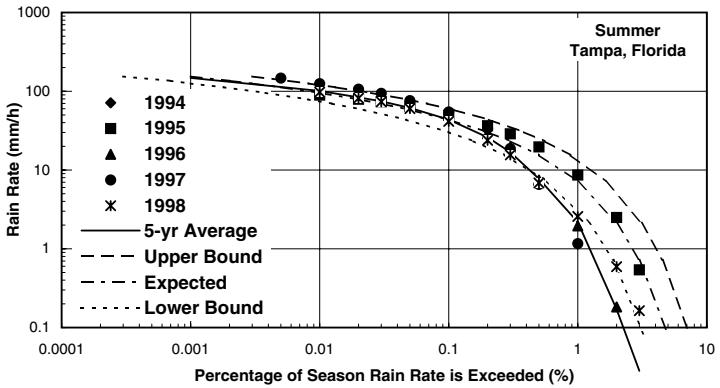

Figure 5.46 Summer season empirical rain-rate distributions and model predictions for Tampa, FL.

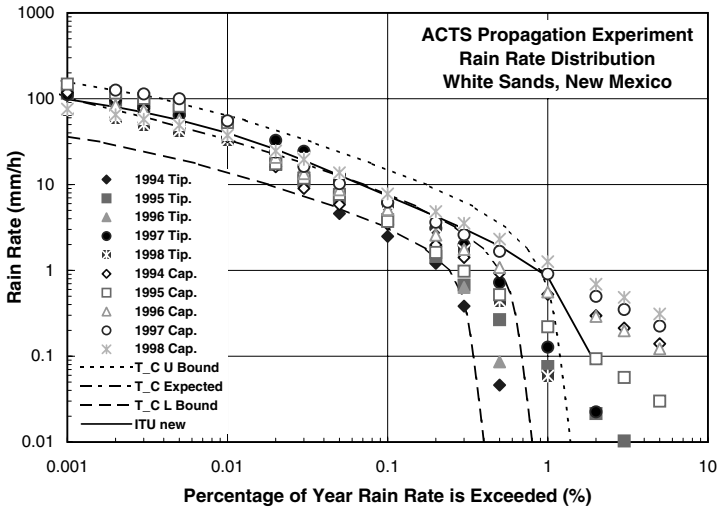

Figure 5.47 Annual empirical rain-rate distributions and model predictions for White Sands, NM.

to gauge siting, for example, the Oklahoma, Florida, and Virginia sites used rooftop gauges.

The new monthly distribution model allows for different ways to visualize the changes in the rain-rate distribution with month and season. The monthly probabilities of exceeding a 5-mm/h threshold rate are plotted in Figure 5.51 through Figure 5.57. In each figure, the monthly distribution is displayed for each year of observations. The parameters of the lognormal variability distribution are also plotted. As before, the bounding curves are the expected to be exceeded 5% and 95% of the years plotted. For the Alaska

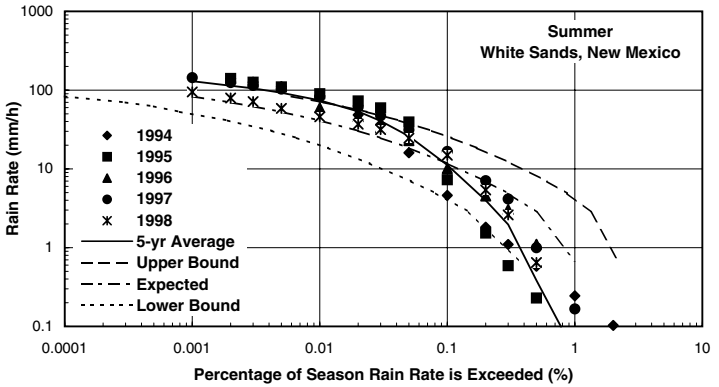

Figure 5.48 Summer season empirical rain-rate distributions and model predictions for White Sands, NM.

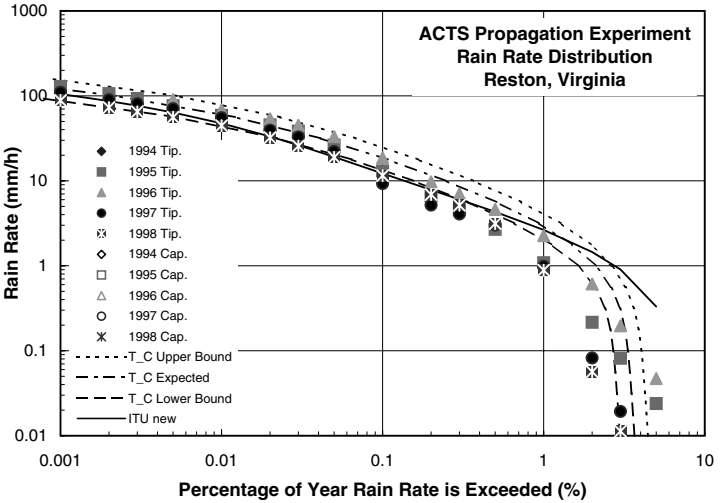

Figure 5.49 Annual empirical rain-rate distributions and model predictions for Reston, VA.

site at this rain-rate threshold, the upper bound is exceeded for two of the seven months of data for one of the years. For the British Columbia site, the observed monthly probability fell below the lower bounding curve for two months each from a different year. For Colorado, the rains came earlier in the year than expected for one of the two years with data. The rest of the figures show that the upper bounding curve is rarely exceeded, but the occurrence probabilities are often below the lower bound for the Florida, Oklahoma, and Virginia sites. One of the sources of the lower occurrence probabilities could be the reduced catch of the rooftop gauges. For predicting

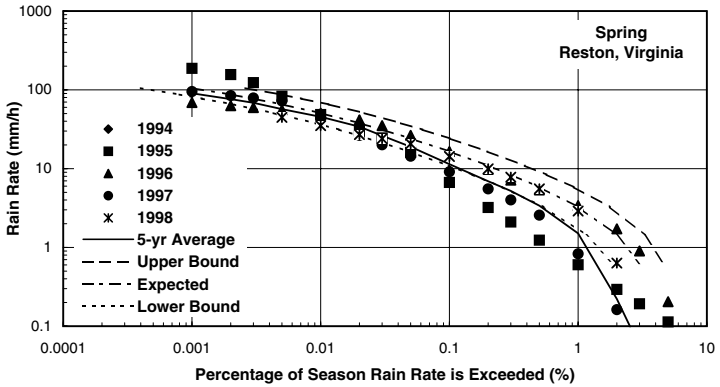

Figure 5.50 Spring season empirical rain-rate distributions and model predictions for Reston, VA.

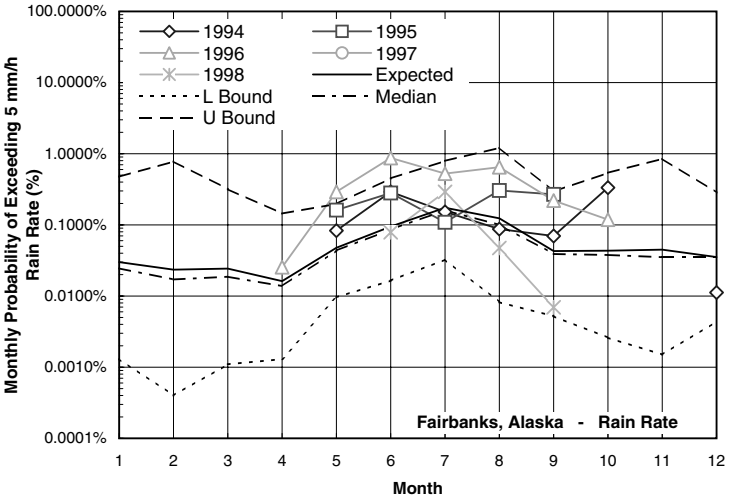

Figure 5.51 Empirical monthly probabilities of exceeding the 5-mm/h threshold and model predictions for Fairbanks, AK.

rain attenuation, missing the high attenuation values is more of a problem to system users than having better availabilities than expected.

5.6.2 *Two-component path attenuation model*

The two-component model calculates the expected path attenuation distribution, given the rain-rate distribution and the length of the path. The length of a terrestrial path is the distance between terminals. The length of a slant path is the slant distance from the terminal to the rain height for the path.

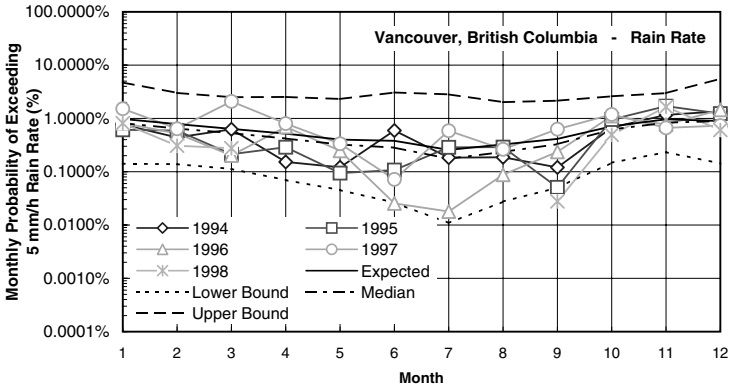

Figure 5.52 Empirical monthly probabilities of exceeding the 5-mm/h threshold and model predictions for Vancouver, British Columbia.

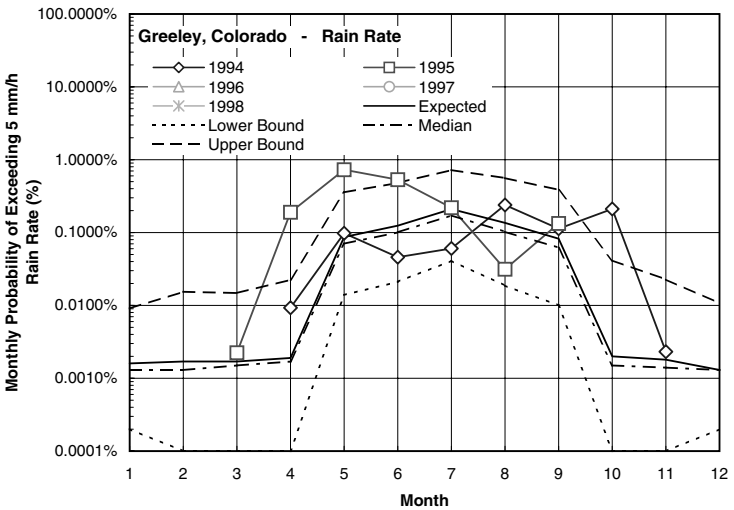

Figure 5.53 Empirical monthly probabilities of exceeding the 5-mm/h threshold and model predictions for Greeley, CO.

Earlier versions of the model picked a zonal annual 0°C isotherm height as the rain height. The zonal average is the average over longitude for a fixed latitude. The average was compiled from rawinsonde soundings and primarily represents overland locations. The most recent version uses a geographical map of the monthly averaged 0°C isotherm height for each month. With monthly rain-rate statistics, the rain height can be matched to the rain-rate distribution. The 0°C isotherm height maps can be extracted from long-term numerical model reanalyses or from the published Global Gridded Upper Air Statistics (GGUAS) compiled from a 15-year reanalysis by ECMWF,

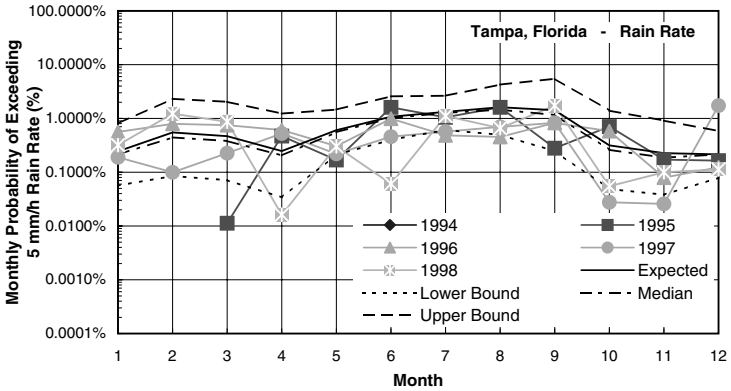

Figure 5.54 Empirical monthly probabilities of exceeding the 5-mm/h threshold and model predictions for Tampa, FL.

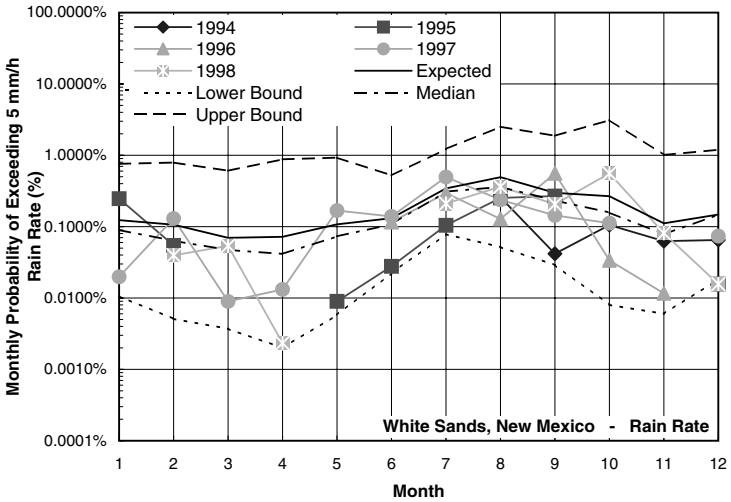

Figure 5.55 Empirical monthly probabilities of exceeding the 5-mm/h threshold and model predictions for White Sands, NM.

which is available at NCDC. Version 1.1 of the GGUAS database was used. A 40-year reanalysis is now available from the National Center for Atmospheric Research (NCAR). It can be used to generate maps of rain-height statistics that can provide rain height distributions for a location of interest that can be combined with the two-component model predictions conditioned on the value of rain height.

The two-component model starts with the seven parameters for the closest location with available maximum short-term precipitation and hourly rain accumulation statistics. A table of these statistics is presented by month

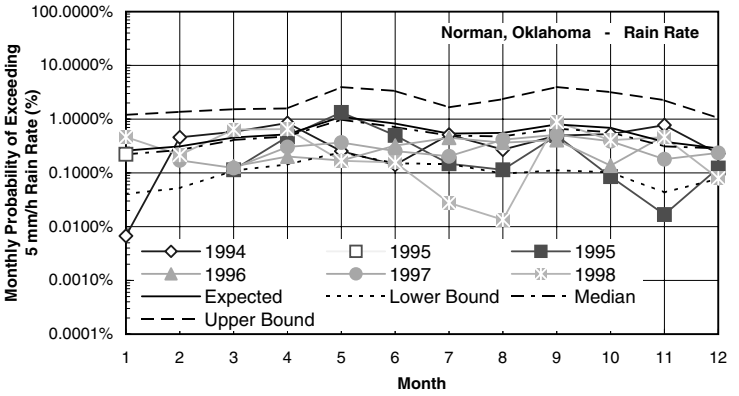

Figure 5.56 Empirical monthly probabilities of exceeding the 5-mm/h threshold and model predictions for Norman, OK.

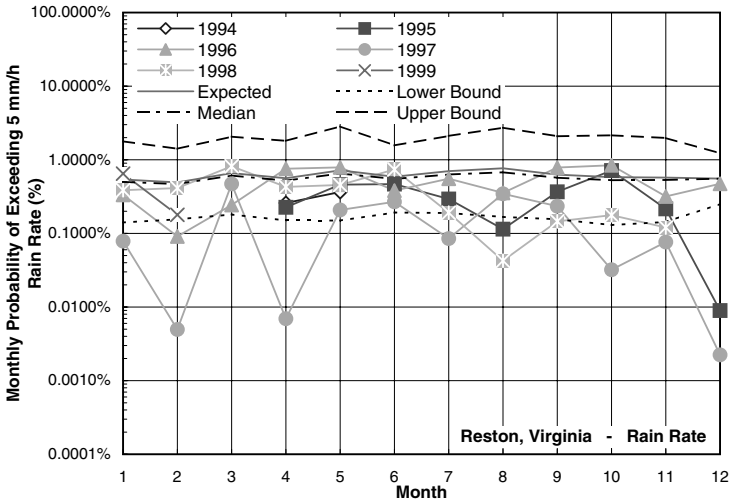

Figure 5.57 Empirical monthly probabilities of exceeding the 5-mm/h threshold and model predictions for Reston, VA.

in Appendix 5.1 for 109 locations in the United States. The maximum short-term precipitation records are available at NCDC for about 200 sites in the United States. They are also available in other countries that archive 5-min accumulation data. Archives of hourly data are available from NCDC for a much larger collection of recording stations. They are available in many other countries. Both hourly and maximum short-term precipitation data were available at the same location for 106 of the sites listed in the Appendix 5.1. Distribution parameters for the hourly data sites closest to three of the ACTS APT sites were combined with data from the closest but more distant

short-term precipitation site. In general, the cell parameters are valid over a wider geographical area than are the debris component parameters.

The application of the two-component model for locations outside the United States must employ the use of the Crane global rain zone model[8] unless a complete set of local parameters is generated for the location of interest. An intermediate step of using the closest hourly data and the cell components parameters from the global rain zone model should provide an improvement over the use of a complete set of rain zone parameters. The new ITU-R model cannot be used with the two-component model because it does not provide a complete set of cell and debris parameters.

The two-component model is given by:

$$P(a \geq A) = P_V(a \geq A) + P_W(a \geq A) \tag{5.10}$$

where P_V is the volume cell contribution and P_W the debris contribution. A volume cell anywhere over the horizontal projection of the part of a slant path below the rain height or a terrestrial path will produce attenuation. The volume cell is assumed to have no variation of the specific attenuation with height up to the rain height for any horizontal location within the cell. The volume cell is assumed to have a circularly symmetric shape in the horizontal with a gaussian rain-rate profile along any horizontal path through the center of the cell. A path through the edge of a cell will still have a gaussian rain-rate profile but with maximum intensity lower than the peak intensity of the cell. For a given value of attenuation, A_H, on the horizontal projection of the path, the peak rain-rate intensity $R_V(x,y,A_H)$ is obtained from:[8]

$$A = \int_{\text{path}} \kappa\left[R(s)\right]^{\alpha} ds = \kappa\left[R_V(x,y)\right]^{\alpha} e^{-\frac{y^2}{2S_V^2}} \int_{-0.5D_C - x}^{0.5D_C - x} e^{-\frac{s^2}{2S_V^2}} ds \tag{5.11}$$

where x, y are the cell center locations measured from the center of the path of length D_C, with x parallel to the path and y perpendicular to the path, and $A = A\cos(\text{elevation angle})$ for a slant path with elevation angles above 5°. This integral can be evaluated by using error functions. The S_V parameter is given by:

$$S_V = \frac{\eta R_C^{-\nu}}{\sqrt{3.96\alpha}} \tag{5.12}$$

where the parameters $\eta = 1.70$ and $\nu = 0.002$ and R_C is one of the volume cell distribution parameters.

The parameters κ and α in the approximate power law relationship between specific attenuation and rain rate are available in the literature for

a number of different rain-rate distributions. The ITU-R recommended parameters for a Laws and Parsons[14] rain-rate distribution are tabulated as a function of frequency in Appendix 5.2 for vertical and horizontal polarization on a horizontal path.[15] The differences between the use of other drop size distribution models are small, except at frequencies above about 70 GHz. At the higher frequencies, the numbers of small drops relative to the number of large drops can change the specific attenuation values.

The volume cell component model is completed by computing the probability for a cell of intensity $R_V(x,y,A_H)$ to occur at random at any location x, y that would affect the path. Assuming that over the month or annual period for the probability distribution, the cells could fall anywhere in the area and be independent of any other cell placement:

$$P_C(a \geq A) = \frac{P_C}{\pi r_C^2} \int_{-\infty}^{\infty} \int_{-\infty}^{\infty} e^{-\frac{R_V(x,y,A_H)}{R_C}} dxdy$$

$$\approx 2P_C \int_{0}^{\frac{3}{2}S_V} \int_{-\frac{D_C+3}{2}S_V}^{\frac{D_C+3}{2}S_V} e^{-\frac{R_V(x,y,A_H)}{R_C}} dxdy \tag{5.13}$$

where the average cell area $\pi r_C^2 \approx 1\ \text{km}^2$. This equation was evaluated using a two-dimensional numerical Gaussian quadrature employing Legendre polynomials.

The debris component is based on a lognormal distribution for path attenuation. The median path attenuation and the standard deviation of the natural logarithm of the path attenuation must be determined. The average path attenuation is computed along the path, the horizontal path for a terrestrial system and the slant path to the rain height for an Earth-space system. Again, the assumption is made that the specific attenuation does not vary with height up to the rain height and is zero above. The bright band or melting layer is often observed in the rain debris near the height of the 0°C isotherm. Although the specific attenuation may increase by a factor of 3 or more within the melting region, the melting region is thin, less than a few hundred meters thick, and its effects are lost within the larger uncertainty in melting layer height as a function of time of day, day of the month, synoptic rain type and season. The effect of the melting layer is small and is negligible.

The rain-rate process contributing to the specific attenuation as a function of position along the path is jointly lognormal at two separated points on the path with an assumed spatial correlation function. The spatial correlation function was derived from weather radar observations.[8] The average attenuation on the path (linear) is calculated by:

$$\mu_A = E[A] = E\left[\int_{\text{path}} \gamma(s)ds\right] = \mu_\gamma L_D$$

$$\mu_\gamma = \kappa e^{\alpha \ln(R_D) + 0.5a^2 S_D^2} \tag{5.14}$$

$$\sigma_\gamma^2 = \kappa^2 e^{2\alpha \ln(R_D) + 2a^2 S_D^2} - \mu_\gamma^2$$

The notation used is to reserve the symbols μ and σ for the mean and standard deviation of attenuation, respectively (linear), and m and s for the mean and standard deviation, respectively, of the natural logarithm of the attenuation or specific attenuation (log). The standard deviation of attenuation is:

$$\begin{aligned}
\sigma_A^2 &= E\left[\left(A - \mu_A\right)^2\right] = \int_0^{L_D}\int_0^{L_D} E\left[\left(\kappa R(x')^\alpha - \mu_\gamma\right)\left(\kappa R(x'')^\alpha - \mu_\gamma\right)\right]dx'dx'' \\
&= \int_0^{L_D}\int_0^{L_D} E\left[\left(\gamma(x') - \mu_\gamma\right)\left(\gamma(x'') - \mu_\gamma\right)\right]dx'dx'' \\
&= \sigma_\gamma^2 \int_0^{L_D}\int_0^{L_D} \rho_\gamma(x' - x'')dx'dx''
\end{aligned} \tag{5.15}$$

where the spatial correlation functions are given by:[16]

$$\begin{aligned}
\rho_R &= \frac{e^{S_D^2 \rho_{\text{LNR}}(x' - x'')} - 1}{e^{S_D^2} - 1} \\
\rho_\gamma &= \frac{e^{\alpha^2 S_D^2 \rho_{\text{LNR}}(x' - x'')} - 1}{e^{S_D^2} - 1}
\end{aligned} \tag{5.16}$$

and the correlation function for the logarithm of rain rate, ρ_{LNR}, was determined from the weather radar data. The correlation function may be approximated by:

$$\rho_{\text{LNR}}(s) = 1 + 2\left(e^{-\frac{|s|}{48.572}}\right) + 1.038\left(1 - e^{-\left(\frac{|s|}{79.95} + \left(\frac{s}{2600}\right)^2\right)}\right) \quad |s| < 256 \text{ km} \tag{5.17}$$

and $\rho_{\text{LNR}} = 0$ otherwise.

The parameters for the lognormal model then are given by:

$$s_A^2 = \ln\left(1 + \frac{\sigma_A^2}{\mu_A^2}\right)$$
$$m_A = \ln(\mu_A) - \frac{1}{2}s_A^2 \tag{5.18}$$

and

$$P_W(a \geq A) = P_D Q\left(\frac{\ln(A) - m_A}{s_A}\right) \tag{5.19}$$

The individual monthly distributions can be combined to generate the seasonal or even annual distribution. Because the volume cell and debris probability predictions are of the form P_C times a factor that depends on location but not on month and P_D times a factor that depends on location but not on month or year, the monthly statistics can be combined by simply averaging the P_C and P_D values and multiplying each by the appropriate fixed factors. The interannual variability parameters, s_P and s_R, vary from one month to the next, and therefore each has to be weighted by the cell and debris probabilities prior to combining.

5.6.3 *Application of the models*

The two-component model provides rain-attenuation distribution predictions for the time period used to calculate the seven rain-rate distribution parameters, the average month or year. Five of the parameters were used in Equation 5.10 through Equation 5.19. The model predicts the median distribution expected on average for the site of interest. Experimentally, half the distributions observed over a period of years should lie above the median model prediction and half below. The extension to estimate the expected distribution and the distribution expected to be exceeded once in Y years on average follow from the lognormal behavior of the interannual fluctuations and are computed using Equation 5.9.

The annual rain-rate distribution parameters have been given for Oklahoma City. Using these parameters, the median cell and debris distributions predicted for the ACTS APT in Norman were generated for display in Figure 5.58. The figure shows the relative contributions of the volume cells and debris to the total probability of exceeding the path attenuation values. At the lower, 1-dB, attenuation, the debris probability component is three times higher than the cell component, but at a 5-dB path attenuation, the debris and cell components are nearly equal. The cells have a small horizontal cross section, having an average area at the half peak cell rain-rate

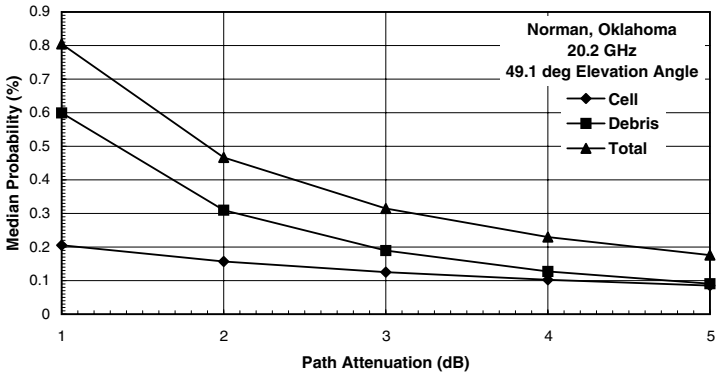

Figure 5.58 Volume cell and debris component contributions to the probability of attenuation at 20.2 GHz for Norman, OK.

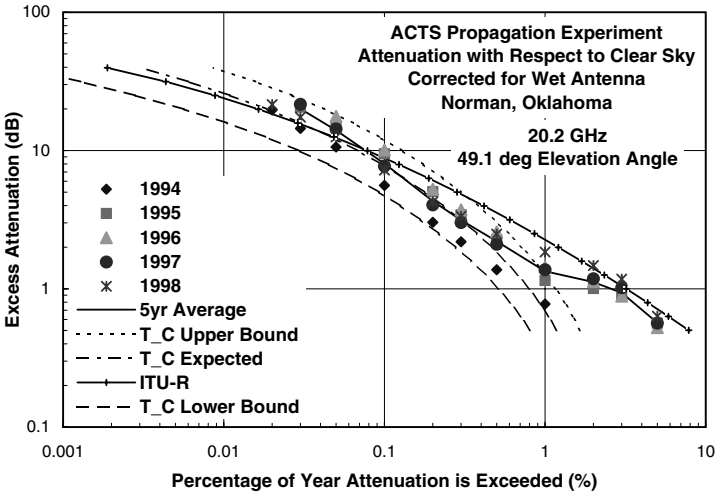

Figure 5.59 Annual empirical 20.2-GHz excess attenuation distributions and model predictions for Norman, OK.

intensity contour level of 1 km^2. The correlation distance for the debris component is about 25 km at a 0.5 correlation value.[8] A simple model for space diversity is to neglect the cell component when the site spacing is larger than two or more cell widths. A correct accounting of the cell and debris statistics provides the space diversity model presented by Crane.[8]

The expected 20.2-GHz annual excess attenuation distribution prediction is displayed in Figure 5.59 with the bound expected to enclose 90% of the independent yearly empirical distributions. The bounds enclose the observations down to a 2-dB threshold. Below 2 dB, the observed distributions abruptly veer to higher probability values. This change is produced by

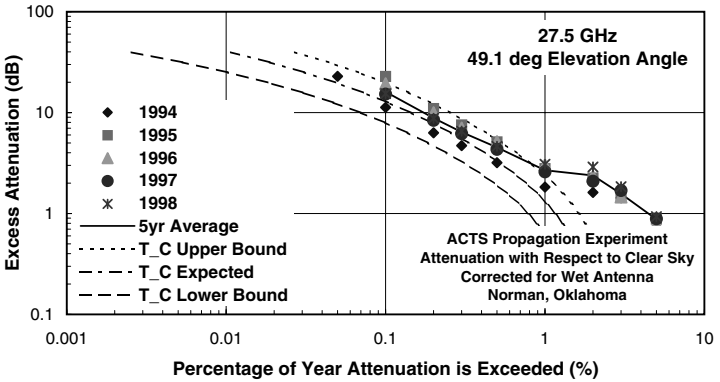

Figure 5.60 Annual empirical 27.5-GHz excess attenuation distributions and model predictions for Norman, OK.

nonraining clouds. Individual clouds can produce more than 2-dB excess attenuation. Below the 2-dB level, the empirical distributions lie well outside the expected bounds. The UTU-R prediction for excess attenuation due to rain is also presented in the figure.[3] The ITU-R model is the result of a regression analysis that compares measured attenuation statistics with simultaneously obtained rain-rate statistics. If clouds are regularly observed on a path, the attenuation statistics would include cloud effects at the lower attenuation values as well as rain effects. The ITU-R model nicely fits the high attenuation values and the low attenuation values, but misses in the 2- to 10-dB attenuation range. For predominantly rain effects, the shape of the ITU-R model is not correct. This model employs only the rain-rate statistics at 0.01% of a year and extends the attenuation prediction at 0.01% of a year to other percentages. The local model rain-rate statistics at 0.01% were used to generate the predictions. At 0.01% of the year, the two-component model and the ITU-R model generate nearly equal predictions.

Figure 5.60 presents the two-component model predictions and the Norman, OK, measured annual distributions at the higher beacon frequency. As at 20.2-GHz, the measurements and predictions match 3 dB above. At lower path attenuation values the added effects of clouds become important. The spring season empirical distributions and two-component model predictions are presented in Figure 5.61 and Figure 5.62 for 20.2 and 27.5 GHz, respectively. The seasonal predictions are in reasonable agreement with the observations. The interannual variability parameters seem to be too small because the empirical distributions lie both above the upper bound and below the lower bound for different years. An insufficient number of years of observations were collected to make any adjustment in the modeling procedure.

Figure 5.59 through Figure 5.74 present the comparisons between the two-component model predictions and the measured distributions. All calculations used the local rain-rate distribution model to generate the rain-rate parameters. The calculations also used the GGUAS rain heights

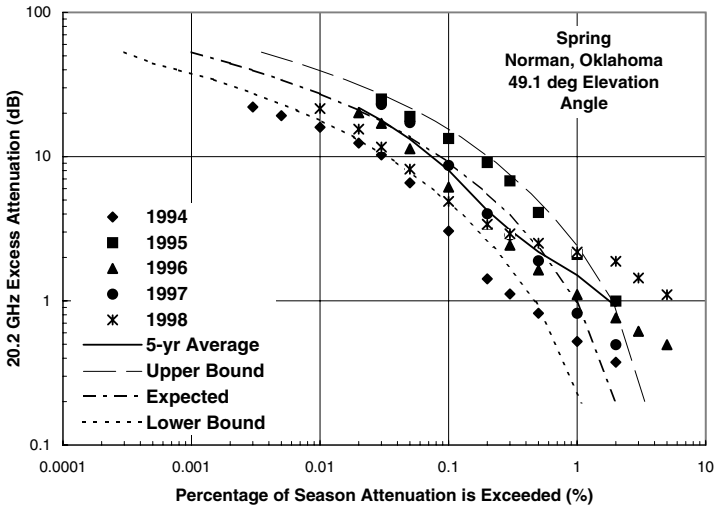

Figure 5.61 Spring season empirical 20.2-GHz excess attenuation distributions and model predictions for Norman, OK.

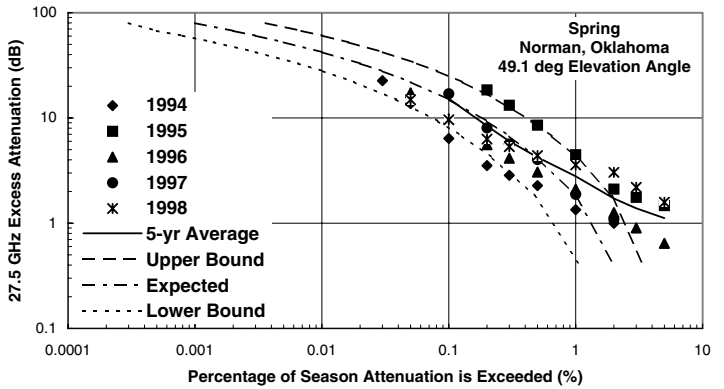

Figure 5.62 Spring season empirical 27.5-GHz excess attenuation distributions and model predictions for Norman, OK.

for the month or year and location. The measured distributions were corrected to remove the effects of water on the antenna feed window and on the antenna reflector surface.[1] The annual empirical distributions for Alaska all lie within the expected bounds except for the low attenuation values obtained for the last year of observations. The summer season observations were all consistent with the model predictions.

For British Columbia, the annual model predictions were consistent with the observations except for 1997. The convective rain occurrences during the summer of 1997 were the second highest in 100 years. The winter observations were generally outside the predicted bounds except at the higher

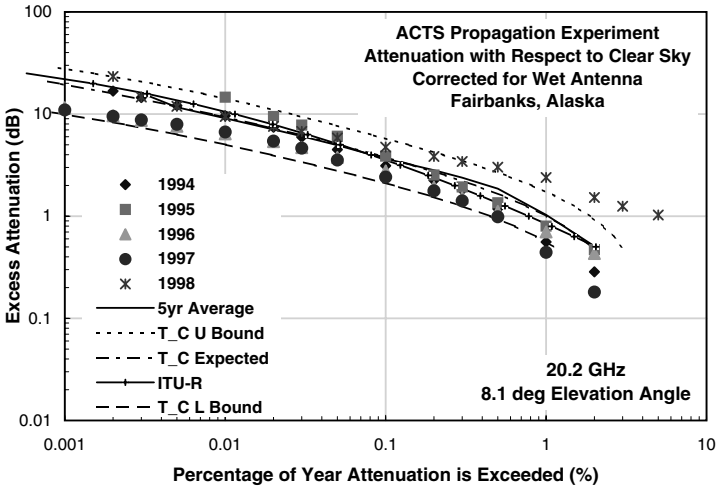

Figure 5.63 Annual empirical 20.2-GHz excess attenuation distributions and model predictions for Fairbanks, AK.

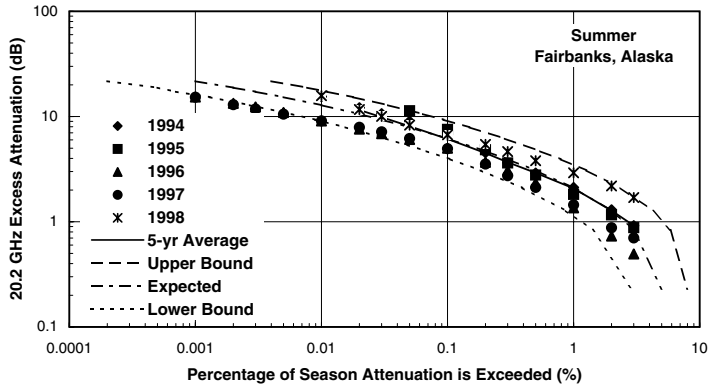

Figure 5.64 Summer season empirical 20.2-GHz excess attenuation distributions and model predictions for Fairbanks, AK.

recorded attenuation values. This result could be due to increased cloudiness during the winter months, an increased rain height relative to the average monthly value during rainy conditions, or the additional attenuation in the bright band when the rain height is not much larger than the width of the melting region. The GGUAS statistics predict a 0-km rain height for January. Because rain does occur during that month at most mid-latitude sites, a minimum 0.5-km rain height was assumed for mid-latitude sites whenever the model predicted a zero height.

The annual empirical distributions from Colorado showed a wide spread due to the interannual variations. The summer season empirical distributions

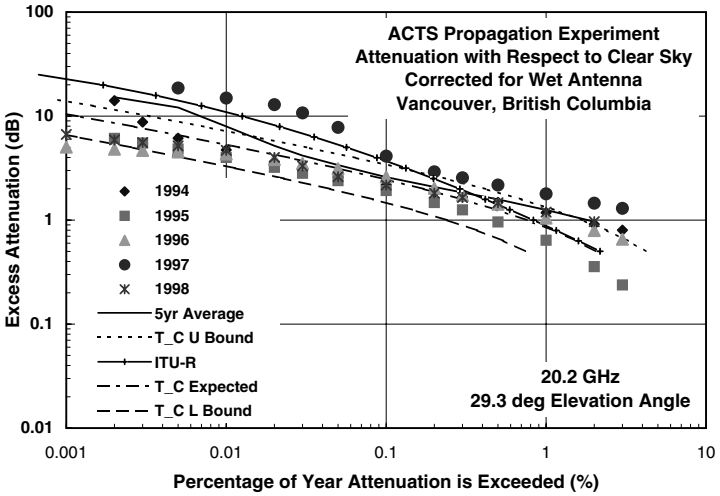

Figure 5.65 Annual empirical 20.2-GHz excess attenuation distributions and model predictions for Vancouver, British Columbia.

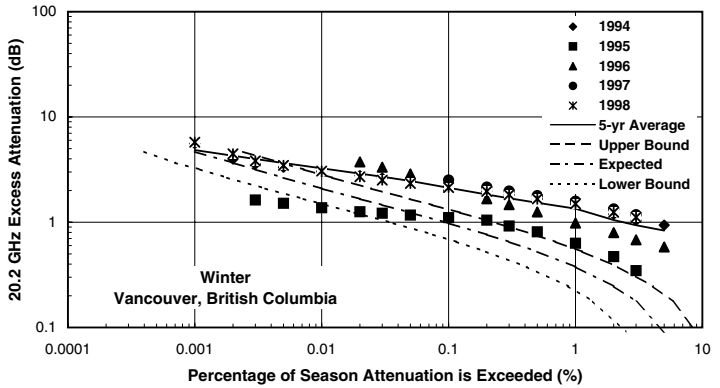

Figure 5.66 Winter season empirical 20.2-GHz excess attenuation distributions and model predictions for Vancouver, British Columbia.

also showed a wide spread in value from one year to the next. For the Florida site, the measured annual distributions were generally higher than the predicted upper bound. Cloud effects were also evident. The ITU-R model produced a good match to the low attenuation values. The summer season model predictions provided a good match to the observations for this site. The measurements and predictions for the New Mexico site were in good agreement, except for the effects of clouds at excess attenuation values less than 1 dB. Again, the ITU-R model matched the high attenuation and low attenuation values but departed from the observations in the mid-range of attenuation values.

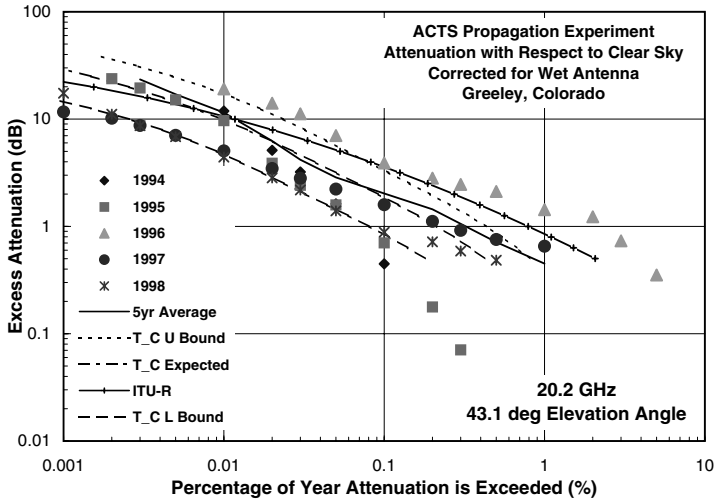

Figure 5.67 Annual empirical 20.2-GHz excess attenuation distributions and model predictions for Greeley, CO.

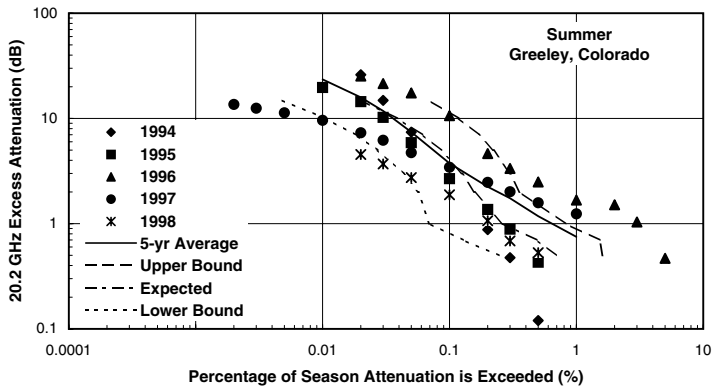

Figure 5.68 Summer season empirical 20.2-GHz excess attenuation distributions and model predictions for Greeley, CO.

The empirical distributions obtained during the COMSTAR experiment were plotted in addition to the ACTS data in the annual distribution presentation. These earlier data were included to show that the statistics had not changed over a period of 20 years. The rainy season for the Washington, D.C., area is spring. The spring season distribution predictions enclosed three of five years of observations. This site has a wide range of rain height values during the winter and early spring.

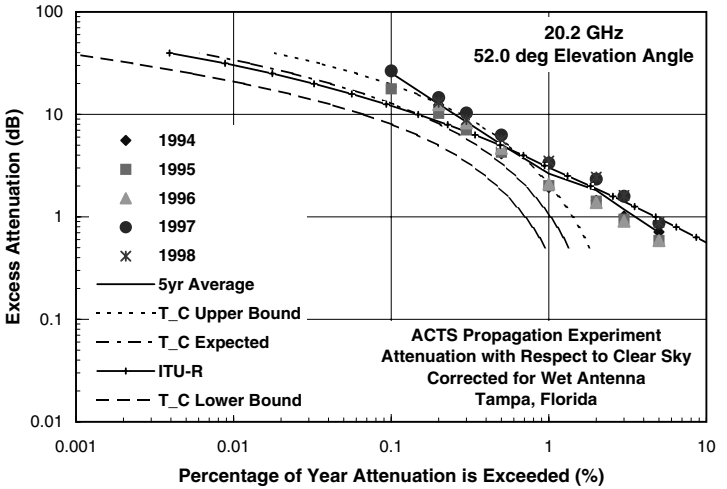

Figure 5.69 Annual empirical 20.2-GHz excess attenuation distributions and model predictions for Tampa, FL.

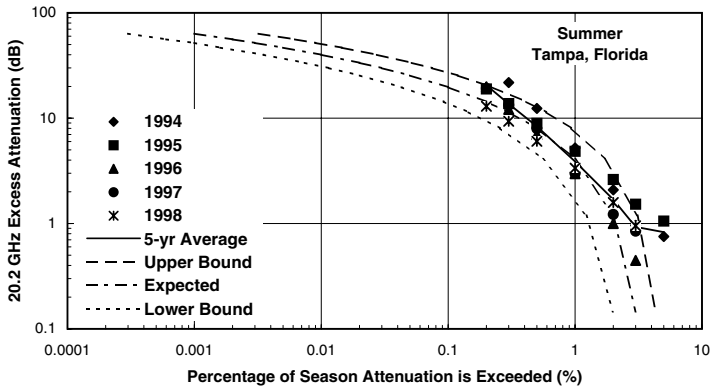

Figure 5.70 Summer season empirical 20.2-GHz excess attenuation distributions and model predictions for Tampa, FL.

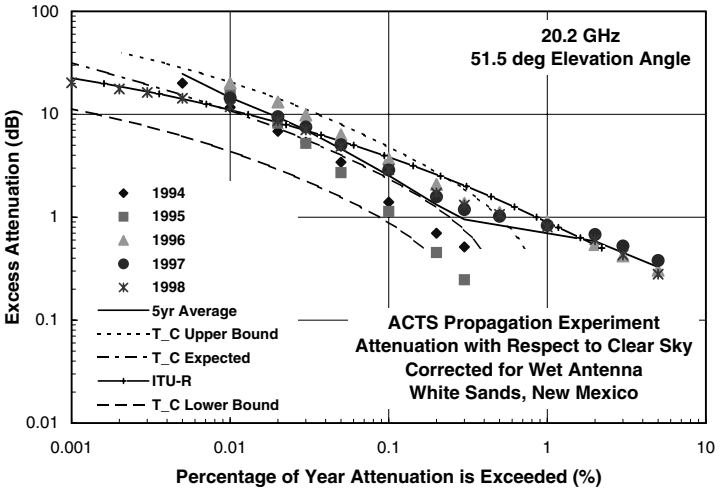

Figure 5.71 Annual empirical 20.2-GHz excess attenuation distributions and model predictions for White Sands, NM.

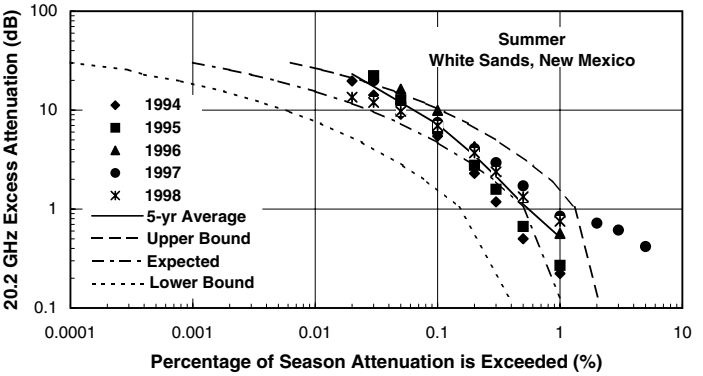

Figure 5.72 Summer season empirical 20.2-GHz excess attenuation distributions and model predictions for White Sands, NM.

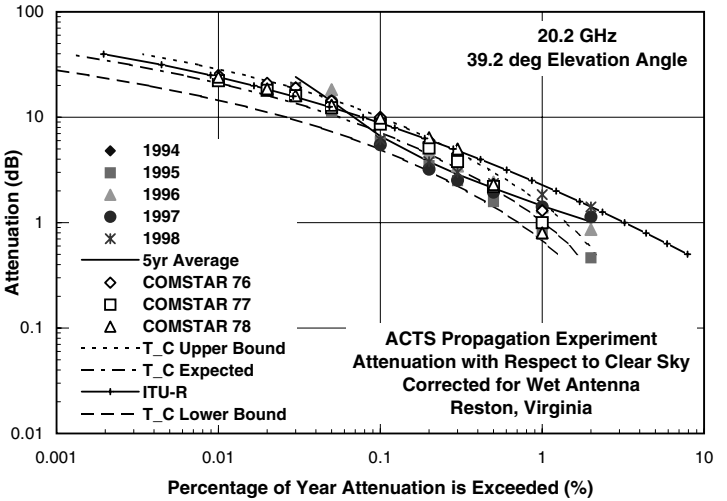

Figure 5.73 Annual empirical 20.2-GHz excess attenuation distributions and model predictions for Reston, VA.

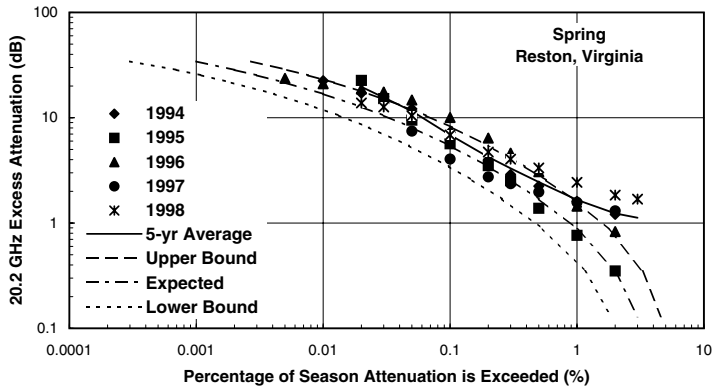

Figure 5.74 Spring season empirical 20.2-GHz excess attenuation distributions and model predictions for Reston, VA.

5.7 List of symbols

Symbol	Quantity	Units	Equation
A	Excess path attenuation	dB	5.10
A_{Fi}	Excess path attenuation	dB	5.1
A_H	Reduced attenuation on the horizontal projection of a path	dB	5.11
D_C	Length of horizontal path prjection in rain	km	5.11
f_i	Frequeency	GHz	5.1
M	Rain accumulation	mm	5.7
m_H	Mean of the natural logarithm of hourly rain accumulation values		5.7
P	Probability	%	5.3
P_A	Annual probability	%	5.2
P_C	Probability of a volume cell	%	5.3
P_D	Probability of debris region rain	%	5.3
P_V	Volume cell probability	%	5.3
P_W	Worst-month probability	%	5.2
P_W	Debris region probability	%	5.3
P_Y	Probability at return period Y	%	5.9
P_μ	Expected probability	%	5.8
Q	Ratio of worst-month to annual probability		5.2
Q	Upper tail of the normal probability distribution		5.3
Q_1	Parameter in Q ratio model		5.2
R	Rain rate	mm/h	5.3
R_C	Cell average peak rain rate	mm/h	5.3
R_D	Median debris region rain rate	mm/h	5.3
R_V	Peak cell rain rate needed to produce a specified attenuation on a path	mm/h	5.11
S_D	Standard deviation of ln(R) in debris region		5.3
s_H	Standard deviation of the natural logarithm of hourly rain accumulation values		5.7
s_P	Standard deviation of the natural logarithm of the annual number of hours with rain		5.8
s_R	Standard deviation of the natural logarithm of the annual rain accumulation		5.8
S_V	Cell size parameter	km	5.11
Y	Return period	years	5.9
z_i	Reduced variate of a probability distribution		5.4
β	Parameter in Q ratio model		5.2
μ_E	Mean of an exponential distribution		5.5
μ_A	Mean path attenuation	dB	5.14
μ_g	Mean specific attenuation	dB/km	5.14
ρ_{LNR}	Spatial correlation function for the natural logarithn of rain rate		5.17
ρ_R	Spatial correlation function for rain rate		5.16
ρ_g	Spatial correlation function for specific attenuation		5.16
σ_E	Standard deviation of an exponential distribution		5.5
σ_A	Standard deviation of spath attenuation	dB	5.15
σ_g	Standard deviation of specific attenuation	dB/km	5.14

References

1. Crane, R.K., Analysis of the effects of water on the ACTS propagation terminal antenna, *IEEE Trans. Ant. Propag.*, 50(7), 954, 2002.
2. Crane, R.K. and Robinson, P.C., ACTS propagation experiment: Rain-rate distribution observations and prediction model comparisons, *Proc. IEEE*, 85(6), 946, 1997.
3. ITU-R, Recommendation ITU-R P.618–4, Propagation Data and Prediction Methods Required for the Design of Earth-Space Telecommunication Systems, International Telecommunications Union, Geneva, 1995.
4. Crane, R.K. and Debrunner, W.E., Worst-month statistics, *Electron. Lett.*, 14(2), 38, 1978.
5. ITU-R, Recommendation ITU-R P.581–2, The Concept of "Worst-Month," International Telecommunications Union, Geneva, 1994.
6. ITU-R, Recommendation ITU-R P.841, Conversion of Annual Statistics to Worst-Month Statistics, International Telecommunications Union, Geneva, 1994.
7. Helmken, H., Henning, R.E., Feil, J., Ipplito, L.J., and Mayer, C.E., Three-site comparison of fade-duration measurements, *Proc. IEEE*, 85(6), 917, 1997.
8. Crane, R.K., *Electromagnetic Wave Propagation Through Rain*, J. Wiley, New York, 1996.
9. Crane, R.K., Wang, X., Westenhaver, D.B., and Vogel, W.J., ACTS propagation experiment: Experiment design, calibration, and data preparation and archival, *Proc. IEEE*, 85(7), 863, 1997.
10. Crane, R.K., A local model for the prediction of rain-rate statistics for rain-attenuation models, *IEEE Trans. Ant. Propag.*, accepted.
11. Bury, K.V., *Statistical Models in Applied Science,* Robert E. Krieger Publishing Company, Malabar, FL, 1986.
12. ITU-R, Recommendation ITU-R P.837–2, Characteristics of Precipitation for Propagation Modeling, International Telecommunications Union, Geneva, 1999.
13. Poiares Baptista, J.P.V. and Salonen, E.T., Review of Rainfall Rate Modelling and Mapping, Proceedings of the URSI Commission-F Open Symposium on Climatic Parameters in Radiowave Propagation Prediction, Communications Research Centre, Ottawa, 1998.
14. Laws, J.O. and Parsons, D.A., The relationship of raindrop-size to intensity, *Am. Geophys. Union Trans.*, 24, 452, 1943.
15. ITU-R, Recommendation ITU-R P.838, Specific Attenuation Model for Rain for Use in Prediction Methods, International Telecommunications Union, Geneva, 1994.
16. Aitchison, J. and Brown, J.A.C., *The Lognormal Distribution*, Cambridge University Press, Cambridge, 1966.
17. Maggiori, D., Computed transmission through rain in the 1–400 Ghz frequency range for spherical and elliptical drops and any polarization, *Alta Frequenza*, L5,262, 1981.
18. Nowland, W.L., Olsen, R.L., and Shkarofsky, I.P., Theoretical relationship between rain depolarization and attenuation, *Electron. Lett.*, 13, 676, 1977.

Appendix 5.1

Parameters for the Local Rain Rate Prediction Model

Location	Latitude	Longitude	*M*	Annual						
				Pc	*Rc*	*Pd*	*Rd*	*Sd*	*sR*	*sP*
Fairbanks, AK	64.82	–147.83	271.351	0.004	18.131	2.812	0.769	0.828	0.2738	0.2153
Huntsville, AL	34.65	–86.77	1448.192	0.024	36.382	2.878	2.401	1.114	0.1553	0.1063
Mobile, AL	30.68	–88.25	1635.774	0.021	42.112	2.677	2.714	1.208	0.1585	0.1521
Montgomery, AL	32.30	–86.40	1331.397	0.059	30.956	1.782	2.029	1.184	0.2009	0.1473
Little Rock, AR	34.73	–92.23	1247.113	0.080	28.014	1.322	1.498	1.224	0.2578	0.2247
Flagstaff, AZ	35.13	–111.67	571.618	0.014	25.695	2.292	1.367	0.996	0.2632	0.2686
Tucson, AZ	32.13	–111.00	300.395	0.017	27.478	0.642	1.223	1.105	0.2755	0.2443
Yuma, AZ	32.67	–114.67	73.860	0.002	37.907	0.269	1.211	1.117	0.4398	0.4267
Bakersfield, CA	35.42	–119.00	147.482	0.001	24.146	0.813	1.329	0.906	0.3278	0.2884
Eureka, CA	40.80	–124.17	973.813	0.003	21.774	4.340	1.640	0.925	0.2295	0.1725
Fresno, CA	36.78	–119.67	274.453	0.001	30.379	1.281	1.562	0.926	0.3313	0.2643
Los Angeles, CA	33.93	–118.33	305.729	0.002	40.975	0.982	2.033	0.961	0.4242	0.3408
San Diego, CA	32.82	–117.17	251.466	0.005	24.154	0.963	1.554	0.973	0.3906	0.3106
San Francisco, CA	37.62	–122.33	499.855	0.001	39.957	2.054	1.751	0.942	0.3377	0.2664
Alamosa, CO	37.45	–105.83	178.276	0.003	26.033	1.157	0.992	0.969	0.2715	0.2508
Denver, CO	39.77	–104.83	396.229	0.006	38.090	2.025	1.131	0.988	0.2455	0.1851
Grand Junction, CO	39.12	–108.50	218.186	0.004	25.676	1.320	1.205	0.697	0.2870	0.2517
Greeley, CO	40.42	–104.68	237.646	0.006	38.090	0.805	2.019	0.267	0.2940	0.3640
Hartford, CT	41.93	–72.68	1141.307	0.015	32.614	3.827	1.739	1.000	0.1743	0.1226
Jacksonville, FL	30.48	–81.70	1325.920	0.027	40.540	2.209	2.222	1.244	0.1883	0.1537
Miami, FL	25.80	–80.30	1455.207	0.036	38.735	1.910	2.491	1.276	0.2190	0.1780
Tallahassee, FL	30.38	–84.37	1674.528	0.032	42.402	2.230	2.919	1.195	0.1930	0.1557
Tampa, FL	27.97	–82.53	1170.365	0.08852	30.416	0.358	1.328	1.349	0.2224	0.1796
Atlanta, GA	33.65	–84.43	1273.308	0.0615	31.838	1.807	1.779	1.065	0.1433	0.1236
Savannah, GA	32.13	–81.20	1284.613	0.090	28.885	0.972	1.269	1.363	0.1890	0.1506
Des Moines, IA	41.53	–93.65	831.850	0.014	40.702	2.619	1.452	1.147	0.2367	0.2272
Boise, ID	43.57	–116.17	363.583	0.009	13.662	0.682	4.805	0.373	0.1557	0.1617

Chicago, IL	42.00	–87.88	931.918	0.020	35.125	3.006	1.338	1.171	0.1630	0.1319
Springfield, IL	39.85	–89.68	896.281	0.084	22.850	0.929	0.908	1.244	0.1850	0.1583
Ft. Wayne, IN	41.00	–85.20	934.370	0.029	27.467	3.052	1.303	1.131	0.1758	0.1255
Indianapolis, IN	39.73	–86.27	1033.661	0.015	41.055	3.169	1.614	1.098	0.1538	0.1346
Goodland, KS	39.37	–101.67	446.717	0.008	46.474	1.569	1.172	1.213	0.2523	0.2064
Wichita, KS	37.65	–97.43	736.379	0.011	38.850	1.870	1.786	1.192	0.2375	0.1934
Louisville, KY	38.18	–85.73	1118.667	0.018	37.561	3.144	1.800	1.062	0.1658	0.1394
New Orleans, LA	29.98	–90.25	1580.769	0.012	46.042	2.567	2.968	1.206	0.2210	0.1639
Shreveport, LA	32.47	–93.82	1204.682	0.085	28.410	1.027	1.308	1.322	0.2350	0.1582
Boston, MA	42.37	–71.03	1111.171	0.012	26.154	4.055	1.672	1.026	0.1849	0.1224
Caribou, ME	46.87	–68.02	930.933	0.011	27.154	5.185	1.156	1.005	0.1509	0.0920
Portland, ME	43.65	–70.30	1129.933	0.007	35.116	4.360	1.653	1.013	0.1874	0.1230
Detroit–Metro, MI	42.23	–83.33	830.401	0.015	35.227	3.295	1.274	1.081	0.1545	0.1123
Grand Rapids, MI	42.88	–85.52	960.391	0.013	36.817	3.819	1.308	1.132	0.1267	0.0923
Sault Ste. Marie, MI	46.47	–84.35	864.802	0.015	27.253	5.641	0.776	1.272	0.1432	0.1100
Duluth, MN	46.83	–92.18	765.515	0.011	39.153	3.467	1.165	1.102	0.1759	0.1475
International Falls, MN	48.57	–93.38	621.690	0.017	28.916	3.074	0.913	1.177	0.1605	0.1473
Minneapolis, MN	44.88	–93.22	713.317	0.011	38.270	2.853	1.163	1.202	0.2223	0.1741
Kansas City, MO	39.32	–94.72	993.213	0.013	34.818	2.688	1.716	1.216	0.2209	0.2136
St. Louis, MO	38.75	–90.37	926.072	0.020	32.404	2.559	1.654	1.134	0.2124	0.1729
Jackson, MS	32.32	–90.08	1419.242	0.086	30.600	1.272	1.569	1.262	0.2078	0.1219
Glasgow, MT	48.22	–106.67	275.322	0.004	39.400	1.737	0.878	1.097	0.2719	0.1931
Missoula, MT	46.93	–114.17	340.326	0.003	28.053	2.701	0.986	0.788	0.1906	0.1717
Charlotte, NC	35.22	–80.93	1100.977	0.011	40.167	2.910	2.039	1.082	0.1562	0.1166
Raleigh, NC	35.87	–78.78	1072.670	0.016	36.933	2.771	1.918	1.097	0.1215	0.1116
Bismarck, ND	46.77	–100.83	399.209	0.020	26.197	1.590	0.888	1.061	0.2271	0.1679
Fargo, ND	46.90	–96.80	501.012	0.008	43.629	2.337	0.835	1.39	0.2145	0.1777
Grand Island, NE	40.97	–98.32	621.832	0.014	36.670	1.895	1.268	1.254	0.2242	0.1990
No. Platte, NE	41.13	–100.67	505.500	0.007	43.615	1.821	1.260	1.219	0.2366	0.1848
Scottsbluff, NE	41.87	–103.67	385.693	0.004	45.146	1.969	1.045	1.162	0.2614	0.1872
Concord, NH	43.20	–71.50	946.658	0.017	24.089	3.831	1.456	0.998	0.1624	0.1129

Parameters for the Local Rain Rate Prediction Model (continued)

Location	Latitude	Longitude	M	Annual						
				Pc	Rc	Pd	Rd	Sd	sR	sP
Albuquerque, NM	35.03	–106.67	217.777	0.017	20.478	0.561	1.194	0.804	0.2736	0.2435
Jornada, NM	32.62	–106.73	228.415	0.010	24.469	0.417	2.401	0.913	0.3840	0.3780
Roswell, NM	33.30	–104.50	336.448	0.017	22.100	0.563	1.813	1.257	0.3937	0.5343
Elko, NV	40.83	–115.83	229.267	0.001	20.597	1.509	1.035	1.050	0.3686	0.4619
Ely, NV	39.28	–114.83	240.538	0.001	32.561	1.718	1.043	0.937	0.2772	0.2384
Las Vegas, NV	36.08	–115.17	106.403	0.002	23.077	0.526	1.201	1.056	0.4286	0.4181
Reno, NV	39.50	–119.83	188.122	0.002	22.498	1.205	1.162	0.857	0.2853	0.2591
Albany, NY	42.75	–73.80	929.313	0.011	35.642	3.776	1.502	0.963	0.1649	0.1154
Buffalo, NY	42.93	–78.73	995.398	0.066	19.917	3.552	0.994	1.008	0.1354	0.1131
NY/Kennedy, NY	40.65	–73.78	1029.208	0.019	33.720	2.986	1.825	1.018	0.2368	0.1991
Syracuse, NY	43.12	–76.12	995.974	0.013	33.823	5.007	1.123	1.086	0.1877	0.1171
Cleveland, OH	41.42	–81.87	950.784	0.032	25.583	3.675	1.177	1.072	0.1699	0.1115
Columbus, OH	40.00	–82.88	961.949	0.022	35.140	3.239	1.357	1.082	0.1463	0.1078
Oklahoma City, OK	35.40	–97.60	845.127	0.022	36.830	1.622	1.853	1.213	0.2213	0.1836
Burns, OR	43.58	–119.00	263.843	0.005	11.833	2.122	0.901	0.928	0.3420	0.3423
Eugene, OR	44.12	–123.17	1215.424	0.005	22.632	5.196	1.747	0.894	0.1813	0.1548
Medford, OR	42.38	–122.83	484.649	0.002	26.309	2.895	1.270	0.886	0.2276	0.1569
Portland, OR	45.60	–122.67	928.240	0.004	25.425	5.485	1.359	0.809	0.1727	0.1530
Philadelphia, PA	39.88	–75.25	1052.666	0.015	34.077	3.262	1.708	1.093	0.1439	0.1237
Pittsburgh, PA	40.50	–80.22	930.570	0.040	27.886	3.075	1.275	0.889	0.1383	0.1115
Columbia, SC	33.95	–81.12	1234.580	0.043	32.329	2.264	1.761	1.211	0.2042	0.1536
Rapid City, SD	44.05	–103.00	411.333	0.006	40.873	2.138	1.037	1.068	0.2100	0.1665
Sioux Falls, SD	43.57	–96.73	621.376	0.045	23.764	1.360	0.900	1.248	0.2348	0.2072
Memphis, TN	35.05	–90.00	1314.052	0.049	30.352	2.191	1.980	1.165	0.1722	0.1700
Nashville, TN	36.12	–86.68	1216.227	0.014	37.241	3.120	2.045	1.106	0.1911	0.1377

Abilene, TX	32.42	–99.68	590.626	0.019	36.309	1.115	1.664	1.215	0.2706	0.2521
Amarillo, TX	35.23	–101.67	516.204	0.009	43.411	1.310	1.498	1.246	0.2437	0.2107
Austin, TX	30.28	–97.70	826.343	0.025	38.382	1.538	1.566	1.281	0.2691	0.2370
Brownsville, TX	25.90	–97.43	679.009	0.010	28.974	1.520	1.807	1.347	0.2661	0.2153
Dallas/Ft Worth, TX	32.90	–97.03	919.002	0.015	34.189	1.684	2.407	1.169	0.2328	0.1990
Del Rio, TX	29.37	–101.00	394.188	0.009	43.626	0.940	1.349	1.344	0.3652	0.3203
El Paso, TX	31.80	–106.33	219.847	0.010	24.469	0.695	1.164	1.126	0.3410	0.2980
Houston, TX	29.97	–95.35	1218.893	0.008	48.180	2.440	2.371	1.250	0.2149	0.1979
Lubbock, TX	33.65	–101.83	495.410	0.021	29.727	1.027	1.363	1.256	0.2718	0.2124
Midland, TX	31.95	–102.17	395.608	0.008	40.702	0.951	1.488	1.261	0.3272	0.2656
Salt Lake City, UT	40.78	–112.00	399.869	0.003	29.654	2.279	1.281	0.867	0.2315	0.2075
Norfolk, VA	36.90	–76.20	1140.193	0.028	33.420	2.791	1.710	1.152	0.1699	0.1366
Richmond, VA	37.52	–77.33	1109.201	0.030	33.751	2.721	1.599	1.151	0.1808	0.1372
Roanoke, VA	37.32	–79.97	1018.469	0.012	41.507	3.157	1.834	1.008	0.1668	0.1287
Wallops Is., VA	37.93	–75.48	956.068	0.004	48.051	3.038	1.709	1.192	0.3051	0.2503
Washington, DC	38.95	–77.45	1012.105	0.029	32.226	2.654	1.497	1.128	0.1686	0.1220
Burlington, VT	44.47	–73.15	880.878	0.022	27.703	4.009	1.148	1.011	0.1501	0.1341
Blaine, WA	49.00	–122.75	985.383	0.005	16.469	3.947	2.060	0.767	0.1540	0.5020
Quillayute, WA	47.95	–124.50	2624.911	0.005	16.469	10.324	1.835	0.920	0.1769	0.1236
Seattle–Tacoma, WA	47.45	–122.33	922.931	0.003	10.745	5.360	1.390	0.841	0.1581	0.1298
Spokane, WA	47.63	–117.50	427.307	0.002	23.102	3.127	1.105	0.812	0.1696	0.1532
Walla Walla, WA	46.10	–118.33	416.938	0.001	34.853	2.844	1.160	0.851	0.2388	0.2237
Madison, WI	43.13	–89.33	809.413	0.034	31.704	2.126	1.230	1.077	0.1678	0.1703
Cheyenne, WY	41.15	–104.83	373.086	0.008	31.269	2.108	0.905	1.120	0.2295	0.1956
Lander, WY	42.82	–108.67	337.447	0.003	29.418	2.084	1.197	0.842	0.2150	0.1834
Sheridan, WY	44.77	–107.00	374.565	0.003	33.151	2.651	1.017	0.903	0.2007	0.1447

Parameters for the Local Rain Rate Prediction Model (continued)

Location	January				February				March			
	Pc	*Pd*	*sR*	*sP*	*Pc*	*Pd*	*sR*	*sP*	*Pc*	*Pd*	*sR*	*sP*
Fairbanks, AK	0.00024	1.976	0.7701	0.5920	0.00024	1.347	0.7907	0.6330	0.00024	1.482	1.0292	0.8000
Huntsville, AL	0.00598	3.766	0.4536	0.3282	0.00969	3.446	0.4839	0.3711	0.02212	4.490	0.4898	0.3609
Mobile, AL	0.01696	2.884	0.5144	0.3675	0.01065	3.125	0.4396	0.4001	0.01994	3.334	0.4393	0.3241
Montgomery, AL	0.01948	3.345	0.4543	0.3558	0.02619	3.590	0.4776	0.4005	0.04627	3.728	0.4392	0.3375
Little Rock, AR	0.02019	4.337	0.6195	0.4957	0.03141	3.670	0.5036	0.4401	0.02200	4.467	0.4702	0.4271
Flagstaff, AZ	0.00028	3.545	0.7740	0.6832	0.00418	3.278	0.8087	0.6574	0.00028	3.971	0.6755	0.6141
Tucson, AZ	0.00371	1.413	0.8283	0.6868	0.00303	1.056	0.7850	0.6789	0.00366	1.043	0.7434	0.7118
Yuma, AZ	0.00027	0.686	0.9052	0.8396	0.00027	0.436	1.0704	0.9395	0.00027	0.418	1.0241	0.9257
Bakersfield, CA	0.00210	1.698	0.6376	0.5849	0.00223	1.654	0.8303	0.6999	0.00256	1.809	0.7257	0.6942
Eureka, CA	0.00272	8.917	0.4840	0.4052	0.00347	7.042	0.4776	0.4128	0.00255	7.217	0.4333	0.3446
Fresno, CA	0.00155	2.966	0.6855	0.5336	0.00000	2.727	0.7515	0.6624	0.00436	2.585	0.7204	0.6778
Los Angeles, CA	0.00417	2.873	0.7897	0.6822	0.00413	2.482	0.8475	0.7144	0.00436	1.912	0.7904	0.7071
San Diego, CA	0.00822	2.631	0.7888	0.7015	0.00808	1.855	0.7912	0.7143	0.00948	2.381	0.8214	0.7075
San Francisco, CA	0.00362	5.461	0.6027	0.5167	0.00145	4.173	0.6717	0.5743	0.00138	3.812	0.6410	0.5600
Alamosa, CO	0.00016	0.575	0.7143	0.5959	0.00016	0.596	0.7973	0.5704	0.00016	0.866	0.7469	0.5739
Denver, CO	0.00014	1.060	0.6434	0.5254	0.00014	1.233	0.5949	0.5153	0.00014	2.655	0.6150	0.4335
Grand Junction, CO	0.00023	1.448	0.6337	0.6069	0.00023	1.204	0.6421	0.6026	0.00023	1.947	0.6108	0.5162
Greeley, CO	0.00014	0.384	0.7120	0.724	0.00014	0.337	0.5930	0.6290	0.00014	0.916	0.8080	0.7410
Hartford, CT	0.00282	3.944	0.5774	0.4183	0.00270	3.784	0.4119	0.3131	0.00016	4.692	0.3951	0.3288
Jacksonville, FL	0.00952	2.073	0.6180	0.4838	0.01173	2.208	0.5024	0.4693	0.01638	2.241	0.6096	0.4740
Miami, FL	0.01425	0.843	0.7796	0.661	0.01161	0.954	0.6870	0.5401	0.02068	0.824	0.7462	0.6151
Tallahassee, FL	0.01222	2.810	0.6035	0.3830	0.01620	2.757	0.4489	0.4127	0.02588	2.927	0.4908	0.4201
Tampa, FL	0.01774	1.452	0.6395	0.5424	0.05040	1.120	0.5665	0.5203	0.03219	2.530	0.7560	0.6529
Atlanta, GA	0.01877	4.380	0.4208	0.3258	0.02213	4.228	0.4639	0.3482	0.05806	3.616	0.3980	0.3289
Savannah, GA	0.01485	3.521	0.6145	0.4807	0.01659	3.010	0.4951	0.4115	0.02730	3.533	0.5553	0.4855
Des Moines, IA	0.00012	1.403	0.6809	0.4734	0.00012	1.534	0.5864	0.4688	0.00621	2.593	0.5547	0.4290
Boise, ID	0.00038	1.034	0.5700	0.5379	0.00623	0.852	0.6573	0.6562	0.00939	0.937	0.6472	0.6523
Chicago, IL	0.00014	2.249	0.5955	0.3977	0.00014	1.877	0.5442	0.3979	0.00771	3.449	0.4190	0.2809
Springfield, IL	0.00533	3.283	0.6651	0.4736	0.01142	3.084	0.5080	0.4081	0.03381	4.117	0.4567	0.3146

Ft. Wayne, IN	0.00328	3.417	0.6734	0.3833	0.00320	2.975	0.5548	0.3826	0.00407	4.171	0.3900	0.2479
Indianapolis, IN	0.00013	3.197	0.6924	0.4105	0.00286	2.911	0.4639	0.3773	0.00424	4.194	0.4887	0.2672
Goodland, KS	0.00011	0.616	0.7473	0.5878	0.00011	0.667	0.8340	0.7267	0.00011	1.719	0.7099	0.5976
Wichita, KS	0.00010	0.694	0.6972	0.6097	0.00010	0.854	0.7718	0.6827	0.00547	1.923	0.7620	0.6352
Louisville, KY	0.00238	3.730	0.5626	0.4501	0.00234	3.770	0.5487	0.3560	0.01239	4.389	0.5129	0.3021
New Orleans, LA	0.00712	2.881	0.6334	0.4807	0.00830	3.058	0.5031	0.4453	0.01137	2.386	0.4726	0.3358
Shreveport, LA	0.02408	4.044	0.5915	0.462	0.03716	3.200	0.4409	0.4185	0.05582	2.027	0.4208	0.3937
Boston, MA	0.00305	4.588	0.5454	0.3925	0.00274	4.506	0.4103	0.3291	0.00316	5.008	0.4817	0.3134
Caribou, ME	0.00026	4.697	0.3879	0.2577	0.00026	4.034	0.3828	0.3417	0.00026	4.651	0.4334	0.3401
Portland, ME	0.00013	4.761	0.5657	0.4365	0.00219	4.296	0.4540	0.3301	0.00241	5.041	0.4763	0.3303
Detroit–Metro, MI	0.00014	3.014	0.5017	0.3309	0.00014	2.752	0.5894	0.4069	0.00262	3.864	0.3973	0.2728
Grand Rapids, MI	0.00011	2.866	0.4914	0.2926	0.00011	2.094	0.5346	0.3972	0.00246	3.891	0.3833	0.2899
Sault Ste. Marie, MI	0.00022	5.631	0.3883	0.2995	0.00022	3.862	0.4952	0.3807	0.00326	4.941	0.4766	0.3455
Duluth, MN	0.00014	1.961	0.7194	0.5211	0.00014	1.393	0.6342	0.4477	0.00014	2.946	0.6130	0.4601
International Falls, MN	0.00021	1.800	0.6222	0.4778	0.00021	1.448	0.5586	0.4779	0.00021	2.308	0.5724	0.4446
Minneapolis, MN	0.00011	1.369	0.7189	0.5165	0.00011	1.328	0.6214	0.5145	0.00011	2.988	0.5061	0.4361
Kansas City, MO	0.00014	1.201	0.5676	0.5075	0.00237	1.138	0.5010	0.4479	0.00733	2.523	0.3618	0.3923
St. Louis, MO	0.00292	2.088	0.696	0.4712	0.00272	2.443	0.5183	0.4098	0.01142	3.327	0.395	0.3565
Jackson, MS	0.05010	3.236	0.5897	0.4091	0.04919	3.048	0.4720	0.4322	0.07327	2.759	0.4981	0.3854
Glasgow, MT	0.00014	0.877	0.6700	0.5866	0.00014	0.663	0.5911	0.6186	0.00014	0.999	0.5710	0.5304
Missoula, MT	0.00022	3.169	0.5473	0.492	0.00022	2.081	0.5248	0.4428	0.00022	2.435	0.4123	0.3818
Charlotte, NC	0.00592	3.314	0.4299	0.3349	0.00186	3.564	0.4506	0.3887	0.00851	4.019	0.4052	0.3259
Raleigh, NC	0.00637	3.264	0.4468	0.3089	0.00523	3.331	0.4072	0.3303	0.01001	3.314	0.3955	0.3381
Bismarck, ND	0.00027	1.198	0.5525	0.4942	0.00027	1.084	0.6619	0.5469	0.00027	1.919	0.7533	0.5654
Fargo, ND	0.00014	1.234	0.6705	0.558	0.00014	0.836	0.7125	0.5218	0.00014	1.816	0.5642	0.4897
Grand Island, NE	0.00014	0.709	0.7034	0.5913	0.00014	1.016	0.7579	0.5622	0.00246	2.264	0.7423	0.5544
No. Platte, NE	0.00011	0.626	0.7725	0.6050	0.00011	0.801	0.7898	0.7285	0.00011	1.769	0.6878	0.4735
Scottsbluff, NE	0.00009	0.844	0.6420	0.5922	0.00009	0.891	0.8148	0.6846	0.00009	1.907	0.6198	0.4996
Concord, NH	0.00352	3.928	0.5672	0.4189	0.00347	3.588	0.4969	0.3822	0.00419	4.117	0.4542	0.3316
Albuquerque, NM	0.00039	0.891	0.7210	0.6728	0.00039	0.913	0.7069	0.6390	0.00394	0.888	0.7407	0.5967
Jornada, NM	0.00321	0.343	0.8110	0.8830	0.00027	0.294	0.7250	0.7970	0.00316	0.142	0.7720	1.019
Roswell, NM	0.00000	0.360	0.5804	0.7511	0.00000	0.371	0.7679	0.8869	0.00000	0.257	0.9412	0.8362
Elko, NV	0.00000	2.204	0.7165	0.6811	0.00000	1.398	0.6581	0.6576	0.00000	1.877	0.6069	0.6355
Ely, NV	0.00010	1.687	0.6296	0.5451	0.00010	1.473	0.6855	0.6554	0.0001.0	2.229	0.5746	0.5546

Parameters for the Local Rain Rate Prediction Model (continued)

Location	January				February				March			
	Pc	*Pd*	*sR*	*sP*	*Pc*	*Pd*	*sR*	*sP*	*Pc*	*Pd*	*sR*	*sP*
Las Vegas, NV	0.00018	0.884	0.8994	0.8829	0.00192	0.746	1.0234	0.8946	0.00185	0.803	1.1205	0.9265
Reno, NV	0.00031	2.301	0.6936	0.5844	0.00031	2.065	0.8436	0.7030	0.00031	1.562	0.6896	0.6526
Albany, NY	0.00013	3.532	0.5263	0.4097	0.00013	3.515	0.4201	0.3420	0.00013	4.455	0.3964	0.3219
Buffalo, NY	0.00543	6.403	0.4588	0.3686	0.00395	5.536	0.4554	0.3136	0.00581	6.521	0.3900	0.2089
NY/Kennedy, NY	0.00622	3.520	0.5899	0.4297	0.00661	2.697	0.5052	0.3923	0.00029	3.948	0.5096	0.4053
Syracuse, NY	0.00015	4.745	0.3924	0.3169	0.00015	4.706	0.4506	0.3314	0.00015	5.708	0.3700	0.2729
Cleveland, OH	0.00296	4.352	0.4913	0.3248	0.00021	4.115	0.4510	0.3036	0.00379	5.269	0.4033	0.2213
Columbus, OH	0.00275	4.058	0.6143	0.3757	0.00270	3.241	0.4909	0.3509	0.00313	4.536	0.4772	0.2605
Oklahoma City, OK	0.00200	1.003	0.7952	0.6130	0.00236	1.212	0.6694	0.5674	0.01528	1.467	0.6421	0.5548
Burns, OR	0.00041	2.103	0.6836	0.6464	0.00041	2.765	0.7641	0.6509	0.00041	3.065	0.6522	0.4916
Eugene, OR	0.00357	10.365	0.4838	0.3950	0.00339	7.271	0.5196	0.3923	0.00389	7.240	0.4776	0.3653
Medford, OR	0.00031	5.446	0.5638	0.4821	0.00031	4.061	0.5856	0.4648	0.00031	3.409	0.5882	0.4543
Portland, OR	0.00018	10.567	0.5111	0.4065	0.00018	7.362	0.4167	0.3434	0.00305	6.728	0.3834	0.3401
Philadelphia, PA	0.00289	3.582	0.4497	0.3336	0.00213	3.245	0.3931	0.3134	0.00313	3.980	0.4107	0.3155
Pittsburgh, PA	0.00352	4.726	0.4581	0.3403	0.00364	4.246	0.4619	0.2971	0.00442	6.173	0.3754	0.2367
Columbia, SC	0.00993	4.008	0.4454	0.3717	0.01283	3.392	0.4653	0.3963	0.02642	3.728	0.4782	0.4072
Rapid City, SD	0.00012	0.772	0.648	0.6029	0.00012	1.142	0.6863	0.5529	0.00012	2.119	0.5902	0.4379
Sioux Falls, SD	0.00035	1.073	0.7169	0.6034	0.00035	1.560	0.8649	0.5963	0.00464	3.202	0.5079	0.4438
Memphis, TN	0.01336	3.596	0.6391	0.4704	0.01970	3.390	0.5033	0.3970	0.03806	3.444	0.4060	0.3705
Nashville, TN	0.00236	3.882	0.5915	0.4259	0.00575	3.701	0.4631	0.3205	0.00897	4.284	0.4553	0.3152
Abilene, TX	0.00013	1.055	0.8486	0.7490	0.00270	1.015	0.7214	0.6351	0.00806	0.823	0.7508	0.6402
Amarillo, TX	0.00011	0.621	0.8207	0.7379	0.00011	0.659	0.7286	0.7009	0.00255	0.789	0.8602	0.7570
Austin, TX	0.00443	1.856	0.8052	0.6013	0.00916	2.140	0.5703	0.4689	0.01807	1.139	0.6410	0.4959

Brownsville, TX	0.00098	1.217	0.7683	0.6091	0.00258	1.126	0.9388	0.5957	0.00057	0.477	0.9110	0.7467
Dallas/Ft Worth, TX	0.01006	1.006	0.6317	0.6355	0.00380	1.648	0.5662	0.4978	0.01494	1.971	0.4778	0.4441
Del Rio, TX	0.00009	0.465	0.7530	0.7535	0.00488	0.541	0.7302	0.7374	0.00624	0.296	0.8571	0.7790
El Paso, TX	0.00321	0.630	0.7666	0.7377	0.00027	0.712	0.7940	0.7449	0.00316	0.359	0.9621	0.8099
Houston, TX	0.00526	2.416	0.6097	0.5103	0.00240	1.874	0.4933	0.4717	0.00764	2.204	0.5217	0.4226
Lubbock, TX	0.00020	0.611	0.9243	0.7392	0.00261	0.740	0.7860	0.5855	0.00768	0.831	0.8376	0.7498
Midland, TX	0.00011	0.546	0.8601	0.7592	0.00217	0.589	0.8360	0.7282	0.00218	0.423	0.9516	0.8924
Salt Lake City, UT	0.00018	2.507	0.5056	0.4719	0.00018	2.307	0.4821	0.4426	0.00018	3.373	0.4886	0.4440
Norfolk, VA	0.00305	4.076	0.3997	0.2848	0.00358	3.493	0.3743	0.3772	0.00485	3.986	0.4111	0.3424
Richmond, VA	0.00919	3.258	0.4902	0.3141	0.00347	3.454	0.3956	0.3796	0.01376	3.637	0.4514	0.3261
Roanoke, VA	0.00012	3.157	0.4867	0.3712	0.00012	3.693	0.4580	0.3489	0.00370	4.086	0.4500	0.3744
Wallops Is., VA	0.00000	3.585	0.4596	0.3282	0.00000	2.953	0.4823	0.4221	0.00000	3.610	0.4640	0.3719
Washington, DC	0.00336	3.440	0.4658	0.3355	0.00275	3.235	0.4678	0.3862	0.00978	3.917	0.4119	0.3206
Burlington, VT	0.00022	3.543	0.5138	0.4309	0.00022	3.446	0.5224	0.3683	0.00022	4.153	0.3332	0.2741
Blaine, WA	0.00336	6.494	0.4550	0.6240	0.00310	5.116	0.4960	0.598	0.00857	4.010	0.3930	0.6210
Quillayute, WA	0.00336	16.518	0.4270	0.3518	0.00310	14.709	0.4168	0.3032	0.00857	13.598	0.3299	0.2618
Seattle–Tacoma, WA	0.00202	9.506	0.4039	0.3321	0.00179	6.869	0.4295	0.3513	0.00218	6.426	0.4249	0.3611
Spokane, WA	0.00014	5.233	0.5061	0.4132	0.00014	3.563	0.4639	0.4295	0.00178	3.424	0.4392	0.4025
Walla Walla, WA	0.00000	4.339	0.5990	0.5118	0.00000	3.514	0.4678	0.4391	0.00000	3.571	0.4944	0.4386
Madison, WI	0.00021	1.908	0.5280	0.3969	0.00021	1.872	0.5950	0.4530	0.00405	3.447	0.4754	0.3651
Cheyenne, WY	0.00021	1.069	0.9376	0.6306	0.00021	0.945	0.8090	0.6572	0.00021	2.486	0.6547	0.4986
Lander, WY	0.00030	1.032	0.6438	0.6435	0.00030	1.248	0.7068	0.6076	0.00030	2.405	0.5859	0.4761
Sheridan, WY	0.00019	1.693	0.5474	0.5203	0.00019	1.671	0.6178	0.4721	0.00019	2.584	0.5562	0.4255

Parameters for the Local Rain Rate Prediction Model (continued)

Location	April				May				June			
	Pc	*Pd*	*sR*	*sP*	*Pc*	*Pd*	*sR*	*sP*	*Pc*	*Pd*	*sR*	*sP*
Fairbanks, AK	0.00024	1.074	0.7359	0.7291	0.00499	1.825	0.6215	0.5668	0.00782	4.362	0.4738	0.4269
Huntsville, AL	0.02073	3.088	0.5495	0.4292	0.05064	2.225	0.4374	0.3562	0.03640	1.950	0.6082	0.4862
Mobile, AL	0.01744	2.393	0.7097	0.5199	0.02615	2.777	0.5763	0.5174	0.02221	2.506	0.5345	0.4456
Montgomery, AL	0.04938	2.289	0.6350	0.4540	0.05956	1.478	0.5693	0.4222	0.08788	0.270	0.5922	0.4786
Little Rock, AR	0.12373	0.46	0.6341	0.4706	0.12650	0.552	0.6202	0.5047	0.08901	0.331	0.6666	0.5358
Flagstaff, AZ	0.00384	1.981	0.7319	0.7016	0.00378	0.999	0.8684	0.7796	0.00396	0.714	0.9803	0.8490
Tucson, AZ	0.00262	0.338	0.9987	0.9622	0.00299	0.149	1.0433	0.9766	0.00323	0.207	1.0332	0.8473
Yuma, AZ	0.00027	0.180	1.2795	1.1889	0.00027	0.043	1.3608	1.1788	0.00020	0.001	1.7010	1.5377
Bakersfield, CA	0.00194	0.981	0.8195	0.8000	0.00017	0.335	1.2789	1.0098	0.00017	0.142	1.3912	1.2909
Eureka, CA	0.00216	3.943	0.6405	0.5024	0.00216	2.329	0.7151	0.6192	0.00159	0.828	0.8376	0.6579
Fresno, CA	0.00147	1.455	0.8419	0.7840	0.00011	0.485	1.0193	0.9608	0.00011	0.156	1.3862	1.0105
Los Angeles, CA	0.00016	0.905	0.9439	0.8978	0.00016	0.134	1.5330	1.2965	0.00016	0.039	1.4912	1.2538
San Diego, CA	0.00588	0.845	0.9255	0.8446	0.00199	0.192	1.2127	0.9859	0.00020	0.096	1.3153	1.0421
San Francisco, CA	0.00121	1.669	0.9010	0.7839	0.00000	0.389	1.2634	1.0020	0.00000	0.146	1.1642	1.0540
Alamosa, CO	0.00016	1.088	0.7011	0.5695	0.00490	1.221	0.6639	0.6439	0.00586	0.873	0.7793	0.6624
Denver, CO	0.00014	3.473	0.5074	0.4367	0.00833	4.196	0.6081	0.4593	0.01205	2.356	0.6219	0.4507
Grand Junction, CO	0.0032	1.392	0.5848	0.5259	0.00374	1.671	0.6030	0.5660	0.00307	0.730	0.9239	0.7158
Greeley, CO	0.00014	1.599	0.5800	0.5140	0.00833	2.748	0.5500	0.5560	0.01205	1.103	0.7060	0.6510
Hartford, CT	0.00397	4.692	0.3991	0.3291	0.01121	3.915	0.6130	0.4092	0.04477	2.270	0.6331	0.4890
Jacksonville, FL	0.01213	1.734	0.7140	0.4866	0.02504	1.890	0.6887	0.5287	0.04898	2.098	0.5017	0.3691
Miami, FL	0.02056	1.414	0.8520	0.6410	0.03551	2.715	0.6859	0.5497	0.07904	3.076	0.4958	0.4516
Tallahassee, FL	0.02448	1.459	0.7224	0.5418	0.03968	1.638	0.5891	0.4909	0.05237	2.523	0.4597	0.3968
Tampa, FL	0.02078	0.863	0.7283	0.6409	0.07099	0.287	0.8626	0.6170	0.12984	0.525	0.4353	0.4098
Atlanta, GA	0.06098	1.925	0.4969	0.4206	0.08807	0.361	0.4833	0.3722	0.08095	0.332	0.5572	0.5236
Savannah, GA	0.04911	1.632	0.5580	0.3854	0.10430	0.415	0.5449	0.5002	0.13709	0.546	0.5025	0.4310
Des Moines, IA	0.01224	3.468	0.4898	0.4054	0.02298	3.678	0.4329	0.3677	0.04472	2.588	0.4519	0.3386
Boise, ID	0.00767	1.044	0.5691	0.5334	0.02109	0.780	0.6784	0.6706	0.00895	0.534	0.8012	0.7587
Chicago, IL	0.01351	4.408	0.4044	0.3141	0.02289	3.235	0.4890	0.4017	0.06204	1.470	0.5124	0.3779
Springfield, IL	0.08529	2.431	0.5140	0.3771	0.10709	0.572	0.5028	0.4128	0.11873	0.634	0.5708	0.4366

Ft. Wayne, IN	0.02342	4.072	0.3919	0.3489	0.04318	3.199	0.3953	0.3370	0.07727	1.751	0.4405	0.3782
Indianapolis, IN	0.00502	4.181	0.4205	0.3336	0.01966	3.570	0.5184	0.4052	0.03124	2.676	0.4401	0.4196
Goodland, KS	0.00256	1.646	0.6333	0.5669	0.01321	3.755	0.4874	0.3643	0.02333	2.599	0.6531	0.4896
Wichita, KS	0.00506	1.924	0.5847	0.4914	0.01747	3.202	0.5446	0.4605	0.0356	2.389	0.5331	0.4330
Louisville, KY	0.02113	3.287	0.5288	0.4003	0.02425	3.637	0.4418	0.3160	0.03081	2.464	0.5121	0.4291
New Orleans, LA	0.01173	2.299	0.7209	0.4804	0.01311	2.373	0.6221	0.5521	0.01970	2.623	0.5529	0.5086
Shreveport, LA	0.08488	1.118	0.7681	0.4636	0.12651	0.495	0.5421	0.4405	0.11359	0.445	0.7668	0.6511
Boston, MA	0.00356	4.677	0.4494	0.3501	0.00403	3.981	0.6393	0.3967	0.02412	2.860	0.6793	0.5422
Caribou, ME	0.00026	4.985	0.3725	0.2678	0.01508	4.532	0.4150	0.3566	0.02181	4.782	0.4023	0.3627
Portland, ME	0.00261	5.081	0.4241	0.2986	0.00303	4.282	0.5418	0.4864	0.01510	3.298	0.4105	0.4240
Detroit–Metro, MI	0.00766	4.258	0.3427	0.3251	0.02291	3.005	0.4140	0.3574	0.04917	2.426	0.3924	0.3091
Grand Rapids, MI	0.00893	4.812	0.3280	0.2407	0.01300	3.825	0.5213	0.3866	0.03409	3.246	0.4735	0.4055
Sault Ste. Marie, MI	0.00400	5.604	0.3951	0.3098	0.01806	5.172	0.4904	0.3707	0.01756	6.379	0.4655	0.3713
Duluth, MN	0.00290	3.788	0.4841	0.3900	0.00976	4.804	0.4820	0.3756	0.02404	4.984	0.4000	0.3505
International Falls, MN	0.00384	3.075	0.5103	0.4219	0.01244	4.550	0.5509	0.4018	0.04590	4.813	0.4266	0.3238
Minneapolis, MN	0.00844	2.899	0.5262	0.3586	0.01400	4.064	0.4636	0.3266	0.03513	3.539	0.5121	0.3631
Kansas City, MO	0.01021	2.885	0.5081	0.4537	0.02489	4.261	0.4551	0.3929	0.02511	2.991	0.3606	0.3401
St. Louis, MO	0.01609	3.288	0.4935	0.3824	0.03282	2.858	0.5138	0.3795	0.04182	2.398	0.5452	0.4885
Jackson, MS	0.13156	0.522	0.6818	0.5108	0.09268	1.893	0.5415	0.4364	0.07256	0.269	0.5748	0.4828
Glasgow, MT	0.00014	1.693	0.6058	0.5575	0.00320	3.554	0.5709	0.5214	0.01672	3.181	0.5257	0.3770
Missoula, MT	0.00022	2.594	0.5225	0.3899	0.00377	4.383	0.6204	0.4252	0.00540	4.387	0.4740	0.4148
Charlotte, NC	0.00802	2.513	0.4686	0.3954	0.01614	2.670	0.4956	0.3598	0.01894	2.374	0.4924	0.4495
Raleigh, NC	0.00797	2.475	0.5040	0.4265	0.02978	2.424	0.3976	0.3354	0.03176	2.082	0.5413	0.4368
Bismarck, ND	0.00403	3.263	0.7204	0.6392	0.02620	3.458	0.5266	0.4475	0.06957	1.337	0.4656	0.4180
Fargo, ND	0.00284	2.981	0.6790	0.5448	0.00482	4.061	0.5614	0.4244	0.02024	3.840	0.5155	0.3677
Grand Island, NE	0.00767	2.873	0.5804	0.4554	0.02097	4.065	0.4594	0.3976	0.03861	2.864	0.5500	0.3866
No. Platte, NE	0.00283	2.456	0.5633	0.4643	0.01052	4.246	0.4463	0.4148	0.02579	2.891	0.5157	0.3942
Scottsbluff, NE	0.00009	2.781	0.5118	0.4361	0.00787	4.255	0.5379	0.5050	0.01584	3.883	0.5289	0.3810
Concord, NH	0.00422	4.402	0.3476	0.2727	0.01591	3.820	0.5555	0.4367	0.02827	3.292	0.4280	0.4664
Albuquerque, NM	0.00429	0.730	0.9003	0.759	0.01142	0.527	0.7879	0.6304	0.01757	0.170	0.8307	0.7640
Jornada, NM	0.00298	0.120	0.9550	0.8840	0.00417	0.239	1.1540	1.0490	0.01022	0.247	0.9310	0.8800

Parameters for the Local Rain Rate Prediction Model (continued)

Location	April				May				June			
	Pc	*Pd*	*sR*	*sP*	*Pc*	*Pd*	*sR*	*sP*	*Pc*	*Pd*	*sR*	*sP*
Roswell, NM	0.00000	0.502	0.8674	0.7301	0.00000	1.194	0.7555	0.6297	0.00000	1.604	0.8493	0.7623
Elko, NV	0.00000	1.640	0.6252	0.7161	0.00000	1.997	0.7606	0.7450	0.00000	1.577	0.7292	0.8090
Ely, NV	0.00010	1.983	0.7173	0.6052	0.00166	2.361	0.6656	0.6307	0.00151	1.630	0.9011	0.7831
Las Vegas, NV	0.00175	0.284	1.2451	1.1098	0.00192	0.255	1.0139	0.9708	0.00018	0.181	1.2225	1.0532
Reno, NV	0.00031	0.956	0.8516	0.7004	0.00375	1.138	0.8929	0.7041	0.00363	0.697	0.8485	0.7611
Albany, NY	0.00013	4.583	0.3884	0.3077	0.01341	4.274	0.4895	0.4155	0.03170	2.693	0.4524	0.4130
Buffalo, NY	0.00598	6.853	0.3366	0.2311	0.04828	4.316	0.4296	0.4152	0.11334	0.583	0.5379	0.4182
NY/Kennedy, NY	0.00789	4.066	0.4603	0.3359	0.01497	3.900	0.5282	0.4006	0.04640	1.725	0.5523	0.4521
Syracuse, NY	0.00318	5.924	0.4254	0.2882	0.01385	4.923	0.4272	0.3945	0.01865	5.006	0.5475	0.4149
Cleveland, OH	0.01133	5.423	0.3550	0.2813	0.03924	3.862	0.4402	0.4253	0.08874	1.013	0.4647	0.3554
Columbus, OH	0.0139	4.081	0.4021	0.3171	0.02126	4.373	0.4004	0.4032	0.07905	0.473	0.4854	0.3989
Oklahoma City, OK	0.02244	1.552	0.5413	0.4554	0.06254	2.620	0.4995	0.4198	0.05830	1.456	0.6033	0.4885
Burns, OR	0.00621	1.776	0.7325	0.6619	0.01488	2.191	0.5002	0.4707	0.00651	1.761	0.9207	0.7244
Eugene, OR	0.00351	4.272	0.5560	0.4521	0.00354	2.965	0.5948	0.4983	0.00305	1.950	0.6614	0.5249
Medford, OR	0.00031	1.942	0.5665	0.4975	0.00475	1.927	0.6611	0.5549	0.00462	1.031	0.7610	0.6873
Portland, OR	0.00326	4.502	0.4253	0.3928	0.00789	3.396	0.447	0.4243	0.00709	2.571	0.5564	0.5215
Philadelphia, PA	0.00891	3.592	0.4147	0.3248	0.01851	3.165	0.5185	0.4113	0.02822	2.879	0.4961	0.3997
Pittsburgh, PA	0.01549	4.925	0.4076	0.3236	0.03089	4.740	0.4166	0.4191	0.09148	0.545	0.4436	0.3639
Columbia, SC	0.02479	2.332	0.4811	0.4578	0.04014	1.997	0.5000	0.4311	0.09364	0.341	0.6026	0.4640
Rapid City, SD	0.00012	3.784	0.6102	0.4670	0.00851	4.671	0.5499	0.4134	0.02649	3.177	0.5164	0.4304
Sioux Falls, SD	0.00769	4.488	0.5502	0.4614	0.06644	2.525	0.5688	0.3872	0.09553	1.534	0.4483	0.3801
Memphis, TN	0.05913	2.987	0.5335	0.4300	0.07922	1.753	0.4539	0.4125	0.07068	0.824	0.5342	0.5107
Nashville, TN	0.01032	3.375	0.4707	0.3810	0.02081	3.417	0.4473	0.3605	0.02498	2.486	0.5431	0.4779
Abilene, TX	0.01848	1.179	0.6616	0.5610	0.03860	1.551	0.6245	0.4569	0.03900	1.108	0.7086	0.5937

Amarillo, TX	0.00339	1.086	0.6686	0.6312	0.01435	2.068	0.6269	0.4874	0.03278	1.900	0.6186	0.4153
Austin, TX	0.03122	1.519	0.6597	0.5306	0.07913	0.622	0.5499	0.4477	0.03623	1.795	0.7372	0.6376
Brownsville, TX	0.00635	1.225	0.9518	0.6700	0.01648	1.738	0.7556	0.6297	0.01457	1.714	0.7101	0.6856
Dallas/Ft Worth, TX	0.01715	1.649	0.5278	0.5083	0.03746	2.845	0.5417	0.4349	0.01765	2.120	0.5523	0.5503
Del Rio, TX	0.02144	0.498	0.7427	0.6064	0.01930	0.93	0.5835	0.4978	0.01087	1.247	0.7850	0.8379
El Paso, TX	0.00298	0.173	1.1175	1.1186	0.00417	0.369	1.2191	0.9805	0.01022	0.557	0.9793	0.8919
Houston, TX	0.00814	2.205	0.6822	0.4891	0.01201	3.296	0.5371	0.4274	0.00957	3.460	0.6755	0.6301
Lubbock, TX	0.00954	0.821	0.6893	0.5930	0.04267	1.239	0.7284	0.5924	0.06730	0.632	0.5717	0.5068
Midland, TX	0.0074	0.443	0.7588	0.7203	0.02255	1.138	0.6604	0.5642	0.02098	0.627	0.5629	0.5008
Salt Lake City, UT	0.00283	3.703	0.5091	0.4470	0.00358	3.211	0.5550	0.4901	0.00274	1.506	0.7409	0.6566
Norfolk, VA	0.00989	2.919	0.4840	0.3264	0.02707	2.718	0.4874	0.3821	0.04002	1.994	0.5114	0.4202
Richmond, VA	0.01146	2.899	0.4611	0.3281	0.03099	2.750	0.4263	0.3715	0.05209	1.554	0.5154	0.4243
Roanoke, VA	0.00404	3.640	0.5478	0.3994	0.01560	3.495	0.4410	0.3461	0.02712	2.092	0.5156	0.4395
Wallops Is., VA	0.00171	2.447	0.4530	0.3940	0.00886	2.962	0.5988	0.5192	0.00000	3.018	0.6115	0.4951
Washington, DC	0.01118	3.201	0.4487	0.3898	0.02621	3.413	0.4682	0.3895	0.05839	1.103	0.5849	0.4433
Burlington, VT	0.00378	5.136	0.3268	0.3064	0.01343	4.993	0.4167	0.4006	0.05512	2.864	0.3884	0.3802
Blaine, WA	0.00302	3.293	0.4130	0.6020	0.00548	2.438	0.4940	0.6490	0.00249	2.210	0.5720	0.6510
Quillayute, WA	0.00302	9.792	0.3985	0.2992	0.00548	6.880	0.5451	0.3296	0.00249	3.906	0.5051	0.4008
Seattle–Tacoma, WA	0.00430	4.600	0.4661	0.3382	0.00359	2.934	0.5011	0.4137	0.00191	2.651	0.5420	0.4217
Spokane, WA	0.00014	2.609	0.5514	0.4796	0.00553	2.834	0.5258	0.4575	0.00602	2.561	0.5392	0.4028
Walla Walla, WA	0.00000	2.771	0.5657	0.4939	0.01200	1.849	0.6008	0.4135	0.00000	2.149	0.6945	0.5841
Madison, WI	0.01503	4.069	0.3923	0.3499	0.03762	2.756	0.4366	0.4263	0.08189	0.845	0.5176	0.3518
Cheyenne, WY	0.00021	3.215	0.5847	0.4541	0.01182	4.760	0.4821	0.4684	0.02010	3.200	0.4848	0.4399
Lander, WY	0.00030	4.247	0.5122	0.4513	0.00514	5.054	0.5446	0.5372	0.00690	2.594	0.7639	0.6669
Sheridan, WY	0.00019	4.408	0.5739	0.4119	0.01020	4.737	0.5390	0.4006	0.01524	3.791	0.5586	0.4763

Parameters for the Local Rain Rate Prediction Model (continued)

Location	July				August				September			
	Pc	*Pd*	*sR*	*sP*	*Pc*	*Pd*	*sR*	*sP*	*Pc*	*Pd*	*sR*	*sP*
Fairbanks, AK	0.02614	3.862	0.4980	0.4368	0.00715	5.775	0.5959	0.404	0.00024	3.197	0.7211	0.6520
Huntsville, AL	0.04854	1.873	0.5141	0.4025	0.03313	1.640	0.5202	0.4121	0.02636	2.263	0.5387	0.4657
Mobile, AL	0.04019	3.046	0.3978	0.3305	0.03609	3.032	0.4128	0.3478	0.02027	2.704	0.5614	0.4787
Montgomery, AL	0.11658	0.359	0.3745	0.4115	0.08023	0.247	0.5385	0.4148	0.06620	1.437	0.5693	0.5418
Little Rock, AR	0.09109	0.339	0.4744	0.3509	0.07909	0.294	0.8055	0.5524	0.07281	1.564	0.5860	0.5509
Flagstaff, AZ	0.05983	0.895	0.4887	0.3981	0.05699	1.642	0.5093	0.3748	0.02556	1.629	0.8303	0.7623
Tucson, AZ	0.03655	1.779	0.5600	0.3832	0.06091	0.314	0.5977	0.4170	0.03637	0.188	0.7446	0.6819
Yuma, AZ	0.00420	0.105	1.3172	1.0223	0.01069	0.076	1.0565	0.8557	0.00439	0.031	1.3631	1.2042
Bakersfield, CA	0.00017	0.010	1.7237	1.5299	0.00017	0.093	1.6906	1.5451	0.00017	0.249	1.2170	1.1881
Eureka, CA	0.00015	0.203	1.1406	0.8714	0.00135	0.514	1.1625	0.9947	0.00351	0.999	0.8352	0.7618
Fresno, CA	0.00000	0.016	1.5745	1.3282	0.00011	0.019	1.4531	1.4143	0.00011	0.300	1.1858	1.1484
Los Angeles, CA	0.00016	0.015	1.4315	1.2831	0.00016	0.108	1.6574	1.5178	0.00016	0.207	1.3005	1.1491
San Diego, CA	0.00020	0.02	1.3953	1.2161	0.00020	0.118	1.6639	1.4540	0.00190	0.196	1.2425	1.1842
San Francisco, CA	0.00007	0.025	1.4838	1.2769	0.00007	0.057	1.3850	1.3310	0.00007	0.272	1.2628	1.0917
Alamosa, CO	0.00901	1.849	0.6012	0.5238	0.00917	2.176	0.6526	0.5004	0.00594	1.345	0.6305	0.5607
Denver, CO	0.03097	0.766	0.5754	0.4137	0.01228	1.893	0.6829	0.4241	0.00740	1.610	0.7449	0.6773
Grand Junction, CO	0.01160	0.428	0.7064	0.5563	0.01144	1.194	0.6500	0.6066	0.01068	1.033	0.7778	0.7183
Greeley, CO	0.02063	0.147	0.7290	0.6480	0.01228	0.249	0.6580	0.6310	0.00740	1.028	0.7720	0.7500
Hartford, CT	0.03352	2.397	0.4628	0.3884	0.04647	2.663	0.7387	0.4466	0.01911	3.896	0.5221	0.4608
Jacksonville, FL	0.05634	2.647	0.4595	0.2567	0.06468	2.842	0.4745	0.3887	0.04276	3.898	0.5397	0.4667
Miami, FL	0.04741	2.394	0.3684	0.2908	0.06870	2.482	0.4203	0.3638	0.06512	3.114	0.4698	0.3596
Tallahassee, FL	0.06679	2.947	0.4917	0.3623	0.06659	2.199	0.3655	0.3375	0.03610	2.059	0.5715	0.5189
Tampa, FL	0.16217	0.656	0.4669	0.3420	0.18575	0.751	0.3484	0.2917	0.14821	0.599	0.4796	0.4601
Atlanta, GA	0.11334	0.464	0.4650	0.4649	0.08077	0.331	0.5261	0.4996	0.03451	2.492	0.5899	0.5373
Savannah, GA	0.16408	0.653	0.5460	0.4368	0.17602	0.700	0.4555	0.4428	0.08237	2.769	0.6241	0.5101
Des Moines, IA	0.03062	2.894	0.5992	0.4943	0.02561	3.736	0.6440	0.4717	0.01879	2.909	0.6243	0.4799
Boise, ID	0.01488	0.171	0.7707	0.7118	0.01527	0.016	0.9277	0.8807	0.01488	0.297	1.0509	0.9908
Chicago, IL	0.03727	2.656	0.4056	0.3543	0.04605	3.223	0.6754	0.5057	0.02818	3.342	0.5702	0.4681
Springfield, IL	0.12035	0.642	0.5108	0.4211	0.09954	0.531	0.5569	0.4077	0.08529	1.135	0.6168	0.4878

Ft. Wayne, IN	0.07555	1.344	0.4744	0.3403	0.06786	1.453	0.4757	0.4000	0.03026	2.540	0.5071	0.4079
Indianapolis, IN	0.03785	3.034	0.4987	0.4142	0.04026	1.640	0.5500	0.3466	0.01504	2.576	0.5794	0.5048
Goodland, KS	0.02923	1.699	0.5811	0.3650	0.01689	1.918	0.6674	0.5150	0.00778	1.362	0.8044	0.6896
Wichita, KS	0.01933	2.509	0.5992	0.4737	0.01845	2.050	0.6541	0.5571	0.01557	2.575	0.6216	0.4857
Louisville, KY	0.04973	2.073	0.4811	0.3833	0.03415	1.957	0.4799	0.4034	0.01915	2.396	0.5522	0.4108
New Orleans, LA	0.01711	3.132	0.4363	0.3623	0.01597	2.984	0.5171	0.4521	0.01367	2.719	0.558	0.4913
Shreveport, LA	0.09179	0.360	0.5995	0.4978	0.06610	0.259	0.6157	0.4359	0.05190	1.772	0.5859	0.4150
Boston, MA	0.03157	2.235	0.5517	0.3992	0.04144	2.809	0.6822	0.4381	0.01306	3.658	0.5983	0.4351
Caribou, ME	0.04212	4.716	0.3435	0.3051	0.04022	5.438	0.4825	0.3637	0.00669	6.014	0.4381	0.3034
Portland, ME	0.02122	2.601	0.5016	0.4115	0.01933	2.900	0.6421	0.3094	0.00854	3.698	0.4933	0.3542
Detroit–Metro, MI	0.0403	2.153	0.4569	0.3330	0.03396	2.933	0.5561	0.5048	0.01443	3.597	0.5304	0.3495
Grand Rapids, MI	0.03604	2.647	0.5006	0.3701	0.02909	3.700	0.4900	0.4946	0.01971	5.092	0.5467	0.4172
Sault Ste. Marie, MI	0.04535	3.271	0.4693	0.3615	0.05656	3.310	0.4257	0.3086	0.02537	7.206	0.3925	0.3583
Duluth, MN	0.04567	2.983	0.4162	0.3660	0.02910	4.432	0.4938	0.4336	0.01686	5.160	0.4996	0.4125
International Falls, MN	0.06839	2.620	0.4685	0.3610	0.04847	2.773	0.4541	0.3778	0.02029	4.962	0.5186	0.4153
Minneapolis, MN	0.03403	3.726	0.6013	0.3582	0.02667	3.840	0.4463	0.3458	0.01021	3.509	0.5681	0.4679
Kansas City, MO	0.02632	3.510	0.7573	0.6892	0.02785	2.634	0.5601	0.4015	0.01746	4.264	0.6463	0.4939
St. Louis, MO	0.05438	1.730	0.5428	0.4493	0.03253	1.556	0.5201	0.4760	0.01674	2.612	0.648	0.5070
Jackson, MS	0.10249	0.380	0.5486	0.3205	0.09043	0.335	0.5052	0.4040	0.08496	0.318	0.4953	0.4011
Glasgow, MT	0.01613	2.446	0.7035	0.6495	0.01081	2.029	0.7918	0.5888	0.00014	2.254	0.8433	0.6319
Missoula, MT	0.01148	1.439	0.6347	0.5684	0.01036	1.890	0.6161	0.6285	0.00344	2.550	0.7007	0.6273
Charlotte, NC	0.02952	2.296	0.4810	0.4570	0.01060	3.251	0.5123	0.4879	0.01355	2.587	0.6413	0.6025
Raleigh, NC	0.03300	2.936	0.4876	0.4299	0.03216	2.941	0.5423	0.4270	0.01714	2.377	0.5244	0.5314
Bismarck, ND	0.06256	0.465	0.7864	0.5474	0.04047	1.201	0.6418	0.4517	0.01412	2.267	0.7600	0.5540
Fargo, ND	0.03207	2.634	0.5923	0.4680	0.02018	2.601	0.5785	0.4625	0.01208	2.176	0.6723	0.5098
Grand Island, NE	0.03810	1.818	0.6530	0.4774	0.03468	1.564	0.5594	0.4014	0.01476	2.432	0.7425	0.6635
No. Platte, NE	0.02532	2.328	0.5099	0.3851	0.01308	2.034	0.6278	0.5112	0.00360	1.842	0.7699	0.6220
Scottsbluff, NE	0.01541	2.181	0.5937	0.4327	0.00605	1.307	0.6406	0.4930	0.00219	1.968	0.7981	0.6394
Concord, NH	0.06393	1.606	0.4358	0.3607	0.03458	3.424	0.4041	0.3068	0.01812	3.842	0.4811	0.4114
Albuquerque, NM	0.04506	0.224	0.5174	0.4198	0.05578	0.277	0.5406	0.3945	0.02297	0.602	0.5803	0.5697

Parameters for the Local Rain Rate Prediction Model (continued)

Location	July				August				September			
	Pc	*Pd*	*sR*	*sP*	*Pc*	*Pd*	*sR*	*sP*	*Pc*	*Pd*	*sR*	*sP*
Jornada, NM	0.03006	0.692	0.5710	0.6280	0.03157	0.894	0.5560	0.4540	0.01977	0.595	0.6810	0.7920
Roswell, NM	0.00000	1.758	0.8510	0.7720	0.00000	2.265	0.6378	0.6830	0.00000	1.983	0.7572	0.9187
Elko, NV	0.00000	0.739	0.9185	0.7485	0.01200	0.418	1.1032	0.8811	0.00000	1.116	1.0105	0.8687
Ely, NV	0.00195	1.342	0.7483	0.6041	0.00441	1.349	0.7255	0.7323	0.00176	1.829	0.9170	0.7903
Las Vegas, NV	0.00550	0.475	1.0573	0.8256	0.00513	0.658	0.9395	0.8045	0.00195	0.385	1.0703	0.9687
Reno, NV	0.00387	0.317	0.8941	0.7601	0.00416	0.302	1.0536	0.9843	0.00317	0.603	0.9543	0.9366
Albany, NY	0.03802	2.164	0.4762	0.3492	0.02572	3.299	0.4365	0.3551	0.01171	3.913	0.4835	0.4032
Buffalo, NY	0.10926	0.562	0.5148	0.3913	0.14100	0.725	0.4407	0.3052	0.08643	2.809	0.4470	0.3403
NY/Kennedy, NY	0.05971	1.397	0.5001	0.4608	0.03501	2.238	0.5850	0.4427	0.02684	2.443	0.5656	0.4363
Syracuse, NY	0.05215	2.653	0.5290	0.4698	0.04169	3.364	0.3998	0.3031	0.02002	5.077	0.4377	0.4019
Cleveland, OH	0.09911	0.512	0.3839	0.3549	0.07210	1.845	0.4656	0.4071	0.03175	4.028	0.4218	0.3624
Columbus, OH	0.05588	2.931	0.4544	0.3356	0.04708	1.789	0.4929	0.4385	0.02312	2.524	0.4914	0.4074
Oklahoma City, OK	0.02510	1.546	0.6952	0.5550	0.01194	1.904	0.5163	0.4094	0.03190	2.146	0.6422	0.5517
Burns, OR	0.00736	0.650	0.7859	0.8398	0.00657	0.868	0.6914	0.6517	0.00041	1.252	1.1336	1.0392
Eugene, OR	0.00252	0.545	0.9831	0.8820	0.00667	0.964	0.9863	0.8856	0.00662	1.676	0.6591	0.6670
Medford, OR	0.00466	0.272	1.0638	1.0204	0.00376	0.584	1.0239	1.0478	0.00403	1.165	0.8789	0.8085
Portland, OR	0.00583	0.741	0.8810	0.7584	0.00822	1.342	0.8468	0.8104	0.00346	2.771	0.6534	0.5975
Philadelphia, PA	0.04852	2.378	0.4771	0.3950	0.03798	3.226	0.5070	0.4675	0.02096	2.870	0.5269	0.4446
Pittsburgh, PA	0.10254	0.611	0.3836	0.3183	0.08266	0.492	0.4902	0.3835	0.03769	2.855	0.5629	0.4272
Columbia, SC	0.10324	1.263	0.6208	0.4940	0.11032	1.218	0.5426	0.4561	0.04737	1.767	0.5473	0.5568
Rapid City, SD	0.02019	2.012	0.6091	0.4563	0.01331	1.845	0.5273	0.4516	0.00266	2.120	0.7360	0.6177
Sioux Falls, SD	0.08678	0.485	0.5582	0.4589	0.08782	0.491	0.5792	0.4153	0.04721	3.139	0.5817	0.5599
Memphis, TN	0.08982	0.284	0.4553	0.4627	0.08056	0.254	0.5345	0.4919	0.04776	1.294	0.5403	0.4951
Nashville, TN	0.03660	1.949	0.4701	0.4345	0.02100	2.153	0.4879	0.4080	0.02040	2.300	0.6145	0.5068

Abilene, TX	0.02970	0.860	0.6980	0.6470	0.03008	0.838	0.7795	0.6365	0.02908	1.442	0.7161	0.6511
Amarillo, TX	0.01029	2.618	0.6008	0.5708	0.02232	2.088	0.5090	0.4397	0.01300	1.358	0.6428	0.5248
Austin, TX	0.01316	1.112	0.8613	0.6526	0.02807	0.671	0.8221	0.7377	0.02377	2.281	0.5373	0.5038
Brownsville, TX	0.00859	1.085	0.9266	0.8187	0.01647	1.710	0.7329	0.6727	0.02992	3.630	0.6543	0.5426
Dallas/Ft Worth, TX	0.02244	0.753	0.5108	0.5117	0.01369	0.923	0.6690	0.6394	0.01393	1.685	0.6706	0.5517
Del Rio, TX	0.00945	1.261	1.2044	1.1485	0.00992	1.120	0.8895	0.8635	0.01182	1.705	0.8890	0.6708
El Paso, TX	0.03006	1.043	0.6534	0.5356	0.03157	0.899	0.7033	0.5696	0.01977	1.297	0.8930	0.7993
Houston, TX	0.01271	1.823	0.5277	0.5022	0.00878	2.103	0.5732	0.4788	0.00969	2.589	0.6230	0.4883
Lubbock, TX	0.04010	1.192	0.6209	0.6097	0.03355	1.175	0.7333	0.6144	0.03003	1.802	0.6870	0.6680
Midland, TX	0.00897	1.635	0.9084	0.7370	0.01482	1.092	0.6600	0.5839	0.00819	2.103	0.7644	0.7350
Salt Lake City, UT	0.01011	0.641	0.7181	0.6284	0.01011	0.887	0.7932	0.6503	0.00283	1.869	0.9436	0.7793
Norfolk, VA	0.10625	0.439	0.5092	0.4533	0.07878	1.890	0.5671	0.4681	0.01295	4.089	0.7290	0.4964
Richmond, VA	0.10589	0.476	0.5639	0.4354	0.07156	2.142	0.5500	0.4433	0.02998	2.348	0.5983	0.4824
Roanoke, VA	0.03675	1.897	0.4756	0.3561	0.03175	2.499	0.4913	0.3935	0.01786	2.727	0.6537	0.5343
Wallops Is., VA	0.01065	2.802	0.5856	0.4559	0.00966	3.951	0.6732	0.5692	0.00510	3.071	0.5806	0.5213
Washington, DC	0.08506	0.401	0.4653	0.3758	0.08070	0.933	0.5748	0.4558	0.03120	2.582	0.6462	0.5008
Burlington, VT	0.09137	0.553	0.3322	0.3015	0.05794	3.729	0.4321	0.2789	0.02293	4.973	0.3705	0.3366
Blaine, WA	0.00185	1.354	0.6940	0.7630	0.00229	1.828	0.8180	0.8760	0.00620	2.455	0.5830	0.8020
Quillayute, WA	0.00185	3.178	0.8574	0.4488	0.00229	3.402	0.9592	0.6068	0.00620	5.224	0.5938	0.5514
Seattle–Tacoma, WA	0.00162	1.305	0.6567	0.6250	0.00368	1.911	0.9095	0.7573	0.00393	3.130	0.7272	0.6603
Spokane, WA	0.00441	1.219	0.8206	0.7089	0.00209	1.501	0.7247	0.6492	0.00170	1.528	0.6968	0.6493
Walla Walla, WA	0.00000	0.809	0.9482	0.8882	0.00000	1.295	0.9488	0.8078	0.00000	1.837	0.6787	0.6784
Madison, WI	0.09262	0.561	0.4528	0.3315	0.08708	0.528	0.4637	0.4232	0.04383	2.345	0.6432	0.4707
Cheyenne, WY	0.03713	1.194	0.5017	0.4121	0.02066	1.975	0.5632	0.4217	0.00481	2.380	0.7175	0.5971
Lander, WY	0.01567	0.381	0.6759	0.5883	0.00590	0.577	0.7736	0.6338	0.00030	2.118	0.8772	0.7618
Sheridan, WY	0.00468	1.990	0.8254	0.6795	0.00438	1.610	0.6528	0.5283	0.00019	3.115	0.5919	0.5783

Parameters for the Local Rain Rate Prediction Model (continued)

Location	October				November				December			
	Pc	*Pd*	*sR*	*sP*	*Pc*	*Pd*	*sR*	*sP*	*Pc*	*Pd*	*sR*	*sP*
Fairbanks, AK	0.00024	3.092	0.5358	0.4329	0.00024	2.873	0.7118	0.5279	0.00024	2.878	0.8423	0.6973
Huntsville, AL	0.00913	2.266	0.6048	0.4596	0.01452	3.203	0.4359	0.3402	0.01078	4.325	0.5805	0.3677
Mobile, AL	0.00998	1.615	0.7964	0.7219	0.01649	2.060	0.7053	0.5439	0.01565	2.645	0.3983	0.2961
Montgomery, AL	0.02560	1.345	0.7297	0.6951	0.03192	2.288	0.5787	0.4728	0.02093	3.761	0.4484	0.3578
Little Rock, AR	0.05725	1.012	0.7373	0.6773	0.04120	2.763	0.5771	0.4454	0.01492	4.237	0.4363	0.3425
Flagstaff, AZ	0.00508	2.360	0.8817	0.7769	0.00393	2.950	0.7358	0.6261	0.00028	3.543	0.7892	0.639
Tucson, AZ	0.01267	0.824	0.9385	0.8343	0.00347	0.797	0.7514	0.6500	0.00327	1.463	0.9194	0.8178
Yuma, AZ	0.00027	0.442	1.2740	1.1558	0.00027	0.356	1.1824	0.9786	0.00027	0.641	1.0203	0.9162
Bakersfield, CA	0.00017	0.514	1.0711	0.9437	0.00199	1.105	0.7793	0.6509	0.00017	1.169	0.7215	0.6323
Eureka, CA	0.00475	3.472	0.6342	0.5217	0.00565	7.791	0.6056	0.5230	0.00593	8.819	0.4833	0.4667
Fresno, CA	0.00134	0.674	0.9055	0.8524	0.00143	1.776	0.6710	0.6908	0.00140	2.219	0.7045	0.6202
Los Angeles, CA	0.00292	0.171	1.1129	0.9220	0.00325	1.438	0.9104	0.8464	0.00421	1.500	0.8068	0.7288
San Diego, CA	0.00242	0.405	1.0156	0.9353	0.01202	1.189	0.8546	0.7300	0.00940	1.626	0.7972	0.6735
San Francisco, CA	0.00133	1.284	1.0051	0.7801	0.00129	2.966	0.7215	0.6542	0.00151	4.399	0.6247	0.5766
Alamosa, CO	0.00016	1.498	0.8101	0.7823	0.00016	0.968	0.8001	0.7183	0.00016	0.833	0.8101	0.7542
Denver, CO	0.00014	1.980	0.8114	0.7313	0.00014	1.891	0.5696	0.5364	0.00014	1.187	0.7893	0.5479
Grand Junction, CO	0.00310	1.895	0.7220	0.7058	0.00023	1.596	0.5821	0.5062	0.00023	1.307	0.6653	0.5757
Greeley, CO	0.00014	0.967	0.8390	0.7530	0.00014	0.599	0.8170	0.7630	0.00014	0.431	0.7760	0.7740
Hartford, CT	0.00910	4.181	0.5415	0.4113	0.00334	4.882	0.3698	0.2956	0.00283	4.604	0.4884	0.3409
Jacksonville, FL	0.01788	2.292	0.6684	0.5641	0.00904	1.142	0.6523	0.5791	0.00952	1.448	0.6489	0.5412
Miami, FL	0.04156	2.875	0.6526	0.4030	0.01762	1.406	0.7876	0.5305	0.00993	0.818	0.7893	0.7032
Tallahassee, FL	0.02109	1.232	0.7945	0.7153	0.01469	1.739	0.6157	0.5142	0.00793	2.469	0.4986	0.4100
Tampa, FL	0.02596	1.178	0.7154	0.6407	0.01572	1.240	0.7760	0.6147	0.01561	1.780	0.6763	0.6225
Atlanta, GA	0.02205	2.195	0.6417	0.5704	0.02368	2.969	0.5120	0.4608	0.00897	4.309	0.5003	0.3589
Savannah, GA	0.02878	1.749	0.8187	0.6336	0.01044	2.168	0.6302	0.4991	0.01510	2.593	0.4651	0.4197
Des Moines, IA	0.00390	2.693	0.6101	0.5671	0.00257	2.334	0.6922	0.6311	0.00012	1.597	0.5665	0.4349
Boise, ID	0.00636	0.497	0.7609	0.7569	0.00038	1.175	0.6985	0.6930	0.00038	0.876	0.8584	0.8627

Chicago, IL	0.01051	2.965	0.6047	0.4553	0.00880	3.815	0.5633	0.3901	0.00275	3.384	0.5733	0.3084
Springfield, IL	0.03436	3.479	0.6039	0.4815	0.03045	3.220	0.5612	0.4434	0.00614	4.605	0.6322	0.3819
Ft. Wayne, IN	0.01163	3.622	0.6312	0.4314	0.00482	4.224	0.4706	0.3610	0.00346	3.850	0.5129	0.3055
Indianapolis, IN	0.01043	2.728	0.5398	0.4135	0.01042	3.635	0.4993	0.3725	0.00285	3.688	0.4937	0.3507
Goodland, KS	0.00246	1.206	0.8625	0.8158	0.00011	1.019	0.7428	0.6099	0.00011	0.621	0.7929	0.6410
Wichita, KS	0.00694	2.062	0.6463	0.5391	0.00606	1.232	0.7396	0.6696	0.00185	1.023	0.7018	0.5204
Louisville, KY	0.00914	2.467	0.5213	0.4417	0.00793	3.650	0.4806	0.3607	0.00259	3.907	0.4806	0.3597
New Orleans, LA	0.00770	1.467	0.7117	0.6520	0.00857	2.245	0.7785	0.5287	0.00965	2.639	0.4316	0.3472
Shreveport, LA	0.06984	1.681	0.6924	0.6595	0.09680	0.738	0.5243	0.433	0.02986	3.913	0.4942	0.4598
Boston, MA	0.01002	3.824	0.4582	0.3700	0.00420	5.377	0.4434	0.3242	0.00305	5.138	0.4923	0.3572
Caribou, ME	0.00452	5.735	0.4994	0.3302	0.00026	6.590	0.4288	0.2905	0.00026	6.047	0.4393	0.3225
Portland, ME	0.00334	4.626	0.5127	0.3281	0.00353	6.239	0.4449	0.3024	0.00257	5.499	0.4951	0.3247
Detroit–Metro, MI	0.00330	3.307	0.5104	0.3743	0.00291	4.104	0.4437	0.3736	0.00246	4.121	0.4812	0.2877
Grand Rapids, MI	0.00680	4.147	0.4112	0.3229	0.00350	5.250	0.4459	0.3197	0.00215	4.258	0.4719	0.2558
Sault Ste. Marie, MI	0.00476	7.780	0.5766	0.4004	0.00443	7.899	0.3512	0.2709	0.00022	6.639	0.3199	0.2405
Duluth, MN	0.00298	3.657	0.644	0.5073	0.00014	3.363	0.5580	0.4084	0.00014	2.129	0.5547	0.4515
International Falls, MN	0.00359	3.864	0.6425	0.4501	0.00021	2.775	0.4741	0.3791	0.00021	1.904	0.4253	0.3410
Minneapolis, MN	0.00294	2.842	0.6733	0.5629	0.00011	2.493	0.7195	0.5385	0.00011	1.637	0.6516	0.5225
Kansas City, MO	0.00893	3.058	0.6012	0.4838	0.00306	2.132	0.5467	0.5398	0.00233	1.661	0.7090	0.4316
St. Louis, MO	0.01322	2.468	0.5444	0.4902	0.01259	3.063	0.5922	0.4764	0.00276	2.882	0.6448	0.4235
Jackson, MS	0.03713	1.939	0.6956	0.6552	0.07439	1.881	0.5105	0.3896	0.03398	4.620	0.5192	0.3148
Glasgow, MT	0.00014	1.458	0.6884	0.5912	0.00014	0.830	0.6653	0.6548	0.00014	0.860	0.6061	0.5558
Missoula, MT	0.00022	2.142	0.6857	0.5818	0.00022	2.353	0.5189	0.4716	0.00022	2.992	0.5404	0.4697
Charlotte, NC	0.00819	2.683	0.7364	0.5787	0.00885	2.450	0.5330	0.4631	0.00190	3.199	0.4595	0.3807
Raleigh, NC	0.00865	2.500	0.5420	0.5184	0.00710	2.601	0.5810	0.4398	0.00283	3.000	0.4390	0.3899
Bismarck, ND	0.00027	2.114	0.8859	0.6883	0.00027	1.414	0.7649	0.7111	0.00027	1.190	0.4854	0.4728
Fargo, ND	0.00306	2.481	0.8736	0.6831	0.00014	1.685	0.7786	0.5564	0.00014	1.698	1.2254	0.5088
Grand Island, NE	0.00803	1.133	0.7069	0.6467	0.00229	1.115	0.8529	0.7704	0.00014	0.886	0.7420	0.5462
No. Platte, NE	0.00233	1.312	0.6528	0.6621	0.00011	0.919	0.7693	0.6423	0.00011	0.627	0.6500	0.5268
Scottsbluff, NE	0.00009	1.508	0.6832	0.6829	0.00009	1.168	0.7311	0.6254	0.00009	0.933	0.6468	0.5875

Parameters for the Local Rain Rate Prediction Model (continued)

Location	October				November				December			
	Pc	*Pd*	*sR*	*sP*	*Pc*	*Pd*	*sR*	*sP*	*Pc*	*Pd*	*sR*	*sP*
Concord, NH	0.01305	4.170	0.4776	0.3513	0.01075	5.145	0.3812	0.3111	0.00399	4.639	0.4721	0.3429
Albuquerque, NM	0.01040	1.258	0.8444	0.8041	0.00433	0.727	0.7807	0.6858	0.00039	1.075	0.7766	0.7017
Jornada, NM	0.00768	0.549	0.8170	0.6990	0.00328	0.285	1.0820	1.0270	0.00363	0.608	0.9360	0.8440
Roswell, NM	0.00000	0.971	0.9209	0.8563	0.00000	0.471	0.9247	0.9952	0.00000	0.413	1.0315	0.9283
Elko, NV	0.00000	1.183	0.7625	0.7400	0.00000	1.898	0.6434	0.6267	0.00000	2.067	0.8157	0.7785
Ely, NV	0.00010	1.748	0.7236	0.6444	0.00010	1.452	0.6693	0.5663	0.00010	1.537	0.6826	0.6070
Las Vegas, NV	0.00171	0.308	1.0079	0.8637	0.00174	0.678	0.9791	0.8370	0.00018	0.655	0.9508	0.8595
Reno, NV	0.00356	0.672	0.9224	0.7886	0.00031	1.618	0.7883	0.7032	0.00031	2.228	0.8192	0.6585
Albany, NY	0.00811	3.889	0.5413	0.3907	0.00269	4.597	0.4305	0.375	0.00013	4.398	0.4656	0.3571
Buffalo, NY	0.01767	6.119	0.5715	0.4337	0.01433	8.046	0.3598	0.3134	0.00492	8.082	0.3972	0.2561
NY/Kennedy, NY	0.01047	2.823	0.4896	0.4332	0.00722	3.517	0.6078	0.4737	0.00638	3.553	0.5458	0.4252
Syracuse, NY	0.00291	5.744	0.5152	0.3708	0.00295	6.348	0.3480	0.2676	0.00015	5.881	0.3216	0.2141
Cleveland, OH	0.01441	3.776	0.5647	0.3884	0.00405	5.613	0.4955	0.3720	0.00304	5.083	0.4245	0.2396
Columbus, OH	0.00381	2.920	0.5229	0.4246	0.00383	4.321	0.5528	0.4222	0.00309	3.920	0.4461	0.2861
Oklahoma City, OK	0.01960	2.097	0.7604	0.5978	0.01017	1.165	0.6936	0.6112	0.00236	1.304	0.8370	0.6229
Burns, OR	0.00560	1.966	0.5900	0.6823	0.00545	3.393	0.6560	0.5844	0.00579	3.670	0.6940	0.7057
Eugene, OR	0.00389	4.381	0.5877	0.4889	0.01052	9.602	0.5287	0.4570	0.00884	11.122	0.5477	0.4235
Medford, OR	0.00031	3.188	0.7711	0.5884	0.00031	5.347	0.6017	0.5132	0.00031	6.369	0.6473	0.5154
Portland, OR	0.00293	5.345	0.5307	0.4825	0.00300	9.564	0.4437	0.3723	0.00289	10.937	0.4170	0.3204
Philadelphia, PA	0.00320	3.035	0.4989	0.4419	0.00306	3.402	0.5541	0.4244	0.00248	3.783	0.4682	0.3587
Pittsburgh, PA	0.01568	3.716	0.5320	0.4052	0.00534	4.586	0.5314	0.3614	0.00024	5.204	0.4904	0.3120
Columbia, SC	0.02394	2.118	0.8215	0.6520	0.01795	1.974	0.5986	0.4996	0.00376	3.107	0.5432	0.3927
Rapid City, SD	0.00012	1.978	0.7141	0.5760	0.00012	1.160	0.6426	0.6034	0.00012	0.874	0.5980	0.5290
Sioux Falls, SD	0.01585	2.307	0.7719	0.6621	0.00427	2.016	0.6745	0.5959	0.00035	1.386	0.7103	0.5739
Memphis, TN	0.01945	1.956	0.5859	0.5759	0.03626	2.830	0.5543	0.4099	0.02022	4.179	0.5457	0.4189

Nashville, TN	0.00740	2.178	0.5288	0.4688	0.00421	3.521	0.4370	0.3612	0.00521	4.193	0.5476	0.3734
Abilene, TX	0.02170	1.563	0.7335	0.6500	0.00798	0.891	0.7483	0.7391	0.00250	1.050	0.9011	0.7361
Amarillo, TX	0.00887	1.111	0.7788	0.6884	0.00011	0.711	0.8481	0.7421	0.00011	0.712	1.0251	0.7248
Austin, TX	0.03291	1.737	0.7532	0.6613	0.01454	1.621	0.7267	0.6353	0.00931	1.957	0.8386	0.6388
Brownsville, TX	0.01732	2.181	0.7576	0.6362	0.00449	1.186	0.8508	0.6714	0.00168	0.953	0.7697	0.6969
Dallas/Ft Worth, TX	0.01955	2.385	0.7090	0.6427	0.00500	1.503	0.5262	0.4598	0.00433	1.716	0.7551	0.5629
Del Rio, TX	0.00984	1.753	0.9431	0.7676	0.00237	0.937	0.8266	0.7861	0.00178	0.523	0.9104	0.6773
El Paso, TX	0.00768	0.970	0.8765	0.7952	0.00328	0.461	0.9475	0.8508	0.00363	0.867	0.9279	0.7777
Houston, TX	0.00793	2.826	0.7048	0.6355	0.00638	2.447	0.5156	0.4656	0.00550	2.041	0.5753	0.5126
Lubbock, TX	0.01264	1.865	0.9825	0.7563	0.00313	0.748	0.8162	0.7054	0.00256	0.667	0.7497	0.6907
Midland, TX	0.00630	1.540	0.8610	0.7326	0.00221	0.576	0.9096	0.8308	0.00011	0.696	0.9589	0.8336
Salt Lake City, UT	0.00291	2.363	0.6473	0.6216	0.00018	2.514	0.4472	0.4554	0.00018	2.468	0.6560	0.5824
Norfolk, VA	0.00832	3.355	0.5749	0.5617	0.00465	2.790	0.5124	0.4479	0.00275	3.347	0.3760	0.3734
Richmond, VA	0.01429	3.418	0.5843	0.4519	0.01191	3.164	0.5644	0.4440	0.00376	3.636	0.4685	0.3959
Roanoke, VA	0.00334	3.855	0.6417	0.5454	0.00347	3.256	0.6164	0.4753	0.00012	3.492	0.4649	0.3630
Wallops Is., VA	0.00701	2.541	0.5604	0.5296	0.00502	2.405	0.5639	0.5368	0.00000	3.114	0.5924	0.4585
Washington, DC	0.01304	3.166	0.5105	0.4397	0.00858	3.412	0.5330	0.4355	0.00315	3.837	0.5002	0.3837
Burlington, VT	0.00440	5.482	0.4232	0.3699	0.00389	5.512	0.3891	0.3193	0.00022	4.444	0.5018	0.3407
Blaine, WA	0.01172	4.618	0.5270	0.6740	0.00803	6.478	0.4000	0.5220	0.00389	7.075	0.3160	0.5360
Quillayute, WA	0.01172	11.051	0.5792	0.4498	0.00803	17.778	0.4014	0.2861	0.00389	17.85	0.3577	0.2493
Seattle–Tacoma, WA	0.00223	5.332	0.5731	0.4979	0.00629	9.353	0.4106	0.3439	0.00244	10.306	0.3891	0.3151
Spokane, WA	0.00175	2.517	0.7302	0.6861	0.00014	4.991	0.5358	0.4560	0.00014	5.550	0.4548	0.3623
Walla Walla, WA	0.00000	3.135	0.6341	0.5433	0.00000	4.289	0.4853	0.4983	0.00000	4.566	0.4862	0.4390
Madison, WI	0.01242	3.017	0.5795	0.4983	0.00424	3.299	0.5449	0.4868	0.00021	2.855	0.5325	0.3827
Cheyenne, WY	0.00021	1.739	0.6745	0.6657	0.00021	1.426	0.7711	0.5948	0.00021	0.907	0.7215	0.5547
Lander, WY	0.00030	2.383	0.6853	0.6665	0.00030	1.845	0.7011	0.5764	0.00030	1.120	0.6778	0.5171
Sheridan, WY	0.00019	2.756	0.6062	0.5656	0.00019	1.949	0.4860	0.4106	0.00019	1.504	0.5509	0.4770

Appendix 5.2

Regression Coefficients for Estimating Specific Attenuation[1]

Frequency (GHz)	κ_H	κ_V	α_H	σ_V
1	0.0000387	0.0000352	0.912	0.880
2	0.000154	0.000138	0.963	0.923
4	0.00065	0.000591	1.121	1.075
6	0.00175	0.00155	1.308	1.265
7	0.00301	0.00265	1.332	1.012
8	0.00454	0.00395	1.327	1.310
10	0.0101	0.00887	1.276	1.264
12	0.0188	0.0168	1.217	1.200
15	0.0367	0.0335	1.154	1.128
20	0.0751	0.0691	1.099	1.065
25	0.124	0.113	1.061	1.030
30	0.187	0.167	1.021	1.000
35	0.263	0.233	0.979	0.963
46	0.350	0.310	0.939	0.929
45	0.442	0.393	0.903	0.897
50	0.536	0.479	0.873	0.868
60	0.707	0.642	0.826	0.824
70	0.851	0.785	0.793	0.793
80	0.975	0.906	0.769	0.769
90	1.06	0.999	0.753	0.754
100	1.12	1.06	0.743	0.744

Source: Maggiori, D., Computed transmission through rain in the 1–400 GHz frequency range for spherical and elliptical drops and any polarization, *Alta Frequenza*, L5,262, 1981.

To calculate κ and α for any polarization and local elevation angle, use:[2]

$$\kappa = \frac{\kappa_H + \kappa_V + (\kappa_H - \kappa_V)\cos^2\theta\cos(2\tau)}{2}$$

$$\alpha = \frac{\alpha_H\kappa_H + \alpha_V\kappa_V + (\alpha_H\kappa_H - \alpha_V\kappa_V)\cos^2\theta\cos(2\tau)}{2\kappa}$$

References

1. Maggiori, D., Computed transmission through rain in the 1–400 Ghz frequency range for spherical and elliptical drops and any polarization, *Alta Frequenza*, L5,262, 1981.
2. Nowland, W.L., Olsen, R.L., and Shkarofsky, I.P., Theoretical relationship between rain depolarization and attenuation, *Electron. Lett.*, 13, 676, 1977.